Acta Pharmacologica Sinica (2012) 33: 981–982
 1671-4083/12 $32.00
www.nature.com/aps

Research Highlight

MicroRNAs: novel factors in clinical diagnosis and prognosis for nasopharyngeal carcinoma

Shu YANG, Yao LI*

Acta Pharmacologica Sinica (2012) 33: 981–982; doi: 10.1038/aps.2012.98; published online 2 Jul 2012

Nasopharyngeal carcinoma (NPC) is a non-lymphomatous, squamous cell malignancy arising from the epithelial cells lining of the nasopharynx. Histologically, NPC has been classified into 3 types: keratinizing squamous cell carcinoma (WHO type I), differentiated non-keratinizing squamous cell carcinoma (WHO type II) and undifferentiated carcinomas (WHO type III). Compared to other malignant tumours of the upper aero digestive tract, NPC is a special type of head and neck cancer in terms of epidemiology, pathology and clinical presentation. The etiology of NPC involves multiple factors, including genetic susceptibility, exposure to chemical carcinogens and Epstein-Barr virus (EBV) infection[1]. In some regions, notably the southern parts of China, and parts of Southeast Asia, this cancer occurs in an endemic form with an incidence 10- to 30-fold higher than in the other regions and, histologically, usually belongs to WHO type II and III. In the west, however, NPC occurs sporadically and usually belongs to WHO type I. There is also increased incidence in northern Africa and the Inuit of Alaska[2, 3].

MicroRNAs (miRNAs) are a class of small non-coding RNA molecules, 19–25 nucleotides in length, that negatively regulate gene expression through binding the 3′-untranslated region (3′-UTR) of targeted transcripts, resulting in mRNA cleavage or translation repression[4]. About 30% of human genes are regulated by miRNAs. MicroRNAs are frequently deregulated in many types of cancers, and play critical roles in tumorigenesis, which regulate the expression of oncogenes or tumour suppressor genes.

In a recent issue of *Lancet Oncol*, Liu *et al*[5] reported that 41 miRNAs were differentially expressed between nasopharyngeal carcinoma and non-cancer nasopharyngitis tissues (fold change≥2.5, false discovery rate 0). Previous reports showed that miRNAs were aberrantly expressed in nasopharyngeal carcinoma compared with normal epithelial tissue, and promoted an aggressive tumour phenotype by changing the expression of their mRNA targets[6–8]. For instance, Sengupta *et al*[6] investigated the expressions of 207 miRNAs in 31 NPCs and 10 normal tissues with miRNA microarrays, and demonstrated the involvement of miR-29c in NPC metastasis by regulating mRNAs encoding extracellular matrix proteins. Chen *et al*[7] studied the expression of 270 human miRNAs in 13 NPC samples in comparison with 9 adjacent normal tissues using a stem-loop real-time PCR assay, and found the expressions of 35 miRNAs were significantly altered in NPC, thus inferred that some cancer-related pathways enriched with targets of down-regulated miRNAs. We also demonstrated with microarray that 34 miRNAs were differentially expressed between 8 NPC and 4 normal tissues[8]. Furthermore, we identified 2 novel pathways, targeted by the altered miRNAs, were strongly associated with NPC development, and a c-Myc centred miRNA regulatory network was inferred in NPC. These reports indicate that some important miRNAs can be used as markers for differential diagnosis of NPC from non-cancer nasopharyngitis patients. Interestingly, in all the 4 studies, miR-34c has been found under-expression in NPC specimens, suggesting that that this miRNA plays a crucial role in NPC development and progression. However, the functions of miR-34c were still unclear in NPC. Additionally, 3 out of the 4 reports showed that 3 miRNAs (miR-34b, miR-29c and miR-100) in NPC were down-regulated. Here, we pay attention to the miR-29 family because miR-29a and miR-29b were also under-expressed in NPC as shown in 2 of the 4 reports. We consider that the miR-29 family is important to judge the development and progression of NPC, at least in clinical NPC samples.

Furthermore, Liu and his colleagues established a signature of 5 miRNAs (miR-142-3p, miR-29c, miR-26a, miR-30e and miR-93) from the 41 differentially expressed miRNAs as independent prognostic factors and risk scores in NPC patients. Compared with patients with low-risk scores, patients with high-

State Key Laboratory of Genetic Engineering, School of Life Science, Fudan University, Shanghai 200433, China
Correspondence to: Prof Yao LI
(yaoli@fudan.edu.cn)

risk scores had shorter disease-free survival (DFS), distant metastasis-free survival (DMFS) and overall survival. This finding shows that the miRNAs have significant value for determing the survival prognosis, in addition to judgement of NPC development and progression. It reminds us that miRNAs may be used as makers in NPC classification and allowing clinicians to diagnose patients more early and accurately. In addition, the authors found that patients of TNM stages III–IV with low risk scores had a favourable response to concurrent chemotherapy, while patients of the same stages with high risk scores did not benefit from concurrent chemotherapy. This finding suggests that miRNA signature has more prognostic values in concurrent chemotherapy than TNM staging, although these two classification systems have same predictive ability of patient survival. The TNM staging system provides a useful benchmark for establishing the prognostic definition and treatment strategy. Usually, early-stage NPC patient should be treated with radiotherapy, whereas patient with advanced disease should receive chemoradiotherapy. However, large variations in the clinical outcomes were found in patients with the same stage and similar treatment regimens[9]. It is suggested that the present staging system is inadequate for definition of prognosis. Thus, a novel signature, independent of TNM staging, is needed for predictive of survival of patients with NPC and allowing clinicians to potentially identify candidates for aggressive therapy to improve treatment outcomes. Combination of the five-miRNA signature and TNM stage has a better prognostic value than did TNM stage alone in the NPC patients.

As the important roles of miRNAs in cancer are gradually revealed, their potential applications as predictive markers and treatment targets have generated great interest in cancer diagnosis, as well as classification, prognosis, risk factor evaluations and therapy strategies. The result of Liu *et al* provide a new insight into NPC development and progression, and have potential implication in NPC patients survival prognosis and personalised therapy.

1 Wei WI, Sham JS. Nasopharyngeal carcinoma. Lancet 2005; 365: 2041–54.
2 Yu MC, Yuan JM. Epidemiology of nasopharyngeal carcinoma. Semin Cancer Biol 2002; 12: 421–9.
3 Nielsen NH, Mikkelsen F, Hansen JP. Nasopharyngeal cancer in Greenland. The incidence in an Arctic Eskimo population. Acta Pathol Microbiol Scand A 1977; 85: 850–8.
4 Bartel DP. MicroRNAs: target recognition and regulatory functions. Cell 2009; 136: 215–33.
5 Liu N, Chen NY, Cui RX, Li WF, Li Y, Wei RR, *et al*. Prognostic value of a microRNA signature in nasopharyngeal carcinoma: a microRNA expression analysis. Lancet Oncol 2012; 13: 633–41.
6 Sengupta S, den Boon JA, Chen IH, Newton MA, Stanhope SA, Cheng YJ, *et al*. MicroRNA 29c is down-regulated in nasopharyngeal carcinomas, up-regulating mRNAs encoding extracellular matrix proteins. Proc Natl Acad Sci U S A 2008; 105: 5874–8.
7 Chen HC, Chen GH, Chen YH, Liao WL, Liu CY, Chang KP, *et al*. MicroRNA deregulation and pathway alterations in nasopharyngeal carcinoma. Br J Cancer 2009; 100: 1002–11.
8 Li T, Chen JX, Fu XP, Yang S, Zhang Z, Chen KhH, *et al*. microRNA expression profiling of nasopharyngeal carcinoma. Oncol Rep 2011; 25: 1353–63.
9 Mao YP, Xie FY, Liu LZ, Sun Y, Li L, Tang LL, *et al*. Re-evaluation of 6th edition of AJCC staging system for nasopharyngeal carcinoma and proposed improvement based on magnetic resonance imaging. Int J Radiat Oncol Biol Phys 2009; 73: 1326–34.

Acta Pharmacologica Sinica (2012) 33: 983–990
 1671-4083/12 $32.00
www.nature.com/aps

Original Article

Sulfur dioxide attenuates LPS-induced acute lung injury via enhancing polymorphonuclear neutrophil apoptosis

Hui-jie MA[1], Xin-li HUANG[2, *], Yan LIU[3], Ya-min FAN[2]

[1]Department of Physiology, Hebei Medical University, Shijiazhuang 050017, China; [2]Department of Pathophysiology, Hebei Medical University, Shijiazhuang 050017, China; [3]Department of Endocrinology, the Third Hospital of Hebei Medical University, Shijiazhuang 050051, China

Aim: We speculated that the enhanced apoptosis of polymorphonuclear neutrophil (PMN) might be responsible for the inhibition of PMN infiltration in the lung. This study was designed to investigate the effects of sulfur dioxide (SO_2) on PMN apoptosis *in vivo* and *in vitro*, which may mediate the protective action of SO_2 on pulmonary diseases.
Methods: Acute lung injury (ALI) was induced by intratracheally instillation of lipopolysaccharide (LPS, 100 μg/100 g, in 200 μL saline) in adult male SD rats. SO_2 solution (25 μmol/kg) was administered intraperitoneally 30 min before LPS treatment. The rats were killed 6 h after LPS treatment. Lung tissues were collected for histopathologic study and SO_2 concentration assay. Bronchoalveolar lavage fluid (BALF) was collected for the measurement of PMN apoptosis. For *in vitro* experiments, rat peripheral blood PMNs were cultured and treated with LPS (30 mg/L) and SO_2 (10, 20 and 30 μmol/L) for 6 h, and apoptosis-related protein expression was detected by Western blotting, and apoptosis rate was measured with flow cytometry.
Results: LPS treatment significantly reduced the SO_2 concentrations in the lung tissue and peripheral blood, as compared with the control group. Pretreatment with SO_2 prevented LPS-induced reduction of the SO_2 concentration in the lung tissue and peripheral blood. LPS treatment significantly reduced PMN apoptosis both *in vivo* and *in vitro*, which could be prevented by the pretreatment with SO_2. The protein levels of caspase-3 and Bax was significantly increased, but Bcl-2 was decreased by the pretreatment with SO_2, as compared with LPS administration alone.
Conclusion: SO_2 plays an important role as the modulator of PMN apoptosis during LPS-induced ALI, which might be one of the mechanisms underlying the protective action of SO_2 on pulmonary diseases.

Keywords: acute lung injury; bronchoalveolar lavage fluid (BALF); lipopolysaccharide; SO_2; apoptosis; polymorphonuclear granulocyte

Acta Pharmacologica Sinica (2012) 33: 983–990; doi: 10.1038/aps.2012.70; published online 16 Jul 2012

Introduction

Acute lung injury (ALI) induced by sepsis and its severe form, acute respiratory distress syndrome (ARDS), are still major causes of morbidity and mortality in clinics[1]. It is generally accepted that ALI is an excessive, uncontrolled inflammatory response within the lung[2]. Inhibiting different stages of ALI with drugs or therapy, along with enhancing the body's own resistance, would delay or mitigate lung injury and minimize the mortality associated with ALI[1, 2].

Gas transmitters such as nitric oxide (NO), carbon monoxide (CO) and hydrogen sulfide (H_2S) play important roles in both physiological and pathological conditions[3–7]. In recent years, interest has been directed towards another naturally occurring gas, sulfur dioxide (SO_2). SO_2 was previously considered a toxic gas, but it has been subsequently shown to be produced endogenously during the metabolism of sulfur-containing amino acids[8]. SO_2 was also previously considered a risk factor for respiratory and cardiovascular disease[9]. Recently, studies have shown that SO_2 plays important pathophysiologic roles during many disease processes, including the attenuation of monocrotaline-induced pulmonary hypertension, the inhibition of hypoxic pulmonary vascular structural remodeling, protection against isoproterenol-induced myocardial injury, and the increase of myocardial antioxidant capacity[10–12]. However, the effects of SO_2 on ALI and its mechanisms are poorly understood.

* To whom correspondence should be addressed.
E-mail mm564300@sina.com
Received 2012-02-01 Accepted 2012-05-11

Our previous study revealed that the administration of SO_2 derivatives alleviated the degree of LPS-induced ALI and reduced the number of polymorphonuclear granulocytes (PMN) in bronchoalveolar lavage fluid (BALF), whereas SO_2 administered alone did not result in functional and morphological changes in rat lungs[13]. PMNs are important inflammatory cells that are implicated in excessive inflammatory responses[2, 14]. Studies have shown that there exists an inhibition and delay in PMN apoptosis in lung tissue during ALI. The delay in apoptosis may lead to the prolonged release of PMN products and direct tissue injury, which then participate in the development of ALI[15]. Therefore, the inhibition of PMN apoptosis leads to inflammation and lung tissue damage, whereas the enhancement of PMN apoptosis may reduce lung inflammation and damage[16]. We speculated that the enhancement of PMN apoptosis might be responsible for the inhibition of PMN infiltration in the lung, thereby mediating the protective effect of SO_2. The aim of this study was to investigate the role of PMN apoptosis in the protective effect of SO_2 in LPS-induced ALI.

Materials and methods

Induction of ALI

All experiments were approved by the Animal Ethics Committee of Hebei Medical University and were carried out in accordance with established guiding principles for animal research. Adult male Sprague Dawley (SD) rats (250–300 g) provided by the Experimental Animal Center of Hebei Province (Shijiazhuang, China) were randomly divided into four groups: control group, SO_2 group, LPS group and LPS plus SO_2 group. The rats were anesthetized via intraperitoneal injections of pentobarbital (50 mg/kg). The control rats were instilled intratracheally with 200 μL normal saline. LPS-treated animals received 200 μL LPS (*Escherichia coli* 055:B5; Sigma-Aldrich Co, St Louis, MO, USA) by intratracheal instillation (100 μg/100 g of body weight, dissolved in 200 μL saline). For the LPS group, LPS was evenly sprayed into both lungs using a microsprayer and laryngoscope for rats (Penn-Century Inc, Philadelphia, PA, USA). For the SO_2 group, 25 μmol/kg SO_2 saline solution was administered intraperitoneally. For the LPS plus SO_2 group, 25 μmol/kg SO_2 saline solution was administered intraperitoneally 30 min before LPS treatment.

For SO_2 solution preparation, pure SO_2 gas (purity: 99.99%, Beijing He-Pu-Bei-Fen Gas Company, Ltd, Beijing, China) was used in this study. The SO_2 solution was freshly prepared before each experiment by bubbling saline with pure SO_2 gas, and it was then diluted to achieve a solution containing the desired SO_2 concentration according to the method described by Zhang *et al*[17].

Histopathologic analyses and ratio of lung wet weight to dry weight (Rw/d)

For histopathologic analyses, excised lung tissues were fixed and then embedded in paraffin and routinely stained with hematoxylin and eosin. Inflammation and alveolar edema were graded as none, mild, moderate, or severe. The level of lung injury was determined based on the degree of cellular and protein exudation and tissue hemorrhage and was assigned a score between 0 (normal) and 3 (severely damaged), as previously described by Kristof *et al*[18]. The severity of lung injury was scored by pulmonologists who were blind to the treatment. Briefly, 10 fields were randomly selected from three lung tissue sections per rat and were examined under a microscope at 200× magnification. The degree (or score) of cellular and protein exudation and tissue hemorrhage per rat were individually determined by adding the scores from 10 randomly selected fields. The total lung injury score per rat was determined as the sum of three individual scores for alveolar cellularity, protein exudation and tissue hemorrhage.

A portion of lung tissue was weighed and placed into an 80 °C oven to be dried completely, and the Rw/d was then calculated.

Measurement of SO_2 concentrations in lung tissue and blood

The right lung samples were homogenized and immediately subjected to sample preparation according to the method established by Sun *et al* and Mitsuhashi *et al*[11, 19]. Lung or blood samples (100 μL) were mixed with 70 μL of 0.212 mol/L sodium borohydride in 0.05 mol/L Tris-HCl (pH 8.5) and incubated at room temperature for 30 min. The samples were then mixed with 10 μL of 70 mmol/L monobromobimane in acetonitrile. After incubation for 10 min at 42 °C, 40 μL of 1.5 mmol/L perchloric acid solution was added to the mixture, followed by vortex mixing. The protein precipitates were removed by centrifugation at 12400×*g* for 10 min at room temperature. The supernatant was immediately neutralized by adding 10 μL of 2 mmol/L Tris (pH 3.0). It was then gently mixed and centrifuged again at 12400×*g* for 10 min. Ten microliters of the neutralized supernatant was injected into an HPLC column (Hitachi 655-A11 system, Japan). All sample preparation procedures were completed within 2 h after tissue sample homogenization. Serum sulfite was determined using reversed phase HPLC with fluorescence detection. The samples were resolved on a 4 mm×250 mm C8 reversed phase column (5 μm packing, GL Science, Tokyo, Japan). The column was equilibrated with methanol/acetic acid/water (5.00:0.25:94.75, by volume, pH 3.4) and developed with a gradient of methanol at a flow rate of 0.8 mL/min as follows: 0–5 min, 30 mL/L; 5–13 min, 30–500 mL/L; 13–30 min, 350–620 mL/L; 30–31 min, 620–1000 mL/L; 31–39 min, 1000 mL/L; 39–40 min, 1000–30 mL/L; and 40–46 min, 30 mL/L. Sulfite-bimane was detected by excitation at 390 nm and emission at 472 nm with the use of a cutoff filter and eluted at 45 mL/L of methanol concentration.

Isolation and purification of PMNs in BALF

The isolation and purification of BALF were performed after the rats were killed. BALF was collected and centrifuged, and the sediment was collected and then resuspended in RPMI-1640 medium containing 10% calf serum. The cell suspension was cultured in the incubator (37 °C, 5% CO_2) for 2 h. The

attached cells in the culture dish were discarded and suspension cells were collected for further purification. BALF neutrophils were isolated using a two-step Percoll gradient (1080 g/mL followed by 1090 g/mL) centrifugation method. The purity of the PMNs isolated by gradient centrifugation was greater than 98% (identified using Wright's staining), and the cell survival rate was more than 95% (identified using trypan blue). PMN apoptosis was further detected by acridine orange/ethidium bromide (AO/EB, Sigma-Aldrich Co, St Louis, MO, USA) staining and flow cytometry (FCM).

PMN apoptosis by AO/EB staining and FCM

A fluorescent assay with AO/EB double staining was used[20] to display the morphological alterations of apoptotic PMNs in BALF. The BALF PMNs were suspended in PBS (pH 7.2) and aliquoted for the staining procedure. One microliter of the dye mixture (100 mg/mL AO and 100 mg/mL EB in distilled water) was mixed with 9 mL of cell suspension on a clean microscope slide and examined immediately by fluorescence microscopy at 400× magnification. A minimum of 500 cells was counted in every sample. The percentage of apoptotic cells was defined as the average number of apoptotic cells per 100 counted cells.

FCM was performed as previously described[21]. The BALF PMNs were double-labeled with Annexin V-FITC/PI. Approximately 5000 cells from each sample were measured by flow cytometry with an excitation wavelength of 488 nm and emission wavelengths of 515 nm and 610 nm. Annexin V-positive cells were considered viable apoptotic cells (early apoptotic cells), propidium iodine (PI)-positive cells were defined as necrotic cells, and Annexin V and PI double positive cells were defined as non-viable apoptotic cells (late apoptotic cells). Because PMNs were absent from the BALF of the control group, we replaced BALF with peripheral blood in the analysis of the control group according to Feng *et al*[16].

Preparation of rat lymphocyte separating medium

The separating medium was prepared according to the method described by Feng *et al*[16]. Solution A (9% Ficoll solution): 3.4 parts normal saline was added to 1 part 40% Ficoll and mixed thoroughly. Solution B (34% diatrizoate meglumine solution): 24.71 mL normal saline was added to 20 mL 76% diatrizoate meglumine solution and mixed thoroughly. Ten parts of solution A and 5.5 parts of solution B were mixed thoroughly. A Baumé hydrometer was used to measure the specific density of the mixture. The specific density of the solution was adjusted to 1.084 by adding solution A or solution B. A G6 fritted-glass filter was applied to filtrating sterilization. The lymphocyte separating medium was stored at 4 °C in dark. Ficoll and sodium diatrizoate hydrate were purchased from Sigma-Aldrich Co (St Louis, MO, USA).

Isolation and purification of peripheral blood PMNs

Heparinized venous blood (4 mL per rat) was collected by jugular vein catheterization. Density gradient centrifugation was applied to isolate and purify the PMNs in peripheral blood using lymphocyte separating medium. The cell suspension and the thin film layer (containing mononuclear cells) were discarded. The sediment was collected, and erythrocyte lysis buffer was applied to remove the red blood cells. After the sediment was washed with D-Hanks' buffer three times and then centrifuged (2000 r/min×10 min each), the PMN sediment was resuspended at 5×10^6 cells/mL in RPMI-1640 (containing 10% calf serum) in preparation for further treatment.

Peripheral blood PMN cell culture and evaluation of PMN apoptosis by FCM

Peripheral blood PMNs were cultured in RPMI-1640 medium at 37 °C in 5% CO_2 and treated with 30 mg/L LPS and different concentration of SO_2 (10, 20, and 30 μmol/L SO_2) *in vitro* for 6 h for the detection of apoptosis-related protein expression using the Western blotting method. To determine the rate of apoptosis, PMNs were cultured for 24 h and then submitted to FCM. After culture, the cell suspension was centrifuged, washed and resuspended for western blotting analysis and FCM. FCM for the peripheral blood PMNs was performed as described above for the BALF cells.

Western blotting analysis of apoptosis-related protein expression in peripheral blood PMNs

To measure the Caspase-3, Bax, and Bcl-2 protein expression levels by western blotting, cellular proteins were extracted from the peripheral blood PMNs of rats, as previously described[22]. The PMNs were pelleted and lysed in 1×Laemmli-buffer [2% (*wt*/*vol*) SDS, 6% (*vol*/*vol*) 2-mercaptoethanol, 10% (*vol*/*vol*) glycerol, and a trace amount of bromophenol blue in 200 mmol/L Tris-HCl, pH 7.5]. The samples were immediately heated for 5 min at 100 °C. The concentration of the proteins was determined using the BCA method. Samples containing 50 μg of total protein were subjected to SDS-PAGE on gels containing 12% (*wt*/*vol*) acrylamide and then transferred to a polyvinylidene difluoride membrane. Nonspecific binding sites were blocked with TBST (40 mmol/L Tris, pH 7.6, 300 mmol/L NaCl, 0.1% Tween 20) containing 5% nonfat dry milk for 12 h at 4 °C. The membranes were incubated in rabbit polyclonal anti-rat antibodies to Caspase-3, Bax, and Bcl-2 (1:500, Santa Cruz Biotechnology, Santa Cruz, CA, USA) and a mouse anti-rat antibody to β-actin (diluted 1:10 000 in 0.01 mol/L PBS, Santa Cruz Biotechnology, Santa Cruz, CA, USA). After the membranes were washed three times in TBST, they were then incubated in a 1:5000 dilution of HRP-conjugated goat anti-rabbit IgG (Amersham-Pharmacia Biotech, UK). After again washing with TBST, the membranes were incubated with horseradish peroxidase-conjugated streptavidin (diluted 1:4000 in 0.01 mol/L PBS, Zymed, USA) for 1 h at 37 °C. The immunoreactions were visualized using an ECL detection kit (Pierce, Thermo Scientific, USA). The X-ray film was scanned by an image documentation system (Labworks Inc, USA). The integral optical density (IOD) of each band was measured using a gel image analysis system (Alpha Image 2200, Alpha, USA). The changes in the relative expression of Caspase-3, Bax, and Bcl-2 were represented by the ratio of the

band's IOD of Caspase-3, Bax, and Bcl-2 compared to β-actin.

Statistical analysis

All data were expressed as the mean±SD. Comparisons between groups were performed using analysis of variance (ANOVA) followed by the Student Newman-Keuls test using SPSS 13.0 statistical analysis software. *P* values less than 0.05 were considered statistically significant.

Results

Effects of SO_2 on LPS-induced lung damage

In control rats and rats given SO_2 alone rats, few infiltrating PMN cells were observed, and there was no evidence of hemorrhage or edema (Figure 1Aa and 1Ab). In contrast to the control group, patching hemorrhage was observed at 6 h after LPS infusion. Typical pathologic alterations induced by LPS were also observed, including the accumulation of inflammatory cells in the alveolar space, interalveolar septum thickening, edema of the lung interstitium and alveoli, interstitial and intra-alveolar hemorrhage, and even some alveolus atelectasis and fusion (Figure 1Ac). Meanwhile, compared with the control group, LPS treatment led to a significant increase in the total lung injury score and the Rw/d 6 h after LPS treatment ($P<0.01$, Figure 1B and 1C). SO_2 pretreatment may partially protect the lung tissue from damage induced by LPS (Figure 1 Ad) and may prevent the increased total lung injury score and Rw/d ($P<0.05$, Figure 1B and 1C). SO_2 alone had no significant effect on total lung injury score and lung weight ($P>0.05$, Figure 1B and 1C).

Changes in SO_2 concentration in the different treatment groups

Compared with the control group, the SO_2 concentration in the lung tissue and peripheral blood decreased at 6 h after LPS treatment. Pretreatment with SO_2 significantly elevated the SO_2 concentration compared with that of the LPS group ($P<0.05$, Figure 2). Our results indicate that the reduction of endogenous SO_2 production may participate in the development of ALI and exogenously supplemented SO_2 may ameliorate lung injury.

PMN apoptosis observed by AO/EB staining and FCM

AO/EB staining indicated that alveolar macrophages were predominant, but PMNs were absent in the BALF of control rats (Figure 3Aa). Apoptotic PMNs were found in the BALF of LPS-treated rats, but only a few early apoptotic PMNs, which were characterized by strong nuclear green fluorescence staining, were observed (Figure 3Ab). Compared with the control group, LPS treatment also led to a significant reduction in PMN apoptosis in BALF, as determined by FCM ($P<0.05$, Figure 3B). However, a large number of apoptotic PMNs were found in the lungs of SO_2-treated rats, which were characterized by condensed and fragmented nuclear staining by orange EB (Figure 3Ac). The percentage of apoptotic PMN cell determined by FCM was also significantly increased in the LPS plus SO_2 group compared with the group treated only with LPS ($P<0.05$, Figure 3B).

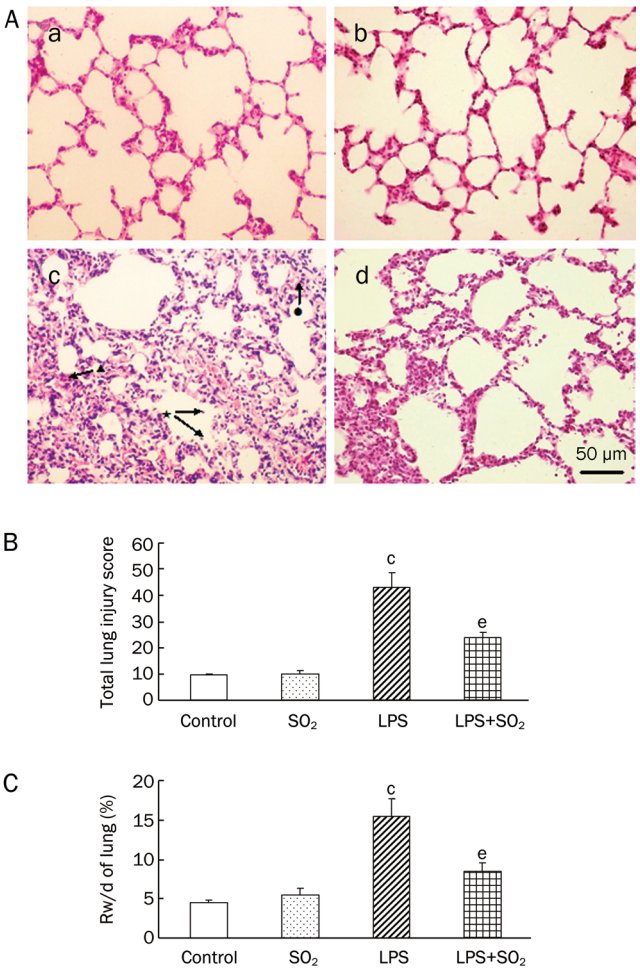

Figure 1. Morphological and lung Rw/d changes in lungs at 6 h after the induction of ALI with or without SO_2 pretreatment. (A) Morphological changes in the lung by H&E staining. a) Control group with normal lung morphology; b) SO_2 administration alone with lung morphology similar to the control group; c) Six hours after induction of LPS-induced ALI we observed patching hemorrhage and inflammatory cell accumulation in the alveolar space (★), interalveolar septum thickening (●), edema of lung interstitium and alveoli, interstitial and intra-alveolar hemorrhage (▲), and even some alveolus atelectasis and fusion; d) SO_2 pretreatment ameliorated the lung injury induced by LPS. Scale bar, 50 μm. (B) Effect of SO_2 on the total lung injury score. (C) Effect of SO_2 on lung Rw/d 6 h after intratracheal instillation of LPS. Data are presented as the mean±SD ($n=7$ in each group). $^cP<0.01$ compared with the control group; $^eP<0.05$ compared with the LPS group.

In the peripheral blood, the changes of apoptotic PMNs were similar to those observed in BALF. The percentage of apoptotic PMNs was reduced in the LPS treatment group, whereas the percentage increased in the SO_2 plus LPS group relative to the group treated with LPS alone ($P<0.05$ or $P<0.01$, Figure 3C).

Effect of SO_2 on apoptosis-related protein expression

Compared with the control group, LPS treatment significantly decreased Caspase-3 (Figure 4) and Bax (Figure 5) protein expression in the peripheral blood PMNs of rats, whereas

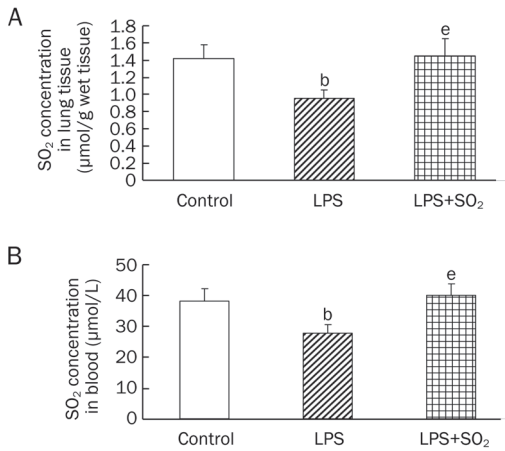

Figure 2. Changes in SO_2 concentration in the lung tissue (A) and peripheral blood (B) 6 h after intratracheal instillation of LPS. Data are presented as the mean±SD (n=6 in each group). ^bP<0.05 compared with the control group; ^eP<0.05 compared with the LPS group.

Bcl-2 (Figure 6) protein levels increased. The effects of LPS were significantly reversed by the administration of SO_2 in a concentration-dependent manner (P<0.05 or P<0.01, Figure 4, 5 and 6).

Discussion

In the present study, we found that SO_2 enhanced PMN apoptosis in LPS-induced ALI. We also found that the SO_2 content decreased in ALI, and exogenously administered SO_2 significantly increased the SO_2 levels in the lung tissue compared with the LPS group. These results suggest that the down-regulation of endogenous SO_2 results in the inhibition and delay of PMN apoptosis during ALI might be involved in the pathogenesis of LPS-induced ALI, which may be reversed by SO_2. Moreover, our results showed that the SO_2 levels in control plasma was 38.12±4.13 μmol/L, so the SO_2 concentration selected in our study was within a physiological concentration range.

ALI is a life-threatening disease that often leads to acute hypoxemic respiratory failure with intensive pulmonary inflammation, accompanied by various cellular and molecular changes[23, 24]. The pathogenesis of endotoxin-induced ALI remains obscure and has not yet been fully elucidated. However, it is generally accepted that PMNs have well characterized effects on the pathogenesis of LPS-induced lung injury, and PMN accumulation in the lung is the key pathological basis for the development of ALI[2, 14]. PMNs are vital to the body's defense against infections. However, the uncontrolled release of their formidable array of toxic substances may inflict damage on the surrounding tissues and propagate inflammatory responses, leading to tissue scarring and destruction. Normally, PMNs are removed by apoptosis to limit their activation[25]. When PMNs die by apoptosis, they retain their granular contents but lose chemotactic and secretory responsiveness. These PMNs are recognized and phagocytosed by

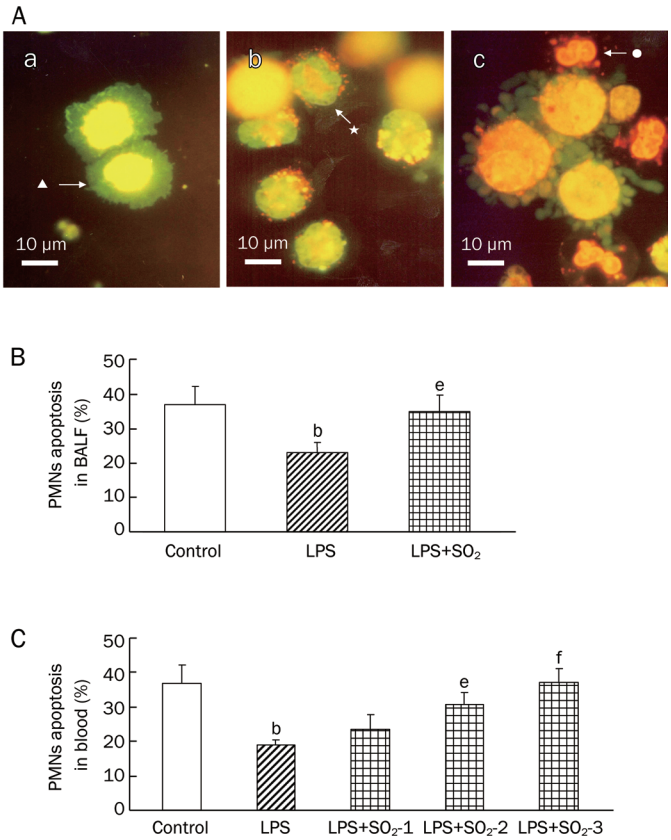

Figure 3. PMN apoptosis determined by AO/EB-staining and FCM at 6 h after induction of ALI with or without SO_2 pretreatment. (A) PMN apoptosis determined by AO/EB-staining in BALF. a) No apoptotic PMNs, only alveolar macrophages (▲), were observed in the lungs of control rats; b) Only a few early apoptotic PMNs (★) were observed (strong nuclear green fluorescence staining) in the LPS group. c) A large number of apoptotic PMNs (●) were found in the lungs of rats pretreated with SO_2 before LPS administration (LPS+SO_2) rat. Condensed and fragmented nuclear were stained by orange EB and apoptotic PMNs in LPS+SO_2 group. Scale bar, 10 μm. (B) The percentage of apoptotic PMN cells in BALF, as determined by flow cytometry. Control, control group; LPS, LPS administration group; LPS+SO_2 refers to SO_2 pretreatment before LPS administration. (C) The percentage of apoptotic PMNs in the peripheral blood, as determined by flow cytometry. SO_2-1, pretreatment with 10 μmol/L SO_2; SO_2-2, pretreatment with 20 μmol/L SO_2; SO_2-3, pretreatment with 30 μmol/L SO_2. Because PMNs were absent in the BALF of the control group, we replaced BALF with peripheral blood for the control group. Data are presented as the mean±SD (n=7 in each group). ^bP<0.05 compared with the control group; ^eP<0.05, ^fP<0.01 compared with the LPS group.

macrophages. Thus, by down-regulating the potentially harmful PMN functions and triggering their clearance by phagocytes, apoptosis provides a mechanism for the safe removal of inflammatory cells[25]. Moreover, studies in recent years have shown that the inhibition and delay of PMN apoptosis occurs in the lung tissue during ALI, which leads to the prolonged release of PMN products and direct tissue injury[15]. Inhibiting the delay in apoptosis of PMN may ameliorate the lung injury.

SO_2 and its derivatives were previously considered systemic

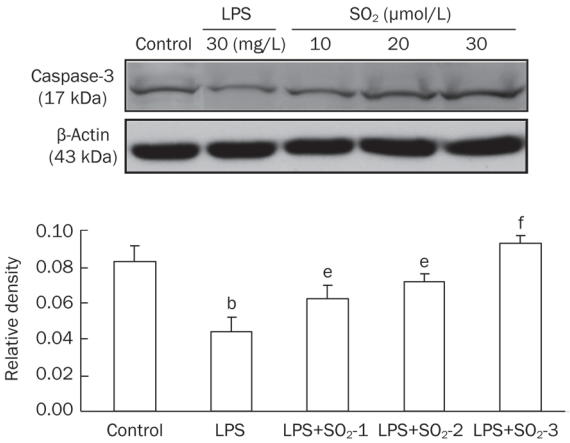

Figure 4. Protein expression of Caspase-3 extracted from the peripheral blood PMNs of rats in the different groups. The upper panels are Western blots, and the lower panels are summaries of the densitometric analysis of Caspase-3 protein expression in the different groups. Control, control group; LPS, LPS administration group; LPS+SO_2-1, pretreatment with 10 μmol/L SO_2 before LPS administration; LPS+SO_2-2, pretreatment with 20 μmol/L SO_2 before LPS administration; LPS+SO_2-3, pretreatment with 30 μmol/L SO_2 before LPS administration. Data are shown as the mean±SD (n=6 rats in each group). ^{b}P<0.05 compared with the control group; ^{e}P<0.05, ^{f}P<0.01 compared with the LPS group.

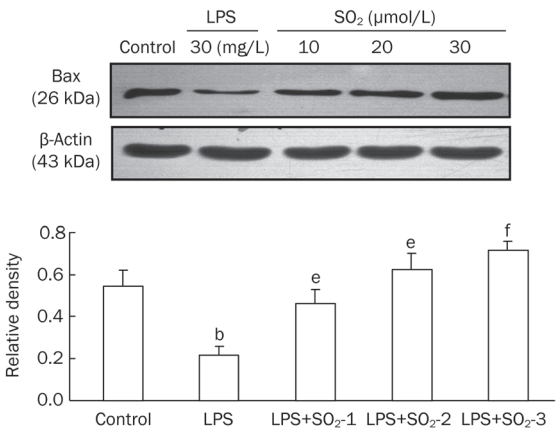

Figure 5. Protein expression of Bax extracted from the peripheral blood PMNs of rats in the different groups. The upper panels are Western blots, and the lower panels are summaries of the densitometric analysis of Bax protein expression in the different groups. Control, control group; LPS, LPS administration group; LPS+SO_2-1, pretreatment with 10 μmol/L SO_2 before LPS administration; LPS+SO_2-2, pretreatment with 20 μmol/L SO_2 before LPS administration; LPS+SO_2-3, pretreatment with 30 μmol/L SO_2 before LPS administration. Data are shown as the mean±SD (n=6 rats in each group). ^{b}P<0.05 compared with the control group; ^{e}P<0.05, ^{f}P<0.01 compared with the LPS group.

toxic agents that can cause many types of toxic effects, such as chromosomal aberrations, micronuclei, sister-chromatid exchanges[19, 26–29], gene mutations[30], lipid peroxidative damage[31], DNA damage[32, 33], and changes in some enzyme activities[34] in multiple organs in mice and rats. Studies have also indicated that SO_2 inhalation can also cause gene expression changes and alter cytokine levels in the rat lung[35]. However, increasing attention has recently been paid to understanding its physiological roles in biological cells and its role in the pathology of various diseases. Endogenous SO_2 was found to be generated during cysteine metabolism in many types of mammalian cells. It was found that the SO_2 derivatives as physiological condition are a neuron modulator in rat hippocampal neurons[36] and dorsal root ganglion (DRG) neurons[37–39] and can also function as cardiovascular modulators in cardiomyocytes[40–42] by affecting their ion channels. Studies have also showed that SO_2 and its derivatives can cause a significant decrease in rat blood pressure *in vivo* and the vasorelaxation of rat blood vessel rings *in vitro*[30, 43]. However, as a biological mediator, its role in ALI needs to be clarified.

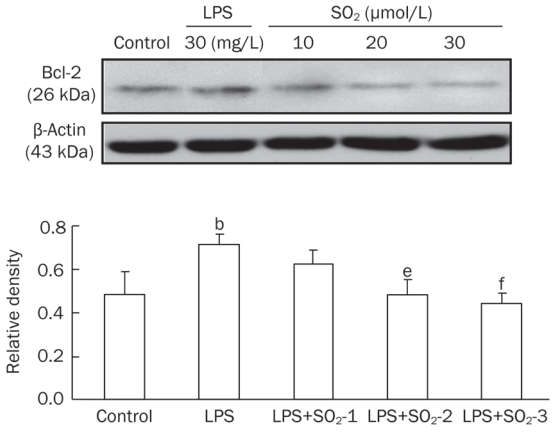

Figure 6. Protein expression of Bcl-2 extracted from the peripheral blood PMNs of rats in the different groups. The upper panels are Western blots, and the lower panels are summaries of the densitometric analysis of Bcl-2 protein expression in the different groups. Control, control group; LPS, LPS administration group; LPS+SO_2-1, pretreatment with 10 μmol/L SO_2 before LPS administration; LPS+SO_2-2, pretreatment with 20 μmol/L SO_2 before LPS administration; LPS+SO_2-3, pretreatment with 30 μmol/L SO_2 before LPS administration. Data are shown as the mean±SD (n=6 rats in each group). ^{b}P<0.05 compared with the control group; ^{e}P<0.05, ^{f}P<0.01 compared with the LPS group.

In our previous study, we demonstrated that SO_2 derivatives play an important role in the development LPS-induced ALI[4]. Our results showed that the administration of SO_2 derivatives to LPS-treated rats reduced the lung weight/body weight ratio, PMN number, ICAM-1 expression and IL-1, IL-6 and IL-10 levels, and alleviated the degree of ALI. In the present study, we found that treatment with a physiological concentration of SO_2 solution can attenuate the inflammatory response and reverse the increased lung Rw/d induced by LPS treatment. However, there were no significant differences in the above parameters between the rats treated with SO_2 alone and the control rats. The results indicate that the concentration used in our experiment had no toxic effects on

the lung. More interestingly, it has been reported that SO_2 can induce the apoptosis of hippocampal neurons[44] and enhance the apoptosis of smooth muscle cells in spontaneously hypertensive rats (SHRs)[45]. As of yet, there are no reports indicating whether a low dose of SO_2 can induce PMN apoptosis while ameliorating lung injury.

The present study provides new evidence that there is a certain correlation between SO_2 and PMN apoptosis, which was inhibited and delayed in LPS-induced acute lung injury. LPS challenge overwhelmingly inhibited the apoptosis of PMNs in the BALF and peripheral blood in ALI rats, indicating that an inhibition and delay of PMN apoptosis during LPS-induced ALI. FCM revealed that the changes in the percentage of apoptotic PMNs were similar in the peripheral blood and BALF. These results showed that PMNs emigrate from blood vessels to the lung and remain highly active in releasing their noxious contents, thus triggering lung tissue damage. The living PMNs adhere to endothelial cells and release inflammatory mediators and destructive toxic substances, damaging blood vessels and surrounding tissues[2, 15]. On the other hand, secondary necrotic PMNs release toxic products such as active oxygen, free radicals and lysosomal enzyme, causing tissue damage[14, 15, 46]. The accidents may result in systemic inflammatory response syndrome (SIRS) or even multiple organ dysfunction syndrome (MODS)[15]. SO_2 treatment could enhance the apoptosis of PMNs in the BALF of rats, which could indicate that SO_2 can play an important role as a modulator in PMN apoptosis during LPS-induced acute lung injury.

Because we discovered that a physiological concentration of SO_2 can improve lung injury by promoting PMN apoptosis, we need to further explore the mechanism by which it promotes apoptosis. The mammalian Bcl-2 family of apoptosis-associated proteins consists of members that inhibit apoptosis (Bcl-2, Bcl-xL, Mcl-1, A1, *etc*) and others that induce apoptosis (Bax, Bak, Bad, Bcl-xs, Bik, *etc*), and the balance between pro-apoptotic and anti-apoptotic members determines the fate of the cells in many systems. The Bcl-2 family regulates apoptosis by controlling the activity of caspases, the executioners of apoptosis, via the release of cytochrome *c* from mitochondria[22]. Caspases are a family of cysteine proteases that exist in normal cells as inactive enzymes. They are activated by sequential proteolytic events that lead to the degradation or functional alteration of cellular proteins, which contributes to cell death, characterized by the typical apoptotic morphology. Caspase-3 activation is one of the main requirements for the execution phase of apoptosis[25]. To further investigate the molecular mechanisms of PMN apoptosis, we assessed Caspase-3, Bax, and Bcl-2 protein expression in PMNs. In LPS-induced ALI, PMNs emigrated from the blood vessels to the lung, and the reactions of PMNs in BALF and the peripheral blood were similar in our study. Because alveolar macrophages were predominant but PMNs were absent in normal rat BALF, we substituted BALF PMNs with peripheral blood PMNs for our apoptosis-related protein expression study *in vitro*. After co-incubation with different doses of SO_2 (10, 20, and 30 μmol/L), the expression of apoptosis-related genes changed. The present study indicated that SO_2 modulates the expression of apoptosis-related proteins and then enhances PMN apoptosis, thereby alleviating LPS-induced ALI. Performing the research *in vitro* obviated the influence of the complex internal environment and directly reflected the impact of SO_2 on PMN apoptosis.

In summary, our study demonstrates that physiological concentrations of SO_2 play an important role as a modulator in the inhibition and delay of PMN apoptosis during LPS-induced ALI. The modulation of SO_2 may be one of the important mechanisms for LPS-induced ALI. SO_2-targeted treatment may bring new light to the prevention and treatment of LPS-induced ALI. This study may provide a basis for the development of drugs about increasing endogenous SO_2 in the body and provide new ideas for the clinical treatment of ALI.

Acknowledgements

This research program was supported by the National Natural Science Foundation of China (No 81070050 and 30800440) and the Natural Science Foundation of Hebei Province (No C2007000830, C2008001040, and H2012206009).

Author contribution

Xin-li HUANG designed the study; Hui-jie MA, Yan LIU, and Ya-min FAN performed the research; Yan LIU analyzed the data; and Hui-jie MA wrote the paper.

References

1 Kneyber MC, Markhorst DG. Management of acute lung injury and acute respiratory distress syndrome in children: a different perspective. Crit Care Med 2009; 37: 3191–2.
2 Fujishima S, Aikawa N. Neutrophil-mediated tissue injury and its modulation. Intensive Care Med 1995; 21: 277–85.
3 Arias-Diaz J, Villa N, Hernandez J, Vara E, Balibrea JL. Carbon monoxide contributes to the cytokine-induced inhibition of surfactant synthesis by human type II pneumocytes. Arch Surg 1997; 132: 1352–60.
4 Huang XL, Ma HJ, Zhou XH, Fan YM, Xian XH, Cao H. Effect of exogenous hydrogen sulfide on polymorphonuclear neutrophil accumulation in acute lung injury rat induced by lipopolysaccharides and its mechanism. Zhongguo Ying Yong Sheng Li Xue Za Zhi 2010; 26: 477–80.
5 Huang XL, Zhou XH, Zhou JL, Ding CH, Xian XH. Role of polymorphonuclear neutrophil in exogenous hydrogen sulfide attenuating endotoxin-induced acute lung injury. Sheng Li Xue Bao 2009; 61: 356–60.
6 Connelly L, Palacios-Callender M, Ameixa C, Moncada S, Hobbs AJ. Biphasic regulation of NF-kappa B activity underlies the pro- and anti-inflammatory actions of nitric oxide. J Immunol 2001; 166: 3873–81.
7 Morisaki H, Katayama T, Kotake Y, Ito M, Handa M, Ikeda Y, *et al*. Carbon monoxide modulates endotoxin-induced microvascular leukocyte adhesion through platelet-dependent mechanisms. Anesthesiology 2002; 97: 701–9.
8 Stipanuk MH. Metabolism of sulfur-containing amino acids. Annu Rev Nutr 1986; 6: 179–209.
9 Yun Y, Hou L, Sang N. SO_2 inhalation modulates the expression of pro-inflammatory and pro-apoptotic genes in rat heart and lung. J Hazard Mater 2011; 185: 482–8.

10 Jin HF, Du SX, Zhao X, Wei HL, Wang YF, Liang YF, *et al.* Effects of endogenous sulfur dioxide on monocrotaline-induced pulmonary hypertension in rats. Acta Pharmacol Sin 2008; 29: 1157–66.
11 Sun Y, Tian Y, Prabha M, Liu D, Chen S, Zhang R, *et al.* Effects of sulfur dioxide on hypoxic pulmonary vascular structural remodeling. Lab Invest 2010; 90: 68–82.
12 Liang Y, Liu D, Ochs T, Tang C, Chen S, Zhang S, *et al.* Endogenous sulfur dioxide protects against isoproterenol-induced myocardial injury and increases myocardial antioxidant capacity in rats. Lab Invest 2011; 91: 12–23.
13 Huang XL, Zhou JL, Zhou XH, Xian XH, Ding CH. Ameliorative effects of exogenous sulfur dioxide on lipopolysaccharide-induced acute lung injury in rats. Sheng Li Xue Bao 2009; 61: 499–503.
14 Mecklenburgh K, Murray J, Brazil T, Ward C, Rossi AG, Chilvers ER. Role of neutrophil apoptosis in the resolution of pulmonary inflammation. Monaldi Arch Chest Dis 1999; 54: 345–9.
15 Lee WL, Downey GP. Neutrophil activation and acute lung injury. Curr Opin Crit Care 2001; 7: 1–7.
16 Feng Y, Yang Q, Xu J, Qian G, Liu Y. Effects of HMGB1 on PMN apoptosis during LPS-induced acute lung injury. Exp Mol Pathol 2008; 85: 214–22.
17 Zhang Q, Meng Z. The vasodilator mechanism of sulfur dioxide on isolated aortic rings of rats: Involvement of the K^+ and Ca^{2+} channels. Eur J Pharmacol 2009; 602: 117–23.
18 Kristof AS, Goldberg P, Laubach V, Hussain SN. Role of inducible nitric oxide synthase in endotoxin-induced acute lung injury. Am J Respir Crit Care Med 1998; 158: 1883–9.
19 Mitsuhashi H, Ikeuchi H, Yamashita S, Kuroiwa T, Kaneko Y, Hiromura K, *et al.* Increased levels of serum sulfite in patients with acute pneumonia. Shock 2004; 21: 99–102.
20 Baskic D, Popovic S, Ristic P, Arsenijevic NN. Analysis of cycloheximide-induced apoptosis in human leukocytes: fluorescence microscopy using annexin V/propidium iodide versus acridin orange/ethidium bromide. Cell Biol Int 2006; 30: 924–32.
21 Vermes I, Haanen C, Steffens-Nakken H, Reutelingsperger C. A novel assay for apoptosis. Flow cytometric detection of phosphatidylserine expression on early apoptotic cells using fluorescein labelled Annexin V. J Immunol Methods 1995; 184: 39–51.
22 Weinmann P, Gaehtgens P, Walzog B. Bcl-Xl- and Bax-alpha-mediated regulation of apoptosis of human neutrophils via caspase-3. Blood 1999; 93: 3106–15.
23 Chen HI, Yeh DY, Liou HL, Kao SJ. Insulin attenuates endotoxin-induced acute lung injury in conscious rats. Crit Care Med 2006; 34: 758–64.
24 Ritter C, da Cunha AA, Echer IC, Andrades M, Reinke A, Lucchiari N, *et al.* Effects of N-acetylcysteine plus deferoxamine in lipopolysaccharide-induced acute lung injury in the rat. Crit Care Med 2006; 34: 471–7.
25 Dyugovskaya L, Polyakov A, Lavie P, Lavie L. Delayed neutrophil apoptosis in patients with sleep apnea. Am J Respir Crit Care Med 2008; 177: 544–54.
26 Meng ZQ, Zhang LZ. Observation of frequencies of lymphocytes with micronuclei in human peripheral blood cultures from workers in a sulphuric acid factory. Environ Mol Mutagen 1990; 15: 218–20.
27 Meng ZQ, Zhang LZ. Chromosomal aberrations and sister-chromatid exchanges in lymphocytes of workers exposed to sulphur dioxide. Mutat Res 1990; 241: 15–20.
28 Meng Z, Zhang B. Polymerase chain reaction-based deletion screening of bisulfite (sulfur dioxide)-enhanced gpt-mutants in CHO-AS52 cells. Mutat Res 1999; 425: 81–5.
29 Meng Z, Geng H, Bai J, Yan G. Blood pressure of rats lowered by sulfur dioxide and its derivatives. Inhal Toxicol 2003; 15: 951–9.
30 Meng Z, Zhang H. The vasodilator effect and its mechanism of sulfur dioxide-derivatives on isolated aortic rings of rats. Inhal Toxicol 2007; 19: 979–86.
31 Meng Z, Liu Y. Cell morphological ultrastructural changes in various organs from mice exposed by inhalation to sulfur dioxide. Inhal Toxicol 2007; 19: 543–51.
32 Meng Z, Zhang B, Ruan A, Sang N, Zhang J. Micronuclei induced by sulfur dioxide inhalation in mouse bone-marrow cells *in vivo*. Inhal Toxicol 2002; 14: 303–9.
33 Meng Z, Qin G, Zhang B, Bai J. DNA damaging effects of sulfur dioxide derivatives in cells from various organs of mice. Mutagenesis 2004; 19: 465–8.
34 Zhang B, Nie A, Bai W, Meng Z. Effects of aluminum chloride on sodium current, transient outward potassium current and delayed rectifier potassium current in acutely isolated rat hippocampal CA1 neurons. Food Chem Toxicol 2004; 42: 1453–62.
35 Meng Z, Qin G, Zhang B. DNA damage in mice treated with sulfur dioxide by inhalation. Environ Mol Mutagen 2005; 46: 150–5.
36 Meng Z, Zhang B. Induction effects of sulfur dioxide inhalation on chromosomal aberrations in mouse bone marrow cells. Mutagenesis 2002; 17: 215–7.
37 Fujishima S, Morisaki H, Ishizaka A, Kotake Y, Miyaki M, Yoh K, *et al.* Neutrophil elastase and systemic inflammatory response syndrome in the initiation and development of acute lung injury among critically ill patients. Biomed Pharmacother 2008; 62: 333–8.
38 Du Z, Meng Z. Modulation of sodium currents in rat dorsal root ganglion neurons by sulfur dioxide derivatives. Brain Res 2004; 1010: 127–33.
39 Du Z, Meng Z. Sulfur dioxide derivatives modulation of high-threshold calcium currents in rat dorsal root ganglion neurons. Neurosci Lett 2006; 405: 147–52.
40 Olman MA, White KE, Ware LB, Simmons WL, Benveniste EN, Zhu S, *et al.* Pulmonary edema fluid from patients with early lung injury stimulates fibroblast proliferation through IL-1 beta-induced IL-6 expression. J Immunol 2004; 172: 2668–77.
41 Nie A, Meng Z. Sulfur dioxide derivative modulation of potassium channels in rat ventricular myocytes. Arch Biochem Biophys 2005; 442: 187–95.
42 Nie A, Meng Z. Study of the interaction of sulfur dioxide derivative with cardiac sodium channel. Biochim Biophys Acta 2005; 1718: 67–73.
43 Meng Z, Li Y, Li J. Vasodilatation of sulfur dioxide derivatives and signal transduction. Arch Biochem Biophys 2007; 467: 291–6.
44 Yun Y, Li H, Li G, Sang N. SO_2 inhalation modulates the expression of apoptosis-related genes in rat hippocampus via its derivatives *in vivo*. Inhal Toxicol 2010; 22: 919–29.
45 Zhao X, Jin HF, Tang CS, Du JB. Effects of sulfur dioxide, on the proliferation and apoptosis of aorta smooth muscle cells in hypertension: experiments with rats. Zhonghua Yi Xue Za Zhi 2008; 88: 1279–83.
46 Chopra M, Reuben JS, Sharma AC. Acute lung injury: apoptosis and signaling mechanisms. Exp Biol Med (Maywood) 2009; 234: 361–71.

Acta Pharmacologica Sinica (2012) 33: 991–997
 1671-4083/12 $32.00
www.nature.com/aps

Original Article

Tissue plasminogen activator attenuates ventilator-induced lung injury in rats

Liang-ti HUANG[1, 2], Hsiu-chu CHOU[3], Leng-fang WANG[4], Chung-ming CHEN[5, 6, *]

[1]Graduate Institute of Clinical Medicine, College of Medicine, Taipei Medical University, Taipei, Taiwan, China; [2]Department of Pediatrics, Wan Fang Hospital, Taipei Medical University, Taipei, Taiwan, China; [3]Department of Anatomy and [4]Department of Biochemistry, School of Medicine, College of Medicine, Taipei Medical University, Taipei, Taiwan, China; [5]Department of Pediatrics, Taipei Medical University Hospital, Taipei, Taiwan, China; [6]Department of Pediatrics, School of Medicine, College of Medicine, Taipei Medical University, Taipei, Taiwan, China

Aim: To test the hypothesis that the tissue plasminogen activator (tPA) may counteract the inhibitory effect of plasminogen activator inhibitors (PAI) and attenuate lung injury in a rat model of ventilator-induced lung injury (VILI).
Methods: Adult male Sprague-Dawley rats were ventilated with a HVZP (high-volume zero PEEP) protocol for 2 h at a tidal volume of 30 mL/kg, a respiratory rate of 25 breaths/min, and an inspired oxygen fraction of 21%. The rats were divided into 3 groups (n=7 for each): HVZP+tPA group receiving tPA (1.25 mg/kg, iv) 15 min before ventilation, HVZP group receiving HVZP+vehicle injection, and a control group receiving no ventilation. After 2 h of ventilation, the rats were killed; blood and lungs were collected for biochemical and histological analyses.
Results: HVZP ventilation significantly increased total protein content and the concentration of macrophage inflammatory protein-2 (MIP-2) in the bronchoalveolar lavage fluid (BALF) as well as the lung injury score. Rats that received HVZP ventilation had significantly higher lung PAI-1 mRNA expression, plasma PAI-1 and plasma D-dimer levels than the control animals. tPA treatment significantly reduced the BALF total protein and the lung injury score as compared to the HVZP group. tPA treatment also significantly decreased the plasma D-dimer levels and the HVZP ventilation-induced lung vascular fibrin thrombi. tPA treatment showed no effect on MIP-2 level in BALF.
Conclusion: These results demonstrate that VILI increases lung PAI-1 mRNA expression, plasma levels of PAI-1 and D-dimers, lung injury score and vascular fibrin deposition. tPA can attenuate VILI by decreasing capillary-alveolar protein leakage as well as local and systemic coagulation as shown by decreased lung vascular fibrin deposition and plasma D-dimers.

Keywords: tissue plasminogen activator (tPA); ventilator-induced lung injury (VILI); plasminogen activator inhibitor-1 (PAI-1); macrophage inflammatory protein-2 (MIP-2); D-dimer; fibrin; bronchoalveolar lavage fluid (BALF)

Acta Pharmacologica Sinica (2012) 33: 991–997; doi: 10.1038/aps.2012.66; published online 16 Jul 2012

Introduction

Mechanical ventilation is a life-saving treatment that has become the mainstay of management for patients with acute respiratory failure over the last several decades. However, there are several potential complications regardless of the life-saving potential of mechanical ventilation[1]. Ventilator-induced lung injury (VILI) can be caused by mechanical ventilation with a high tidal volume that damages the alveolar-capillary barrier and activates local and systemic inflammation[2]. The spectrum of VILI includes disruption of endothelial and epithelial cells, increases in endothelial and epithelial permeability, and alterations in pulmonary and systemic inflammatory mediators[2–4].

Pulmonary fibrin turnover, the deposition of fibrin in the alveolar space, and increased procoagulant activity of bronchoalveolar lavage fluid (BALF) are the pathognomonic features of VILI[5, 6]. Alveolar fibrin deposition may lead to surfactant dysfunction, poor gas exchange, decreased lung compliance, and increased ventilatory dependence[7]. Alveolar fibrin deposition is the net result of an imbalance of coagulation and fibrinolysis. Consequently, anticoagulant and fibrinolytic therapies in acute lung injury have recently been investigated with various compounds such as heparin and active site inactivated recombinant factor VIIa[8–10]. Anticoagulant

* To whom correspondence should be addressed.
E-mail cmchen@tmu.edu.tw
Received 2012-01-28 Accepted 2012-05-09

therapy might be a useful tool in the treatment of VILI. The major mechanisms that contribute to increased alveolar fibrin turnover are increased local tissue factor-mediated thrombin generation and depressed urokinase plasminogen activator-mediated fibrinolysis, which is caused by an increase in plasminogen activator inhibitors (PAIs)[11]. PAI-1, a fibrinolytic antiprotease, is the major plasminogen inactivator in the plasma and the primary inhibitor of tissue plasminogen activator (tPA); therefore, it is responsible for decreased plasmin activity and fibrinolytic potential[12, 13]. High pulmonary and systemic PAI-1 levels and increased alveolar fibrin deposition are features of animal models of VILI[14]. Increased plasma levels of PAI-1 are associated with adverse clinical outcomes and increased mortality in adults with acute lung injury[15]. tPA is responsible for fibrin degradation via the activation of plasminogen and has been used for thrombolysis in patients with acute myocardial infarction[16]. Aerosolized tPA improves pulmonary function in burn/smoke-induced lung injury in sheep[17]. tPA has both fibrinolytic and anti-inflammatory activity[18]. The distinctive combination of fibrinolytic and anti-inflammatory properties of tPA has made it an important natural anticoagulant. Theoretical considerations suggest that fibrinolytic therapy with tPA might benefit animals with VILI. We hypothesized that tPA may counteract the inhibitory effect of PAI-1, balance coagulation-fibrinolysis, and attenuate lung injury in an animal model of VILI. The aims of this study were to investigate the effects of tPA on gas exchange, lung cytokine and alveolar protein leakage, and local and systemic coagulation-fibrinolytic activity in a rat model of VILI and to find a potential treatment modality against high tidal volume-induced lung injury.

Materials and methods

Animals and protocol

This study was approved by the Animal Care and Use Committee of Taipei Medical University and was performed with adult male Sprague-Dawley rats weighing 250–300 g. The rats were maintained on a 12-h light/dark cycle with free access to food and water. The rats were intraperitoneally anesthetized with pentobarbital (50 mg/kg, Abbott, North Chicago, IL, USA). Fifteen minutes before ventilation, the rats received tPA (1.25 mg/kg in 0.5 mL saline, Actilyse, Boehringer Ingelheim, Germany; n=7) or an equal volume of normal saline (vehicle; n=7) through a tail vein injection. The dosage of tPA was based on recommendations by Choi *et al*[19]. A polyethylene catheter (PE-50, Becton Dickinson, Sparks, MD, USA) containing isotonic saline was placed in one femoral artery to sample blood for gas analysis. A tracheostomy was performed, and a 14-gauge plastic cannula was inserted into the trachea. The animals were then ventilated with a high-volume zero positive end-expiratory pressure (PEEP) (HVZP) protocol by a volume-cycled ventilator (Small Animal Ventilator, Model SAR-830/AP; CWE, Ardmore, PA, USA) for 2 h at a tidal volume of 30 mL/kg, zero PEEP, a respiratory rate of 25 breaths/min, and an FiO_2 of 0.21. The rats were selected at random to receive this ventilation strategy. Another group that received no ventilation served as the control (n=7). All animals were kept supine for the duration of the experiment, and arterial blood gases were measured with a blood gas analyzer (Model 1620, Instrumentation Laboratories, Lexington, MA, USA) at the beginning and every hour after randomization.

After 2 h of ventilation, the rats were killed with an intravenous injection of pentobarbital (100 mg/kg). Blood was collected from the femoral artery in citrated (0.109 mol/L) vacutainer tubes, placed on ice, and spun at 4 °C, and the resulting plasma was stored at -70 °C until analyzed. The chest was opened, and the lungs were removed intact from the animal with the tracheostomy tube in place. The right lung was ligated, and the left lung was lavaged with 2 mL of 0.9% saline at 4 °C that was washed in and out of the lungs three times and then recovered. This washing procedure was repeated two more times for each animal, with the three washes being pooled, and the total volume was recorded. There were no differences in the total volume of saline infused or recovered after the lavage procedure between the three experimental groups. The right superior lobe was fixed in 10% buffered formalin and embedded in paraffin. An aliquot of the BALF from each animal was used to measure the total protein content with bovine serum albumin as the standard. The value was expressed as mg/kg body weight.

Histology

Specimens were embedded in paraffin, stained with hematoxylin and eosin, and examined by a pathologist who was blinded to the protocol and experimental groups. Lung injury was scored according to the following items: 1) alveolar congestion, 2) hemorrhage, 3) infiltration of neutrophils into the airspace or the vessel wall, and 4) thickness of the alveolar wall[14]. Each item was graded according to a five-point scale: 0, minimal (little) damage; 1, mild damage; 2, moderate damage; 3, severe damage; and 4, maximal damage.

BALF macrophage inflammatory protein-2 (MIP-2) and plasma PAI-1 and D-dimer assays

BALF MIP-2 was tested by an enzyme-linked immunosorbent assay (ELISA) kit (R&D Systems, Minneapolis, MN, USA), and the value was expressed as pg/mL lavage fluid. Plasma PAI-1 was assayed by a commercially available ELISA kit (Innovative Research, Southfield, MI, USA). Fibrinolytic activity was assessed by measuring plasma concentrations of D-dimers with an ELISA kit purchased from American Diagnostica (Stamford, CT, USA).

Lung PAI-1 mRNA expression by real-time polymerase chain reaction (PCR)

The right middle lobe was ground into a powder in liquid nitrogen, and PAI-1 mRNA expression was measured using real-time PCR. Total RNA was extracted using TRIzol reagent (Invitrogen Life Technologies, Paisley, UK). Reverse transcription was performed on 1 μg of RNA with oligo-dT primers and the avian myeloblastosis virus reverse transcriptase (Roche, Indianapolis, IN, USA). The primer sequences for

the SYBR green real-time PCR included the following: PAI-1 sense (5′-ATGGCTCAGAACAACAAGTTCAAC-3′) and antisense (5′-CAGTTCCAGGATGTCGTACTCG-3′), and GAPDH mRNA sense (5′-ATGATTCTACCCACGGCAAG-3′) and antisense (5′-CTGGAAGATGGTGATGGGTT-3′). Gene expression was quantitatively analyzed using the comparative CT (ΔCT) method, in which CT is the threshold cycle number (the minimum number of cycles needed before the product can be detected). The arithmetic formula for the ΔCT method is the difference in the number of threshold cycles for a target (PAI-1) and an endogenous reference (the GAPDH housekeeping gene). The amount of target normalized to an endogenous reference and relative to a calibration normalized to an endogenous reference is given by $2^{\Delta\Delta CT}$. The values of the control group were normalized to a value of one, and the values of other groups were normalized to the control group values. Four samples were analyzed for each gene in each group.

Immunohistochemistry of PAI-1 and fibrin

Immunohistochemical staining for PAI-1 and fibrin were performed on paraffin sections with immunoperoxidase visualization. After deparaffinization in xylene and rehydration in an alcohol series, the sections were first preincubated for 1 h at room temperature in 0.1 mol/L PBS containing 10% normal goat serum and 0.3% H_2O_2 to block endogenous peroxidase activity and nonspecific binding of the antibody before being incubated for 20 h at 4 °C with a rabbit polyclonal antibody against rat PAI-1 or a monoclonal antibody against human fibrin (1:50; American Diagnostica). The sections were then treated for 1 h at room temperature with biotinylated goat anti-rabbit immunoglobulin G (IgG; 1:200, Vector Laboratories, Burlingame, CA, USA). This process was followed by reaction with the reagents from an ABC kit (Avidin-Biotin Complex, Vector) per the manufacturer's recommendations, and the reaction products were visualized by 3,3′-diaminobenzidine and 0.003% H_2O_2 in 0.5 mol/L TRIS buffer (pH 7.6) before the sections were mounted on gelatin-coated slides using Permount (Fisher Scientific, Pittsburgh, PA, USA). The sections for PAI-1 were mounted in glycerin gelatin and counterstained with hematoxylin.

Quantification of PAI-1 immunoreactivity and fibrin thrombi

A minimum of four random lung fields of immunohistochemically stained sections per animal were captured with a digital camera and imported into the computerized image analysis system, Image-Pro Plus 5.1 for Windows. The automatic object counting and measuring process was used to quantify the immunoreactivity of the sections[14]. We used the "count/size" command to perform cell number counting operations for PAI-1. These operations generated a percentage of positively stained cells, and the value was expressed as a labeling index. The denominator of the labeling index was the number of cells in the field. The fixed lung was cut into 1-mm-thick horizontal slices, and two slices were systematically and uniformly sampled at random. Slices were sampled with a periodicity of two (*eg*, 1, 3 or 2, 4). Vascular fibrin thrombi per visual field were counted at a magnification of ×20.

Statistical analysis

The lung injury score data are given as the medians (range); other data are presented as the mean±SD. Statistically significant differences were analyzed by one-way ANOVA with a *post-hoc* Bonferroni test. The Mann-Whitney U test was used for the analysis of lung injury score. Differences were considered significant at $P<0.05$.

Results

Effects on gas exchange

The arterial blood gas tensions were comparable among the three study groups before mechanical ventilation (Table 1). Rats that received HVZP ventilation showed a higher mean pH and lower mean carbon dioxide tension than control animals, and tPA treatment exhibited no further effects on gas exchange.

Table 1. Arterial blood P_{aO_2}, P_{aCO_2}, and pH at the baseline (0 h) and after 1 and 2 h of ventilation. Rats were randomly divided into the control, the high-volume zero positive end-expiratory pressure (HVZP), and the HVZP+tissue plasminogen activator (tPA) group. Arterial blood gases were measured at baseline (0 h), 1 h, and 2 h of mechanical ventilation. Values are expressed as mean±SD.

Group	*n*	pH	P_{aO_2} (mmHg)	P_{aCO_2} (mmHg)
Control	7			
0 h		7.42±0.04	91±7	43±2
HVZP	7			
0 h		7.43±0.02	85±14	42±9
1 h		7.65±0.07	107±9	22±3
2 h		7.61±0.02	109±9	21±2
HVZP+tPA	7			
0 h		7.44±0.04	80±10	44±5
1 h		7.71±0.03	103±5	23±2
2 h		7.65±0.10	95±12	21±6

Total protein, MIP-2, and PAI-1 in the BALF

The total protein contents recovered from the BALF were significantly higher in rats ventilated with the HVZP protocol than in the control group (Figure 1A). Treatment with tPA significantly reduced the HVZP ventilation-induced increase in the BALF protein content. The MIP-2 concentrations in the BALF increased after HVZP ventilation, and the values were approximately two-fold higher in the HVZP group compared to the control group (Figure 1B). The addition of tPA did not decrease MIP-2 levels. PAI-1 was undetectable in all BALF samples from control animals and barely detectable in HVZP and HVZP+tPA animals (data not shown).

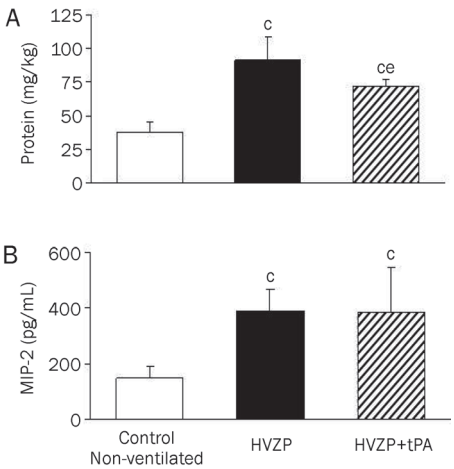

Figure 1. Total protein and MIP-2 in BALF in the control, HVZP, and HVZP+tPA groups. All rats were randomly divided into three groups: the control group (n=7) did not receive ventilation; the HVZP group (n=7) received 2 h of ventilation at a tidal volume of 30 ml/kg, a respiratory rate of 25 breaths/min, and an FiO_2 of 0.21; and the HVZP+tPA group (n=7) received an intravenous injection of tPA (1.25 mg/kg) 15 min before the HVZP ventilation. (A) Rats that received HVZP and HVZP+tPA ventilation had significantly higher bronchoalveolar lavage fluid (BALF) total protein contents than that of the control group (^cP<0.01 *vs* control group). Compared to the HVZP group, the HVZP+tPA group had significantly lower BALF protein content (^eP<0.05 *vs* HVZP group). (B) MIP-2 concentrations in BALF were significantly higher in rats of the HVZP and HVZP+tPA groups than in the control group (^cP<0.01 *vs* control group).

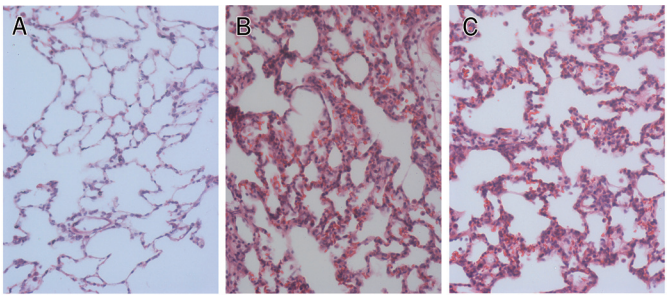

Figure 2. Representative lung tissue photomicrographs (×200). (A) Control group showed no major histological abnormalities. (B) HVZP group showed patchy areas of hemorrhage and thickened alveolar walls. (C) HVZP+tPA group showed less hemorrhage and alveolar congestion than the HVZP group.

Histology

After 2 h of ventilation, lung injury was characterized by alveolar congestion, hemorrhage, and inflammatory cell infiltration (Figure 2). The HVZP group showed patchy areas of hemorrhage and thickened alveolar walls, and the HVZP+tPA group showed less hemorrhage and alveolar congestion. No major histological abnormalities were present in the control animals. The HVZP group had a significantly higher lung injury score than did the control group (Table 2). Treatment with tPA significantly decreased the lung injury score compared to the HVZP group.

Lung PAI-1 mRNA expression, plasma PAI-1 levels, and immunohistochemistry of PAI-1

Rats that received HVZP and HVZP+tPA ventilation had significantly higher levels of lung PAI-1 mRNA expression and plasma PAI-1 than that of the control group (Figure 3). PAI-1 immunoreactivities were mainly detected in airway epithelial and mesenchymal cells, and the immunoreactivity significantly increased in the rats that received HVZP when compared with the control group. Treatment with tPA significantly reduced the HVZP ventilation-induced increase in PAI-1 immunoreactivity (Figure 4).

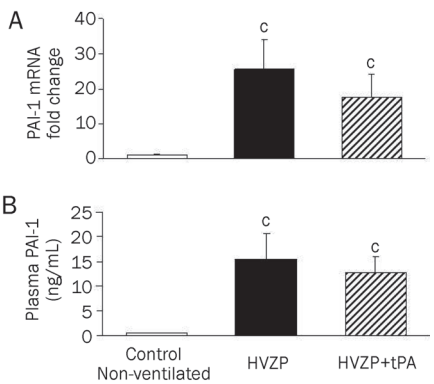

Figure 3. Lung PAI-1 mRNA expression and plasma PAI-1 levels in the control, HVZP, and HVZP+tPA groups. (A) Rats that received HVZP and HVZP+tPA ventilation had significantly higher levels of lung PAI-1 mRNA expression than that of the control group (^cP<0.01 *vs* control group). (B) Compared to the control group, rats that received HVZP and HVZP+tPA ventilation had significantly higher plasma PAI-1 levels (^cP<0.01 *vs* control group).

Table 2. Lung injury score in the control, the high-volume zero positive end-expiratory pressure (HVZP), and the HVZP+tissue plasminogen activator (tPA) group. Values are expressed as median (range). ^cP<0.01 *vs* control group; ^fP<0.01 *vs* HVZP group.

Treatment	n	Alveolar congestion	Hemorrhage	Alveolar thickness	Neutrophil infiltration	Lung injury score
Control	7	0 (0–1)	1 (0–2)	0 (0–1)	1 (1–2)	2 (1–3)
HVZP	7	3 (2–4)	3 (2–4)	2 (2–4)	2 (1–2)	10 (7–14)^c
HVZP+tPA	7	1 (1–2)	2 (1–2)	2 (1–2)	1 (1–2)	6 (5–7)^{cf}

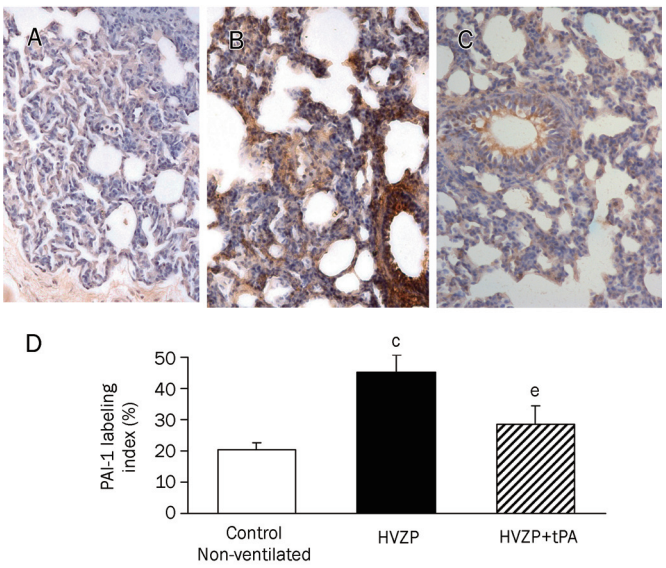

Figure 4. Immunohistochemical staining for PAI-1 in the (A) control, (B) HVZP, (C) HVZP+tPA groups (×100), and (D) quantitative analysis of PAI-1 immunoreactivity. Positive staining is shown as brown. PAI-1 immunoreactivities were mainly detected in airway epithelial and some mesenchymal cells, and the immunoreactivity markedly increased in rats that received HVZP ventilation when compared with the control group (^{c}P<0.01 *vs* control group). Treatment with tPA significantly reduced the HVZP ventilation-induced increase in PAI-1 immunoreactivity (^{e}P<0.05 *vs* HVZP group).

Plasma D-dimers

Rats that received HVZP ventilation exhibited significantly higher levels of plasma D-dimers than did the control animals (Figure 5). Treatment with tPA significantly reduced HVZP ventilation-induced increases in the plasma levels of D-dimers.

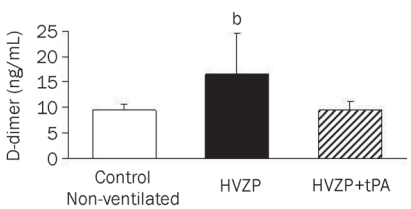

Figure 5. Plasma D-dimers in the control, HVZP, and HVZP+tPA groups. Rats that received HVZP ventilation had a significantly higher plasma D-dimer concentration than that of the control and HVZP+tPA groups (^{b}P<0.05 *vs* control and HVZP+tPA groups).

Lung vascular fibrin thrombi

After 2 h of ventilation, the HVZP+tPA group exhibited significantly lower numbers of fibrin thrombi per field than did the HVZP group (Figure 6). The HVZP group exhibited significantly higher numbers of vascular fibrin thrombi per lung field than the control group did.

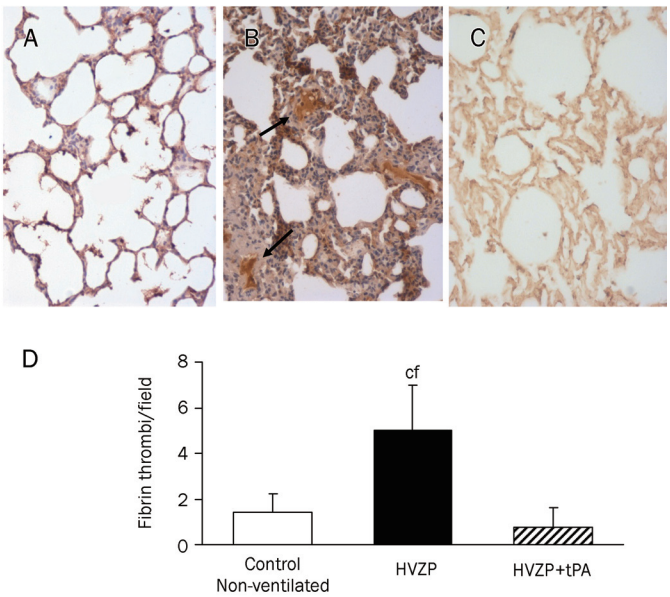

Figure 6. Photomicrograph of fibrin thrombi in the (A) control, (B) HVZP, (C) HVZP+tPA groups (×200), and (D) the number of fibrin thrombi per lung field. Fibrin thrombi (arrow) were stained as brown. The HVZP group had a significantly higher number of fibrin thrombi per field than did the control and HVZP+tPA groups (^{c}P<0.01, ^{f}P<0.01 *vs* control and HVZP+tPA groups).

Discussion

The spectrum of VILI includes the disruption of endothelial and epithelial cells, as well as increases in endothelial and epithelial permeability and pulmonary inflammatory mediators[2–4]. The outcomes of our *in vivo* lung injury model are consistent with alterations known to occur in VILI. The main findings of this study are that VILI is associated with increased lung PAI-1 mRNA expression, plasma levels of PAI-1 and D-dimer, lung injury score, PAI-1 immunoreactivity, and vascular fibrin deposition. Administration of tPA reduced plasma D-dimer levels, the lung injury score, PAI-1 immunoreactivity, and vascular fibrin deposition. These data indicate that high tidal volume ventilation may enhance local and systemic coagulation and suppress systemic fibrinolysis.

Deposition of fibrin in the alveolar space and increased procoagulant activity of the BALF are pathognomonic features of acute lung injury[8, 20]. Studies of animal models of VILI showed that high tidal volume ventilation increases alveolar fibrin deposition and systemic PAI-1 activity while lung-protective mechanical ventilation decreases BALF levels of PAI-1, attenuates coagulation, and enhances fibrinolysis[14, 21]. Although aerosol administration offers the theoretical advantage of the lungs receiving high concentrations of tPA, we chose intravenous administration because intra-alveolar and intravascular fibrin deposition and high systemic PAI-1 levels are frequently found in the setting of acute lung injury or VILI[5, 15]. Intraperitoneal tPA lavage could also reduce intra-abdominal PAI-1 concentrations in experimental peritonitis[20]. The half-life of active tPA is very short, and the majority of the

administered tPA forms complexes with PAI-1[22]. tPA inhibits PAI-1 by forming these stable complexes and attenuates the expression of PAI-1 in lung tissue but not the production of plasma PAI-1[23]. Plasma PAI-1 is synthesized from endothelial cells of the vessel wall and is quickly induced by high tidal volume ventilation[14, 23]. We speculate that the reduction of plasma PAI levels by tPA administration is partially reversed by ongoing PAI production during VILI. This reversal may explain why the decreased plasma levels of PAI-1 after tPA administration compared with HVZP are not significant. In the animal model of VILI, we found tPA intervention reduced vascular fibrin deposition and decreased local PAI-1 expression. These results support our hypothesis that tPA treatment balances coagulation-fibrinolysis in the VILI animal model.

D-dimers are derived from the degradation of cross-linked fibrin polymers, which come from clots, not from free circulating fibrin or fibrinogen. Elevated levels of D-dimers indicate increases in blood coagulation and turnover of cross-linked intravascular fibrin activation[24]. In this rat model of VILI, we found that high tidal volume ventilation caused a substantial increase in lung vascular fibrin formation and plasma levels of D-dimers, and the administration of tPA reduced intravascular fibrin formation and decreased plasma levels of D-dimers. The decreasing effects of tPA therapy on plasma D-dimer levels have been reported with profibrinolytic drugs in animal and human studies[25, 26]. Teke *et al* found that recombinant human activated protein C therapy significantly reduced plasma D-dimer levels in intestinal reperfusion-induced acute lung injury. Bernard *et al* also found significantly reduced plasma D-dimer levels in sepsis patients after administrating recombinant human activated protein C.

tPA is an endogenous serine protease with anti-inflammatory actions in addition to its fibrinolytic properties. MIP-2 is associated with leukocyte migration and activation and has been found to be closely associated with animal models of pneumonia and VILI[27, 28]. In this study, although lung vascular fibrin deposition was significantly decreased, the BALF levels of MIP-2 were not decreased in the HVZP+tPA group. These changes imply that the fibrinolytic effect of tPA is independent of its anti-inflammatory activity. Although tPA influences neutrophil function *in vitro*, no data exists regarding the effect of exogenous tPA on MIP-2 levels *in vivo*[27]. In this study, we found that tPA treatment decreased HVZP ventilation-induced increases in plasma D-dimers but did not decrease BALF levels of MIP-2. These data on BALF MIP-2 are consistent with those of Stringer *et al* who demonstrated that tPA did not change interleukin-1-induced increases in lung myeloperoxidase activity and the dose of tPA required for anti-inflammatory activity was higher than that needed for fibrinolysis[20, 29]. These results suggest that tPA attenuates high tidal volume-induced lung injury mostly through fibrinolytic effects rather than anti-inflammatory effects in this animal model.

In conclusion, this study shows that high tidal volume ventilation increased lung capillary-alveolar permeability and induced lung and systemic coagulation-fibrinolysis ab-normalities. Intravenous administration of tPA attenuates VILI by decreasing the protein leakage from plasma to alveoli and local and systemic coagulation, as indicated by decreasing lung vascular fibrin deposition and plasma D-dimers. tPA is not only a serine protease that converts plasminogen into biologically active plasmin but also a cytokine that activates intracellular signaling pathways and controls gene expression. Although tPA improves pulmonary function in burn/smoke-induced lung injury and attenuates VILI in this study, both the protease activity and the cytokine functions of tPA have been reported to play potential roles in the pathogenesis of renal fibrosis[30]. Therefore, more studies are needed to develop specific therapeutic agents that discretely target the fibrinolytic activity and avoid the fibrotic function of tPA in the treatment of VILI.

Author contribution

Chung-ming CHEN performed research, coordinated experiments, analyzed the data, wrote part of the paper, and drafted the manuscript; Leng-fang WANG performed animal and molecular experiments; Hsiu-chu CHOU performed histological experiments and was responsible for image analysis; Liang-ti HUANG performed part of the research and wrote the paper.

Abbreviations

BALF, bronchoalveolar lavage fluid; ELISA, enzyme-linked immunosorbent assay; MIP-2, macrophage inflammatory protein-2; PAI, plasminogen activator inhibitor; PCR, polymerase chain reaction; PEEP, positive end-expiratory pressure; tPA, tissue plasminogen activator; VILI, ventilator-induced lung injury.

References

1 Mutlu GM, Factor P. Complications of mechanical ventilation. Respir Care Clin N Am 2000; 6: 213–52.
2 Dos Santos CC, Slutsky AS. Invited review: mechanisms of ventilator-induced lung injury: a perspective. J Appl Physiol 2000; 89: 1645–55.
3 Jaecklin T, Otulakowski G, Kavenagh BP. Do soluble mediators cause ventilator-induced lung injury and multi-organ failure? Intensive Care Med 2010; 36: 750–7.
4 Peng XQ, Damarla M, Skirball J, Nonas S, Wang XY, Han EJ, *et al*. Protective role of PI3-kinase/Akt/eNOS signaling in mechanical stress through inhibition of p38 mitogen-activated protein kinase in mouse lung. Acta Pharmacol Sin 2010; 31: 175–83.
5 Dahlem P, Bos AP, Haitsma JJ, Schultz MJ, Meijers JC, Lachmann B. Alveolar fibrinolytic capacity suppressed by injurious mechanical ventilation. Intensive Care Med 2005; 31: 724–32.
6 Abraham E. Coagulation abnormalities in acute lung injury and sepsis. Am J Respir Cell Mol Biol 2000; 22: 401–4.
7 Idell S. Coagulation, fibrinolysis, and fibrin deposition in acute lung injury. Crit Care Med 2003; 31: S213–20.
8 Li LF, Huang CC, Lin HC, Tsai YH, Quinn DA, Liao SK. Unfractionated heparin and enoxaparin reduce high-stretch ventilation augmented lung injury: a prospective, controlled animal experiment. Crit Care 2009; 13: R108.
9 Dixon B, Schultz MJ, Hofstra JJ, Campbell DJ, Santamaria JD.

Nebulized heparin reduces levels of pulmonary coagulation activation in acute lung injury. Crit Care 2010; 14: 445.
10 Vincent JL, Artigas A, Petersen LC, Meyer C. A multicenter, randomized, double-blind, placebo-controlled, dose-escalation trial assessing safety and efficacy of active site inactivated recombinant factor VIIa in subjects with acute lung injury or acute respiratory distress syndrome. Crit Care Med 2009; 37: 1874–80.
11 Choi G, Schultz MJ, Levi M, Van Der Poll T, Millo JL, Garrard CS. Protein C in pneumonia. Thorax 2005; 60: 705–6.
12 Urano T, Ihara H, Suzuki Y, Takada Y, Takada A. Coagulation-associated enhancement of fibrinolytic activity via a neutralization of PAI-1 activity. Semin Thromb Hemost 2000; 26: 39–42.
13 Cesarman-Maus G, Hajjar KA. Molecular mechanisms of fibrinolysis. Br J Haematol 2005; 3: 307–21.
14 Chen CM, Chou HC, Wang LF, Lang YD. Captopril decreases plasminogen activator inhibitor-1 in rats with ventilator-induced lung injury. Crit Care Med 2008; 36: 1880–5.
15 Prabhakaran P, Ware LB, White KE, Cross MT, Matthay MA, Olman MA. Elevated levels of plasminogen activator inhibitor-1 in pulmonary edema fluid are associated with mortality in acute lung injury. Am J Physiol 2003; 285: L20–8.
16 Sakamoto T, Ogawa H, Takazoe K, Yoshimura M, Shimomura H, Moriyama Y, *et al*. Effect of activated protein C on plasma plasminogen activator inhibitor activity in patients with acute myocardial infarction treated with alteplase: comparison with unfractionated heparin. J Am Coll Cardiol 2003; 42: 1389–94.
17 Enkhbaatar P, Murakami K, Cox R, Westphal M, Morita N, Brantley K, *et al*. Aerosolized tissue plasminogen inhibitor improves pulmonary function in sheep with burn and smoke inhalation. Shock 2004; 22: 70–5.
18 Stringer KA, Dunn JS, Gustafson DL. Administration of exogenous tissue plasminogen activator reduces oedema in mice lacking the tissue plasminogen activator gene. Clin Exp Pharmacol Physiol 2004; 31: 327–30.
19 Choi G, Hofstra JJ, Roelofs JJ, Florquin S, Bresser P, Levi M, *et al*. Recombinant human activated protein C inhibits local and systemic activation of coagulation without influencing inflammation during Pseudomonas aeruginosa pneumonia in rats. Crit Care Med 2007; 35: 1362–8.
20 Van Veen SQ, Meijers JCM, Levi M, Van Gulik TM, Boermeester MA. Effects of intra-abdominal administration of recombinant tissue plasminogen activator on coagulation, fibrinolysis and inflammatory responses in experimental polymicrobial peritonitis. Shock 2007; 27: 534–41.
21 Ware LB, Matthay MA, Parsons PE, Thompson BT, Januzzi JL, Eisner MD, *et al*. Pathogenetic and prognostic significance of altered coagulation and fibrinolysis in acute lung injury/acute respiratory distress syndrome. Crit Care Med 2007; 35: 1821–8.
22 Levin EG, Santell L, Osborn KG. The expression of endothelial tissue plasminogen activator *in vivo*: a function defined by vessel size and anatomic location. J Cell Sci 1997; 110: 139–48.
23 Binder B, Christ G, Gruber F, Grubic N, Hufnagl P. Plasminogen activator inhibitor 1: physiological and pathological roles. News Physiol Sci 2002; 17: 56–61.
24 Dahlbäck B, Villoutreix BO. Regulation of blood coagulation by the protein C anticoagulant pathway: Novel insights into structure-function relationships and molecular recognition. Arterioscler Thromb Vasc Biol 2005; 25: 1311–20.
25 Teke Z, Sacar M, Yenisey C, Atalay AO, Bicakci T, Erdem E. Activated protein C attenuates intestinal reperfusion-induced acute lung injury: an experimental study in a rat model. Am J Surg 2008; 195: 861–73.
26 Bernard GR, Vincent JL, Laterre PF, LaRosa SP, Dhainaut JF, Lopez-Rodriguez A, *et al*. Efficacy and safety of recombinant human activated protein C for severe sepsis. N Engl J Med 2001; 344: 699–709.
27 Jiang JS, Wang LF, Chou HC, Chen CM. Angiotensin-converting enzyme inhibitor captopril attenuates ventilator-induced lung injury in rats. J Appl Physiol 2007; 102: 2098–103.
28 Bonville CA, Bennett NJ, Koehnlein M, Haines DM, Ellis JA, DelVecchio AM, *et al*. Respiratory dysfunction and proinflammatory chemokines in the pneumonia virus of mice (PVM) model of viral bronchiolitis. Virology 2006; 349: 87–95.
29 Stringer KA, Hybertson BM, Cho OJ, Cohen Z, Repine JE. Tissue plasminogen activator (tPA) inhibits interleukin-1 induced acute lung leak. Free Radic Biol Med 1998; 25: 184–8.
30 Hu K, Mars WM, Liu Y. Novel actions of tissue-type plasminogen activator in chronic kidney disease. Front Biosci 2008; 13: 5174–86.

Acta Pharmacologica Sinica (2012) 33: 998–1003
 1671-4083/12 $32.00
www.nature.com/aps

Original Article

Association between fibroblast growth factor 7 and the risk of chronic obstructive pulmonary disease

Si-cheng XU[#], Jiang-ying KUANG[#], Jin LIU, Chun-lan MA, Yu-lin FENG, Zhi-guang SU[*]

Molecular Medicine Research Center, West China Hospital, and State Key Laboratory of Biotherapy, Sichuan University, Chengdu 610041, China

Aim: Fibroblast growth factor 7 (FGF7) is involved in a number of physiological and pathological processes, including lung disease. However, relatively little is known about the effect of FGF7 gene polymorphisms on chronic obstructive pulmonary disease (COPD) susceptibility. This study aimed to investigate the association between FGF7 polymorphisms with COPD susceptibility in a Chinese Han population.
Methods: We conducted a case-control study of 279 COPD patients and 367 age- and gender-distribution-matched control subjects. The tagging SNPs rs10519225 and rs7170426 in FGF7 were genotyped by SNaPshot. The associations of each SNP genotype and haplotype constructed by these loci with COPD were analyzed.
Results: A multivariate analysis showed that rs10519225 was significantly associated with an increased risk of COPD (P=0.011, OR=1.535, FDR q=0.022), whereas no association was found for rs7170426. Linkage disequilibrium (LD) analysis showed that these loci were in weak LD, with an r^2 of 0.033 and a D′ of 0.232 (95% CI: 0.150–0.520). The haplotype constructed by allele G at rs10519225 and allele A at rs7170426 was associated with a decreased susceptibility to COPD (P=0.012, OR=0.751, FDR q=0.048).
Conclusion: These findings suggest that FGF7 may be one susceptibility factor for COPD.

Keywords: chronic obstructive pulmonary disease; fibroblast growth factor 7; genetic polymorphism; haplotype

Acta Pharmacologica Sinica (2012) 33: 998–1003; doi: 10.1038/aps.2012.69; published online 16 Jul 2012

Introduction

Chronic obstructive pulmonary disease (COPD) is currently the leading cause of decreases in disability-adjusted life years (DALY). Globally, it is projected to be the third most important cause of DALY by the year 2020[1], and it is estimated that COPD affects nearly 8.2% of the Chinese adult population[2]. Cigarette smoking is the major environmental risk factor for COPD; however, only approximately 15% of smokers develop clinically relevant airflow obstruction[3]. The variation in the susceptibility to cigarette smoke, in combination with the familial inheritance pattern of COPD, suggests that there may be a genetic component to the development of COPD[4]. Multiple studies in diverse populations have demonstrated the genetic contribution to the variability in pulmonary function and the familial aggregation of COPD. As expected, segregation analysis suggests that multiple genes may be involved in COPD susceptibility. The associations between COPD and polymorphisms in genes with potential importance in COPD pathogenesis have been investigated[5]; however, only α1-antitrypsin has been unequivocally identified as relevant to the development of COPD. Recently, polymorphisms in the CHRNA3-CHRNA5-IREB2, HHIP, and FAM13A loci have been found to be associated with COPD by genome-wide association studies (GWAS)[6–8].

Fibroblast growth factor 7 (FGF7), also known as keratinocyte growth factor (KGF), has a variety of effects in the lung. FGF7 stimulates epithelial cell proliferation in the airway and alveoli[9, 10] and affects the morphology of the developing lung. The disruption of FGF7 receptor function significantly reduces airway branching during development[11]. The over-expression of FGF7 in the airways of developing mice severely alters lung growth[12]. FGF7 also stimulates fluid and electrolyte secretion. When applied to fetal lung explants, FGF7 stimulates dramatic intra-luminal swelling and expansion[13]. FGF7 may also play a role in airway repair following injury. FGF7 induces alveolar type II pneumocyte proliferation *in vitro* and *in vivo*[9]. FGF7 stimulates surfactant protein and phospholipid expression as well as the transepithelial transport of fluids and electrolytes, minimizes injury, enhances the repair of dam-

[#] These authors contributed equally to this work.
[*] To whom correspondence should be addressed.
E-mail zhiguang_su@hotmail.com
Received 2011-12-23 Accepted 2012-05-09

aged epithelia, and may dampen the epithelial response to inflammatory mediators[14]. Exogenous FGF7 treatment has been used as a protective agent after oxidant or bleomycin-induced lung injury[15, 16]. Endogenous FGF7 mRNA expression is induced in neonatal rabbits exposed to hyperoxia, and FGF7 protein expression is increased in adult respiratory distress syndrome[17], suggesting that FGF7 may play a role in lung repair. Thus, this protein could help repair the damaged lungs of individuals who are smokers and who are at a risk of developing COPD.

In addition, FGF7 has been identified to play roles in several clinical diseases or phenotypes, including nonsyndromic cleft lip and palate[18], thyroid volume and goiter risk[19]. Moreover, FGF7 was identified as a COPD susceptibility locus in a recent report[20].

With these considerations in mind, we hypothesized that polymorphisms in the FGF7 gene might modulate susceptibility to COPD. To test this hypothesis, we investigated the association between FGF7 gene polymorphisms and the risk of COPD in a Chinese Han population.

Materials and methods

Subjects

As described previously[21], 279 patients with COPD and 367 age-matched non-COPD control subjects were recruited for this study. The subjects in both groups were unrelated ethnic Han Chinese individuals recruited from Chengdu city or surrounding regions in the Sichuan Province of western China. Each subject was personally interviewed face-to-face by trained interviewers who collected the patient's demographic data as well as information related to risk factors such as tobacco smoking. The recruitment and the clinical analyses were conducted at the Department of Respiratory Medicine in West China Hospital of Sichuan University; clinical analyses were performed according to the Global Initiative for Chronic Obstructive Lung Disease (GOLD) criteria[22]. COPD patients were enrolled when they suffered from cough, sputum production and dyspnea at least upon exertion and showed chronic irreversible airflow limitation defined by an FEV_1 (forced expiratory volume in 1 s) to FVC (forced vital capacity) ratio <70%, and FEV_1 predicted <80% after the inhalation of a β_2-agonist. Patients were excluded from this study if they had other significant respiratory disease, such as bronchial asthma, bronchiectasis, lung cancer, or pulmonary tuberculosis. The age-matched non-COPD control subjects were volunteers who came to the West China Hospital of Sichuan University for physical examination only. The inclusion criteria for controls were as follows: (1) FEV_1/FVC ratio >70%, FEV_1% and FVC% predicted >80% and (2) without pulmonary disease. Individuals were excluded if they had a history of chronic lung disease, atopy, an acute pulmonary infection in the 4 weeks before assessment for this study, or a family history of COPD.

This study was approved by the Ethics Committee of the West China Hospital, Sichuan University, and written informed consent was obtained from all subjects before their participation in the study. The investigator explained the nature, purpose and risks of the study and provided the subject with a copy of the information sheet.

SNP selection

Based on the linkage disequilibrium and haplotype block analysis of the HapMap project data (http://www.hapmap.org; Public Release #24/Phase II, Nov 2008), we excluded SNPs with low heterozygosity (below 0.1), with low minor allele frequency (below 0.05), or without genotype information. Finally, we chose two TagSNPs at the FGF7 locus, rs10519225 and rs7170426, using the program Tagger with a cut-off of 0.8 for r^2 and a MAF (minor allele frequency) of >0.1. rs10519225 is located at bp 49720778 of chromosome 15 (build 37.3) and captures SNPs, including rs17479589, rs11855798, rs17478785, rs4389093, rs10519225, rs12916839, rs12595692, rs4480740, rs17478694, rs12148764, rs2899434, rs7174135, rs9920722, and rs10519224. Meanwhile, rs7170426 is located at bp 49751853 (build 37.3) and captures SNPs, including rs11630629, rs2899433, and rs7167041. Overall, SNPs rs10519225 and rs7170426 provided 62% coverage of the genetic information at the FGF7 locus of the Han Chinese population based on MAF >10% and r^2 >0.8.

SNP genotyping

Venous blood was collected from each subject in sterile tubes with EDTA-Na_2 anticoagulants and stored at -20 °C. Genomic DNA was extracted from the stored blood using a commercial extraction kit (Bioteke Corporation, Beijing, China) according to the manufacturer's instructions. SNPs were genotyped using the ABI SNaPshot method (Applied Biosystems, CA, USA). PCR was performed using the specific primers: rs10519225 forward 5′-GAAGAAGAGCATTGAGAAC-3′, rs10519225 reverse 5′-TCTGTCTTCCACATCTGTC-3′, rs7170426 forward 5′-GAACCTGCATTTCAGCATTG-3′, and rs7170426 reverse 5′-CTACAAGTCTCAAGCACAGC-3′. The specific SNaPshot primers were used for a SNaPshot reaction using the purified PCR products as templates. The following primers were used for the SNaPshot reaction: rs10519225: 5′-ATTCTGCACCTGACAGAAATAACACTGCTCTTTAAGCTGA-3′ and rs7170426: 5′-TTTATGTAAATTTATAGAGTTTGAGGAATAATTAAAACTAGTATTTCT-3′. The SNaPshot reaction products were then analyzed on an ABI 3130 Genetic Analyzer (Applied Biosystems, CA, USA). To confirm the genotyping results, 10% of the samples were randomly selected and re-genotyped by direct sequencing using a BigDye terminator (Applied Biosystems, CA, USA); no more than a 2% discrepancy was observed for any SNP between the two genotyping methods.

Statistical analysis

The demographic and clinical data between the COPD patients and the control subjects were compared using the chi-squared test and Student's *t*-test. Hardy-Weinberg equilibrium was tested with a goodness of fit chi-squared test (with one degree of freedom) to compare the observed and expected genotype frequencies. The differences between the COPD patients and

the controls with respect to the genotype distributions were analyzed using one-way analysis of variance for univariate analysis and logistic regression for multivariate analysis. Age and sex were used as covariates in the multivariable analyses. A two-sided significance level of q<0.05 was used for all significant tests. Statistical analyses were performed in SPSS version 17.0 and Microsoft Excel. To correct for testing for multiple dependent parameters, the false discovery rate (FDR) was calculated using the Benjamini-Hochberg procedure[23]. The FDR significance level was set at q<0.05. We used SVS7 (SNP & Variation Suite 7, available at http://www.goldenhelix.com/SNP_Variation/index.html) to calculate the linkage disequilibrium (LD) (r^2) and performed the haplotype association.

Results

General characteristics

The baseline characteristics and the results of the pulmonary function tests for the 279 patients with COPD and 367 control subjects were presented in Table 1. All patients had FEV_1 values <80% of predicted and thus were diagnosed with moderate-to-severe COPD according to the Global Initiative for Chronic Obstructive Lung Disease (classification of severity: mild=FEV_1 ≥80% of predicted; moderate=FEV_1 ≥30% to <80% of predicted; and severe=FEV_1 <30% of predicted). The COPD cases and control subjects did not significantly differ in sex, age or smoking history. The FEV_1, FEV_1/predicted and FEV_1/FVC were significantly lower in the COPD case subjects compared with the controls (P<0.01).

Table 1. Description of study population.

Variable	Controls (n=367)	Cases (n=279)	P
Age, years	65±8	63±9	NS
Sex (Male/Female)	323/44	239/40	NS
Smoking history			
0–20 pack years	88	75	NS
≥20 pack years	279	204	NS
FEV_1	1.87±0.60	0.97±0.32	<0.01
FEV_1 percentage of predicted, %	93.7±3.4	46.0±0.4	<0.01
FEV_1/FVC, %	78.0±4.6	49.2±8.3	<0.01

FEV_1=Forced Expiratory Volume in 1 s, FVC=Forced Vital Capacity.
NS: not significant.
Data are presented as mean±SEM.

rs10519225 is associated with COPD

All subjects were genotyped at both rs10519225 and rs7170426 using the SNaPshot method. The genotype distributions are indicated in Table 2. The distributions of each genotype of rs10519225 and rs7170426 in COPD patients and controls were compatible with the Hardy-Weinberg equilibrium (χ^2=1.752 and 0.347 for COPD patients, respectively; χ^2 =0.652 and 0.347 for controls, respectively; all P values were higher than 0.05). For rs10519225, the frequencies of the GG, GA, and AA genotypes were 63.8%, 33.7%, and 2.5% in COPD patients and 70.8%, 26.2%, and 3.0% in controls, respectively. For rs7170426, the observed frequencies of the AA, AG, and GG genotypes were 51.6%, 39.1%, and 9.3% in COPD patients and 55.9%, 37.6%, and 6.5% in controls, respectively. In the univariate analysis, the genotypes of rs10519225 were distributed dramatically differently between COPD patients and healthy controls (P=0.022), whereas the distribution of rs7170426 was not different between two groups. Genotypes containing the minor rs10519225 A allele were associated with COPD susceptibility in an additive pattern (Table 2). After adjustment for age and sex, the association of rs10519225 and COPD remained significant (P=0.011, FDR q=0.022). Multivariate binary logistic regression to estimate the magnitude of effect showed that the odds ratio (OR) for the presence of at least one minor allele

Table 2. Associations of genotypes in rs10519225 and rs7170426 with COPD.

Genotype	Frequency		Univariate	Multivariate P value* (FDR q value†)	OR (95% CI)§
	COPD	Controls			
rs10519225 G/A					
GG	0.638	0.708	**0.023**	**0.011** (**0.022**)	1.535 (1.104–2.134)
GA	0.337	0.262			
AA	0.025	0.030			
rs7170426 A/G					
AA	0.516	0.559	0.135	0.079 (0.079)	1.324 (0.968–1.810)
AG	0.391	0.376			
GG	0.093	0.065			
Age			0.931	0.933 (0.931)	0.998 (0.945–1.053)
Sex			0.379	0.419 (0.762)	1.212 (0.760–1.932)

*Binary logistic regression.
† FDR (false discovery rate) evaluated for association with SNP only. q<0.05 is significant.
§ Both rs10519225 and rs7170426 entered using additive model.

of rs10519225 (additive model) was 1.535 (95% CI: 1.104–2.134) (Table 2).

Association between haplotype of rs10519225 and rs7170426 with COPD

LD analysis showed that rs10519225 and rs7170426 were in weak LD, with r^2=0.033, D'=0.232, and D' 95% CI (0.150–0.520). Multivariate logistic regression was used to incorporate age, sex, and different rs10519225 and rs7170426 haplotypes into the models. As shown in Table 3, the G–A haplotype of rs10519225–rs7170426 was associated with a lower risk of COPD under the additive model (OR=0.751, 95% CI: 0.598-0.944, P=0.012, FDR q=0.048), whereas none of the other haplotypes were found to have significant effects.

Table 3. Associations of haplotypes between rs10519225 and rs7170426 with COPD*.

Haplotype	CASE	Controls	OR (95% CI)	*P* value†	FDR q§
rs10519225–rs7170426					
G–A	0.594	0.660	0.751 (0.598–0.944)	**0.012**	**0.048**
G–G	0.200	0.179	1.149 (0.868–1.521)	0.318	0.318
A–A	0.111	0.094	1.193 (0.831–1.714)	0.304	0.405
A–G	0.095	0.066	1.485 (0.990–2.227)	**0.032**	0.065

*The association analyses were performed with sex, and age as covariates.
† Significant *P* values are shown in boldface.
§ FDR, false discovery rate, q<0.05 is significant.

Discussion

Case-control association studies of a candidate gene can be a very powerful approach toward identifying the genetic causes of complex diseases such as COPD[24]. In this case-control study, we evaluated the possible association of FGF7 gene polymorphisms with susceptibility to COPD in a Chinese Han population for the first time. Our results suggested that the rs10519225 polymorphism in the FGF7 gene correlated with modestly higher risks of COPD, with an OR of 1.54 (95% CI: 1.104–2.134), whereas the rs7170426 polymorphism was not correlated with COPD risk. Haplotype analysis, in which several SNPs within the same gene are evaluated simultaneously, can provide more information than a single SNP and thus elevates the statistical power of the analysis[25]. LD analysis showed that these loci were in weak LD. Therefore, we assayed each of the haplotypes constructed by polymorphisms rs10519225 and rs7170426. The G–A haplotype was associated with a lower risk of COPD in the additive genetic model (OR=0.751, 95% CI: 0.598–0.944, P=0.012, FDR q=0.048). This suggested that the G-A haplotype might serve as a protective genetic factor against COPD in Chinese Han population. Nonetheless, further studies are required to confirm this hypothesis. These results indicated that certain polymorphisms in the FGF7 gene may be crucial in the pathogenesis of COPD. Intriguingly, the human FGF7 gene is located on chromosome 15 at position q21.2, and a previous genome-wide linkage study for generalized COPD identified chromosome 15q21 as meeting genome-wide criteria for suggestive linkage[26]. Moreover, another polymorphism within the FGF7 gene, rs4480740, was recently reported to be associated with COPD in an additional population[20]. We assessed the extent of LD between rs10519225, rs7170426, and rs4480740 in the Han Chinese population using HapMap project data. Both rs10519225 and rs7170426 were found to be in strong LD with rs4480740 (Figure 1). Although we did not carry out this association study in an independent population, the strong LD between rs10519225 and rs4480740 suggested that the association of rs10519255 with COPD observed in the current study was unlikely to have occurred by chance.

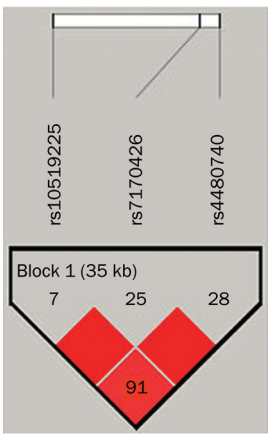

Figure 1. Relative position of SNPs and linkage disequilibrium map for FGF7 in the Han Chinese population populations studied. Polymorphisms are identified by their dbSNP rs numbers, and their relative positions are marked by vertical lines within the white horizontal bar. The numbers within squares indicate the D' value, expressed as a percentile.

It should be acknowledged that the SNPs associated with the statistical signal might simply play a role as a surrogate marker for the causal functional SNP or SNPs. That is, rs10519225 in FGF7 gene could be in linkage disequilibrium with another polymorphism of the gene that impacts FGF7 activity. Moreover, rs10519225 is located within an intronic region of FGF7, which is usually removed during the gene-splicing process. Intronic SNPs may modify gene function by affecting the regulation of gene expression[27]. The dysfunction of FGF7 may pose a risk for the improper development of the airway and alveoli. It has been proposed that persons with smaller initial lung volumes are more likely to develop overt manifestations of disease during the accelerated decline of lung function in COPD. Alternatively, FGF7 may play a role in disease susceptibility through its role in the protection against the oxidative stress response specifically in the lung

epithelium.

The direction of association with disease is noteworthy; rs10519225 heterozygosity was associated with susceptibility to COPD in this study. The finding of heterozygote susceptibility is unusual in genetic disease association studies, but is well described in the study of genetic susceptibility to human pulmonary or airway diseases, including COPD and asthma[28-30].

We are aware that the significant results in this study could prove to be false positives because of the relatively small sample size, but even with a larger sample, the functional and biological impacts of the described polymorphisms would require further study. Possible gene-gene and gene-environment interactions also pose a challenge for genetic analysis of COPD association studies. Further studies using larger populations are needed, and other variants in the FGF7 gene should be investigated to clarify the association of FGF7 and individual susceptibility to the development of COPD.

In conclusion, we have investigated the link between FGF7 gene polymorphisms and the risk of COPD in the Chinese Han population for the first time. The rs10519225 genotype frequencies are significantly different in COPD patients and controls, suggesting that this SNP may be useful for predicting COPD susceptibility. Similarly, the rs10519225G-rs7170426A haplotype may be protective against COPD in the Chinese Han population. Further functional characterization of these SNPs is required to clarify the significance of FGF7 in the pathogenesis of COPD.

Acknowledgements

This study was financially supported by the National Natural Science Foundation of China (No 31071108), the Program for New Century Excellent Talents in University (NCET-10-0600), the Scientific Research Foundation for Returning Overseas Chinese Scholars, the Chinese Ministry of Education (2011-508-4-3), and the General Administration of Quality Supervision, Inspection and Quarantine (GAQSIQ) Public Benefit Research Foundation (No 201210046).

Author contribution

Si-cheng XU, Jiang-ying KUANG, Jin LIU, Chun-lan MA, and Yu-lin FENG contributed to the study design and genotyping; Zhi-guang SU contributed to the study design and data analysis and wrote the manuscript.

References

1 Murray CJ, Lopez AD. Evidence-based health policy — lessons from the Global Burden of Disease Study. Science 1996; 274: 740–3.
2 Zhong N, Wang C, Yao W, Chen P, Kang J, Huang S, *et al*. Prevalence of chronic obstructive pulmonary disease in China: a large, population-based survey. Am J Respir Crit Care Med 2007; 176: 753–60.
3 Davis RM, Novotny TE. The epidemiology of cigarette smoking and its impact on chronic obstructive pulmonary disease. Am Rev Respir Dis 1989; 140: S82–4.
4 Khoury MJ, Beaty TH, Tockman MS, Self SG, Cohen BH. Familial aggregation in chronic obstructive pulmonary disease: use of the loglinear model to analyze intermediate environmental and genetic risk factors. Genet Epidemiol 1985; 2: 155–66.
5 Castaldi PJ, Cho MH, Cohn M, Langerman F, Moran S, Tarragona N, *et al*. The COPD genetic association compendium: a comprehensive online database of COPD genetic associations. Hum Mol Genet 2010; 19: 526–34.
6 Cho MH, Boutaoui N, Klanderman BJ, Sylvia JS, Ziniti JP, Hersh CP, *et al*. Variants in FAM13A are associated with chronic obstructive pulmonary disease. Nat Genet 2010; 43: 200–2.
7 Pillai SG, Ge D, Zhu G, Kong X, Shianna KV, Need AC, *et al*. A genome-wide association study in chronic obstructive pulmonary disease (COPD): identification of two major susceptibility loci. PLoS Genet 2009; 5: e1000421.
8 Wilk JB, Chen TH, Gottlieb DJ, Walter RE, Nagle MW, Brandler BJ, *et al*. A genome-wide association study of pulmonary function measures in the Framingham Heart Study. PLoS Genet 2009; 5: e1000429.
9 Ulich TR, Yi ES, Longmuir K, Yin S, Biltz R, Morris CF, *et al*. Keratinocyte growth factor is a growth factor for type II pneumocytes *in vivo*. J Clin Invest 1994; 93: 1298–306.
10 Yano T, Mason RJ, Pan T, Deterding RR, Nielsen LD, Shannon JM. KGF regulates pulmonary epithelial proliferation and surfactant protein gene expression in adult rat lung. Am J Physiol Lung Cell Mol Physiol 2000; 279: L1146–58.
11 Peters K, Werner S, Liao X, Wert S, Whitsett J, Williams L. Targeted expression of a dominant negative FGF receptor blocks branching morphogenesis and epithelial differentiation of the mouse lung. EMBO J 1994; 13: 3296–301.
12 Simonet WS, DeRose ML, Bucay N, Nguyen HQ, Wert SE, Zhou L, *et al*. Pulmonary malformation in transgenic mice expressing human keratinocyte growth factor in the lung. Proc Natl Acad Sci U S A 1995; 92: 12461–5.
13 Cardoso WV, Itoh A, Nogawa H, Mason I, Brody JS. FGF-1 and FGF-7 induce distinct patterns of growth and differentiation in embryonic lung epithelium. Dev Dyn 1997; 208: 398–405.
14 Prince LS, Karp PH, Moninger TO, Welsh MJ. KGF alters gene expression in human airway epithelia: potential regulation of the inflammatory response. Physiol Genomics 2001; 6: 81–9.
15 Baba Y, Yazawa T, Kanegae Y, Sakamoto S, Saito I, Morimura N, *et al*. Keratinocyte growth factor gene transduction ameliorates acute lung injury and mortality in mice. Hum Gene Ther 2007; 18: 130–41.
16 Sakamoto S, Yazawa T, Baba Y, Sato H, Kanegae Y, Hirai T, *et al*. Keratinocyte growth factor gene transduction ameliorates pulmonary fibrosis induced by bleomycin in mice. Am J Respir Cell Mol Biol 2011; 45: 489–97.
17 Ware LB, Matthay MA. Keratinocyte and hepatocyte growth factors in the lung: roles in lung development, inflammation, and repair. Am J Physiol Lung Cell Mol Physiol 2002; 282: L924–40.
18 Riley BM, Mansilla MA, Ma J, Daack-Hirsch S, Maher BS, Raffensperger LM, *et al*. Impaired FGF signaling contributes to cleft lip and palate. Proc Natl Acad Sci U S A 2007; 104: 4512–7.
19 Teumer A, Rawal R, Homuth G, Ernst F, Heier M, Evert M, *et al*. Genome-wide association study identifies four genetic loci associated with thyroid volume and goiter risk. Am J Hum Genet 2011; 88: 664–73.
20 Brehm JM, Hagiwara K, Tesfaigzi Y, Bruse S, Mariani TJ, Bhattacharya S, *et al*. Identification of FGF7 as a novel susceptibility locus for chronic obstructive pulmonary disease. Thorax 2011; 66: 1085–90.
21 Su ZG, Wen FQ, Feng YL, Xiao M, Wu XL. Transforming growth factor-beta1 gene polymorphisms associated with chronic obstructive pulmonary disease in Chinese population. Acta Pharmacol Sin 2005; 26: 714–20.
22 Fabbri LM, Hurd SS. Global strategy for the diagnosis, management

and prevention of COPD: 2003 update. Eur Respir J 2003; 22: 1–2.
23 Benjamini Y, Hochberg Y. Controlling the false discovery rate: a practical and powerful approach to multiple testing. J R Stat Soc Series B Stat Methodol 1995; 57: 289–300.
24 Silverman EK, Palmer LJ. Case-control association studies for the genetics of complex respiratory diseases. Am J Respir Cell Mol Biol 2000; 22: 645–8.
25 Morris RW, Kaplan NL. On the advantage of haplotype analysis in the presence of multiple disease susceptibility alleles. Genet Epidemiol 2002; 23: 221–33.
26 Silverman EK, Palmer LJ, Mosley JD, Barth M, Senter JM, Brown A, *et al*. Genomewide linkage analysis of quantitative spirometric phenotypes in severe early-onset chronic obstructive pulmonary disease. Am J Hum Genet 2002; 70: 1229–39.
27 Korb M, Ke YB, Johnson LF. Stimulation of gene expression by introns: conversion of an inhibitory intron to a stimulatory intron by alteration of the splice donor sequence. Nucl Acids Res 1993; 21: 5901–8.
28 Gaspar P, Moreira J, Kvitko1 K, Torres M, Moreira A, Weimer T. CYP1A1, CYP2E1, GSTM1, GSTT1, GSTP1, and TP53 polymorphisms: do they indicate susceptibility to chronic obstructive pulmonary disease and non-small-cell lung cancer? Genet Mol Biol 2004; 27: 133–8.
29 Dahl M, Tybjaerg-Hansen A, Lange P, Nordestgaard BG. DeltaF508 heterozygosity in cystic fibrosis and susceptibility to asthma. Lancet 1998; 351: 1911–3.
30 Seersholm N, Wilcke JT, Kok-Jensen A, Dirksen A. Risk of hospital admission for obstructive pulmonary disease in alpha(1)-antitrypsin heterozygotes of phenotype PiMZ. Am J Respir Crit Care Med 2000; 161: 81–4.

Acta Pharmacologica Sinica (2012) 33: 1004–1012
 1671-4083/12 $32.00
www.nature.com/aps

Original Article

The dual role of osteopontin in acetaminophen hepatotoxicity

Chun-yan HE[1, 2, #], Bei-bei LIANG[1, 2, #], Xiao-yu FAN[2], Lei CAO[1, 2], Rui CHEN[2], Ya-jun GUO[1, 2, 3, *], Jian ZHAO[2, *]

[1]*School of Medicine and School of Pharmacy, Shanghai Jiao Tong University, Shanghai 200025, China;* [2]*International Joint Cancer Institute, The Second Military Medical University, Shanghai 200433, China;* [3]*PLA General Hospital Cancer Center, PLA Postgraduate School of Medicine, Beijing 100863, China*

Aim: Osteopontin (OPN), a multifunctional protein, has been reported to be protoxicant in acetaminophen hepatotoxicity. In this study, the mechanisms underlying the detrimental role of OPN in acetaminophen toxicity were explored.
Methods: Male C57BL/6 (wild-type, WT) and *OPN*$^{-/-}$ mice were administered with acetaminophen (500 mg/kg, ip). After the treatment, serum transaminase (ALT), as well as OPN expression, histology changes, oxidative stress and inflammation response in liver tissue were studied. Freshly isolated hepatocytes of WT and *OPN*$^{-/-}$ mice were prepared.
Results: Acetaminophen administration significantly increased OPN protein level in livers of WT mice. OPN expression was mainly localized in hepatic macrophages 6 h after the administration. In *OPN*$^{-/-}$ mice, acetaminophen-induced serum ALT release was reduced, but the centrilobular hepatic necrosis was increased. In *OPN*$^{-/-}$ mice, the expression of CYP2E1 and CYP1A2 in livers was significantly increased; GSH depletion and lipid peroxidation in livers were enhanced. On the other hand, *OPN*$^{-/-}$ mice exhibited less macrophage and neutrophil infiltration and reduced expression of proinflammatory cytokines TNF-α and IL-1α in livers. An anti-OPN neutralizing antibody significantly reduced acetaminophen-induced serum ALT level and inflammatory infiltration in livers of WT mice.
Conclusion: OPN plays a dual role in acetaminophen toxicity: OPN in hepatocytes inhibits acetaminophen metabolism, while OPN in macrophages enhances acetaminophen toxicity via recruitment of inflammatory cells and production of proinflammatory cytokines.

Keywords: acetaminophen; osteopontin; liver; hepatotoxicity; macrophage; hepatocyte; cytokine

Acta Pharmacologica Sinica (2012) 33: 1004–1012; doi: 10.1038/aps.2012.47; published online 25 Jun 2012

Introduction

Acetaminophen (APAP), an effective analgesic and antipyretic drug, is safe at therapeutic doses. However, overdoses of APAP commonly cause drug-induced liver failure[1]. At therapeutic doses, about 90% of APAP is conjugated through sulfation or glucuronidation and then excreted into bile and urine, whereas 5%–10% of APAP is oxidized into *N*-acetylpbenzoquinone imine (NAPQI) by cytochrome P450s (CYPs). NAPQI is inactivated by conjugation with reduced glutathione (GSH) to form a 3-*S*-glutathionyl conjugate of APAP. At toxic doses, sulfation and glucuronidation pathways become saturated; hence, more NAPQI are formed with rapid depletion of hepatic GSH and then covalently bind to cellular proteins. APAP hepatotoxicity occurs after the depletion of GSH stores[2]. In mice and hamsters, phase I biotransformation is mostly limited to the P450 enzymes, CYP2E1 and CYP1A2[2]. CYP2E1 is a major CYP contributing to the metabolism of acetaminophen to NAPQI. CYP2E1 knockout mice was more resistant to APAP hepatotoxicity than WT mice[3, 4]. CYP2E1 is the main CYP that bioactivates APAP at low doses[5]. At a higher dose, CYP1A2 was shown to contribute to the bioactivation and toxicity of APAP[2]. Mice deficient in CYP2E1 and CYP1A2 exhibited high resistance to APAP hepatotoxicity[6]. CYP3A11 was also implicated in APAP hepatotoxicity[7]. Thus, genetic modulation of CYPs may influence the susceptibility to APAP toxicity.

Osteopontin (OPN), a highly modified integrin-binding extracellular matrix glycophosphoprotein, has been implicated in cell signaling that controls inflammation, tumor progression, and metastasis[8]. Recently, OPN was shown to act as a key stress protein in mechanic, oxidative and physical stress[9–11]. OPN mediates diversely biological activities, such as cell survival, motility and proliferation, through interaction with certain integrins and CD44 variants with its arginine-

# The first two authors contributed equally to this work.
* To whom correspondence should be addressed.
E-mail zhaojian@smmu.edu.cn (Jian ZHAO);
yjguo@smmu.edu.cn (Ya-jun GUO)
Received 2012-02-22 Accepted 2012-04-01

glycine-aspartate (RGD) and non-RGD motifs. The activities of OPN are closely involved in macrophage-mediated proinflammatory responses. OPN induces interleukin (IL)-12 in macrophages and suppresses anti-inflammatory cytokine IL-10 production, which results in the promotion of T helper cell type 1 differentiation[12]. OPN was shown to increase the expression of tumor necrosis factor (TNF)-α but not IL-6 or IL-1β in mouse resident peritoneal macrophages[13]. OPN is expressed in activated Kupffer cells (KCs), hepatic macrophages and stellar cells in response to CCl_4 treatment[14]. The activation of KCs directly or indirectly mediates hepatic toxicity and carcinogenesis through the release of multiple inflammatory cytokines, growth factors, and reactive oxygen species[15]. OPN was reported to modulate the ability of reactive oxygen species (ROS) production and the synthesis of inflammatory cytokines in KCs following a *Propionibacterium acnes* challenge[16]. APAP hepatotoxicity is frequently associated with inflammatory infiltration, and the nature and extent of the inflammation determine the progression and the severity of the injury[17]. Thus, the modulation of OPN on macrophage functions may influence APAP toxicology. OPN has been reported to play a protoxicant role in APAP-induced liver injury[18]. As demonstrated by microarray data, higher OPN mRNA was identified in APAP-sensitive strain C57BL/6 mice as compared to the resistant SJL mice after APAP treatment. OPN knockout mice were more resistant to APAP-mediated liver injury[18]. Nevertheless, the cellular origin of OPN and the mechanisms underlying its role in APAP hepatotoxicity remains unknown.

Accumulating evidence demonstrates that hepatic damage may be the event that triggers an immune response and then contributes to APAP toxicity. Despite increasing oxidative stress, the hepatocytes did not die after GSH depletion. Massive death of hepatocytes occurred 6 h after APAP administration and 4 h after GSH depletion[19]. Macrophages were shown to aggravate hepatic injury through the production of proinflammatory mediators, such as TNF-α, IL-1α, and nitric oxide[20, 21]. The cytotoxic and inflammatory mediators generated by activated inflammatory cells may aggravate cell damage and promote APAP toxicity[22]. In various liver inflammation models, OPN is a chemotactic factor for macrophages and neutrophils[23]. OPN deficiency caused reduced macrophage accumulation in many diseases, such as renal injury and colitis[24]. Moreover, OPN is a critical chemoattractant for neutrophils in liver inflammation models[23]. Depletion of neutrophils before APAP treatment was reported to provide protection against APAP-induced liver injury[25]. In this study, we explore the role of OPN in APAP metabolism and inflammation-mediated liver injury.

Materials and methods

Mice

C57BL/6 mice were purchased from the Shanghai Experimental Animal Center of Chinese Academic of Sciences (Shanghai, China). $OPN^{-/-}$ mice (B6.Cg-Spp1tm1blh/J, Cat No 004936) were obtained from the Jackson Laboratory (Genetics research, Bar Harbor, Maine, USA). All animals in this study were kept and bred in the Animal Unit of Shanghai Second Military Medical University in environmentally controlled and specific pathogen-free conditions.

The animals received considerate human care. All animal experimental procedures and protocols were approved by and conducted in accordance with the guidelines of the Animal Experiment Committee of the Shanghai Second Military Medical University of China.

Animal treatment

Eight-week-old male C57BL/6 and $OPN^{-/-}$ mice were intraperitoneally administered APAP (500 mg/kg, dissolved in PBS) and sacrificed at the indicated time. The mouse mAb 23C3 against human OPN were generated in our laboratory. The mouse mAb 23C3 showed cross-reactivity with mouse OPN[26]. For anti-OPN antibody treatment, 200 μg of anti-OPN Ab or mouse IgG (Sigma, St Louis, MO, USA) was intraperitoneally injected 2 h before APAP administration. Serum was collected for transaminase (ALT) assay and aspartate aminotransferase (AST) assay. The livers were rapidly removed and snap frozen in liquid nitrogen for RNA isolation, OPN quantification, and biochemical analysis or fixed in 10% neutral formalin buffer for histological assay.

Quantification of OPN protein in liver tissues

The livers were removed and snap frozen in liquid nitrogen. The frozen livers were homogenized in ice-cold cell lysis buffer (Cell Signaling, Danvers, MA, USA). After centrifugation at 20 000×*g* for 30 min at 4 °C, supernatant was pooled for OPN qualification using mouse OPN ELISA kit (R&D Systems, Minneapolis, MN, USA). The total protein was quantified using the BCA kit (Pierce, Rockford, IL, USA).

RNA isolation and quantitative real-time PCR

Total liver RNA was isolated using the Nucleospin RNA (Macherey-Nagel, Germany). The first strand synthesis was performed with random primers and reverse transcription with Quant Reverse Transcriptase (Tiangen Biotech, China). The quantitative real-time PCR was performed using a SYBR Green reagent in a Light Cycler (Roche, Germany). The reactions were performed twice in triplicate, and actin values were used to normalize gene expression. The primer sequences are presented in the Supplementary Data (Table 1).

Biochemistry analysis

Serum ALT and AST levels were measured with a colorimetric endpoint method utilizing diagnostic reagent kits (Pointe Scientific Inc, Canton, MI, USA) according to the manufacturer's protocol using a Roche Cobas Mira Classic Chemistry Analyzer (Roche Diagnostic systems, Inc, Branchburg, NJ, USA). ALT and AST levels were expressed as units per liter of serum. For GSH and myeloperoxidase (MPO) assay, liver tissue was weighed and homogenized in cold phosphate buffer (20 mmol/L, pH 7.2). For GSH analysis, homogenized liver was centrifuged at 10 000×*g* for 10 min at 4 °C. Supernatant was

Table 1. Primers for real-time PCR.

Gene	Primer	Sequence
mACTIN	Forward	5′-TGTTACCAACTGGGACGACA-3′
	Reverse	5′-CTGGGTCATCTTTTCACGGT-3′
mCYP2E1	Forward	5′-CCTTTCCCAATTCCTTTCTTTG-3′
	Reverse	5′-TCTTGTGGTTCAGTAGCACCTCC-3′
mCYP1A2	Forward	5′-AGTACATCTCCTTAGCCCCAG-3′
	Reverse	5′-GGTCCGGGTGGATTCTTCAG-3′
mCYP3A11	Forward	5′-ATGGAGATCACAGCCCAGTC-3′
	Reverse	5′-ATGCAGGGTGAAGGAAAGTG-3′
mIL6	Forward	5′-GCTACCAAACTGGATATAATCAGGA-3′
	Reverse	5′-CCAGGTAGCTATGGTACTCCAGAA-3′
mTNF-α	Forward	5′-ACTCAAATGGGCTTTCCGAAT-3′
	Reverse	5′-CACAGGGAAGAATCTGGAAAGG-3′
mIL-1a	Forward	5′-TGCATGGCATTCTTAGGAGG-3′
	Reverse	5′-TCAACTGGCATTTTGAAGCC-3′

used for the quantification of GSH level using a commercial kit (Nanjing Jiancheng Biotech, China). Total protein in the supernatant was quantified using a BCA kit (Pierce). GSH levels were expressed as microgram per gram of protein. MPO activity in liver homogenate was measured using commercial kits (Nanjing Jiancheng Biotech, China) and expressed as units per gram of liver. For malondialdehyde (MDA) analysis, liver tissue was weighed and homogenized in Tris-HCl buffer (20 mmol/L, pH 7.4). MDA in homogenate was measured using commercial kits (Nanjing Jiancheng Biotech, China). MDA content was expressed as micromole per gram of liver.

Histochemical analysis

Liver tissue was removed from mice with different treatment. Liver samples were fixed in 10% neutral formalin buffer and embedded in paraffin wax, and the sections were stained with H&E. The tissue sections were examined under a light microscope and photographed using a Nikon camera fitted to the microscope. Images were acquired as mentioned above, and the quantitative data were obtained using a computerized image analysis system (KS 300, Carl Zeiss Vision). The analysis was performed on an average of 25 fields per section using ×10 objective. The necrosis was expressed as a percentage of necrotic areas per field area.

The expression of OPN protein in mouse livers was detected by immunohistochemistry (IHC) with mouse anti-OPN mAb 23C3 as the primary antibody and rabbit anti-mouse IgG as the secondary antibody. The expression of F4/80 in mouse livers was detected by a rat anti-mouse F4/80 antibody (Cell Signaling, Danvers, MA, USA) and Cy3-labeled anti-rat IgG (Beyotime, China) as the primary and secondary antibody, respectively. Nuclei were visualized by DAPI staining. F4/80 staining was observed by fluorescent microscopy and photographed. The number of F4/80 positive cells per field was determined in the centrilobular areas by morphometric analysis using the SPOT advanced software package (Diagnostic Instruments, Inc, Sterling Heights, MI, USA). The analysis was performed on an average of 10 fields per section using the ×40 objective.

Isolation of liver cells and cell culture

Hepatocytes were isolated using a standard collagenase procedure as described[27]. The hepatocyte viability, as determined by trypan blue exclusion, was generally >95%, and the cell purity was >95%. Cells were plated in collagen I-coated 12-well plates (6×10^5 cells per well) (BD BioCoat™, BD Biosciences, San Jose, CA, USA) in HepatoZYME-SFM medium (Gibco, Grand Island, NY, USA) containing 100 U/mL penicillin/streptomycin and cultured at 37 °C in 5% CO_2. After 3-h attachment, the cultures were washed with PBS and then plain culture medium (controls) or media containing 100 μmol/L H_2O_2 were added for 6 h or 12 h. Cell viability was measured with MTS-based assay (Promega, Southampton, UK) according to the manufacturer's instructions.

Statistical analysis

Data are expressed as mean±SEM. Differences were analyzed by Student's *t* test, and *P* values <0.05 were considered significant.

Results

OPN expression was increased after APAP administration

Wild-type (WT) mice were ip injected with a toxic dose of APAP and OPN protein in livers was assayed at different time points (Figure 1A). OPN protein increased 2 h later and doubled 6 h after APAP administration. The OPN level in livers remained high 12 h after APAP treatment.

We detected the distribution of OPN in liver using IHC staining. The normal liver did not show OPN staining (Figure 1B). Six hours after APAP exposure, strong positive staining

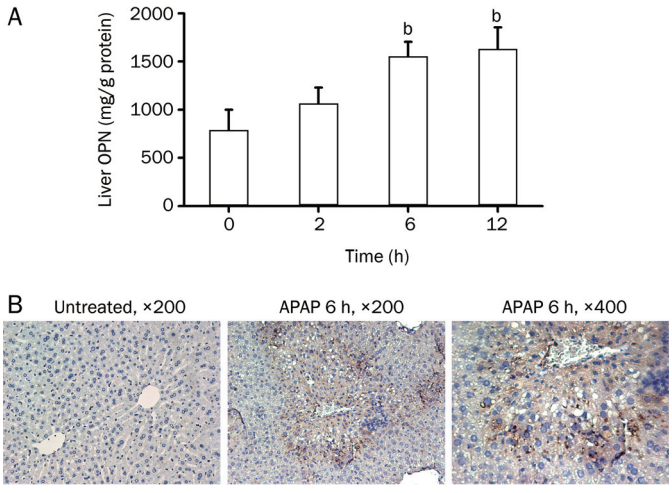

Figure 1. OPN expression in livers of wild-type (WT) male mice after APAP administration. (A) WT male mice were ip administered with 500 mg/kg APAP and sacrificed at different time. Livers were removed for the measurement of OPN protein level. *n*=5 for each time point; (B) Immunohistochemical staining for OPN in the livers of WT mice 6 h after APAP administration. Data are mean±SEM. $^bP<0.05$ vs 0 h.

was observed in hepatic macrophages adjacent to necrotic hepatocytes in Zone III (Figure 1B). OPN expression was mainly localized in hepatic macrophages. We also observed a slight increase of OPN expression in necrotic hepatocytes.

These results indicate that OPN expression was increased after APAP administration and this increase is mainly localized in hepatic macrophages.

OPN deficiency mice exhibited reduced serum ALT but more necrosis after APAP treatment

To determine the involvement of OPN in APAP hepatotoxicity, WT and *OPN*$^{-/-}$ male mice were injected with APAP and serum ALT was assayed at different time points. As previously reported[18], OPN knockout mice showed significantly lower ALT levels than WT mice (Figure 2A). The maximum ALT appeared 6 h after APAP treatment in *OPN*$^{-/-}$ mice and rapidly recovered to the basal level. In comparison, serum ALT in WT mice was twice that of the *OPN*$^{-/-}$ mice at 6 h and reached the maximum 24 h after APAP treatment. Both ALT and AST levels in WT and *OPN*$^{-/-}$ mice exhibited similar trend (Figure 2B).

We further examined the histopathology of the livers of APAP-treated mice. APAP causes severe hepatic damage with massive necrotic hepatocytes in the central lobular zones (Figure 2C). The necrosis area of the livers from *OPN*$^{-/-}$ mice was significantly greater than that of WT mice (Figure 2D), which was inconsistent with the results of serum ALT. The discrepancy between the ALT results and the histological grades was also observed in other studies[28].

The data indicated that OPN enhanced the release of serum ALT level despite the inhibition of necrosis.

OPN deficiency enhanced APAP metabolism and oxidative stress

APAP-induced hepatic necrosis was closely related to the oxidative stress caused by APAP metabolism[19]. To examine whether OPN deficiency enhanced the formation of NAPQI, the key CYP enzymes involved in APAP metabolism were analyzed. CYP2E1 is an important CYP in APAP toxicity[3]. APAP treatment caused the reduction of CYP2E1 mRNA expression, whereas *OPN*$^{-/-}$ mice showed significantly higher CYP2E1 expression than WT mice, 2 h and 6 h after treatment (Figure 3A). At toxic doses, CYP1A2 and CYP3A may be the predominant CYPs in APAP oxidation. When untreated, *OPN*$^{-/-}$ mice exhibited higher CYP1A2 expression than WT mice (Figure 3B). APAP treatment remarkably increased the expression of CYP1A2. The expression of CYP1A2 was significantly higher in APAP-exposed *OPN*$^{-/-}$ mice than WT mice. The basal level of CYP3A11 expression in *OPN*$^{-/-}$ mice was lower than that of WT mice. However, no significant difference was observed in CYP3A11 expression between the groups after APAP treatment (Figure 3C).

Higher level of CYPs is related to increased formation of NAPQI, which results in the depletion of reduced GSH. The hepatic GSH levels were measured at 0, 2, and 6 h after APAP treatment. OPN deficiency did not cause a significant change on the basal GSH level (Figure 3D). APAP treatment resulted in GSH depletion in both mice. Interestingly, a significantly higher GSH level was observed in WT mice at 2 h and 6 h after APAP treatment compared to *OPN*$^{-/-}$ mice. At 6 h, the hepatic GSH level in *OPN*$^{-/-}$ mice was fully restored to the pretreatment level while the GSH level in WT mice was slightly upregulated by about 10% above the pretreatment level. Oxidative stress following GSH depletion was often accompanied

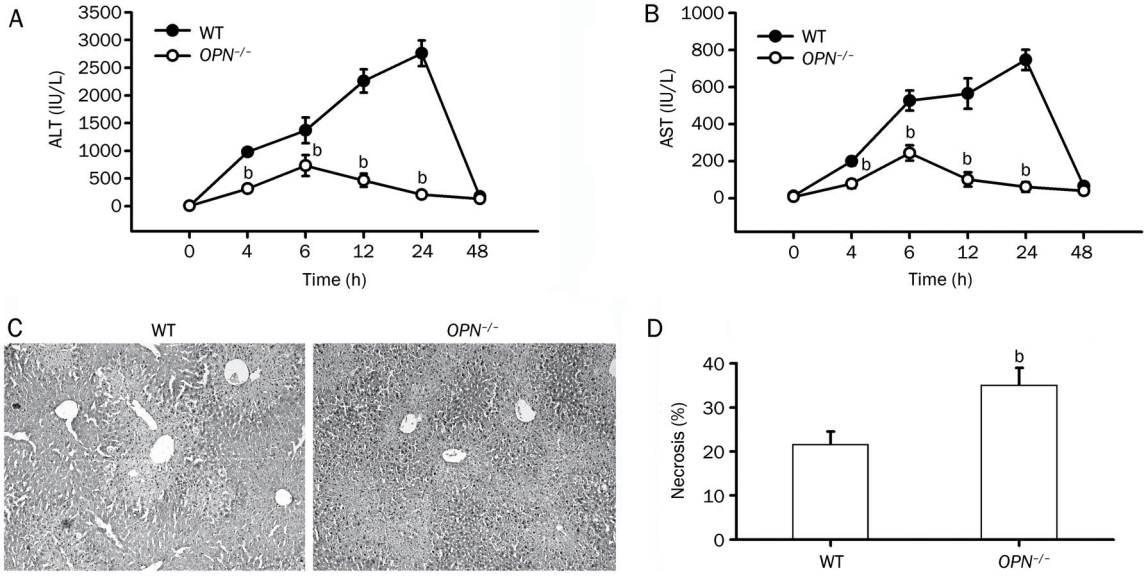

Figure 2. Serum ALT and AST level and histologic necrosis in APAP-treated WT and *OPN*$^{-/-}$ mice. (A and B) WT male and *OPN*$^{-/-}$ mice were given APAP (500 mg/kg), and ALT level (A) and AST (B) were measured at indicated time points. (n=6 mice per time point). (C and D) Representative hematoxylin/eosin staining of liver section (C) (200×magnification) and average necrosis (D) 6 h after APAP treatment. Data are mean±SEM. ^{b}P<0.05 vs WT.

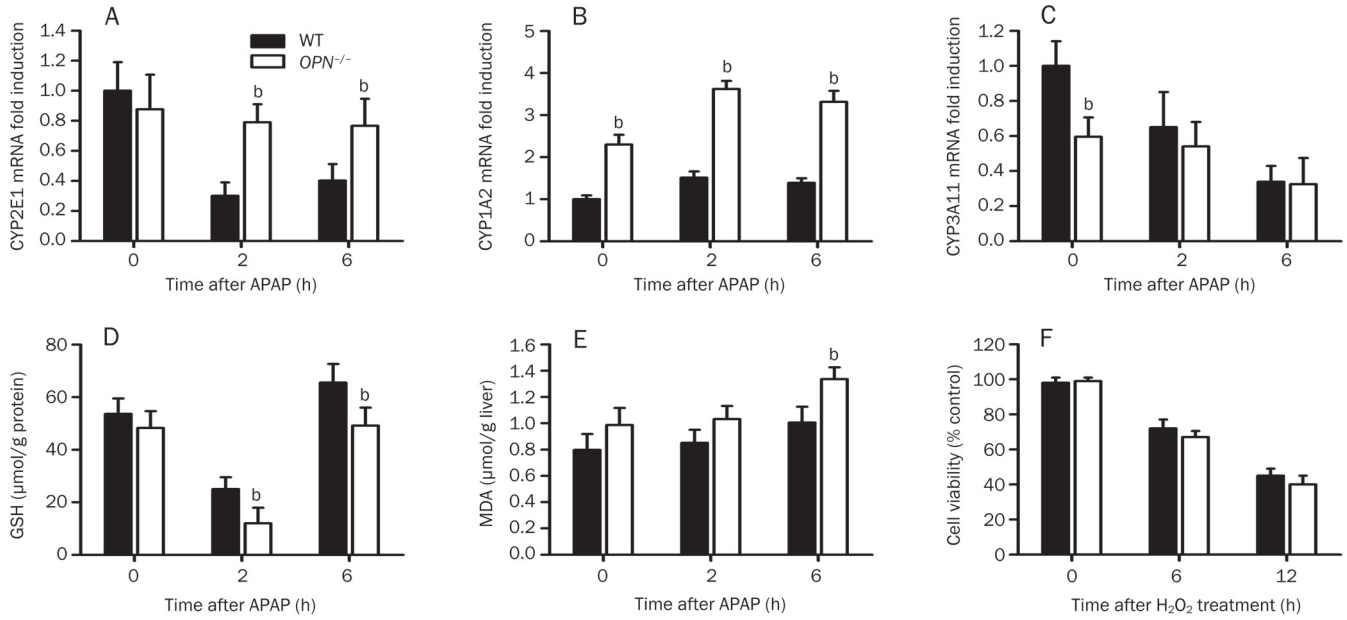

Figure 3. Effects of OPN deficiency on the expression of CYPs genes and redox homeostasis after APAP administration. WT or *OPN*$^{-/-}$ mice (n=4) were treated with APAP and their livers were removed at indicated time. (A–C) The expression of CYP2E1 (A), CYP1A2 (B), and CYP3A11 (C) in livers after APAP administration were detected by real-time PCR. Actin values were used to normalize gene expression. (D and E) liver lysates were analyzed for GSH content (D) and MDA content (E). n=4 for each time point. (F) Viability of WT and *OPN*$^{-/-}$ hepatocytes after H_2O_2 treatment. Freshly isolated WT and *OPN*$^{-/-}$ hepatocytes were inoculated with or without 100 μmol/L H_2O_2 and cell viability was measured with MTS assay at different time points. Data are mean±SEM. ^bP<0.05, Student's t-test.

by lipid peroxidation (LPO). The LPO, measured by MDA level (Figure 3E), was not significantly increased in APAP-treated WT mice, indicating relatively low lipid peroxidation. The MDA level of *OPN*$^{-/-}$ mice was significantly higher than that of WT mice 6 h after APAP exposure.

We further examine whether OPN deficiency enhances the susceptibility of hepatocytes to oxidative stress. Using isolated hepatocytes, we found that *OPN*$^{-/-}$ hepatocytes did not exhibit significantly higher necrosis than WT hepatocytes under H_2O_2 treatment (Figure 3F). Thus, OPN deficiency did not enhance the sensitivity of hepatocytes to oxidative stress.

These results show that OPN deficiency accelerated the formation of reactive metabolites and enhanced oxidative stress, which partly resulted in enhanced hepatic necrosis.

OPN promotes APAP toxicity through the enhancement of inflammatory accumulation and the production of proinflammatory mediators

Although the oxidative stress caused by APAP metabolism leads to direct hepatic cellular dysfunction and death, the release of a variety of inflammatory mediators may influence individual susceptibility. OPN is chemotactic for macrophages in liver inflammation[23]. Using F4/80 IHC, greater macrophage accumulation was observed in WT mice than in OPN$^{-/-}$ mice 6 h after APAP administration (Figure 4). Hepatic macrophage was implicated in APAP toxicity as a result of the production of a variety of proinflammatory cytokines[29]. We examined the expression of TNF-α, IL-1α, and IL-6 expression in APAP-treated mice. Similar to previous reports[30], APAP administration greatly enhanced TNF-α and IL-1α expression. OPN deficiency resulted in lower TNF-α and IL-1α expression in *OPN*$^{-/-}$ mice compared with WT mice after APAP treatment (Figure 5A). This lower production of proinflammatory cytokines coincided with reduced macrophage infiltration. IL-6 expression did not change significantly after APAP administration in both WT mice and *OPN*$^{-/-}$ mice (Figure 5C).

OPN plays a role in the recruitment of neutrophils in liver inflammation[23]. We examined the neutrophil infiltration in the livers of the treated mice. The neutrophil accumulation, evidenced by MPO level (Figure 5D), was increased in WT mice after APAP and correlated with OPN expression. In comparison, the MPO level did not significantly increase after APAP administration in *OPN*$^{-/-}$ mice. This result shows that OPN is critical for APAP-induced neutrophil recruitment.

These results indicate that OPN promotes APAP hepatotoxicity through the enhancement of inflammatory infiltration and proinflammatory cytokine expression.

Anti-OPN antibody reduced hepatic damage through the inhibition of inflammatory infiltration

To corroborate the role of OPN in APAP toxicity, we examined the therapeutic activity of anti-OPN antibody. The anti-OPN neutralizing antibody, 23C3, was shown to reduce hepatic damage through inhibition of NK and NKT cell infiltration in mural ConA-induced hepatitis model[31]. WT mice

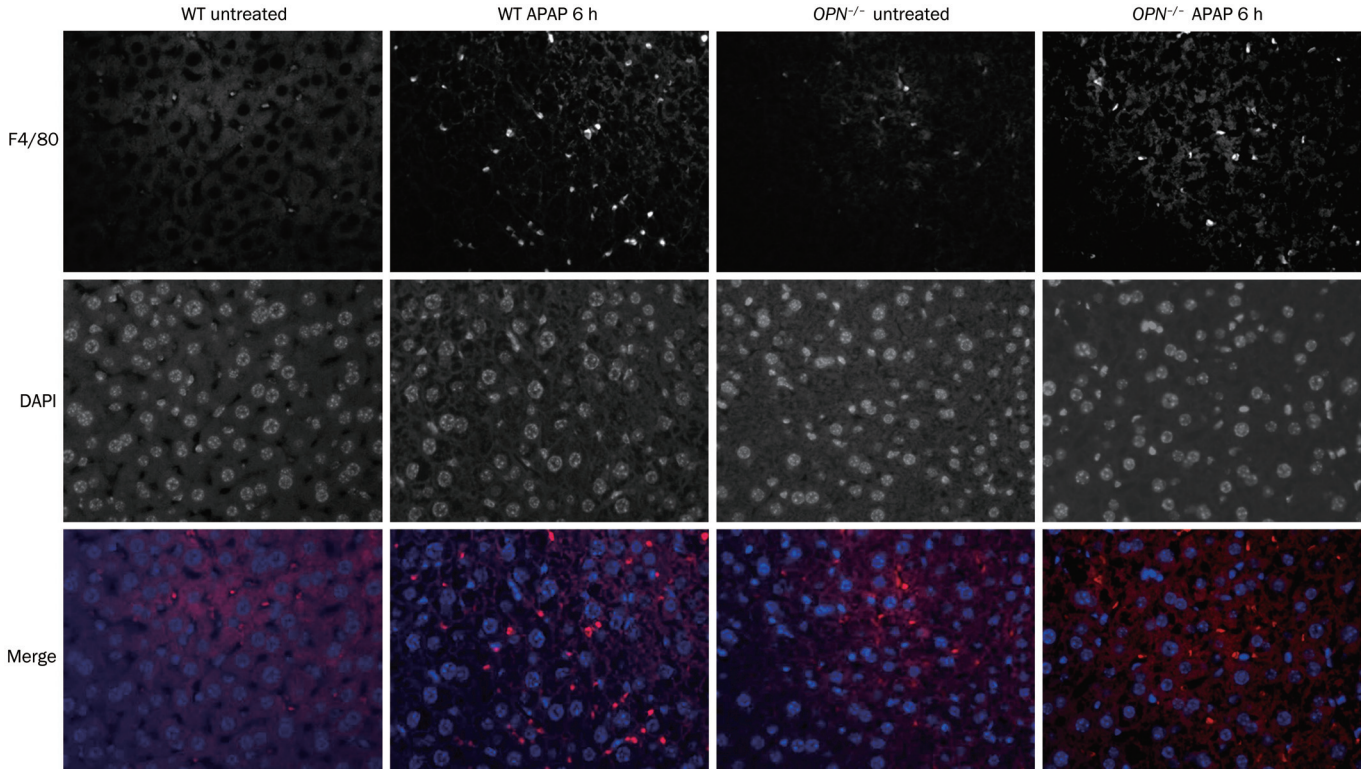

Figure 4. F4/80 staining in livers of APAP-treated mice. WT and *OPN*$^{-/-}$ mice were administered with APAP. Six hours later, the expressions of F4/80 in mouse livers were detected by rat anti-mouse F4/80 antibody and Cy3-labeled anti-rat IgG as primary and secondary antibody, respectively. Nuclei were visualized by DAPI staining (×400).

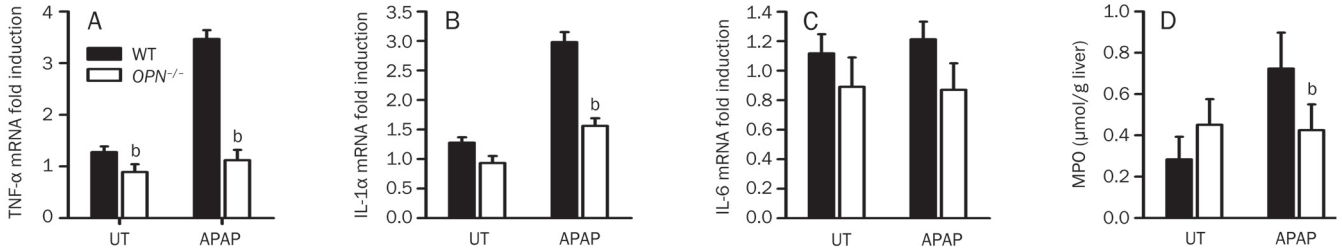

Figure 5. Effects of OPN deficiency on proinflammatory cytokines and neutrophil infiltration. WT or *OPN*$^{-/-}$ mice (n=4) were treated with APAP and their livers were removed 6 h later. (A–C) The expression of TNF-α (A), IL-1α (B), and IL-6 (C) in livers were detected by real-time PCR. Actin values were used to normalize gene expression. (D) Liver lysates were analyzed for MPO level 6 h after APAP. n=4 for each time point. Data are mean±SEM. ^{b}P<0.05, Student's t-test.

were pretreated with 23C3 and then challenged with toxic doses of APAP. Pretreatment with 23C3 in WT mice significantly reduced ALT level (Table 2). Similarly, the accumulation of F4/80 positive cells and the MPO level were markedly reduced as a result of 23C3 pretreatment (Table 2). Moreover, 23C3 also reduces APAP-induced hepatocellular necrosis, although not significantly. The anti-OPN neutralizing antibody effectively prevented APAP-induced hepatotoxicity through the inhibition of inflammatory infiltration.

Discussion

The pathogenesis of APAP-induced hepatotoxicity consists of direct cellular damage as well as the innate immune system. Our study demonstrates that OPN plays a dual role in APAP hepatotoxicity.

The mechanism of APAP detoxification and the sensitivity of hepatocytes may have a direct effect on hepatocyte death. The level of hepatic phase I oxidative enzymes is correlated with the sensitivity of APAP toxicity. CYP2E1 and CYP1A2 are the two major CYPs in APAP metabolism in mice[6]. OPN deficiency enhanced the expression of both CYP2E1 and CYP1A2, which may accelerate the production of the reactive metabolite. Increased oxidative stress caused higher GSH depletion and lipid peroxidation. Because the metabolism

Table 2. Pretreatment with anti-OPN antibody 23C3 reduced ALT, histological necrosis, macrophage and neutrophil infiltration in WT mice 6 h after APAP administration. n=6 for each group. [b]P<0.05 compared to IgG-treated mice. *ND, Not done.

Treatment	ALT (IU/L)		Necrosis %		F4/80 positive cells per field		MPO (μmol/g tissue)	
	IgG	23C3	IgG	23C3	IgG	23C3	IgG	23C3
Untreated	6±1	5.4±1.2	ND	ND	ND*	ND	0.30±0.09	0.32±0.11
APAP	1440±80	870±120[b]	23±4	18±4	37±5	22±3[b]	0.75±0.18	0.35±0.15[b]

of APAP occurs mainly in hepatocytes, OPN deficiency may interfere with the bioactivation of APAP. OPN can be synthesized in hepatocytes in low levels[32] and can be upregulated under pathologic conditions[33]. Recent studies have revealed that an intracellular form of OPN (iOPN), except the secreted isoform of OPN (sOPN), regulates cell motility, cell division and cytokine expression[34]. Nevertheless, the mechanism by which hepatocyte-derived iOPN or sOPN modulates CYP gene expression requires further investigation. Another possible reason for enhanced necrosis observed in $OPN^{-/-}$ mice is the prosurvival activity of OPN. Necrosis is the main mode of hepatocyte death after APAP overdose[35]. OPN was reported to inhibit cardiac fibroblast necrosis in response to hydrogen peroxide (H_2O_2) in caspase-3-independent pathway. Under H_2O_2 treatment, $OPN^{-/-}$ hepatocytes did not exhibit higher necrosis than WT hepatocytes (Figure 3F). This inconsistency may be due to the relatively low expression of OPN in hepatocytes. Thus, increased hepatocyte necrosis in $OPN^{-/-}$ mice may be explained by the enhanced oxidative stress caused by APAP metabolism.

Serum ALT is routinely measured as part of the diagnostic evaluation of hepatocellular injury. Although they may be identified as necrotic, not all necrotic hepatocytes die with the release of ALT. Thus, it is not surprising to observe a discrepancy between the necrosis and the ALT results in reports[28, 36, 37]. On the basis of ALT results, we conclude that OPN-mediated inflammatory response plays an important role in the progression of APAP hepatotoxicity. After GSH depletion, stressed hepatocytes release damage signals, such as HMGB1[30] and IL-1α[38], which activate KCs and recruit inflammatory cells. KCs activate the expression of TNF-α, IL-6, and IL-1β as early as 1 h after APAP challenge[30]. The expression of OPN was reported to be upregulated in APAP toxicology, whereas the cells expressing OPN within the liver is unclear[18]. We found that activated KCs around necrotic hepatocytes were also the main source of OPN in livers after overdose APAP exposure. As a critical chemotactic factor for macrophages, the upregulation of OPN at sites of injury enhances macrophage infiltration. This macrophage accumulation can be effectively blocked by the pretreatment with anti-OPN antibody. Thus, OPN deficiency markedly reduced APAP-induced macrophage infiltration. The production of cytotoxic mediators by macrophages was one of the mechanisms underlying immune-mediated liver injury[17]. OPN deficiency in APAP-exposed mice resulted in the dysfunction of cytokine production. In comparison to WT mice, OPN-deficient mice exhibited markedly reduced production of proinflammatory cytokine TNF-α and IL-1α after APAP challenge. TNF-α has been linked to increased oxidative stress, such as ROS and nitric oxide[39, 40], and it is known to recruit and activate other inflammatory cells[41]. IL-1ra knockout mice exhibited a reduction in APAP toxicity with less liver injury and reduced leukocytes infiltration[42]. APAP hepatotoxicity was partially reduced by treatment with either anti-TNF-α or anti-IL-1α in acetaminophen-intoxicated mice[43]. Nonetheless, the role of OPN in the modulation of macrophage function requires further investigation. Moreover, both TNF-α and IL-6 also contributed to the restoration of liver function by promoting liver regeneration[40, 44]. The enhanced liver repair does not contribute to the reduced hepatic damage in $OPN^{-/-}$ mice, which showed reduced expression of TNF-α and IL-6 when compared to WT mice. Therefore, OPN may promote APAP toxicity through the enhancement of macrophage accumulation and the production of proinflammatory cytokines.

The primary role of neutrophil influx in APAP toxicity is postulated to serve to remove damaged cells and cellular debris[45]. Although the detrimental role of neutrophils in APAP hepatotoxicity in animal models is still controversial, the recruited neutrophils may likely aggravate the injury by attacking and killing some of the stressed hepatocytes. Deletion of neutrophil using the anti-Gr-1 antibody was shown to significantly attenuate APAP toxicity in mice[25]. OPN is important for the migration of neutrophils *in vitro* and *in vivo*[46]. Thus, neutrophil infiltration was not increased by APAP administration in $OPN^{-/-}$ mice compared to WT mice. The inflammation and cytotoxic cytokines caused by elevated OPN production further aggravated the death of stressed hepatocytes. Consequently, serum ALT level in $OPN^{-/-}$ mice rapidly recovered to the basal level as a result of decreased inflammation, while increased inflammation in WT mice caused higher levels of serum ALT.

The dual role of OPN may be explained by its role in different liver cells during the process of APAP-induced liver injury. In the early stage, iOPN deficiency in hepatocytes caused increased CYP expression and enhanced APAP metabolism-induced oxidative stress. After hepatocyte damage, the elevation of sOPN in macrophages resulted in massive inflammatory infiltration and the release of proinflammatory cytokines. Pretreatment with anti-OPN antibody effectively inhibited APAP-induced inflammation infiltration with the reduction

of serum ALT level through neutralizing sOPN. These results indicate that sOPN plays a protoxicant role in inflammation-induced liver injury, while iOPN in hepatocytes may play a hepatoprotective role. Thus, anti-OPN treatment may represent a promising therapy for APAP-induced liver diseases through the inhibition of inflammation-induced liver injury. OPN is a heterogeneous protein found with different degrees of phosphorylation in different cell types[47]. The function of OPN can be affected by its cell-specific post-translational modification, enzyme cleavage or different isoforms[34, 48, 49]. Hepatocyte-derived OPN may function differently from that produced by inflammatory cells. Hence, mice lacking OPN only in hepatocytes or in macrophages should be developed to examine the exact mechanism of OPN in APAP toxicity.

In conclusion, we find that OPN plays a dual role in APAP toxicity. At the APAP metabolism stage, iOPN in hepatocytes plays a protective role through the inhibition of APAP metabolism; however, at the inflammation stage, subsequent to metabolism, sOPN promotes inflammation-induced hepatic damage through the recruitment of macrophages and neutrophils. The anti-OPN antibody therapy may provide an effective treatment for APAP-induced liver diseases through inhibition of inflammation. Our findings may facilitate a better understanding of the mechanism underlying APAP toxicity and provide new avenues for the prevention and treatment of drug-induced liver injury.

Acknowledgements

This work is supported in part by grants from Ministry of Science and Technology of China (2010CB945600, 2011CB966200), National Natural Science Foundation of China, the Special Project for Infection Disease (2008ZX10002-019), New Drug Development and Program of Shanghai Subject Chief Scientists (10XD1405400).

Author contribution

Chun-yan HE (performing the major experiments and writing manuscript), Bei-bei LIANG (performing animal experiments), Xiao-yu FAN (RNA extraction and RT PCR), Lei CAO (expression of recombinant OPN and OPN antibody), Rui CHEN (Western blotting and IHC analysis), Jian ZHAO (analysis of data and manuscript writing), and Ya-jun GUO (study design, data analysis and writing the manuscript).

Abbreviations

ALT, transaminase; APAP, acetaminophen; AST, aspartate aminotransferase; CYPs, cytochrome P450s; GSH, glutathione; IHC, immunohistochemical; KC, Kupffer cell; LPO, lipid peroxidation; MDA, malondialdehyde; MPO, myeloperoxidase; NAPQI, *N*-acetyl-pbenzoquinone imine; OPN, osteopontin; RGD, arginine-glycine-aspartate.

References

1 Larson AM, Polson J, Fontana RJ, Davern TJ, Lalani E, Hynan LS, *et al*. Acetaminophen-induced acute liver failure: results of a United States multicenter, prospective study. Hepatology 2005; 42: 1364–72.
2 Bessems JG, Vermeulen NP. Paracetamol (acetaminophen)-induced toxicity: Molecular and biochemical mechanisms, analogues and protective approaches. Crit Rev Toxicol 2001; 31: 55–138.
3 Cheung C, Yu AM, Ward JM, Krausz KW, Akiyama TE, Feigenbaum L, *et al*. The cyp2e1-humanized transgenic mouse: role of cyp2e1 in acetaminophen hepatotoxicity. Drug Metab Dispos 2005; 33: 449–57.
4 Chen C, Krausz KW, Idle JR, Gonzalez FJ. Identification of novel toxicity-associated metabolites by metabolomics and mass isotopomer analysis of acetaminophen metabolism in wild-type and Cyp2e1-null mice. J Biol Chem 2008; 283: 4543–59.
5 Lee SS, Buters JT, Pineau T, Fernandez-Salguero P, Gonzalez FJ. Role of CYP2E1 in the hepatotoxicity of acetaminophen. J Biol Chem 1996; 271: 12063–7.
6 Zaher H, Buters JT, Ward JM, Bruno MK, Lucas AM, Stern ST, *et al*. Protection against acetaminophen toxicity in CYP1A2 and CYP2E1 double-null mice. Toxicol Appl Pharmacol 1998; 152: 193–9.
7 Guo GL, Moffit JS, Nicol CJ, Ward JM, Aleksunes LA, Slitt AL, *et al*. Enhanced acetaminophen toxicity by activation of the pregnane X receptor. Toxicol Sci 2004; 82: 374–80.
8 Rangaswami H, Bulbule A, Kundu GC. Osteopontin: role in cell signaling and cancer progression. Trends Cell Biol 2006; 16: 79–87.
9 Ishijima M, Tsuji K, Rittling SR, Yamashita T, Kurosawa H, Denhardt DT, *et al*. Osteopontin is required for mechanical stress-dependent signals to bone marrow cells. J Endocrinol 2007; 193: 235–43.
10 Baliga SS, Merrill GF, Shinohara ML, Denhardt DT. Osteopontin expression during early cerebral ischemia-reperfusion in rats: enhanced expression in the right cortex is suppressed by acetaminophen. PLoS One 2011; 6: e14568.
11 Wang KX, Denhardt DT. Osteopontin: role in immune regulation and stress responses. Cytokine Growth Factor Rev 2008; 19: 333–45.
12 Ashkar S, Weber GF, Panoutsakopoulou V, Sanchirico ME, Jansson M, Zawaideh S, *et al*. Eta-1 (osteopontin): an early component of type-1 (cell-mediated) immunity. Science 2000; 287: 860–4.
13 Weber GF, Zawaideh S, Hikita S, Kumar VA, Cantor H, Ashkar S. Phosphorylation-dependent interaction of osteopontin with its receptors regulates macrophage migration and activation. J Leukoc Biol 2002; 72: 752–61.
14 Kawashima R, Mochida S, Matsui A, YouLuTuZ Y, Ishikawa K, Toshima K, *et al*. Expression of osteopontin in Kupffer cells and hepatic macrophages and Stellate cells in rat liver after carbon tetrachloride intoxication: a possible factor for macrophage migration into hepatic necrotic areas. Biochem Biophys Res Commun 1999; 256: 527–31.
15 Roberts RA, Ganey PE, Ju C, Kamendulis LM, Rusyn I, Klaunig JE. Role of the Kupffer cell in mediating hepatic toxicity and carcinogenesis. Toxicol Sci 2007; 96: 2–15.
16 Yang H, Guo H, Fan K, Zhang B, Zhao L, Hou S, *et al*. Clearance of *Propionibacterium acnes* by kupffer cells is regulated by osteopontin through modulating the expression of p47phox. Mol Immunol 2011; 48: 2019–26.
17 Adams DH, Ju C, Ramaiah SK, Uetrecht J, Jaeschke H. Mechanisms of immune-mediated liver injury. Toxicol Sci 2010; 115: 307–21.
18 Welch KD, Reilly TP, Bourdi M, Hays T, Pise-Masison CA, Radonovich MF, *et al*. Genomic identification of potential risk factors during acetaminophen-induced liver disease in susceptible and resistant strains of mice. Chem Res Toxicol 2006; 19: 223–33.
19 Hinson JA, Roberts DW, James LP. Mechanisms of acetaminophen-induced liver necrosis. Handb Exp Pharmacol 2010; (196): 369–405.
20 Laskin DL, Gardner CR, Price VF, Jollow DJ. Modulation of macrophage functioning abrogates the acute hepatotoxicity of acetaminophen. Hepatology 1995; 21: 1045–50.

21 Michael SL, Pumford NR, Mayeux PR, Niesman MR, Hinson JA. Pretreatment of mice with macrophage inactivators decreases acetaminophen hepatotoxicity and the formation of reactive oxygen and nitrogen species. Hepatology 1999; 30: 186–95.
22 Jaeschke H. Role of inflammation in the mechanism of acetaminophen-induced hepatotoxicity. Expert Opin Drug Metab Toxicol 2005; 1: 389–97.
23 Ramaiah SK, Rittling S. Pathophysiological role of osteopontin in hepatic inflammation, toxicity, and cancer. Toxicol Sci 2008; 103: 4–13.
24 Rittling SR. Osteopontin in macrophage function. Exp Rev Mol Med 2011; 13: e15.
25 Liu ZX, Han D, Gunawan B, Kaplowitz N. Neutrophil depletion protects against murine acetaminophen hepatotoxicity. Hepatology 2006; 43: 1220–30.
26 Fan K, Dai J, Wang H, Wei H, Cao Z, Hou S, *et al*. Treatment of collagen-induced arthritis with an anti-osteopontin monoclonal antibody through promotion of apoptosis of both murine and human activated T cells. Arthritis Rheum 2008; 58: 2041–52.
27 Chen Q, Kon J, Ooe H, Sasaki K, Mitaka T. Selective proliferation of rat hepatocyte progenitor cells in serum-free culture. Nat Protoc 2007; 2: 1197–205.
28 Holt MP, Cheng L, Ju C. Identification and characterization of infiltrating macrophages in acetaminophen-induced liver injury. J Leukoc Biol 2008; 84: 1410–21.
29 Han D, Shinohara M, Ybanez MD, Saberi B, Kaplowitz N. Signal transduction pathways involved in drug-induced liver injury. Handb Exp Pharmacol 2010; (196): 267–310.
30 Martin-Murphy BV, Holt MP, Ju C. The role of damage associated molecular pattern molecules in acetaminophen-induced liver injury in mice. Toxicol Lett 2010; 192: 387–94.
31 Fan K, Zhang B, Yang H, Wang H, Tan M, Hou S, *et al*. A humanized anti-osteopontin antibody protects from Concanavalin A induced-liver injury in mice. Eur J Pharmacol 2011; 657: 144–51.
32 Sahai A, Pan X, Paul R, Malladi P, Kohli R, Whitington PF. Roles of phosphatidylinositol 3-kinase and osteopontin in steatosis and aminotransferase release by hepatocytes treated with methionine-choline-deficient medium. Am J Physiol Gastrointest Liver Physiol 2006; 291: G55–62.
33 Atul Sahai PM, Melin-Aldana H, Green RM, Whitington PF. Upregulation of osteopontin expression is involved in the development of nonalcoholic steatohepatitis in a dietary murine model. Am J Physiol Gastrointest Liver Physiol 2004; 287: G264–73.
34 Cantor H, Shinohara ML. Regulation of T-helper-cell lineage development by osteopontin: the inside story. Nat Rev 2009; 9: 137–41.
35 Gujral JS, Knight TR, Farhood A, Bajt ML, Jaeschke H. Mode of cell death after acetaminophen overdose in mice: apoptosis or oncotic necrosis? Toxicol Sci 2002; 67: 322–8.
36 Agarwal R, Hennings L, Rafferty TM, Letzig LG, McCullough S, James LP, *et al*. Acetaminophen-induced hepatotoxicity and protein nitration in neuronal nitric-oxide synthase knockout mice. J Pharmacol Exp Ther 2012; 340: 134–42.
37 Michael SL, Mayeux PR, Bucci TJ, Warbritton AR, Irwin LK, Pumford NR, *et al*. Acetaminophen-induced hepatotoxicity in mice lacking inducible nitric oxide synthase activity. Nitric Oxide 2001; 5: 432–41.
38 Sakurai T, He G, Matsuzawa A, Yu GY, Maeda S, Hardiman G, *et al*. Hepatocyte necrosis induced by oxidative stress and IL-1 alpha release mediate carcinogen-induced compensatory proliferation and liver tumorigenesis. Cancer Cell 2008; 14: 156–65.
39 Ishida Y, Kondo T, Tsuneyama K, Lu P, Takayasu T, Mukaida N. The pathogenic roles of tumor necrosis factor receptor p55 in acetaminophen-induced liver injury in mice. J Leukoc Biol 2004; 75: 59–67.
40 Schwabe RF, Brenner DA. Mechanisms of liver injury. I. TNF-alpha-induced liver injury: role of IKK, JNK, and ROS pathways. Am J Physiol Gastrointest Liver Physiol 2006; 290: G583–9.
41 Gardner CR, Laskin JD, Dambach DM, Chiu H, Durham SK, Zhou P, *et al*. Exaggerated hepatotoxicity of acetaminophen in mice lacking tumor necrosis factor receptor-1. Potential role of inflammatory mediators. Toxicol Appl Pharmacol 2003; 192: 119–30.
42 Ishibe T, Kimura A, Ishida Y, Takayasu T, Hayashi T, Tsuneyama K, *et al*. Reduced acetaminophen-induced liver injury in mice by genetic disruption of IL-1 receptor antagonist. Lab Invest 2009; 89: 68–79.
43 Blazka ME, Elwell MR, Holladay SD, Wilson RE, Luster MI. Histopathology of acetaminophen-induced liver changes: role of interleukin 1 alpha and tumor necrosis factor alpha. Toxicol Pathol 1996; 24: 181–9.
44 James LP, Lamps LW, McCullough S, Hinson JA. Interleukin 6 and hepatocyte regeneration in acetaminophen toxicity in the mouse. Biochem Biophys Res Commun 2003; 309: 857–63.
45 Ramaiah SK, Jaeschke H. Role of neutrophils in the pathogenesis of acute inflammatory liver injury. Toxicol Pathol 2007; 35: 757–66.
46 Koh A, da Silva AP, Bansal AK, Bansal M, Sun C, Lee H, *et al*. Role of osteopontin in neutrophil function. Immunology 2007; 122: 466–75.
47 Christensen B, Kazanecki CC, Petersen TE, Rittling SR, Denhardt DT, Sorensen ES. Cell type-specific post-translational modifications of mouse osteopontin are associated with different adhesive properties. J Biol Chem 2007; 282: 19463–72.
48 Kazanecki CC, Uzwiak DJ, Denhardt DT. Control of osteopontin signaling and function by post-translational phosphorylation and protein folding. J Cell Biochem 2007; 102: 912–24.
49 Kim HJ, Lee HJ, Jun JI, Oh Y, Choi SG, Kim H, *et al*. Intracellular cleavage of osteopontin by caspase-8 modulates hypoxia/reoxygenation cell death through p53. Proc Natl Acad Sci U S A 2009; 106: 15326–31.

Acta Pharmacologica Sinica (2012) 33: 1013–1022
 1671-4083/12 $32.00
www.nature.com/aps

Original Article

Acute and chronic administration of SHR117887, a novel and specific dipeptidyl peptidase-4 inhibitor, improves metabolic control in diabetic rodent models

Xiao LIU[1], Li-na ZHANG[1], Ying FENG[1], Lei ZHANG[2], Hui QU[1], Guo-qing CAO[2], Ying LENG[1, *]

[1]*State Key Laboratory of Drug Research, Shanghai Institute of Materia Medica, Chinese Academy of Sciences, Shanghai 201203, China;* [2]*Shanghai Hengrui Pharmaceuticals Co, Ltd, Shanghai 201203, China*

Aim: Dipeptidyl deptidase-4 (DPP-4) inhibitors are a new class of anti-diabetic agents. The purpose of this study was to assess the acute and chronic effects of SHR117887, a novel DPP-4 inhibitor, on metabolic control and pancreatic β-cell function in normal or diabetic rodent models.

Methods: In the acute experiments, ICR mice, diet-induced obese (DIO) rats and *ob/ob* mice were subjected to an oral glucose tolerance test (OGTT) following a single oral administration of SHR117887 (0.1, 0.3, 1, or 3 mg/kg). Blood samples were collected to measure glucose, insulin, DPP-4 activity and active GLP-1 level. In the chronic experiments, *ob/ob* mice was administered SHR117887 (3, 10, or 30 mg/kg) twice daily for 33 d to assess the effects on metabolic control and pancreatic β-cell function. Vildagliptin (LAF237) was used as a positive control in all the experiments.

Results: Acute oral administration of SHR117887 dose-dependently decreased the serum DPP-4 activity and improved glucose tolerance in ICR mice, DIO rats and *ob/ob* mice. This was accompanied by significant increases in the serum active GLP-1 and insulin levels. Chronic administration of SHR117887 significantly decreased fasting blood glucose level and improved the lipid profiles in *ob/ob* mice by reducing the serum triglyceride and free fatty acid levels, and its efficacy was comparable with that of vildagliptin at the same molarity. Moreover, chronic administration of SHR117887 increased the insulin staining of islet cells, which is suggestive of improved β-cell function.

Conclusion: SHR117887 is a potent DPP-4 inhibitor that improves metabolic control and β-cell function in diabetic rodent models, suggesting that it could be a new therapeutic agent for the treatment of type 2 diabetes.

Keywords: SHR117887; vildagliptin (LAF237); dipeptidyl peptidase-4 (DPP-4); type 2 diabetes mellitus; glucagon-like peptide-1 (GLP-1); insulin; β-cells

Acta Pharmacologica Sinica (2012) 33: 1013–1022; doi: 10.1038/aps.2012.75; published online 30 Jul 2012

Introduction

Type 2 diabetes mellitus (T2DM) is considered to be a chronic metabolic disease due to insulin resistance and pancreatic β-cell dysfunction. It is characterized by impaired insulin responsiveness and anatomical abnormalities of the pancreatic islets during the course of the disease development[1, 2]. Due to the increasing prevalence of T2DM, the high burden of its complications, the limitation of adequate long-term glycemic control and the adverse effects often associated with current anti-diabetic treatment strategies, efforts to develop new pharmacological agents with better efficacy and fewer side effects are warranted [3–6].

Recently, the role of the incretin hormones, glucagon-like peptide-1 (GLP-1), and their deficiency in patients with T2DM have been explored and targeted for new therapies with novel mechanisms of action. GLP-1 is released from L cells in the intestine after meal intake and plays a key role in the regulation of insulin secretion and glucose homeostasis. It has multiple metabolic effects that would be desirable attributes of an anti-diabetic agent[7], such as glucose-dependent stimulation of insulin and suppression of glucagon release[8], slowing of gastric emptying and appetite suppression[9, 10], stimulation of non-insulin-mediated glucose uptake[11], and suppression of endogenous glucose production independent of pancreatic hormones[12]. Administration of GLP-1 or its mimic agents (*eg*, exendin-4 or liraglutide) is appealing due to their remarkable glucose-lowering efficacy and low frequency of hypoglycemia. The GLP-1-based therapeutics also appear to decrease beta-

* To whom correspondence should be addressed.
E-mail yleng@mail.shcnc.ac.cn
Received 2012-04-18 Accepted 2012-05-22

cell apoptosis and increase beta-cell proliferation[13, 14], which raises the theoretical possibility of slowing the progression of T2DM, a therapeutic strategy that goes beyond those offered by the traditional antidiabetic drugs[3,4,6].

Native GLP-1 has a very short plasma half-life (approximately 2 min) because intact GLP-1 (GLP-1[7–36] amide) is rapidly degraded to an inactive form (GLP-1[9–36] amide) by DPP-4, which cleaves two residues from the NH_2-terminal end of the peptide[15]. Moreover, due to their peptidic nature, GLP-1 and its analogs must be administered parenterally to exert their therapeutic actions. In contrast, small molecule inhibitors of DPP-4 were discovered to leverage the antidiabetic effects of endogenous GLP-1 and could be administered orally. Several orally available specific inhibitors of DPP-4 have been described and have been reported to improve glucose metabolism in various animal models of type 2 diabetes[16–21] and more recently in diabetic patients[22–24]. As one of earliest reported DPP-4 inhibitors, vildagliptin (formerly known as LAF237) was shown to be a selective and orally effective DPP-4 inhibitor, which was able to augment insulin release and reduce glucose excursions during an oral glucose tolerance test (OGTT) in Zucker fatty (*fa/fa*) rats and fat-fed normal rats after single and multiple oral administrations [25, 26].

SHR117887 is a novel DPP-4 inhibitor discovered by Jiangsu Hansoh Pharmaceutical Co, Ltd (Jiangsu, China) for the treatment of type 2 diabetes. It is structurally different from other DPP-4 inhibitors that are currently available or in late-stage clinical development. As a competitive human DPP-4 inhibitor, SHR117887 showed high inhibitory potency against DPP-4 with an IC_{50} of 17 nmol/L, and good selectivity against human DPP-8 or DPP-9 with an IC_{50} of 4.51 μmol/L and 0.63 μmol/L, respectively (unpublished data supplied by Jiangsu Hansoh Pharmaceutical Co, Ltd). In the present study, we have characterized the acute *in vivo* effects of SHR117887 on blood glucose value, serum DPP-4 activity, insulin and active GLP-1 profiles after oral glucose loading in normal mice, diet-induced obese (DIO) rats and *ob/ob* mice. Moreover, the chronic administration of SHR117887 on metabolic control and pancreatic β-cell function in *ob/ob* mice was investigated and compared with LAF237, an approved anti-diabetic drug based on DPP-4 inhibition.

Materials and methods

Chemicals

SHR117887 (5-[2-(2-Cyano-4-fluoro-pyrrolidin-1-yl)-2-oxo-ethylamino]-5-methyl-hexahydrocyclopenta[c]pyrrole-2-carboxylic acid dimethylamide *p*-toluenesulfonate, Figure 1) and vildagliptin (LAF237) were synthesized by Jiangsu Hansoh Pharmaceutical Co, Ltd (Jiangsu, China).

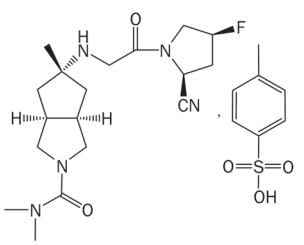

Figure 1. Chemical structure of SHR117887.

Animals

Male ICR mice and Wistar rats were purchased from the Shanghai SLAC Laboratory Animal Co Ltd (Shanghai, China). B6.V-*Lep*^{ob}/*Lep*^{ob} (*ob/ob*) mice and their lean littermates$^{+/+}$ (from Jackson Laboratory, Bar Harbor, ME, USA) were bred at the Shanghai Institute of Materia Medica (SIMM), Chinese Academy of Sciences. The animals were maintained under a 12-h light-dark cycle with free access to water and food. Animal experiments were approved by the Animal Care and Use Committee, Shanghai Institute of Materia Medica, Chinese Academy of Sciences.

Acute effect of SHR117887 on normal mice

To examine the acute effect of SHR117887 on blood glucose and serum DPP-4 activity after an oral glucose challenge, 0.1, 0.3, 1, or 3 mg/kg (0.186, 0.558, 1.86, and 5.58 μmol/kg) of SHR117887, 0.06, 0.19, 0.6, and 1.9 mg/kg of LAF237 (0.186, 0.558, 1.86, and 5.58 μmol/kg) or vehicle (distilled water) was orally administered to 5 h-fasted ICR mice (n=10 in each group) 60 min prior to the oral glucose load (2.5 g/kg). Blood samples were collected 60 min before the glucose load, and at 0, 15, 30, 60, 120, and 240 min after the glucose load in order to measure serum glucose and DPP-4 activity. To examine the acute effect of SHR117887 on the serum active GLP-1 level, blood samples were collected 15 min after the glucose load and placed in Eppendorf tubes containing the DPP-4 inhibitor valine pyrrolidide (Linco Research, DPP4-010) with a final concentration of 1% blood samples and 25 mg/mL EDTA to measure serum active GLP-1[7–36 amide] levels.

Acute effect of SHR117887 on diet-induced obesity (DIO) rats

Four-weeks old male Wistar rats were fed with a high-fat diet (D12492; Research Diets with 60% kcal% fat, New Brunswick, NJ, USA) for approximately 6 weeks and then divided into 7 groups based on serum glucose and body weight (n=10 in each group). The normal diet-fed Wistar rats were used as the lean control.

The rats were cannulated for blood sampling. An indwelling catheter was inserted under anesthesia in the right jugular vein, and externalized at the nape of the neck. Body weights were monitored, and studies were performed only after the rats regained their pre-surgery body weights. The oral glucose tolerance test (OGTT) was performed 3 d after surgery in overnight-fasted, awake, freely moving rats. SHR117887 (1, 3, and 10 mg/kg), LAF237 (0.6, 1.9, and 6.3 mg/kg) or vehicle (distilled water) was orally administered to rats 60 min prior to the oral glucose load (2.0 g/kg). Blood samples were collected from the jugular catheter 60 min before the glucose load, and 0, 5, 10, 15, 30, 60, and 120 min after the glucose load to measure serum DPP-4 activity, glucose and insulin levels. To analyze active GLP-1 levels, blood samples were collected

at 0, 5, 10, 15, 30, and 60 min after the glucose load and placed in Eppendorf tubes containing the DPP-4 inhibitor valine pyrrolidide (Linco Research, DPP4-010) with a final concentration of 1% blood samples and 25 mg/mL EDTA.

Acute effect of SHR117887 on type 2 diabetic *ob/ob* mice

Seven-week old *ob/ob* mice were divided into 7 groups (n=10 in each group) based on 6 h fasting blood glucose, serum insulin level, and body weight. Ten wild-type littermates were set up as the lean control group. SHR117887 (3, 10, and 30 mg/kg), LAF237 (1.9, 6.3, and 19 mg/kg) or vehicle (distilled water) was orally administered to 6 h-fasted *ob/ob* mice and lean mice 60 min prior to the oral glucose load (2.5 g/kg). Blood samples were collected 60 min before the glucose load and at 0, 15, 30, 60, and 120 min after the glucose load to measure serum glucose and insulin levels. Serum DPP-4 activity was measured at 2, 4, 8, and 12 h post-dose.

Chronic anti-diabetic effect of SHR117887 on type 2 diabetic *ob/ob* mice

Seven-week-old *ob/ob* mice were divided into 7 groups (n=11 in each group) based on non-fasting and fasting blood glucose, serum insulin levels and body weight. Wild-type littermates were used as the lean control. SHR117887 (3, 10, and 30 mg/kg), LAF237 (1.9, 6.3, and 19 mg/kg) or vehicle (distilled water) was orally administered twice daily (at 8:30 AM and 8:30 PM) for 33 d. Fasting blood glucose, body weight and food consumption values were determined at 4-d intervals. After 33 d of treatment, blood samples were collected after 6 h of fasting after the last dose for blood glucose and serum lipid level measurement. The pancreases of animals in the SHR117887 (30 mg/kg), LAF237 (19 mg/kg) and control groups were isolated and fixed for immunohistochemical analysis. To determine whether SHR117887 exhibited tachyphylaxis, the serum DPP-4 activity of another ten *ob/ob* mice treated with 30 mg/kg SHR117887 was measured at 2, 4, 8, and 12 h after the morning dose on d 1, d 12, d 24, and d 32.

Immunohistochemical analysis

The pancreatic samples were fixed in 10% buffered formalin for 1 d and subsequently embedded in paraffin. Paraffin sections (3 μm) were cut, deparaffinized, rehydrated and placed in 3% hydrogen peroxide for 10 min at room temperature. The sections were then heated twice for 15 min at 90 °C in a microwave, rinsed with Tris-buffered saline with Tween 80 (TBS-T) twice for 5 min, and then blocked with 5% normal goat serum (Beijing Dingguo Reagent Co, Ltd, Beijing, China) for 45 min. The sections were then incubated with the primary antibody, which was a ready-to-use guinea pig polyclonal anti-insulin antibody (Cat#: 58916, Abcam, Cambridge, UK) overnight at 4 °C. The sections were washed with TBS-T and blocked with 10% normal goat serum for 30 min. Bound antibody was detected using a ready-to-use rabbit polyclonal to guinea pig IgG H&L (Cat#: 105460, Abcam, Cambridge, UK) for 30 min. The sections were rinsed with TBS-T and developed for 15 min using DAB (Beijing Dingguo Reagent Co, Ltd, Beijing, China). Finally, the slides were washed with TBS-T, counterstained with hematoxylin, dehydrated and mounted.

Sample handling and analysis

Blood glucose was measured using a glucometer [ONE TOUCHTM BASICTM plus Glucose Monitor (Lifescan, Milpitas, CA, USA]. Serum glucose was determined with a glucose oxidase method (Shanghai Shensuo Reagent Co, Ltd, Shanghai, China). The serum insulin level was measured with a 96-well ultra-sensitive mouse insulin ELISA kit (Cat#: 90080, Crystal Chem Inc, Downers Grove, IL). Serum free fatty acid (NEFA) level was measured by enzymatic methods with a test kit (Cat#: 994-75409, Wako Chemicals GmbH, Neuss, Germany). The serum total cholesterol (CHOL) level was measured with a test kit (Wenzhou Dongoujinma Reagent Co, Ltd, Wenzhou, China). Serum triglyceride (TG) was measured with a test kit (Shanghai Rongsheng Reagent Co, Ltd, Shanghai, China). Serum DPP-4 activity was measured using a fluorometric assay with the substrate Gly-Pro-AMC, which is cleaved by an enzyme to release a fluorescent label[25]. Briefly, 5 μL of serum sample was added to 96-well plates, followed by the addition of 35 μL of 80 mmol/L $MgCl_2$ in an assay buffer (25 mmol/L HEPES, 140 mmol/L NaCl, 1% BSA, pH 7.8). After 5 min of pre-incubation at room temperature, the enzymatic reaction was started with the addition of 10 μL of assay buffer containing 0.1 mmol/L substrate (Gly-Pro-AMC, Sigma). Liberation of AMC was monitored continuously at excitation 380 nm and emission 460 nm every 3 min for up to 18 min in a 96-well plate. Fluorometric catalysis rates were determined from the linear portion of the curve of the increase in fluorescence and were calculated as the slope of the regression line determined from the line. DPP-4 was expressed as the percentage of each animal's baseline level (the value obtained immediately before compound administration).

Statistical analysis

All data are expressed as the mean±SEM. The statistical analysis between the two groups was performed using an unpaired Student's t-test. P<0.05 was considered to be statistically significant.

Results

Effect of acute administration of SHR117887 on serum DPP-4 activity, active GLP-1 and glucose levels in normal mice

SHR117887 dose-dependently inhibited serum DPP-4 activity (Figure 2A). Overall, 3.0 mg/kg (5.58 μmol/kg) of SHR117887 achieved at least 70% DPP-4 inhibition throughout a 3 h period, which is similar to the inhibition achieved by the same molarity of LAF237. The ED_{50} value of SHR117887 for inhibition of serum DPP-4 activity was 0.69 mg/kg (1.28 μmol/kg) at 1 h post-dose, while the ED_{50} value of LAF237 was 0.35 mg/kg (1.03 μmol/kg). SHR117887 enhanced glucose-induced increases of active GLP-1 level, with the minimum effective dose of 0.3 mg/kg (Figure 2B). SHR117887 3 mg/kg raised the active GLP-1 level 2.7-fold compared with the vehicle control, and this effect was similar to that of 1.9 mg/kg LAF237

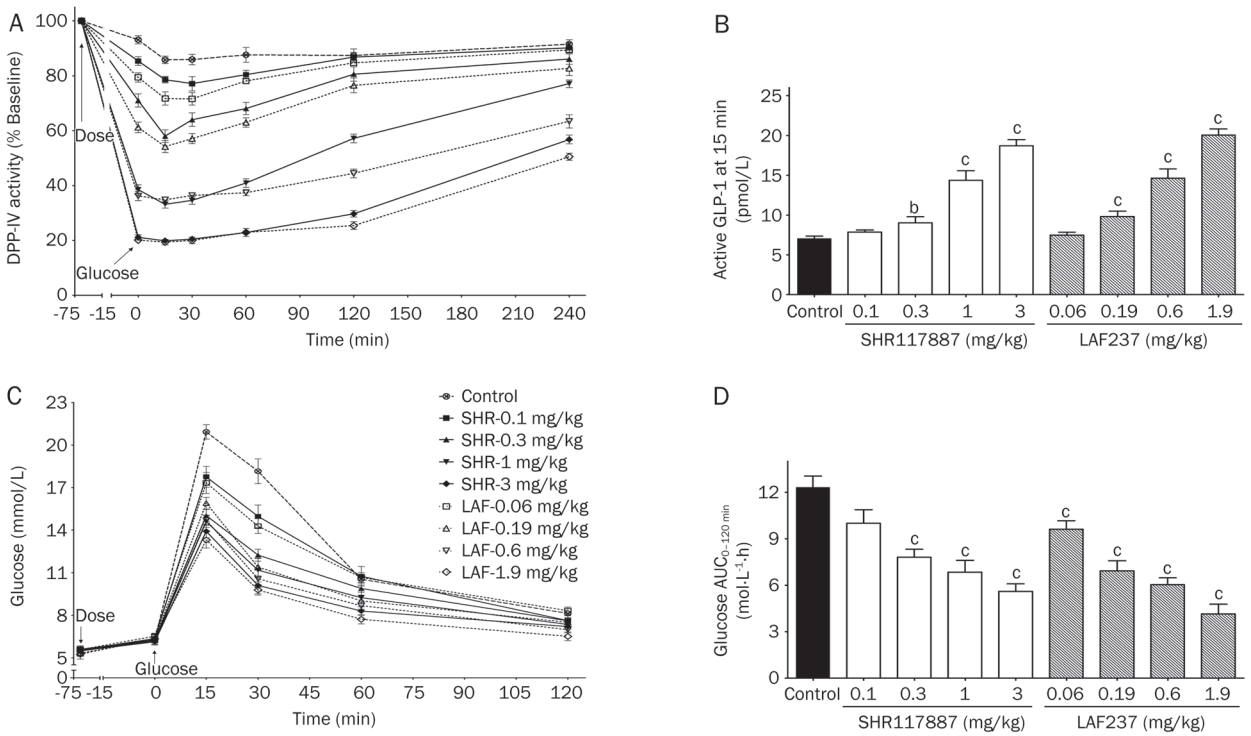

Figure 2. Effect of acute administration of SHR117887 on serum DPP-4 activity (A), active GLP-1 (B) and glucose levels (C, D) in normal mice. SHR117887, LAF237 or vehicle was orally administered to 5 h-fasted normal ICR mice 60 min prior to oral glucose load (2.5 g/kg). *n*=10. Data are mean±SEM. $^{b}P<0.05$, $^{c}P<0.01$ *vs* control.

(2.8-fold *vs* the vehicle control). SHR117887 administration caused a significant decrease in glucose $AUC_{0-120\ min}$ by 36.6%, 44.5%, and 54.6% at the dose of 0.3, 1, and 3 mg/kg ($P<0.01$), respectively, while LAF237 showed a similar glucose-lowering effect with the reduction rate of 43.8%, 51.0% and 66.3% at the equimolar doses (Figures 2C and 2D), respectively. Therefore, a single oral dose of SHR117887 inhibited serum DPP-4 activity, increased serum active GLP-1 levels and improved glucose tolerance in normal mice after a glucose challenge.

Effect of acute administration of SHR117887 on serum DPP-4 activity, active GLP-1, glucose, and insulin levels in DIO rats

To generate a metabolic rodent model mimicking human type 2 diabetes with insulin resistance, Wistar rats were fed a high-fat diet. A single oral administration of SHR117887 inhibited the serum DPP-4 activities in a dose-dependent manner. Then, 10 mg/kg (18.6 μmol/kg) of SHR117887 produced 88.3% inhibition on serum DPP-4 activity at 3 h post-dose, whereas 6.3 mg/kg (18.6 μmol/kg) of LAF237 showed a similar effect (Figure 3A). The active GLP-1 level reached the peak value at 10 min after the oral glucose load in DIO rats, and 10 mg/kg SHR117887 raised the peak serum GLP-1 level by 4.9-fold and GLP-1 $AUC_{0-60\ min}$ by 5.6-fold compared with the vehicle control ($P<0.01$), while the same molarity of LAF237 raised the peak serum GLP-1 level and GLP-1 $AUC_{0-60\ min}$ by 4.9- and 5.8-fold ($P<0.01$), respectively (Figure 3B–3D). As shown in Figures 3E to 3G, DIO rats showed impaired glucose tolerance in response to an oral glucose challenge, while administration of SHR117887 or LAF237 to DIO rats 1 h before the oral glucose load produced a significant decrease in glucose excursion. SHR117887 at the dose of 1, 3, and 10 mg/kg reduced glucose $AUC_{0-120\ min}$ values by 25.9%, 21.4%, and 42.8% ($P<0.01$, 0.05, 0.001), respectively, while LAF237 showed a comparable effect with decreases of 22.1%, 28.3%, and 44.2% ($P<0.05$, 0.01, 0.001), respectively. As shown in Figures 3H to 3J, administration of SHR117887 to DIO rats produced significant increases in insulin levels induced by the oral glucose challenge ($P<0.01$). At the dose of 10 mg/kg, SHR117887 treatment raised the insulin peak value by 2.0-fold compared with the vehicle control, and this effect was similar to that of 6.3 mg/kg of LAF237 (2.1-fold *vs* vehicle control). At the dose of 10 mg/kg, SHR117887 also raised the insulin $AUC_{0-60\ min}$ by 1.7-fold compared to the vehicle control ($P<0.05$), with a comparable effect of LAF237 at the dose of 6.3 mg/kg (2.0-fold *vs* the vehicle control, $P<0.01$).

Effect of acute administration of SHR117887 on serum glucose, insulin levels and DPP-4 activity in *ob/ob* mice

As shown in Figure 4, genetic type 2 diabetic *ob/ob* mice showed hyperglycemia, hyperinsulinemia and impaired glucose tolerance in response to oral glucose challenges. Single oral dose administration of SHR117887 reduced serum glucose levels and glucose $AUC_{0-120\ min}$ in a dose-dependent manner following an OGTT, and the efficacy was similar to that achieved by the same molarity of LAF237 (Figures 4A and 4B). At the oral dose of 3, 10, and 30 mg/kg (5.58, 18.6, and 55.8 μmol/kg), SHR117887 reduced the glucose $AUC_{0-120\ min}$

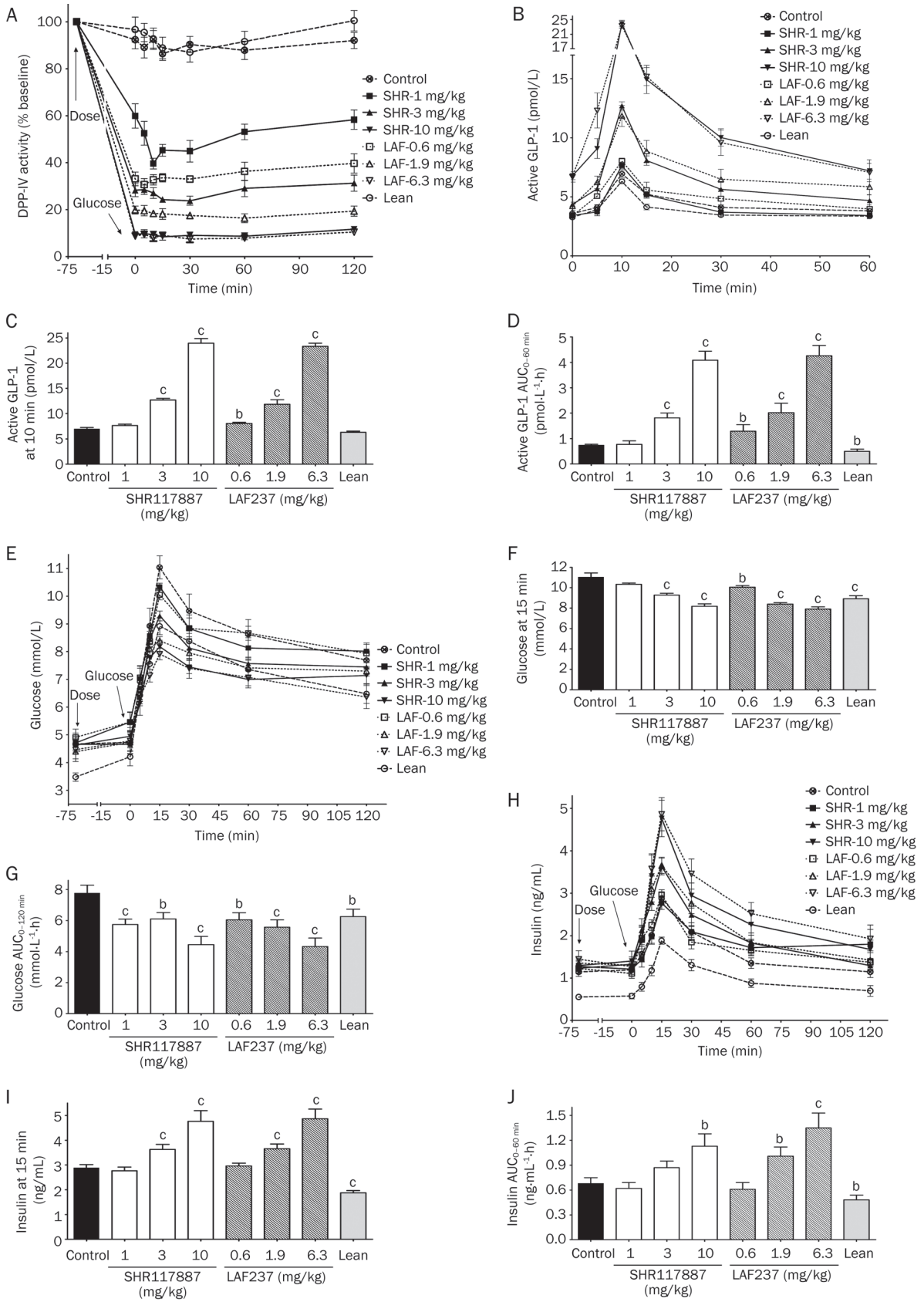

Figure 3. Effect of acute administration of SHR117887 on serum DPP-4 activity (A), active GLP-1 (B, C, D), glucose (E, F, G), and insulin levels (H, I, J) in DIO rats. SHR117887, LAF237 or vehicle was orally administered to overnight-fasted rats 60 min prior to oral glucose load (2 g/kg). *n*=10. Data are mean±SEM. $^{b}P<0.05$, $^{c}P<0.01$ *vs* Control.

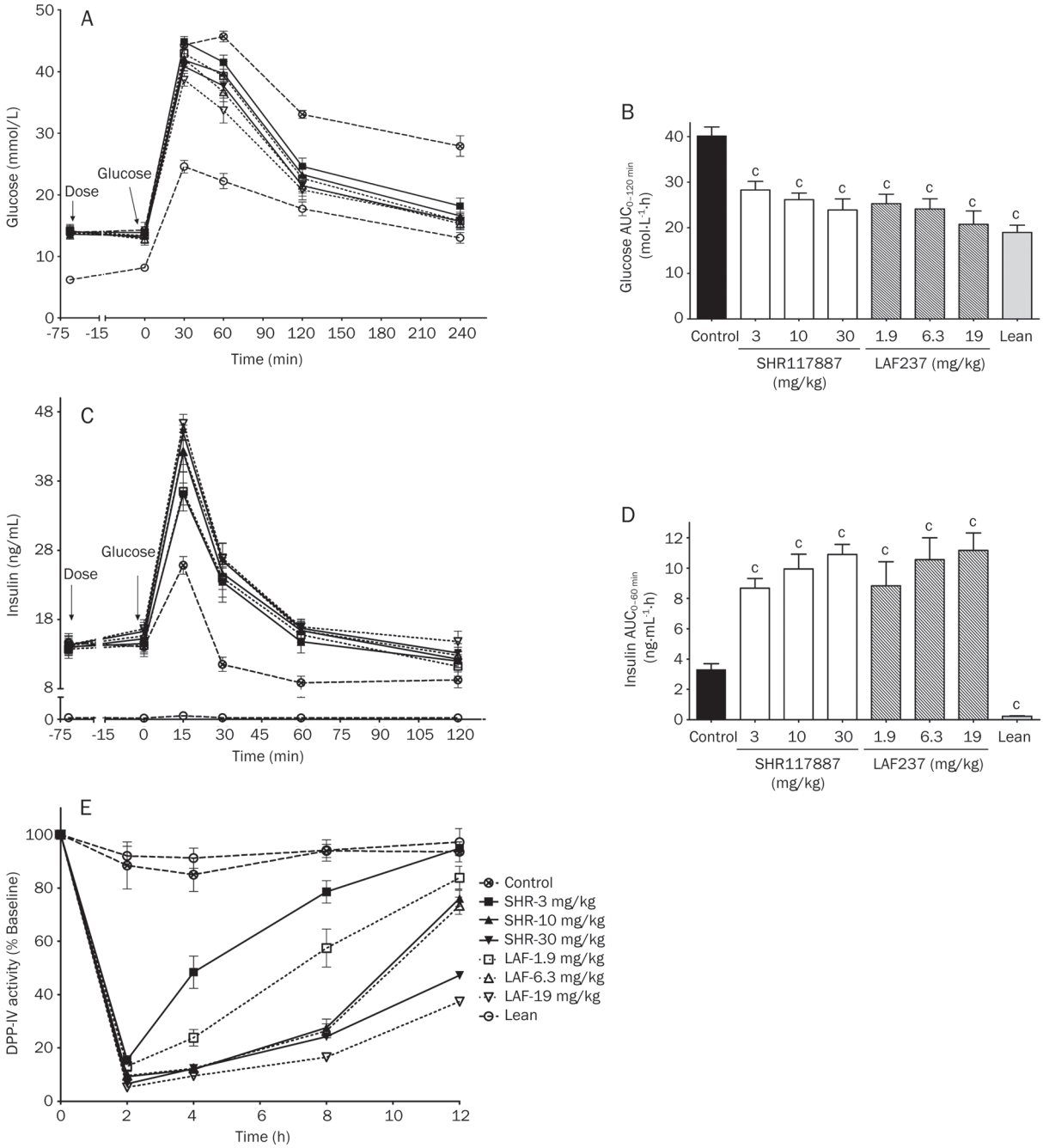

Figure 4. Effect of acute administration of SHR117887 on serum glucose (A, B), insulin levels (C, D) and DPP-4 activity (E) in *ob/ob* mice. SHR117887, LAF237 or vehicle was orally administered to 6 h-fasted *ob/ob* mice and their lean control mice 60 min prior to oral glucose load (2.5 g/kg). *n*=10. Data are mean±SEM. $^{b}P<0.05$, $^{c}P<0.01$ *vs* Control.

by 30.2%, 35.0%, and 40.6%, respectively, while the reduction caused by the same molarity of LAF237 was 37.1%, 40.1%, and 48.4%, respectively (Figure 4B). SHR117887 also enhanced glucose-induced increases in serum insulin levels and insulin $AUC_{0\text{–}60\ min}$ in a dose-dependent manner (Figure 4C and 4D). At doses of 3, 10, and 30 mg/kg, SHR117887 increased insulin $AUC_{0\text{–}60\ min}$ by 2.6-, 3.0-, and 3.3-fold compared with the vehicle *ob/ob* control, while LAF237 was equally potent with increases of 2.7-, 3.2-, and 3.4-fold, respectively (Figure 4D). As shown in Figure 4E, the serum DPP-4 activity was time- and dose-dependently reduced after SHR117887 or LAF237 administration, and the inhibitory effect on serum DPP-4 activity produced by 10 and 30 mg/kg SHR117887 at 8 h post-dose was 72.4% and 75.8%, respectively, which was similar to those of 6.3 and 19 mg/kg doses of LAF237 (73.6% and 83.5%, respectively).

Chronic anti-diabetic effect of SHR117887 in type 2 diabetic *ob/ob* mice

To evaluate the effects of chronic administration of SHR117887 on glucose metabolism and pancreatic β-cell function, 7-week old *ob/ob* mice were treated with SHR117887 (3, 10, and 30 mg/kg), LAF237 (1.9, 6.3, and 19 mg/kg) or vehicle alone twice daily for 33 d. As shown in Table 1, the fasting blood glucose values of *ob/ob* mice were significantly higher than those of lean mice during the entire treatment. Administration of SHR117887 with the dose of 10 and 30 mg/kg caused significant reductions in fasting blood glucose levels, and the average reduction during the entire treatment period was 35.3% and 31.8%, respectively, which was comparable to those of 6.3 and 19 mg/kg doses of LAF237 (31.5% and 35.6%, respectively). Chronic administration of SHR117887 also significantly improved the lipid homeostasis by reducing the serum triglyceride ($P<0.01$) and free fatty acid levels ($P<0.05$) in *ob/ob* mice, but it had no significant effect on total cholesterol levels (Table 2). SHR117887 caused a tendency of reduced food consumption, but had no effect on body weight (Table 2).

To determine whether SHR117887 exhibited tachyphylaxis, serum DPP-4 activity in ten *ob/ob* mice administered with 30 mg/kg SHR117887 was measured at 2, 4, 8, and 12 h after the morning dose on d 1, 12, 24, and 32. As shown in Figure 5, the profiles of serum DPP-4 activity on d 1, 12, 24, and 32 were virtually superimposable, suggesting that the chronic administration of SHR117887 exhibited no tachyphylaxis on the inhibition of DPP-4 activity.

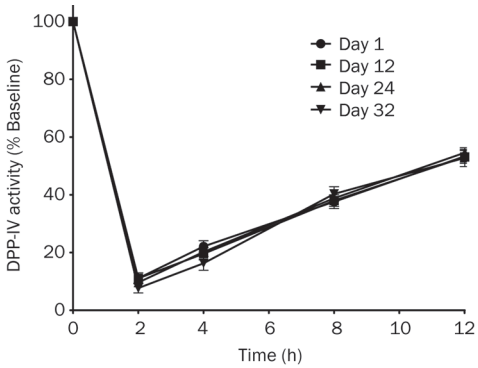

Figure 5. Serum DPP-4 activity profile in *ob/ob* mice treated with 30 mg/kg SHR117887 twice daily by oral administration for 32 days. *n*=10. Data are mean±SEM.

At the end of study, the pancreases of the SHR117887 (30 mg/kg), LAF237 (19 mg/kg), vehicle control and the lean control mice were isolated and analyzed by immunohistochemistry using an anti-insulin antibody. As shown in Figure 6, weak insulin staining with irregular distribution in the β-cells

Table 1. Fasting blood glucose changes in *ob/ob* mice following chronic treatment with SHR117887 or LAF237 (Bid, *po*). Data are mean±SEM. *n*=11. $^bP<0.05$, $^cP<0.01$ *vs* control.

Group	Dose (mg/kg)	Fast blood glucose (mmol/L)									Mean reduction rate of serum glucose (%)
		Pre-dose	d 4	d 8	d 12	d 16	d 20	d 24	d 28	d 33	
Lean mice	–	6.6±0.2	6.0±0.2	5.9±0.3	6.0±0.3	6.4±0.3	5.7±0.1	6.3±0.2	6.4±0.3	5.9±0.2	–
Control	–	15.1±1.1	20.1±2.2	21.3±1.8	20.5±1.7	19.8±2.3	21.6±2.2	20.1±2.0	20.7±2.3	20.4±1.7	–
SHR117887	3	15.2±1.3	14.9±2.4	15.6±2.2	17.8±2.6	15.6±2.2	17.6±2.8	15.2±2.0	15.8±2.3	14.6±2.7	22.8±1.8
	10	15.1±0.9	13.1±1.6^b	16.4±1.3^b	14.1±2.0^b	13.9±2.0	13.9±2.5^b	13.0±2.1^b	11.6±1.8^c	10.6±1.5^c	35.3±2.8
	30	15.1±0.9	16.7±1.5	14.8±1.3^c	12.0±1.4^c	14.1±1.5^b	15.3±1.3^b	12.7±1.6^c	12.4±1.8^b	14.0±2.6^b	31.8±2.7
LAF237	1.9	15.0±1.4	15.7±2.1	14.7±1.7^b	13.3±1.7^c	14.9±1.6	14.6±2.0^b	12.8±1.8^b	14.9±2.0	14.4±2.6	29.7±1.7
	6.3	15.1±1.2	14.3±1.6^b	14.0±1.3^c	17.2±2.1	17.3±2.4	12.3±1.5^c	12.4±1.4^c	12.7±1.6^b	12.2±2.0^c	31.5±4.0
	19	15.2±1.1	14.8±2.0	16.5±2.3	15.3±2.7	12.8±2.2^b	12.6±2.5^b	11.2±1.9^c	11.1±2.0^c	11.6±2.3^c	35.6±3.4

Table 2. Metabolic parameters in *ob/ob* mice following chronic treatment with SHR117887 or LAF237 for 33 days (Bid, *po*). *n*=11. Data are mean±SEM. $^bP<0.05$, $^cP<0.01$ *vs* control.

Parameter (unit)	Control	*ob/ob* mice						Lean mice
		3 mg/kg SHR117887	10 mg/kg SHR117887	30 mg/kg SHR117887	1.9 mg/kg LAF237	6.3 mg/kg LAF237	19 mg/kg LAF237	
Serum NEFA (mmol/L)	1.4±0.1	1.2±0.1	1.1±0.1^b	1.3±0.1	1.1±0.1^c	1.2±0.1^b	1.1±0.04^c	0.9±0.1
Serum total cholesterol (mmol/L)	5.4±0.3	5.2±0.1	5.5±0.3	5.6±0.3	5.8±0.3	4.8±0.3	5.1±0.4	1.9±0.1
Serum triglyceride (mmol/L)	126.6±5.8	97.3±5.6^c	83.6±3.9^c	100.6±5.9^c	89.5±5.5^c	101.4±9.6^c	93.4±4.9^c	82.4±2.6
Food consumption (g/d)	7.5±0.2	6.6±0.2^c	7.0±0.2	7.0±0.3	6.8±0.3	6.9±0.3	6.7±0.2^b	3.1±0.0
Body weight (g)	56.2±0.8	54.2±0.9	55.6±0.8	56.3±1.2	55.4±1.0	56.0±1.0	55.5±1.0	23.4±1.1

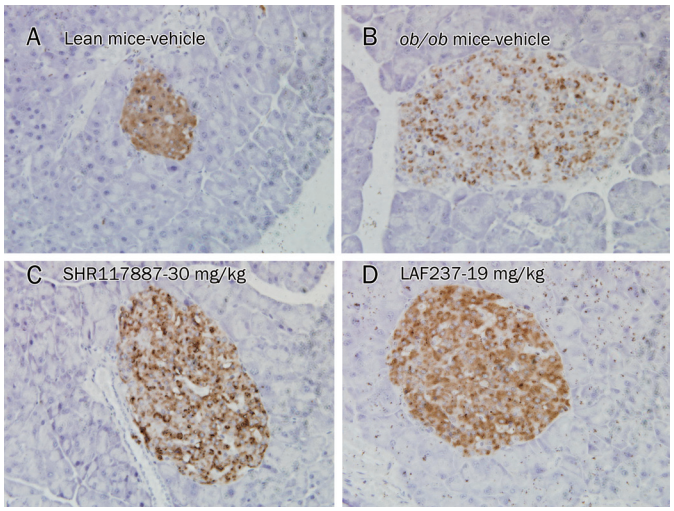

Figure 6. Effects of chronic SHR117887 treatment on pancreatic insulin staining in *ob/ob* mice. Mice were treated with SHR117887 (30 mg/kg), LAF237 (19 mg/kg) or vehicle twice daily by oral administration for 33 days. Pancreata were isolated and pancreatic sections were stained with anti-insulin antibodies after 6 h fasting. (A) Vehicle-treated lean mice. (B) Vehicle-treated *ob/ob* mice. (C) 30 mg/kg SHR117887-treated *ob/ob* mice. (D) 19 mg/kg LAF237-treated *ob/ob* mice. ×100.

was observed in the vehicle-treated *ob/ob* mice compared with the vehicle-treated lean mice, which is indicative of impaired β-cell function in the *ob/ob* mice. The 33-d treatment with SHR117887 significantly increased insulin staining and enhanced insulin antigen positivity with regular distribution in β-cells, indicating the improved β-cell function. Chronic treatment with the dose of LAF237 with similar plasma exposure showed a similar effect.

Discussion

Inhibition of DPP-4 augments the level of active GLP-1 by inhibiting the degradation, and it returns glucose homeostasis toward physiological control levels[27]. Therefore, DPP-4 inhibitors are expected to become a new class of anti-hyperglycemic drugs. SHR117887 is a novel potent DPP-4 inhibitor, which is currently in a phase I clinical study. In the present research, we report the acute and chronic pharmacological effects of SHR117887 on DPP-4 inhibition and metabolic control in normal or diabetic rodent models. Moreover, the efficacy of SHR117887 was compared with LAF237 at the same molar dose in each experiment.

In normal mice, acute administration of SHR117887 exhibited good oral bioavailability and caused dose-dependent inhibition of serum DPP-4 activity, accompanied with enhanced active GLP-1 levels and decreased serum glucose values. The minimum effective dose of SHR117887 to augment active GLP-1 and reduce glucose excursions was 0.3 mg/kg, which caused a 27.8% increase of active GLP-1 level and a 36.6% reduction of glucose $AUC_{0\text{–}120\ min}$. The DPP-4 activity was inhibited by 30% to 40% in the 2 h after a single oral dose of 0.3 mg/kg (0.558 μmol/kg) of SHR117887, suggesting that approximately 40% inhibition of serum DPP-4 activity is sufficient for effectiveness in oral glucose challenge in normal mice, which might be contributed by the normal whole body insulin sensitivity in ICR mice. LAF237 showed comparable efficacy at the same equimolar doses, and the minimum effective dose of LAF237 to augment active GLP-1 and reduce glucose excursions was 0.19 mg/kg (0.558 μmol/kg).

T2DM is often characterized by insulin resistance and is associated with diet-induced obesity and impaired glucose tolerance. We therefore further investigated the acute pharmacological effect of SHR117887 in the DIO rat, a model with modest insulin resistance and glucose intolerance[28]. The minimum effective dose of SHR117887 to augment the peak value of active GLP-1 and GLP-1 $AUC_{0\text{–}60\ min}$ was 3 mg/kg, which is also the minimum effective dose to increase the insulin peak value in 15 min after glucose loading. The acute administration of 3 mg/kg of SHR117887 could inhibit serum DPP-4 activity by 70% in the 2 h after dosing, but caused only a mild reduction of blood glucose $AUC_{0\text{–}120\ min}$ by 21.4%, which suggested that more powerful inhibition of DPP-4 activity was necessary to achieve effective glucose excursions reduction in insulin resistant animal models.

The acute glucose-lowering effect of SHR117887 was further evaluated in *ob/ob* mice, a genetic type 2 diabetic rodent model that exhibits hyperglycemia, hyperinsulinemia, hyperglucagonemia, and severe whole body insulin resistance[29]. A single oral dose of 3, 10, and 30 mg/kg SHR117887 inhibited serum DPP-4 activity by 84%, 91%, and 93%, respectively, at 2 h post-dose, reducing serum glucose $AUC_{0\text{–}120\ min}$ by 30.2%, 35.0%, and 40.6%, respectively. LAF237 showed a similar pharmacological effect to SHR117887, and these findings are consistent with the previous reports using other DPP-4 inhibitors in glucose-intolerant rodents, including high-fat-fed rats[26, 28], Zucker fatty rats[30, 31] and mice[32]. These results suggest that SHR117887 improves glucose tolerance through the elevation of serum insulin and active GLP-1 levels via the inhibition of DPP-4 activity in normal and diabetic animal models, but the achievable glucose lowering effect seems to be correlated with the degree of insulin resistance in different animal models.

Several studies have demonstrated the effectiveness of long-term DPP-4 inhibition on amelioration of metabolic disorder in diabetic animal models[20, 33]. In the present study, the anti-diabetic effects of chronic DPP-4 inhibition by SHR117887 were investigated in *ob/ob* mice. Because the acute study showed that a single oral dose of 3, 10, and 30 mg/kg of SHR117887 in *ob/ob* mice can only inhibit serum DPP-4 activity by 5.1%, 23.9%, and 52.8%, respectively, at 12 h post-dose, a twice-daily administration was chosen for the chronic study to maintain adequate inhibition of DPP-4 activity throughout the experiment. The dose of 30 mg/kg SHR117887 caused 88.9% and 46.6% inhibition of serum DPP-4 activity at 2 h and 12 h post dose, whereas administration of the same dose of SHR117887 on day 12, 24, and 32 of the chronic treatment exerted almost equivalent DPP-4 inhibition, which indicated that SHR117887 does not exhibit tachyphylaxis when given orally twice daily for 32 d. In agreement with previous stud-

ies of the DPP-4 inhibitor[16, 20], SHR117887, significantly decreased fasting blood glucose values and the results were also observed at a comparable level with the same molar dose of LAF237. Moreover, lipid homeostasis was also improved by chronic SHR117887 treatment in *ob/ob* mice by reducing the serum triglyceride and NEFA levels, which is consistent with the results of previous studies conducted with alogliptin on *ob/ob* and *db/db* mice or with a sitagliptin analog (des-fluoro-sitagliptin) in high-fat diet streptozotocin-induced diabetic mice[34–36], suggesting possible beneficial effects of SHR117887 in type 2 diabetic patients associated with lipid dysregulation.

GLP-1 and its analogs have been demonstrated to reduce food intake and decrease the body weight in diabetic animal models and clinical studies[37–39]. Inhibition of DPP-4 activity prevented degradation and enhanced the biological activity of active GLP-1[15]. However, chronic administration of SHR117887 showed only a minor tendency in the reduction of food consumption and had no effect on body weight. These results are similar to the reports of several other studies of DPP-4 inhibitors[34, 35], and the possible reasons might be due to the less effect of the enhanced endogenous active GLP-1 caused by DPP-4 inhibition rather than that of the injection of exogenous GLP-1 or its analogs.

A great challenge in the therapy of type 2 diabetes patients is the progressive loss of β-cell mass and deterioration of β-cell function[2, 3]. In the present study, chronic treatment with SHR117887 increased the insulin staining in islet cells, suggesting improved β-cell function. Because GLP-1 has been reported to decrease β-cell apoptosis and increase β-cell proliferation[13, 14], the improved β-cell function caused by SHR117887 might be due to the enhanced and prolonged endogenous GLP-1 action after long-term inhibition of DPP-4 activity. Moreover, the improvement of glucose control and decreased triglyceride and NEFA levels probably also contributed to the beneficial effects of the chronic administration of SHR117887 on β-cell function in *ob/ob* mice.

In conclusion, this study has demonstrated that SHR117887 is a potent DPP-4 inhibitor, which increases active GLP-1 and insulin levels and improves glucose homeostasis after acute dosing in normal, non-genetic and genetic-type 2 diabetes animal models. Chronic treatment with SHR117887 improves glycemic control, decreases serum triglyceride and NEFA levels, and improves β-cell function in type 2 diabetes *ob/ob* mice. These findings suggest the usefulness of SHR117887 for further development as a new therapeutic agent for impaired glucose tolerance and type 2 diabetes. SHR117887 is currently in phase I clinical studies.

Author contribution

Ying LENG designed the research; Xiao LIU, Li-na ZHANG, Ying FENG, Lei ZHANG, and Hui QU performed the research; Xiao LIU, Ying FENG, and Guo-qing CAO analyzed the data; Xiao LIU, Guo-qing CAO, and Ying LENG wrote the paper.

References

1 Perley MJ, Kipnis DM. Plasma insulin responses to oral and intravenous glucose: studies in normal and diabetic subjects. J Clin Invest 1967; 46: 1954–62.
2 Bonora E. Protection of pancreatic beta–cells: is it feasible? Nutr Metab Cardiovasc Dis 2008; 18: 74–83.
3 Del Prato S, Penno G, Miccoli R. Changing the treatment paradigm for type 2 diabetes. Diabetes Care 2009; 32: 217–22.
4 Cefalu WT, Richards RJ, Melendez-Ramircz LY. Redefining treatment success in type 2 diabetes mellitus: comprehensive targeting of core defects. Cleve Clin J Med 2009; 76: 39–47.
5 Nauck MA, Vilsbøll T, Gallwitz B, Garber A, Madsbad S. Incretin-based therapies: viewpoints on the way to consensus. Diabetes Care 2009; 32: 223–31.
6 Tahrani AA, Piya MK, Kennedy A, Barnett AH. Glycaemic control in type 2 diabetes: targets and new therapies. Pharmacol Ther 2010; 125: 328–61.
7 Holst JJ. Therapy of type 2 diabetes mellitus based on the actions of glucagon-like peptide-1. Diabetes Metab Res Rev 2002; 18: 430–41.
8 Ahren B, Larsson H, Holst JJ. Effects of glucagon-like peptide-1 on islet function and insulin sensitivity in noninsulin–dependent diabetes mellitus. J Clin Endocrinol Metab 1997; 82: 473–8.
9 Willms B, Werner J, Holst JJ, Orskov C, Creutzfeldt W, Nauck MA. Gastric emptying, glucose responses and insulin secretion after a liquid test meal: effects of exogenous glucagon-like peptide-1 (GLP-1)-(7–36) amide in type 2 (noninsulin-dependent) diabetic patients. J Clin Endocrinol Metab 1996; 81: 327–32.
10 Naslund E, Barkeling B, King N, Gutniak M, Blundell JE, Holst JJ, *et al*. Energy intake and appetite are suppressed by glucagon-like peptide-1 (GLP-1) in obese men. Int J Obes Relat Metab Disord 1999; 23: 304–11.
11 D'Alessio DA, Kahn SE, Leusner CR, Ensinck JW. Glucagon–like peptide 1 enhances glucose tolerance both by stimulation of insulin release and by increasing insulin-independent glucose disposal. J Clin Investig 1994; 93: 2263–6.
12 Pospisilik JA, Martin J, Doty T, Ehses JA, Pamir N, Lynn FC, *et al*. Dipeptidyl peptidase IV inhibitor treatment stimulates cell survival and islet neogenesis in streptozotocin-induced diabetic rats. Diabetes 2003; 52: 741–50.
13 Drucker DJ. The biology of incretin hormones. Cell Metab 2006; 3: 153–65.
14 Farilla L, Bulotta A, Hirshberg B, Li Calzi S, Khoury N, Noushmehr H, *et al*. Glucagon-like peptide 1 inhibits cell apoptosis and improves glucose responsiveness of freshly isolated human islets. Endocrinology 2003; 144: 5149–58.
15 Mentlein R, Gallwitz B, Schmidt WE. Dipeptidyl-peptidase IV hydrolyses gastric inhibitory polypeptide, glucagon-like peptide-1 (7–36)amide, peptide histidine methionine and is responsible for their degradation in human serum. Eur J Biochem 1993; 214: 829–35.
16 Thomas L, Tadayyon M, Mark M. Chronic treatment with the dipeptidyl peptidase-4 inhibitor BI1356 [(*R*)-8-(3-amino-piperidin-1-yl)-7-but-2-ynyl-3-methyl-1-(4-methyl-quinazolin-2-ylmethyl) -3,7-dihydro-purine-2,6-dione] increases basal glucagon-like peptide-1 and improves glycemic control in diabetic rodent models. J Pharmacol Exp Ther 2009; 328: 556–63.
17 Yamazaki K, Yasuda N, Inoue T, Nagakura T, Kira K, Shinoda M, *et al*. 7-But-2-ynyl-9-(6-methoxy-pyridin-3-yl)-6-piperazin-1-yl-7,9-dihydro-purin-8-one is a novel competitive and selective inhibitor of dipeptidyl peptidase IV with an antihyperglycemic activity. J Pharmacol Exp Ther 2006; 319: 1253–7.
18 Augeri DJ, Robl JA, Betebenner DA, Magnin DR, Khanna A, Robertson JG, *et al*. Discovery and preclinical profile of saxagliptin (BMS-477118): a highly potent, long-acting, orally active dipeptidyl peptidase IV

inhibitor for the treatment of type 2 diabetes. J Med Chem 2005; 48: 5025–37.
19 Moritoh Y, Takeuchi K, Asakawa T, Kataoka O, Odaka H. Chronic administration of alogliptin, a novel, potent, and highly selective dipeptidyl peptidase-4 inhibitor, improves glycemic control and beta-cell function in obese diabetic *ob/ob* mice. Eur J Pharmacol 2008; 588: 325–32.
20 Furuta Y, Horiguchi M, Sugaru E, Ono-Kishino M, Otani M, Sakai M, *et al*. Chronic administration of DSP-7238, a novel, potent, specific and substrate-selective DPP IV inhibitor, improves glycaemic control and β-cell damage in diabetic mice. Diabetes Obes Metab 2010; 12: 421–30.
21 Thomas L, Eckhardt M, Langkopf E, Tadayyon M, Himmelsbach F, Mark M. (R)-8-(3-Amino-piperidin-1-yl)-7-but-2-ynyl-3-methyl-1-(4-methyl-quinazolin-2-ylmethyl)-3,7-dihydro-purine-2,6-dione (BI1356), a novel xanthine-based dipeptidyl peptidase 4 inhibitor, has a superior potency and longer duration of action compared with other dipeptidyl peptidase-4 inhibitors. J Pharmacol Exp Ther 2008; 325: 175–82.
22 Scott R, Wu M, Sanchez M, Stein P. Efficacy and tolerability of the dipeptidyl peptidase-4 inhibitor sitagliptin as monotherapy over 12 weeks in patients with type 2 diabetes. Int J Clin Pract 2007; 61: 171–80.
23 Pi-Sunyer FX, Schweizer A, Mills D, Dejager S. Efficacy and tolerability of vildagliptin monotherapy in drug-naive patients with type 2 diabetes. Diabetes Res Clin Practice 2007; 76: 132–8.
24 DeFronzo RA, Fleck PR, Wilson CA, Mekki Q. Efficacy and safety of the dipeptidyl peptidase-4 inhibitor alogliptin in patients with type 2 diabetes and inadequate glycemic control. Diabetes Care 2008; 31: 2315–7.
25 Villhauer EB, Brinkman JA, Naderi GB, Burkey BF, Dunning BE, Prasad K, *et al*. 1-[(3-Hydroxy-1-adamantyl)amino]acetyl]-2-cyano-(S)-pyrrolidine: a potent, selective and orally bioavailable dipeptidyl peptidase IV inhibitor with antihyperglycemic properties. J Med Chem 2003; 46: 2774–89.
26 Burkey BF, Li X, Bolognese L, Balkan B, Mone M, Russell M, *et al*. Acute and chronic effects of the incretin enhancer vildagliptin in insulin-resistant rats. J Pharmacol Exp Ther 2005; 315: 688–95.
27 Pratley RE, Salsali A. Inhibition of DPP-4: a new therapeutic approach for the treatment of type 2 diabetes. Curr Med Res Opin 2007; 23: 919–31.
28 Mitani H, Takimoto M, Hughes TE, Kimura M. Dipeptidyl peptidase IV inhibition improves impaired glucose tolerance in high-fat diet-fed rats: study using a Fischer 344 rat substrain deficient in its enzyme activity. Jpn J Pharmacol 2002; 88: 442–50.
29 Herberg L, Leiter EH. Obesity/diabetes in mice with mutations in the leptin or leptin receptor genes. In: Shima AAF, Shafrir E, editors. Animal models of diabetes a primer. Amsterdam: Harwood Academic Publishers; 2001. p 63–107.
30 Pederson RA, White HA, Schlenzig D, Pauly RP, McIntosh CH, Demuth HU. Improved glucose tolerance in Zucker fatty rats by oral administration of the dipeptidyl peptidase IV inhibitor isoleucine thiazolidide. Diabetes 1998; 47: 1253–8.
31 Balkan B, Kwasnik L, Miserendino R, Holst JJ, Li X. Inhibition of dipeptidyl peptidase IV with NVP-DPP728 increases plasma GLP-1 (7–36 amide) concentrations and improves oral glucose tolerance in obese Zucker rats. Diabetologia 1999; 42: 1324–31.
32 Ahren B, Holst JJ, Martensson H, Balkan B. Improved glucose tolerance and insulin secretion by inhibition of dipeptidyl peptidase IV in mice. Eur J Pharmacol 2000; 404: 239–45.
33 Mu J, Woods J, Zhou YP, Roy RS, Li Z, Zycband E, *et al*. Chronic inhibition of dipeptidyl peptidase-4 with a sitagliptin analog preserves pancreatic beta-cell mass and function in a rodent model of type 2 diabetes. Diabetes 2006; 55: 1695–704.
34 Moritoh Y, Takeuchi K, Asakawa T, Kataoka O, Odaka H. Chronic administration of alogliptin, a novel, potent, and highly selective dipeptidyl peptidase-4 inhibitor, improves glycemic control and beta-cell function in obese diabetic *ob/ob* mice. Eur J Pharmacol 2008; 588: 325–32.
35 Moritoh Y, Takeuchi K, Asakawa T, Kataoka O, Odaka H. Combining a dipeptidyl peptidase-4 inhibitor, alogliptin, with pioglitazone improves glycaemic control, lipid profiles and β-cell function in *db/db* mice. Br J Pharmacol 2009; 157: 415–26.
36 Mu J, Woods J, Zhou YP, Roy RS, Li Z, Zycband E, *et al*. Chronic inhibition of dipeptidyl peptidase-4 with a sitagliptin analog preserves pancreatic beta-cell mass and function in a rodent model of type 2 diabetes. Diabetes 2006; 55: 1695–704.
37 Szayna M, Doyle ME, Betkey JA, Holloway HW, Spencer RG, Greig NH, *et al*. Exendin-4 decelerates food intake, weight gain, and fat deposition in Zucker rats. Endocrinology 2000; 141: 1936–41.
38 Moretto TJ, Milton DR, Ridge TD, Macconell LA, Okerson T, Wolka AM, *et al*. Efficacy and tolerability of exenatide monotherapy over 24 weeks in antidiabetic drug-naive patients with type 2 diabetes: a randomized, double-blind, placebo-controlled, parallel-group study. Clin Ther 2008; 30: 1448–60.
39 Feinglos MN, Saad MF, Pi-Sunyer FX, An B, Santiago O. Effects of liraglutide (NN2211), a long-acting GLP-1 analogue, on glycaemic control and body weight in subjects with type 2 diabetes. Diabet Med 2005; 22: 1016–23.

Acta Pharmacologica Sinica (2012) 33: 1023–1029
 1671-4083/12 $32.00
www.nature.com/aps

Original Article

Arecoline improves vascular endothelial function in high fructose-fed rats via increasing cystathionine-γ-lyase expression and activating K_{ATP} channels

Hong-yan LING[1, #], Guang WANG[1, #], Wei ZHANG[2], Xing LI[1], Shou-hong ZHOU[1], Bi HU[1, *]

[1]*Department of Physiology, College of Medicine, University of South China, Hengyang 421001, China;* [2]*Department of Physiology, College of Xiangnan, Chenzhou 423043, China*

Aim: To investigate the effect of arecoline, a major component of betel nut, on vascular endothelial function in high fructose-fed rats and the potential mechanisms underlying the effect.

Methods: Male Wistar rats were fed a high-fructose or control diet for 16 weeks. At the beginning of week 13, the rats were injected ip with low (0.5 mg·kg^{-1}·d^{-1}), medium (1.0 mg·kg^{-1}·d^{-1}) or high (5.0 mg·kg^{-1}·d^{-1}) doses of arecoline for 4 weeks. At the termination of the treatments, blood was collected, fasting blood glucose (FBG) and serum insulin (FSI) levels were measured, and insulin sensitivity index (ISI) was calculated. The thoracic aortas were isolated and aortic rings were prepared for studying ACh-induced endothelium-dependent vasorelaxation (EDVR). The mRNA and protein expression of cystathionine-γ-lyase (CSE) in the thoracic aortas was analyzed using RT-PCR and Western blot analysis, respectively.

Results: In high fructose-fed rats, the levels of FBG and FSI were remarkably increased, whereas the ISI and the mRNA and protein expression of CSE were significantly decreased. ACh-induced EDVR in the aortic rings from high fructose-fed rats was remarkably reduced. These changes were reversed by treatment with high dose arecoline. Pretreatment of the aortic rings rings from high fructose-fed rats with the CSE inhibitor propargylglycine (10 mmol/L) or the ATP-sensitive potassium (K_{ATP}) channel blocker glibenclamide (10 mmol/L) abolished the restoration of ACh-induced EDVR by high dose arecoline. On the contrary, treatment with high dose arecoline significantly impaired ACh-induced EDVR in the aortic rings from control rats, and pretreatment with propargylglycine or glibenclamide did not cause further changes.

Conclusion: Arecoline treatment improves ACh-induced EDVR in high fructose-fed rats, and the potential mechanism of action might be associated with increase of CSE expression and activation of K_{ATP} channels by arecoline.

Keywords: arecoline; betel-quid chewing; propargylglycine; glibenclamide; high fructose-fed rat; endothelium-dependent vasorelaxation; cystathionine-γ-lyase; K_{ATP} channel; diabetes mellitus; vascular endothelial dysfunction

Acta Pharmacologica Sinica (2012) 33: 1023–1029; doi: 10.1038/aps.2012.63; published online 23 Jul 2012

Introduction

Insulin resistance (IR), defined as the decreased ability of cells or tissues to respond to physiological levels of insulin, is thought to be a pathogenic hallmark of type 2 diabetes mellitus (T2DM). Epidemiological evidence has demonstrated that IR is frequently associated with a number of other health disorders, including obesity, hypertension and cardiovascular disease (CVD)[1–3]. Recent research indicates that vascular endothelial dysfunction (VED) plays a key role in linking the pathogenesis of vascular complications and IR[4], and macro- and micro-vascular complications are still the main causes of morbidity and mortality in patients with diabetes mellitus (DM)[5]. Our laboratory has previously demonstrated that fructose-fed rats had attenuated endothelial relaxation in response to ACh compared with controls[6]. Therefore, improvement of VED may be useful for inhibiting the development of vascular complications in IR or DM patients.

Arecoline is a major component of the betel nut and has many important physiological activities. Some studies have indicated that betel-quid chewing is associated with an increased risk of oral cancer and esophageal carcinoma[7, 8]. Epidemiological studies have shown that betel-quid chewing is associated with the risk of T2DM and metabolic syndrome in men[9, 10]. Hsu and Hsieh *et al* reported that arecoline inhibited preadipocyte differentiation and locked insulin signaling

# These authors contributed equally to this paper.
* To whom correspondence should be addressed.
E-mail hubishengli@yahoo.com.cn
Received 2011-11-21 Accepted 2012-05-07

in 3T3-L1 adipocytes[11, 12]. Our previous study found that arecoline improved glucose and lipid metabolism in type 2 diabetic rats and prevented high fructose–induced pancreatic β-cell dysfunction[13, 14]. We also found that arecoline regulated the expression of cystathionine-γ-lyase (CSE), which is suggested to be the only H_2S-generating enzyme in the vascular system[15, 16], and reduced inflammatory factor expression induced by oxidized low-density lipoprotein in RAW264.7 cells[17]. Zhao *et al* reported that H_2S relaxed rat aortic tissues *in vitro* in a K_{ATP} channel-dependent manner[18]. Siebert *et al* showed that H_2S mediated vasorelaxation of the hepatic artery by activation of K_{ATP} channels[19]. Goto *et al* reported that areca seed extract led to endothelium-dependent vasodilation in rat aortas[20]. The above studies suggest that arecoline might play an important role in vasorelaxation mediated by the CSE-H_2S-K_{ATP} pathway. However, it is unclear whether arecoline can improve endothelium-dependent vasorelaxation (EDVR) in high fructose–fed rats. Therefore, in the present study, we sought to investigate the effect of arecoline on high fructose–induced EDVR and its mechanism of action.

Materials and methods

Reagents

Arecoline, ACh, *L*-phenylephrine hydrochloride (*L*-PE), glibenclamide and propargylglycine (PAG) were obtained from Sigma Co (St Louis, MO, USA). *D*-fructose was purchased from Sangon Biotech Co (Shanghai, China). TRIzol and AMV reverse transcriptase were purchased from BBI, and affinity-purified anti-CSE polyclonal antibodies were purchased from Santa Cruz (CA, USA).

Animals and groups

Male Wistar rats (200±20 g) were housed in standard animal laboratories with a 12 h light/dark cycle with free access to food and water. The rats were randomly divided into two groups of twenty four animals each. For 16 weeks, the control group (Con) received a normal chow diet and the high-fructose group (HF) received a high-fructose diet containing 75% fructose, 12% fat and 13% protein[21, 22]. At the beginning of week 13, the two groups of rats were treated with low (L-Are, 0.5 $mg\cdot kg^{-1}\cdot d^{-1}$), medium (M-Are, 1.0 $mg\cdot kg^{-1}\cdot d^{-1}$) or high (H-Are 5.0 mg/kg/d) doses of arecoline by intraperitoneal injection or left untreated for 4 weeks.

Measurement of fasting blood glucose (FBG) and fasting serum insulin (FSI)

At the termination of the study, all rats were fasted for 12 h and anesthetized with sodium pentobarbital (40 mg/kg body wt, ip). Blood was collected by carotid puncture into non anticoagulated plastic centrifuge tubes, and the tubes were centrifuged at 3000 r/min for 10 min at 4 °C. FBG was measured with an HI-TACH717 automatic biochemical analyzer. FSI was measured using a radioimmunoassay method, and the insulin sensitivity index (ISI) was calculated using Li's formula [ISI=-ln(FBS×FSI)][23].

Preparation of thoracic aortas and measurement of vascular reactivity

The thoracic aortas from the rats were isolated and immediately placed into a cold Krebs solution of the following composition (mmol/L): NaCl 118.3, KCl 4.7, $CaCl_2$ 2.5, $MgSO_4$ 1.2, KH_2PO_4 1.2, $NaHCO_3$ 25.0 and glucose 11.0. Aortic segments were cleaned of perivascular fat and connective tissue, cut into 2 to 3-mm segments, and mounted on two stainless steel hooks in a 10 mL organ bath containing Krebs solution at 37 °C, aerated with 95% O_2 and 5% CO_2. One hook was connected to an isometric force transducer to measure tension. The rings were equilibrated for 90 min, during which time the bathing fluid was changed every 15 min. The tissue was kept under a constant tension of 2 g throughout the experiment. Endothelium-dependent vessel relaxation was assessed qualitatively in 1 μmol/L phenylephrine-precontracted rings as the degree of relaxation caused by the cumulative addition of increasing concentrations of acetylcholine (ACh; 10^{-9}–10^{-5} mol/L). The effects of the CSE inhibitor propargylglycine (PAG) and the potassium channel blocker glibenclamide (Glib) were also evaluated. In these experiments, the rings were incubated with PAG (10 mmol/L) or Glib (10 mmol/L) for 30 min and then the ACh-induced EDVR was determined.

Determination of CSE mRNA expression by RT-PCR

Reverse transcription-polymerase chain reaction (RT-PCR) was performed as described previously[24]. Briefly, total RNA was extracted from thoracic aortas with TRIzol according to the manufacturer's instructions. The RNA concentration was determined spectrophotometrically, and cDNA was prepared by reverse transcription of RNA (1 μg) using oligonucleotide primers. Subsequently, the equivalent of 0.05 μg was amplified by PCR using the following primers: CSE 5′-GTATTGAGGCACCAACAGGT-3′ and 5′-GTTGGGTTTGTGGGTGTTTC-3′ (149 bp); and GAPDH 5′-TCAACGGCACAGTCAAGG-3′ and 5′-GGCTAAGCAGTTGGTGGT-3′ (308 bp). The PCR conditions were 94 °C for 4 min, followed by 32 cycles of 94 °C for 60 s, 58 °C for 30 s, and 72 °C for 60 s, followed by a 72 °C extension for 10 min.

Thoracic aorta Western blot analysis

For CSE analysis by Western blot, thoracic aortas were lysed in a buffer containing 10 mmol/L HEPES (pH 7.9), 1.5 mmol/L $MgCl_2$, 10 mmol/L KCl and 0.5% NP-40, followed by centrifugation at 13 000×*g* for 15 min at 4 °C. Protein concentrations were determined with the BCA protein assay. Briefly, 30 μg of each sample was separated on a 10% SDS-PAGE gel and then transferred to polyvinyl difluoride (PVDF) membranes. The membranes were blocked for 60 min in a buffer containing 0.1% Tween 20 and 5% milk. Antibodies against CSE or GAPDH were used to identify the specific proteins and visualized by the ECL method described previously[25]. The intensity of the protein band of interest was quantified by densitometry.

Statistical analysis

Data were presented as the mean±SD. Statistical comparisons

between two groups were made with Student's *t*-test, whereas ANOVA was used to test the differences between multiple groups. $P<0.05$ was considered significant.

Results

Effects of arecoline on FBG, FSI, and the ISI

As shown in Table 1, FBG and FSI were significantly increased, whereas the ISI was remarkably decreased in the HF group, compared with the control group ($P<0.05$). Treatment with arecoline reversed the above parameters in the HF group, and this change was significant in the group treated with the highest dose of arecoline (H-Are; 5.0 mg·kg^{-1}·d^{-1}). Arecoline treatment had no significant effect on the control group.

Table 1. Effect of arecoline on the FBG, FSI, and ISI in rats.

Groups	FBG (mmol/L)	FSI (mmol/L)	ISI
Con	5.67±0.10	22.57±0.46	-4.45±0.33
Con+L-Are	5.76±0.10	22.86±0.49	-4.88±0.03
Con+M-Are	5.50±0.10	23.35±0.65	-4.85±0.02
Con+H-Are	5.57±0.10	24.48±0.54	-4.91±0.04
HF	9.02±0.06^{b}	39.46±0.40^{b}	-5.75±0.24^{b}
HF+L-Are	8.50±0.07	38.06±0.92	-5.77±0.03
HF+M-Are	6.70±0.13	29.80±0.45	-5.29±0.09
HF+H-Are	6.00±0.12^{e}	23.65±0.77^{e}	-4.97±0.05^{e}

Normal control and high-fructose fed rats were treated with and without low, medium, and high dose of arecoline (L-Are, 0.5 mg·kg^{-1}·d^{-1}; M-Are, 1.0 mg·kg^{-1}·d^{-1} and H-Are 5.0 mg·kg^{-1}·d^{-1}, intraperitoneal injection) for 4 weeks as the Con group, Con+L-Are group, Con+M-Are group, Con+H-Are group, HF group, HF+L-Are group, HF+M-Are group, and HF+H-Are group, respectively. The fasting blood glucose (FBG) and fasting serum insulin (FSI) were measured and insulin sensitivity index (ISI) was calculated. [ISI= -ln (FBS×FSI)]. Results are expressed as mean±SD (n=6). $^{b}P<0.05$ *vs* the Con group. $^{e}P<0.05$ *vs* the HF group.

Effects of arecoline on EDVR in high fructose-fed rats

As shown in Figure 1A, ACh-induced EDVR was significantly impaired in aortic rings from the high fructose-fed rats compared with the control group. Treatment of high fructose–fed rats with arecoline restored the EDVR in a concentration-dependent manner, and treatment with the highest dose of arecoline (H-Are; 5.0 mg·kg^{-1}·d^{-1}) significantly increased the potency (EC_{50}) and the maximal response (E_{max}) of endothelial relaxation in response to ACh. However, in the Con group, H-Are treatment significantly decreased the ACh-induced EDVR and significantly impaired maximal relaxation in response to ACh (Figure 1B, Table 2). These results suggest that H-Are treatment improved EDVR and prevented vascular endothelial dysfunction (VED) in rats fed a high-fructose diet, whereas H-Are treatment impaired EDVR in rats fed a normal diet.

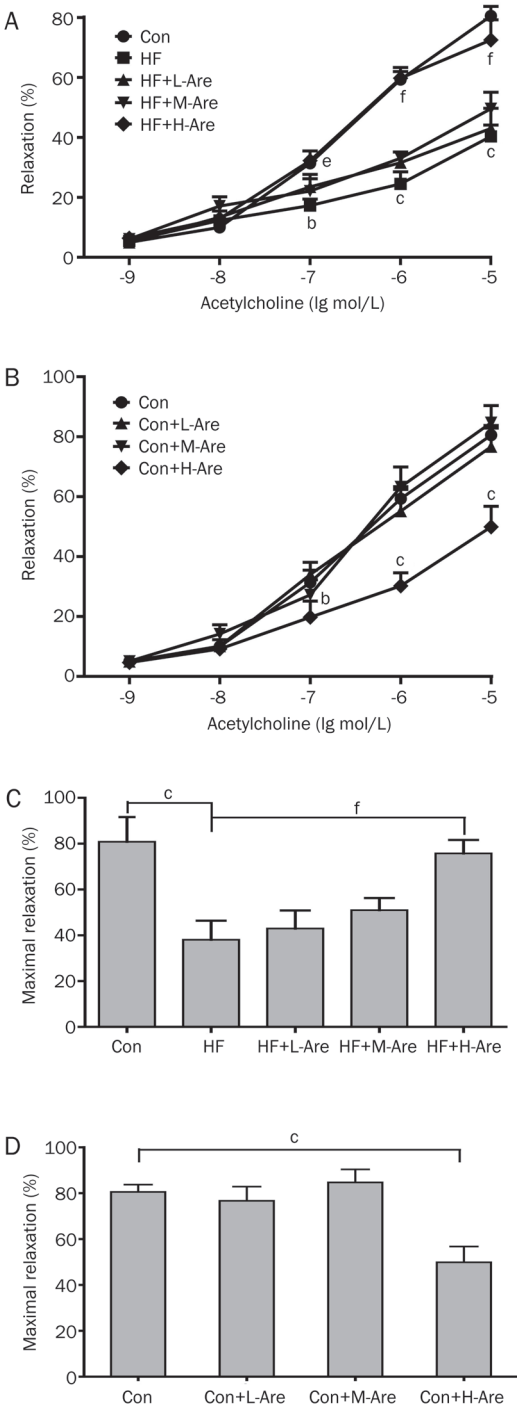

Figure 1. Effects of arecoline on EDVR in high fructose-fed rats. Normal control (Con) and high fructose-fed (HF) rats were treated with low (L-Are, 0.5 mg·kg^{-1}·d^{-1}), medium (M-Are, 1.0 mg·kg^{-1}·d^{-1}) or high (H-Are, 5.0 mg·kg^{-1}·d^{-1}) doses of arecoline by intraperitoneal injection for 4 weeks or were left untreated. Endothelium-dependent vasorelaxation (EDVR) of rings from the thoracic aorta in response to acetylcholine (ACh) was examined. in the high fructose-fed rats (A) and normal control rats (B). Maximal relaxation response to acetylcholine (ACh) was calculated in the high fructose-fed rats (C) and normal control rats (D). Mean±SD (n=6). $^{b}P<0.05$, $^{c}P<0.01$ *vs* the Con group; $^{e}P<0.05$, $^{f}P<0.01$ *vs* the HF group.

Table 2. The potency (EC_{50}; pD_2=-log EC_{50}) and maximum relaxation (E_{max}) values to acetylcholine in rat thoracic aortic rings from Con, Con+PAG, Con+Glib, Con+H-Are, Con+H-Are+PAG, Con+H-Are+Glib, HF, HF+PAG, HF+Glib, HF+H-Are, HF+H-Are+PAG, or HF+H-Are+Glib. Values are expressed as mean±SD, n=6. ^{c}P<0.01 *vs* the Con group; ^{i}P<0.01 *vs* the Con+PAG group or the Con+Glib group; ^{f}P<0.01 *vs* the HF group; ^{l}P<0.01 *vs* the HF+Are group.

Groups	EC_{50}	pD_2	E_{max}
Con	2.44E-7	6.61±0.15	80.52%±3.2%
Con+PAG	4.36E-7	6.36±0.17	74.62%±3.5%
Con+Glib	5.24E-8	7.26±0.19	76.02%±4.5%
Con+H-Are	9.96E-6	5.00±0.14^{c}	49.87%±6.9%^{c}
Con+H-Are+PAG	2.98E-5	4.52±0.15^{i}	46.18%±4.6%^{i}
Con+H-Are+Glib	1.36E-6	5.87±0.12^{i}	52.59%±4.4%^{i}
HF	1.13E-4	3.95±0.11^{c}	40.33%±3.8%^{c}
HF+PAG	5.47E-4	3.26±0.10	37.65%±5.8%
HF+Glib	5.00E-4	3.30±0.11	36.16%±2.2%
HF+H-Are	2.89E-7	6.54±0.16^{f}	72.50%±6.7%^{f}
HF+H-Are+PAG	1.36E-6	5.87±0.17^{l}	52.59%±5.6%^{l}
HF+H-Are+Glib	2.83E-5	4.55±0.14^{l}	44.67%±3.3%^{l}

Effect of the CSE inhibitor PAG or the potassium channel blocker glibenclamide on EDVR in high fructose-fed rats

To examine whether CSE or potassium channels were involved in EDVR, the CSE inhibitor PAG and the potassium channel blocker glibenclamide (Glib) were used. As shown in Figure 2, pretreatment with 10 mmol/L PAG did not significantly change ACh-induced EDVR in the Con group or the HF group. However, endothelial relaxation in response to acetylcholine was partly abolished in aortic rings from rats in the HF group treated with H-Are and PAG compared with those that were not treated with PAG. Similar EDVR results were obtained in high fructose-fed rats after pretreatment with glibenclamide (Figure 3, Table 2). These results indicated that CSE or potassium channels was involved in the arecoline treatment-induced improvement in vessel function in high fructose-fed rats.

Effect of arecoline on CSE mRNA and protein expression in thoracic aorta

Our previous study found that arecoline treatment could regulate the expression of CSE in RAW264.7 cells[17]. To further investigate whether the changes in CSE expression contribute to the arecoline-mediated improvement of EDVR on a high-fructose diet, mRNA and protein levels of CSE were determined. As illustrated in Figure 4, CSE mRNA and protein were expressed and could be detected in rat thoracic aorta. Moreover, a high-fructose diet significantly decreased CSE mRNA and protein expression. However, arecoline treatment resulted in a dose-dependent increase of CSE mRNA and protein expression, which was significant in the H-Are treated

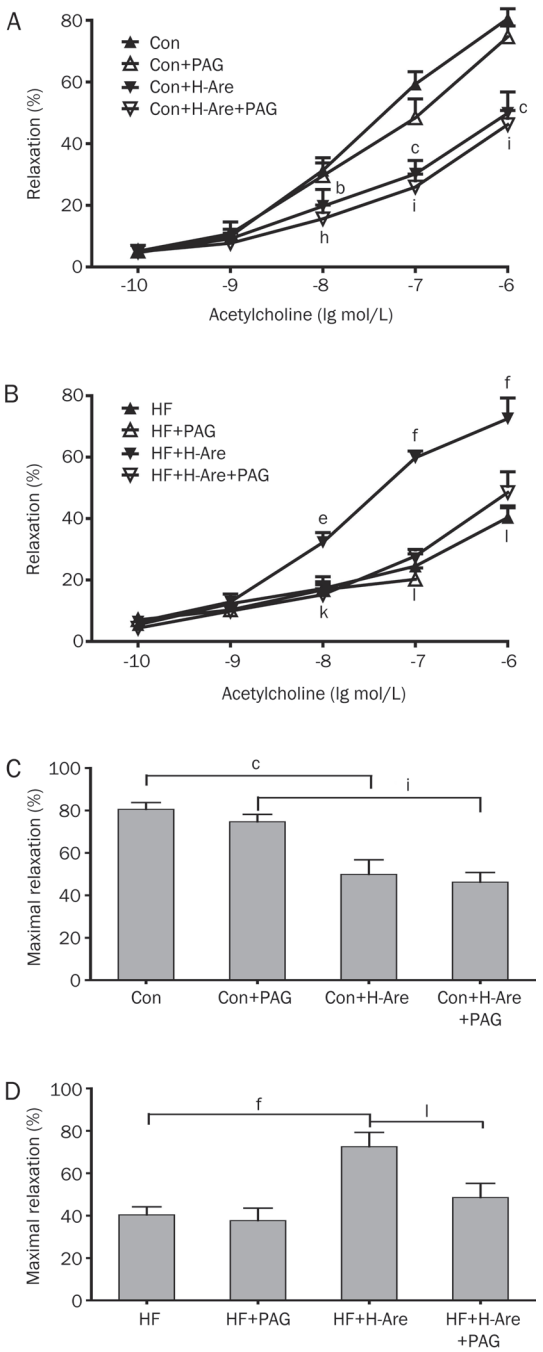

Figure 2. Effect of the cystathionine-γ-lyase (CSE) inhibitor propargylglycine (PAG) on EDVR in high fructose-fed rats. Normal control and high fructose-fed rats were treated with or without high doses of arecoline (H-Are, 5.0 mg·kg^{-1}·d^{-1}) by intraperitoneal injection for 4 weeks. Effects of inhibition of cystathionine-β-synthase (CBS) by 10 mmol/L propargylglycine (PAG) on ACh-induced EDVR were examined. in the normal control rats (A) and high fructose-fed rats(B). Maximal relaxation response to acetylcholine (ACh) was calculated in the normal control rats (C) and high fructose-fed rats(D). Mean±SD(n=6). ^{b}P<0.05, ^{c}P<0.01 *vs* the Con group; ^{e}P<0.05, ^{f}P<0.01 *vs* the HF group; ^{h}P<0.05, ^{i}P<0.01 *vs* the Con+PAG group; ^{k}P<0.05, ^{l}P<0.01 *vs* the HF+Are group.

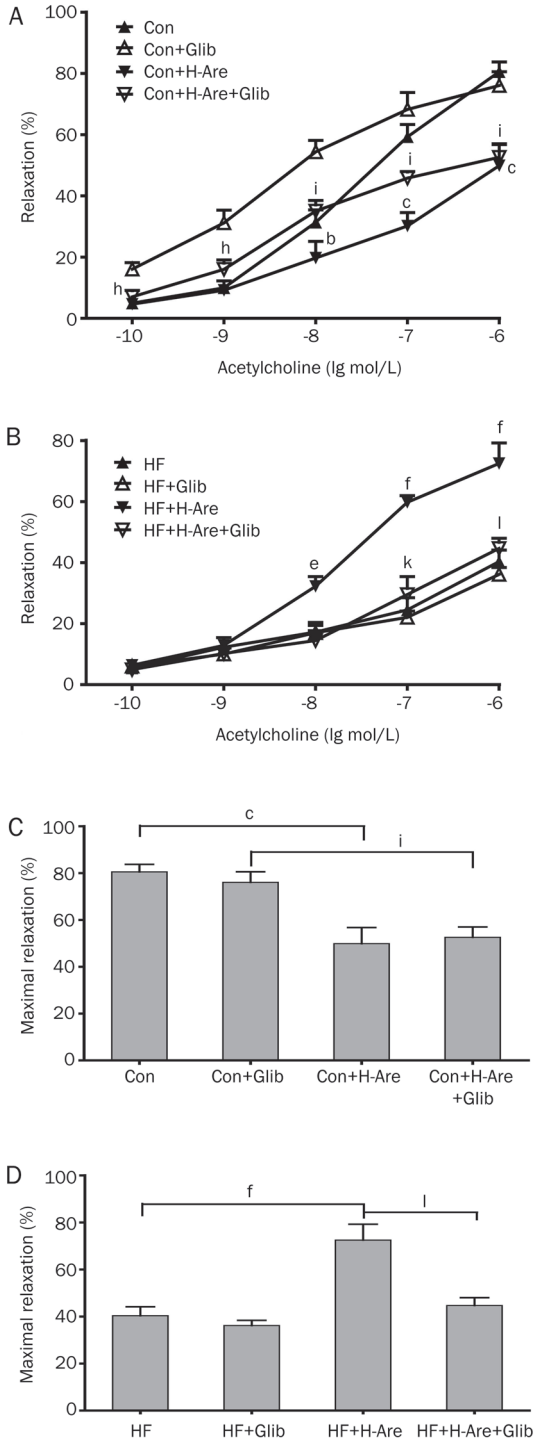

Figure 3. Effect of the potassium channel blocker glibenclamide (Glib) on EDVR in high fructose-fed rats. Normal control and high fructose-fed rats were treated with or without high doses of arecoline (H-Are, 5.0 mg·kg^{-1}·d^{-1}) by intraperitoneal injection for 4 weeks. Effects of inhibition of potassium channels by 10 mmol/L glibenclamide (Glib) on ACh-induced EDVR were examined. in the normal control rats (A) and high fructose-fed rats(B). Maximal relaxation response to acetylcholine (ACh) was calculated in the normal control rats (C) and high fructose-fed rats (D). Mean±SD (n=6). ^{b}P<0.05, ^{c}P<0.01 *vs* the Con group; ^{h}P<0.05, ^{i}P<0.01 *vs* the Con+Glib group; ^{e}P<0.05, ^{f}P<0.01 *vs* the HF group; ^{k}P<0.05, ^{l}P<0.01 *vs* the HF+Are group.

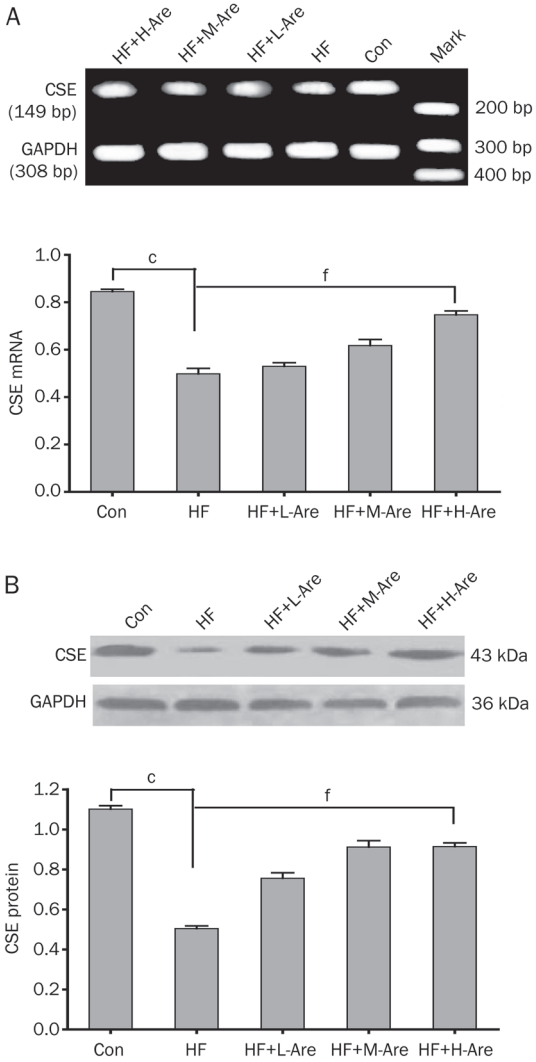

Figure 4. Effect of arecoline on CSE mRNA and protein expression in thoracic aortas. High fructose-fed rats were treated with or without low (L-Are, 0.5 mg·kg^{-1}·d^{-1}), medium (M-Are, 1.0 mg·kg^{-1}·d^{-1}), and high (H-Are 5.0 mg·kg^{-1}·d^{-1}) doses of arecoline by intraperitoneal injection for 4 weeks. Control rats were fed a normal diet. CSE mRNA and protein expression in thoracic aortas was measured by RT-PCR and Western blot, respectively. The results are expressed as the mean±SD (n=6). ^{b}P<0.05 *vs* the control group; ^{e}P<0.05 *vs* the HF group. (A) CSE mRNA expression was measured by RT-PCR. Relative mRNA levels were calculated as the ratio of CSE to GAPDH. (B) CSE protein levels were measured by Western blot. Representative immunoblots (top) and densitometric analyses (bottom) of CSE protein levels normalized to β-actin levels were reported. Values are expressed as the mean±SD (n=6). ^{c}P<0.01 *vs* the Con group; ^{f}P<0.01 *vs* the HF group.

group (mRNA expression 0.48±0.05 *vs* 0.78±0.04, P<0.05; protein expression 0.52±0.04 *vs* 0.73±0.08, P<0.05) (Figure 4).

Discussion

In the present study, FBG was increased, serum insulin was elevated, and the ISI was decreased in high fructose–fed rats compared with controls, suggesting that a high-fructose diet

resulted in insulin resistance (IR), as reported previously[6, 26]. Furthermore, the high-fructose diet impaired EDVR in rat thoracic aortas. The mechanisms involved in the fructose-induced IR and VED are unclear, but some studies have demonstrated that IR and VED may contribute to the development of various cardiovascular diseases[3, 4, 27, 28]. Hence, improvement of VED may reduce the incidence of vascular complications in IR or DM patients.

Arecoline is an alkaloid-type natural product found in betel nuts. It has many important functions such as deworming[29], preventing Alzheimer's disease[30] and inhibiting atherosclerosis[17, 31]. Some studies have reported that arecoline decreased vascular tone and improved EDVR[32, 33]. Our results indicated that high doses of arecoline (H-Are; 5.0 $mg{\cdot}kg^{-1}{\cdot}d^{-1}$) significantly impaired EDVR in the Con group, suggesting that long-term use or high doses of arecoline might induce VED or associated diseases. However, we also found that H-Are treatment improved IR and EDVR in the high fructose-fed rats. These results seem to be contradictory because H-Are treatment had opposite effects on EDVR in the Con group and the HF group; we think that this conflicting result might be the result of a difference in conditions between the groups. In the Con group, H-Are treatment might inhibit cell growth and proliferation of endothelial cells (ECs) and lead to VED, which is consistent with the reports from Kuo and Tseng *et al*[33, 34]. Because arecolin treatment impaired vascular endothelium and inhibited KATP channel in the Con group[27], the improvement in EDVR might be a direct or an indirect effect on vascular smooth muscle cells (VSMCs) in high fructose–fed rats. The underlying mechanisms by which arecoline improved EDVR are still not clear.

Recent studies showed that arecoline treatment increased CSE expression and H_2S production in macrophages[17]. Increasing evidence suggests that H_2S might be the third endogenous signaling gasotransmitter, which shares features with nitric oxide (NO) and carbon dioxide (CO_2). Unlike NO, which can be produced by both ECs and VSMCs, H_2S-producing enzymes are not expressed in the vascular endothelium; therefore, H_2S is only generated by VSMCs[18]. H_2S is produced endogenously from cysteine by pyridoxal-5′-phosphate-dependent enzymes, including cystathionine β-synthase (CBS) and/or cystathionine-γ-lyase (CSE)[26]. CSE, which is localized to smooth muscle, is thought to be the major H_2S-producing enzyme in the thoracic aorta[16]. Some studies also showed that endogenous H_2S functions to regulate smooth muscle tone in synergy with NO. Furthermore, NO appears to be a physiological modulator of endogenous H_2S production by increasing CSE expression and stimulating its activity[16]. Hence, we detected CSE mRNA and protein expression in the thoracic aorta using RT-PCR and Western blotting, respectively. The data showed that high fructose significantly decreased CSE expression; however, H-Are treatment significantly increased CSE expression. We found that pretreatment with the CSE-specific inhibitor PAG further impaired ACh-mediated relaxation in the HF fed and H-Are treated groups, whereas PAG pretreatment had no significant effect on the Con group and HF fed groups. Taken together, these data demonstrated that the improvement in ACh-induced EDVR after arecoline treatment may be partially caused by increased CSE expression and H_2S generation. However, because of the experimental limitations, endogenous H_2S levels in the thoracic aortas were not determined.

Some studies also showed that H_2S is the only endogenous gaseous K_{ATP} channel opener and that H_2S activated K_{ATP} channels at the whole-cell and single channel levels in VSMCs[16, 18, 19]. Opening of K_{ATP} channels leads to membrane hyperpolarization and relaxation of VSMCs. To elucidate whether K_{ATP} channels promoted the effects of arecoline on EDVR in the thoracic aorta, a specific K_{ATP} channel blocker, Glibenclamide (Glib), was administered. We found that pretreatment with Glib impaired ACh-mediated EDVR in the HF+H-Are group. However, there were no significant differences after Glib treatment in the HF rats that were not treated with H-Are, which confirmed that the arecoline-mediated improvement in ACh-induced EDVR may be partly due to H_2S-induced K_{ATP} channel opening in VSMCs. Our findings were consistent with the results of Zhao *et al*[18, 19]. This study demonstrated that H_2S is different from NO and CO_2 and that H_2S-induced vascular relaxation was mediated mainly by K_{ATP} channel opening in VSMCs.

In summary, the present study showed that arecoline can improve EDVR in high fructose-fed rats, and might exert its function by increasing CSE expression and activation of K_{ATP} channels.

Acknowledgements

This work was supported by the National Natural Science Foundation of China (No 81000328), the fifty-first batch of China Postdoctoral Science Foundation (No 2012M511384), and the Fund of the Research Project of Department of Science and Technology of Hunan Province (No 2007TP4018).

Author contribution

Hong-yan LING, Guang WANG, Shou-hong ZHOU, and Bi HU designed the research; Guang WANG and Wei ZHANG performed the research; Xing LI analyzed the data and images; Hong-yan LING wrote the paper.

References

1 Fidan Yaylali G, Akin F, Turgut S, Kursunluoglu R. IGF-1 gene polymorphism in obese patients with insulin resistance. Mol Biol Rep 2010; 37: 529–33.

2 Hamburg NM, Larson MG, Vita JA, Vasan RS, Keyes MJ, Widlansky ME, *et al*. Metabolic syndrome, insulin resistance, and brachial artery vasodilator function in Framingham Offspring participants without clinical evidence of cardiovascular disease. Am J Cardiol 2008; 101: 82–8.

3 McFarlane SI, Banerji M, Sowers JR. Insulin resistance and cardiovascular disease. J Clin Endocrinol Metab 2001; 86: 713–8.

4 Tziomalos K, Athyros VG, Karagiannis A, Mikhailidis DP. Endothelial dysfunction in metabolic syndrome: prevalence, pathogenesis and management. Nutr Metab Cardiovasc Dis 2010; 20: 140–6.

5 Fox CS, Coady S, Sorlie PD, Levy D, Meigs JB, Agostino RB, *et al*.

Trends in cardiovascular complications of diabetes. JAMA 2004; 292: 2495–99.
6 Ling HY, Feng SD, Zhou SH, Wang BX, Liu XQ, Hu B. Effects of rosiglitazone on aortic function in rats with insulin resistant-hypertension. Sheng Li Xue Bao 2005; 57: 125–31.
7 Wiwanitkit V. Oral squamous cell carcinoma and 'chewing betel quid'. Int J Dent Hyg 2011; 9: 308.
8 Akhtar S, Sheikh AA, Qureshi HU. Chewing areca nut, betel quid, oral snuff, cigarette smoking and the risk of oesophageal squamous-cell carcinoma in South Asians: A multicentre case-control study. Eur J Cancer 2012; 48: 655–61.
9 Tung TH, Chiu YH, Chen LS, Wu HM, Boucher BJ, Chen TH. A population based study of the association between areca nut chewing and type 2 diabetes mellitus in men (Keelung Community-based Integrated Screening programme No 2). Diabetologia 2004; 47: 1776–81.
10 Yen AM, Chiu YH, Chen LS, Wu HM, Huang CC, Boucher BJ, *et al*. A population-based study of the association between betel-quid chewing and the metabolic sydrome in men. Am J Clin Nutr 2006; 83: 1153–60.
11 Hsu HF, Tsou TC, Chao HR, Shy CG, Kuo YT, Tsai FY, *et al*. Effects of arecoline on adipogenesis, lipolysis, and glucose uptake of adipocytes-A possible role of betel-quid chewing in metabolic syndrome. Toxicol Appl Pharmacol 2010; 245: 370–7.
12 Hsieh TJ, Hsieh PC, Wu MT, Chang WC, Hsiao PJ, Lin KD, *et al*. Betel nut extract and arecoline block insulin signaling and lipid storage in 3T3-L1 adipocytes. Cell Biol Toxicol 2011; 7: 397–411.
13 Yao QX, Wang G, Zhang W, Zhou SH, Ling HY, Hu B. Arecoline improved glucose and lipid metabolism in type 2 diabetic rats. Chin Phamacol Bull 2009; 25: 1177–81.
14 Qi ZY, Wang G, Zhang W, Zhou SH, Ling HY, Hu B. Effect of arecoline on PDX-1 mRNA expression in rats with type 2 diabetes mellitus. Int J Pathol Clin Med 2010; 30: 14–9.
15 Cheng Y, Ndisang JF, Tang G, Cao K, Wang R. Hydrogen sulfide induced relaxation of resistance mesenteric artery beds of rats. Am J Physiol Heart Circ Physiol 2004; 287: H2316–H2323.
16 Stipanuk MH. Sulfur amino acid metabolism: pathways for production and removal of homocysteine and cysteine. Annu Rev Nutr 2004; 24: 539–77.
17 Zhang W, Zhou SH, Ling HY, Yao QX, Qi ZQ, Wang G, *et al*. Arecoline repressed inflammation factor expression of macrophages stimulated by oxidized low density lipoprotein and its mechanism. Chin J Arterioscler 2009; 17: 269–72.
18 Zhao W, Zhang J, Lu Y, Wang R. The vasorelaxant effect of H(2)S as a novel endogenous gaseous K(ATP) channel opener. EMBO J 2001; 20: 6008–16.
19 Siebert N, Cantré D, Eipel C, Vollmar B. H2S contributes to the hepatic arterial buffer response and mediates vasorelaxation of the hepatic artery via activation of K(ATP) channels. Am J Physiol Gastrointest Liver Physiol 2008; 295: G1266–G1273.
20 Goto H, Tanaka N, Tanigawa K, Shimada Y, Itoh T, Terasawa K. Endothelium-dependent vasodilator effect of extract prepared from the seeds of areca catechu on isolated rat aorta. Phytother Res 1997; 11: 457–9.
21 Hwang IS, Ho H, Hoffman BB, Reaven GM. Fructose induced insulin resistance and hypertension in rats. Hypertension 1987; 10: 512–6.
22 Zhang L, Min D, Chen LM, Xuan ZH. Establishment of a rat model with insulin-resistant fatty liver induced by high-fat and high-sucrose emulsion. Chin Pharma Bull 2009; 25: 825–8.
23 Li GW, Pan XR. A new insulin-sensivity index for the population-based study. Chin J Int Med 1993; 32: 656–60.
24 Ling HY, Hu B, Wang BX, Zu XY, Feng SD, Ou HS, *et al*. Effects of rosiglitazone on the proliferation of vascular smooth muscle cell induced by high glucose. Cardiovasc Drugs Ther 2008; 22: 453–60.
25 Ling HY, Ou HS, Feng SD, Zhang XY, Tuo QH, Chen LX, *et al*. Changes in microRNA profile and effects of miR-320 in insulin-resistant 3T3-L1 adipocytes. Clin Exp Pharmacol Physiol 2009; 38: e32–39.
26 Shibuya N, Mikami Y, Kimura Y, Nagahara N, Kimura H. Vascular endothelium expresses 3-mercaptopyruvate sulfurtransferase and produces hydrogen sulfide. J Biochem 2009; 146: 623–6.
27 Wang Y, Zeng FH, Long CL, Pan ZY, Cui WY, Wang RH, *et al*. The novel ATP-sensitive potassium channel opener iptakalim prevents insulin resistance associated with hypertension via restoring endothelial function. Acta Pharmacol Sin 2011; 32: 1466–74.
28 Kim JA, Montagnani M, Koh KK, Quon MJ. Reciprocal relationships between insulin resistance and endothelial dysfunction: molecular and pathophysiological mechanisms. Circulation 2006; 113: 1888–904.
29 Xu SJ, Chen YJ, Zhou XG, Li GL. Synergic effects of synthesis arecoline in combination with snail-killing drugs niclosamide. Chinese Journal of Schistosomiasis Control. Zhonghua Yu Fang Yi Xue Za Zhi 2006; 40: 253–6.
30 Chandra JN, Malviya M, Sadashiva CT, Subhash MN, Rangappa KS. Effect of novel arecoline thiazolidinones as muscarinic receptor 1 agonist in Alzheimer's dementia models. Neurochem Int 2008; 52: 376–83.
31 Shan LM ,Zhang JC, Zhao YL, Cui WY, Wang H. Molecular mechanisms for arecoline against atherosclerosis. Chin Pharma Bull 2004; 20: 146–51.
32 Jaiswal N, Lambrecht G, Mutschler E , Tacke R , Malik KU. Pharmacological characterization of the vascular muscarinic receptors mediating relaxation and contraction in rabbit aorta. J Pharmacol Exp Ther1991; 258: 842–50.
33 Kuo FC, Wu DC, Yuan SS, Hsiao KM, Wang YY, Yang YC, *et al*. Effects of arecoline in relaxing human umbilical vessels and inhibiting endothelial cell growth. J Perinat Med 2005; 33: 399–405.
34 Tseng SK, Chang MC, Su CY, Chi LY, Chang JZ, Tseng WY, *et al*. Arecoline induced cell cycle arrest, apoptosis, and cytotoxicity to human endothelial cells. Clin Oral Investig 2011. DOI: 10.1007/s00784-011-0604-1.

Acta Pharmacologica Sinica (2012) 33: 1030–1036
 1671-4083/12 $32.00
www.nature.com/aps

Original Article

Calcium mediates high glucose-induced HIF-1α and VEGF expression in cultured rat retinal Müller cells through CaMKII-CREB pathway

Jun LI[1, #], Shu-zhi ZHAO[1, #], Pei-pei WANG[2], Song-ping YU[2], Zhi ZHENG[1], Xun XU[1, *]

[1]*Department of Ophthalmology, Shanghai First People's Hospital Affiliated Shanghai Jiao Tong University, Shanghai 200080, China;*
[2]*Department of Ophthalmology, Lishui City Center Hospital, Lishui 323000, China*

Aim: To investigate the effects of high glucose (HG) medium on expression of hypoxia-inducible factor-1α (HIF-1α) and vascular endothelial growth factor (VEGF) in cultured rat retinal Müller cells and to determine the signaling pathways mediating the effects.
Methods: Primary cultures of retinal Müller cells were prepared from Sprague-Dawley rats, and incubated in a medium containg HG (30 mmol/L) in the presence of the membrane-permeable Ca^{2+} chelator BAPTA-AM (10 μmol/L) or the CaMKII inhibitor KN93 (10 μmol/L). The levels of CaMKII, p-CaMKII, CREB, p-CREB, HIF-1α, and VEGF proteins were measured with Western blotting, while HIF-1á and VEGF mRNA levels were determined using real-time RT-PCR.
Results: The stimulation of retinal Müller cell with HG for 24 h remarkably increased the expression levels of HIF-1α and VEGF. These responses were significantly inhibited in the presence of BAPTA-AM or KN93. Both BAPTA-AM and KN93 also significantly inhibited HG-induced phosphorylation of CaMKII and CREB in the cultured retinal Müller cells. Transfection of the cultured retinal Müller cells with antisense CREB oligonucleotide (300 nmol/L) was similarly effective in blocking the HG-induced increase of HIF-1α and VEGF.
Conclusion: HG-induced HIF-1α and VEGF expression in cultured rat retinal Müller cells depends on intracellular free Ca^{2+} and activation of CaMKII-CREB pathway. The activation of CaMKII-CREB pathway by HG may be a possible mechanism underlying the pathogenesis of diabetic retinopathy.

Keywords: diabetic retinopathy; hyperglycemia; retinal Müller cells; intracellular Ca^{2+}; CaMKII; CREB

Acta Pharmacologica Sinica (2012) 33: 1030–1036; doi: 10.1038/aps.2012.61; published online 16 Jul 2012

Introduction

Hyperglycemia is a pathological hallmark of diabetic complications, such as diabetic retinopathy (DR), and hyperglycemia can also increase the intracellular free calcium concentration ($[Ca^{2+}]_i$) in various cell types[1–4]. An increase in $[Ca^{2+}]_i$ has been shown to play an important role in the pathogenesis of angiogenesis[5, 6], which is the most common cause of blindness in DR. Vascular endothelial growth factor (VEGF) is one of the most potent angiogenic factors produced by retinal ischemia[7]. In addition, VEGF secretion is mediated by elevated $[Ca^{2+}]_i$ in the retina[8–11]. Preventing cellular $[Ca^{2+}]_i$ overload has also been demonstrated as a new pathogenic mechanism in the treatment of diabetic complications such as retinopathy[12]. Thus, as a critical intracellular second messenger, Ca^{2+} may play an important role in high glucose (HG)-induced angiogenesis in DR, but the downstream signaling pathways through which Ca^{2+} signals are mediated remain unknown.

Ca^{2+}/CaM-dependent protein kinase II (CaMKII), a multifunctional serine/threonine protein kinase that catalyzes the phosphorylation of myriad eukaryotic proteins, is highly sensitive to the frequency of Ca^{2+} oscillations and plays an important role in translating changes in $[Ca^{2+}]_i$ into changes in cell function[13]. Activated CaMKII in turn initiates a signaling cascade leading to the phosphorylation of the cAMP response element binding protein (CREB) transcription factor on Ser-133[14]. Phospho-activated CREB (p-CREB) induces target gene expression and regulates various neuronal functions[15]. A recent study also demonstrated that CREB is crucial for promoting prostate cancer bone metastasis by inducing VEGF expression through HIF-1-dependent signaling[16], implicating a (high) glucose-$[Ca^{2+}]_i$-CaMKII-CREB-VEGF signaling cascade in DR-associated angiogenesis.

In the retina, VEGF is mainly expressed in the Müller

# These authors contributed equally to this work.
* To whom correspondence should be addressed.
E-mail drxuxun@sjtu.edu.cn
Received 2012-03-05 Accepted 2012-04-28

cells[17]. The present study aimed to elucidate the effects of $[Ca^{2+}]_i$ on HG-induced HIF-1α and VEGF expression in retinal Müller cells *in vitro*. Prolonged HG increased CaMKII and CREB phospho-activation, further inducing HIF-1α and VEGF expression. The blockade of HIF-1α and VEGF expression by calcium chelators and CaMKII inhibitors suggests that the $[Ca^{2+}]_i$-CaMKII-CREB signaling pathway may contribute to the pathogenesis of DR.

Materials and methods

This study conformed to the Guide for the Care and Use of Laboratory Animals published by the US National Institutes of Health (NIH Publication No 85–23, revised 1996) and was carried out with the approval of the local ethics committee/institutional board. All chemicals were of reagent grade and purchased from Sigma Chemicals (St Louis, MO, USA), unless otherwise stated.

Cell culture

Primary cultures of retinal Müller cells were prepared from 5 to 7-d-old Sprague-Dawley rats (purchased from the Shanghai Laboratory Animal Center of the Chinese Academy of Sciences) following a previously described protocol[18] , with some modifications. Briefly, enucleated eyes were washed under sterile conditions, and the anterior portions were discarded. The retinas were isolated, chopped into 1×1 mm fragments, treated with 0.1% trypsin at 37 °C for 20 min, and then passed through mesh to remove any large retinal pieces. The strained isolates were centrifuged at 800 r/min for 5 min, and the supernatant fluid was removed. The precipitated cells were resuspended and seeded in the plastic culture flask containing Dulbecco's modified Eagle's medium (DMEM) supplemented with 2 mmol/L glutamine, 0.1% penicillin/streptomycin and 10% fetal calf serum (FBS). The cultures were maintained in 5% CO_2 at 37 °C. The medium was routinely replaced every 3–4 d. After 8–10 d, pure Müller cells became confluent and were used for experiments.

Immunocytochemistry

Cultured rat Müller cells were fixed with 4% paraformaldehyde and blocked with 2% BSA in PBS containing 0.3% Triton X-100. Slides were incubated overnight in a humidified chamber at 4 °C with anti-glutamine synthetase (GS) and anti-vimentin primary antibodies (1:1000 dilution). After primary antibody incubation, cells were washed three times with PBS for 10 min each and incubated in the appropriate fluorescent conjugated secondary antibody (goat anti-mouse IgG, 1:200) for 1 h. The cells were counterstained with DAPI. Images were captured with a fluorescence microscope (Olympus, Tokyo, Japan).

Transfection of Müller cells with antisense CREB oligonucleotides

The CREB antisense oligonucleotide synthesis and transfection were conducted as previously described[19]. The CREB antisense oligonucleotide sequence was 5′-TGGTCATCTAGTCACCGGTG-3′, and the corresponding sense oligonucleotide sequence was 5′-CACCGGTGACTAGATGACCA-3′. After transfection with the antisense or sense oligonucleotide for 24 h, the medium was removed from the cells, serum-free DMEM with NG was added, and the cells were allowed to recover for 30 min. The transfected Müller cells were washed once with serum-free DMEM and then growth-arrested for 24 h in the same medium supplemented with either NG (5.5 mmol/L) or HG (30 mmol/L).

Qualitative real-time RT-PCR analysis

To measure HIF-1α and VEGF mRNA expression by qualitative real-time RT-PCR, total cellular RNA was extracted from retinal Müller cells with Trizol Reagent (Invitrogen Life Technologies, Shanghai, China) and stored at -80 °C. A quantitative polymerase chain reaction (qPCR) kit (DyNAmo Flash SYBR Green; Finnzymes Oy, Espoo, Finland) was used according to the manufacturer's instructions. The primer sequences (sense/antisense) used were as follows: HIF-1α, 5′-GACAATAGCTTCGCAGAATGC-3′/5′-TCGTAACTGGTCAGCTGTGG-3′; and VEGF, 5′-AATGATGAAGCCCTGGAGTG -3′/5′-AATGCTTTCTCCGCTCTGAA-3′. The specificity of the amplification product was determined by melting curve analysis. Standard curves were generated for each gene by preparing serial dilutions of the respective cDNA templates. The relative quantities of each gene were obtained by normalizing the signals to β-actin (5′-CGACAACGGCTCCGGCATGT-3′/5′-GGGGCCACACGCAGCTCATT-3′), and each experiment was repeated independently at least three times.

Western blot analysis

Approximately 3×10^6 retinal Müller cells were harvested and lysed in lysis buffer containing 1% NP-40, 10 mmol/L Tris, 200 mmol/L NaCl, 5 mmol/L EDTA, and 10% glycerol plus protease inhibitors (pH 7.0). Lysates from treated cells were centrifuged at 12000 r/min for 20 min at 4 °C, and the cleared supernatants were collected. The protein concentration in the supernatant was measured using the Bio-Rad (Hercules, CA, USA) DC protein assay. A 30-μg aliquot of protein from each sample was subjected to electrophoresis on 10% SDS-PAGE using a Bio-Rad miniature slab gel apparatus. Separated proteins were electrophoretically transferred onto nitrocellulose membranes. The membranes were blocked with 5% nonfat dried milk solution and incubated overnight with partially purified rabbit anti-CaMKII and anti-phosphoThr-286-CaMKII polyclonal antibody (Abcam; 1:500), rabbit anti-CREB and mouse anti-phospho-CREB polyclonal antibody at Ser-133 (Abcam; 1:500), rabbit anti-HIF-1α polyclonal antibody (Santa Cruz Biotechnology; 1:500), and rabbit anti-VEGF polyclonal antibody (Abcam; 1:500). The expression of β-actin (monoclonal anti-β-actin; Santa Cruz Biotechnology; 1:1000) was used as an internal control to confirm equivalent protein loading per gel lane. The immunopositive bands were visualized by the ECL system (Amersham Biosciences, Buckinghamshire, England). Each experiment was performed at least in triplicate.

Statistical analysis

Experimental data are expressed as the mean±SD. Group means were compared by one-way ANOVA followed by the Dunnett *post hoc* test using GraphPad Prism 4.0 (San Diego, CA) and SPSS (Statistical Package for the Social Sciences) 13.0 for Windows (SPSS, Chicago, IL). A value of $P<0.05$ was considered significant in all cases.

Results

Immunocytochemical characterization of cultured retinal Müller cells

The identities of the cultured rat retinal Müller cells were confirmed by immunocytochemistry using antibodies against the Müller cell markers GS and vimentin. Nuclei were stained with DAPI. Almost all cells were positive for GS and vimentin (Figures 1A–1D), indicating that the primary cultures were Müller cells.

Calcium mediates HG-induced HIF-1α and VEGF expression

Intracellular Ca^{2+} signals alter gene expression patterns by activating several nuclear transcription factors[20]. To explore the effects of $[Ca^{2+}]_i$ on HG-induced gene expression in Müller cells, we analyzed the expression of HIF-1α and VEGF. *In vitro* hyperglycemia (30 mmol/L, HG) for 24 h upregulated the expression of HIF-1α and VEGF at both the mRNA and protein levels. Furthermore, the upregulation of HIF-1α and VEGF was most likely caused by increased $[Ca^{2+}]_i$, at least in part, because the Ca^{2+} chelator BAPTA-AM blocked this enhanced expression, while the general Ca^{2+} ionophore A23187 upregulated HIF-1α and VEGF expression in Müller cells in NG (Figures 2A–2D). Summary data for these experi-

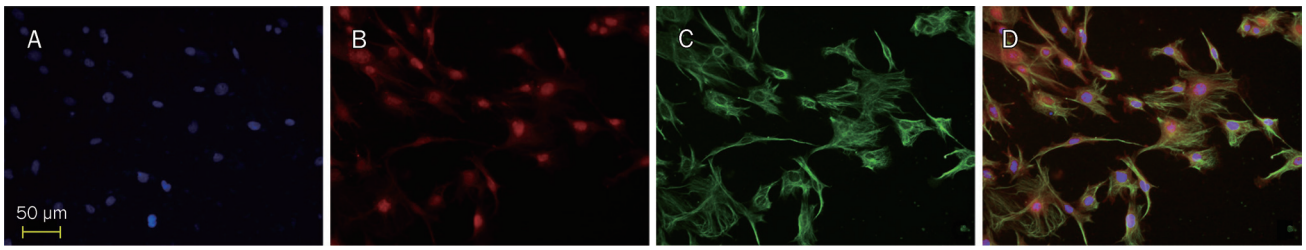

Figure 1. Immunocytochemical analysis of primary Müller cell cultures. Blue: nuclear staining with DAPI (A). Red: Müller cell marker GS (B). Green: Müller cell marker vimentin (C). Merged labeling of GS, vimentin and DAPI (D).

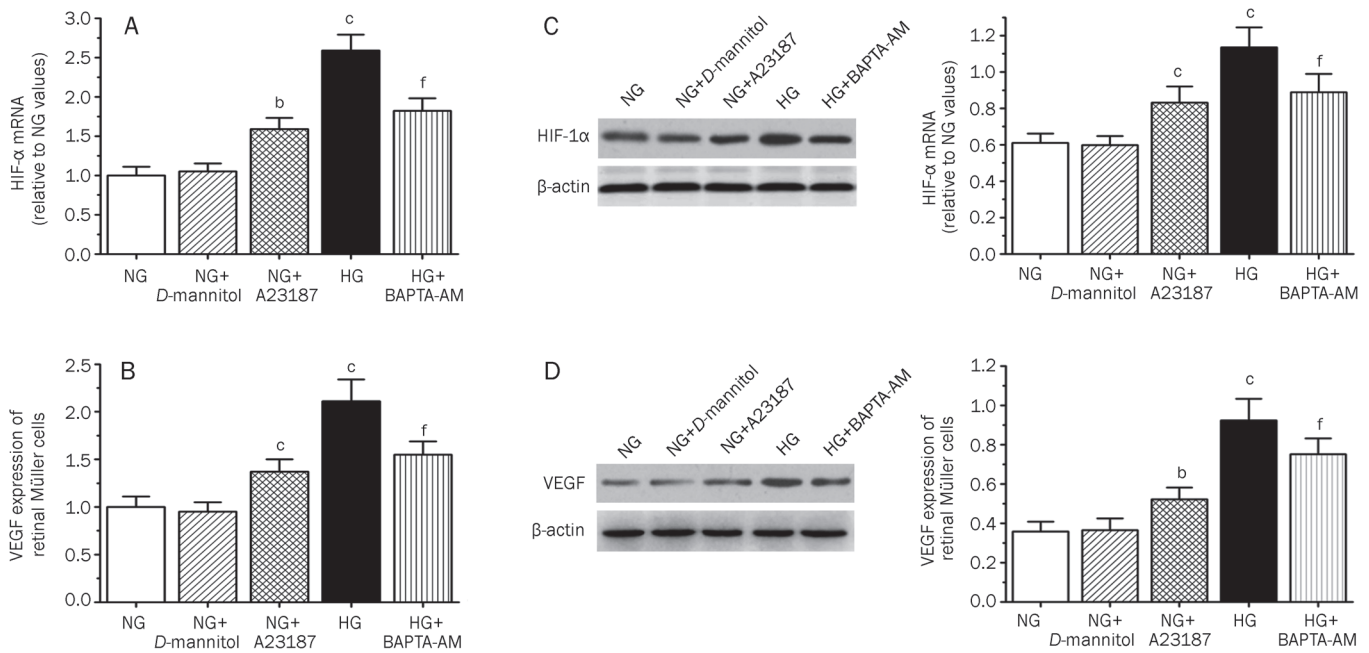

Figure 2. Hyperglycemia induced $[Ca^{2+}]_i$-dependent HIF-1α and VEGF Expession. (A, B) HIF-1α and VEGF mRNA in retinal Müller cells cultured in serum-free DMEM containing normal glucose (NG, 5.5 mmol/L), NG+*D*-mannitol (24.5 mmol/L), high glucose (HG, 30 mmol/L), or HG in the presence of BAPTA-AM (10 μmol/L) (HG+BAPTA-AM) or NG in the presence of A23187 (1 μmol/L) (NG+A23187) for 24 h was quantified by using real time RT-PCR. Results are expressed (relative to the NG values). (C, D) Western blot analysis of HIF-1α and VEGF protein expression in retinal Müller cells incubated in the five groups for 24 h. Equal protein loading was confirmed with the β-actin antibody. Mean±SD from nine cells per group. $^bP<0.05$, $^cP<0.01$ *vs* NG or NG+*D*-mannitol. $^fP<0.01$ *vs* HG.

ments show that HG can enhance the expression of HIF-1α and VEGF and that this effect may be mediated by increased $[Ca^{2+}]_i$ *in vitro*.

HG-induced $[Ca^{2+}]_i$-dependent Serine/Threonine phosphorylation of CaMKII and CREB

Activation of the transcription factor CREB is known to orchestrate a number of signaling and gene expression pathways involved in angiogenesis[21, 22]. The following experiments were performed to examine the downstream signaling pathway(s) through which $[Ca^{2+}]_i$ signals mediated cellular responses, particularly the upregulation of the angiogenic factors HIF-1α and VEGF.

To determine whether HG can induce the threonine phosphorylation of CaMKII (p-CaMKII) and the serine phosphorylation of CREB (p-CREB), retinal Müller cells were incubated for 24 h in serum-free DMEM containing NG, NG+*D*-mannitol, NG+A23187, HG, or HG+BAPTA-AM. As shown in Figure 3, there was no significant threonine phosphorylation of CaMKII or serine phosphorylation of CREB after incubation in NG or NG+*D*-mannitol, indicating that neither NG nor hyperosmolarity induced CaMKII or CREB phosphorylation (at the sites recognized by the antibodies). In contrast, both HG and NG plus A23187 induced a significant increase in CaMKII threonine phosphorylation and CREB serine phosphorylation. In addition, the HG-induced upregulation of p-CaMKII and p-CREB was blocked by the cell permeant Ca^{2+} chelator BAPTA-AM, suggesting that HG promotes the phospho-activation of CaMKII and CREB, possibly by increasing $[Ca^{2+}]_i$.

HG activated CREB through a CaMKII-dependent pathway

To investigate the possible role of CaMKII in CREB phosphorylation, these experiments were repeated in the presence of the CaMKII inhibitor KN93 (10 μmol/L) and the inactive analog KN92 (10 μmol/L). As shown in Figure 4, the incubation of retinal Müller cells with KN93 (but not KN92) partially reversed the HG-induced increase in CREB phosphorylation. These results indicated that CaMKII was involved in the HG-induced activation of CREB.

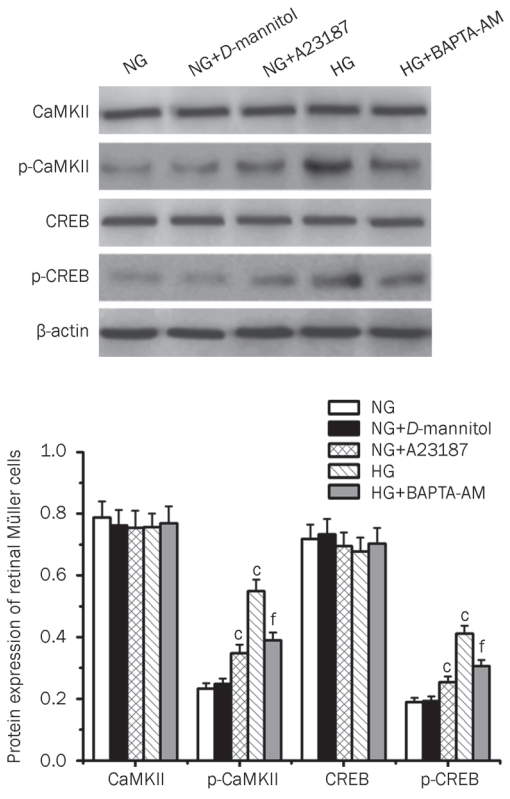

Figure 3. Determination of CaMKII, phosphorylation of CaMKII (p-CaMKII), CREB, and phosphorylation of CREB (p-CREB) levels. Western blot analysis of p-CaMKII, CaMKII, p-CREB, and CREB protein expression in retinal Müller cells incubated in serum-free medium containing NG, NG+D-mannitol (24.5 mmol/L), NG+A23187 (1 μmol/L), HG, HG+BAPTA-AM (10 μmol/L) for 24 h. Equal protein loading was confirmed with the β-actin antibody. Mean±SD from nine cells per group. $^cP<0.01$ *vs* NG or NG+D-mannitol. $^fP<0.01$ *vs* HG.

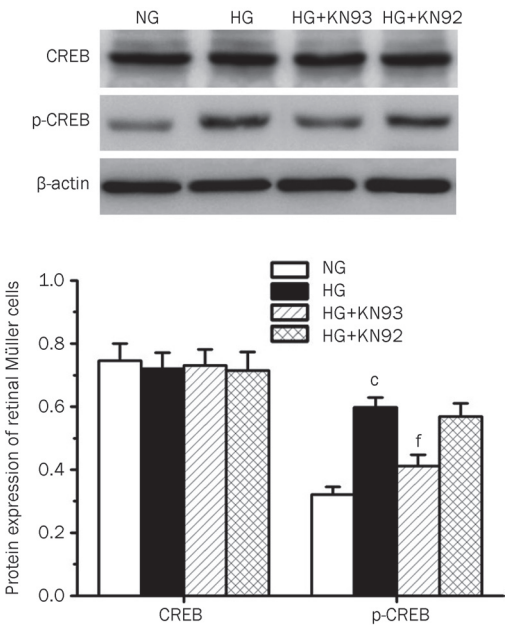

Figure 4. Hyperglycemia induced CaMKII-dependent CREB phosphorylation (p-CREB). Western blot analysis of p-CREB and CREB protein expression in retinal Müller cells incubated in serum-free medium containing NG, HG, HG+KN93 (10 μmol/L), HG+KN92 (10 μmol/L) for 24 h. Equal protein loading was confirmed with the β-actin antibody. Mean±SD from nine cells per group. $^cP<0.01$ *vs* NG. $^fP<0.01$ *vs* HG.

CREB antisense oligonucleotides inhibits CREB expression in retinal Müller cells in NG

As shown in Figure 5, CREB antisense oligonucleotides (CREB ASO) inhibited CREB expression in a dose-dependent manner in retinal Müller cells in NG.

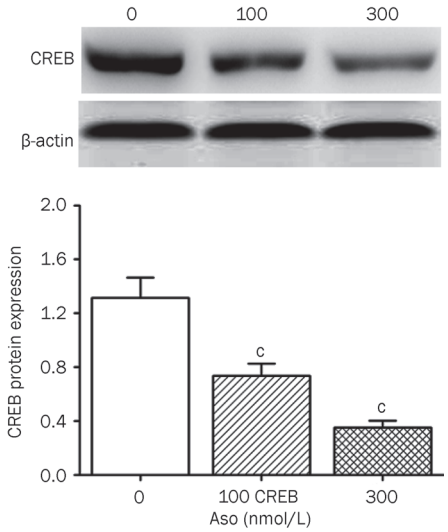

Figure 5. Effect of CREB antisense oligonucleotides on CREB. Western blot analysis of CREB protein expression in retinal Müller cells cultured in serum-free DMEM containing NG in the presence of CREB antisense oligonucleotides (0, 100, and 300 nmol/L) for 24 h. Equal protein loading was confirmed with the β-actin antibody. Mean±SD from nine cells per group. $^{c}P<0.01$ compared to the value without CREB antisense oligonucleotides.

Suppression of CaMKII and CREB expression decreases HG-induced HIF-1α and VEGF overexpression

To test whether CaMKII and CREB activation are required for the HG-induced upregulation of HIF-1α and VEGF expression, we examined the effects of a CaMKII specific inhibitor (KN93) and the effects of the CREB antisense oligonucleotide. We found that both treatments significantly inhibited HG-induced HIF-1α and VEGF mRNA and protein synthesis in retinal Müller cells (Figures 6A, 6B), again suggesting that the activation of CaMKII/CREB signaling may be necessary for HG-induced HIF-1α and VEGF synthesis.

Discussion

DR is a major cause of blindness in working-age individuals in developed countries[23], and aberrant angiogenesis is a central pathogenic event in the growth and progression of this disease. It has been reported that hyperglycemia-induced oxidative stress plays an important role in pathogenic retinal neovascularization and growth factor expression[24]. HIF-1 is a key oxygen sensor and mediator that regulates multiple target genes, such as VEGF, which is a key pro-angiogenic factor in DR[25, 26]. Over the past decade, almost all retinal cells have been shown to express HIF-1α and VEGF in DR. In this context, recent studies using conditional KO mice models have suggested that the Müller cell-derived HIF-1α and VEGF has a causative role in the major pathologic changes in DR[27, 28].

Increasing evidence suggests that hyperglycemia induces changes in the retinal $[Ca^{2+}]_i$ dynamics[2, 4], which have been associated with distinct pathological processes, such as DR. Here, using retinal Müller cells cultured *in vitro*, we have

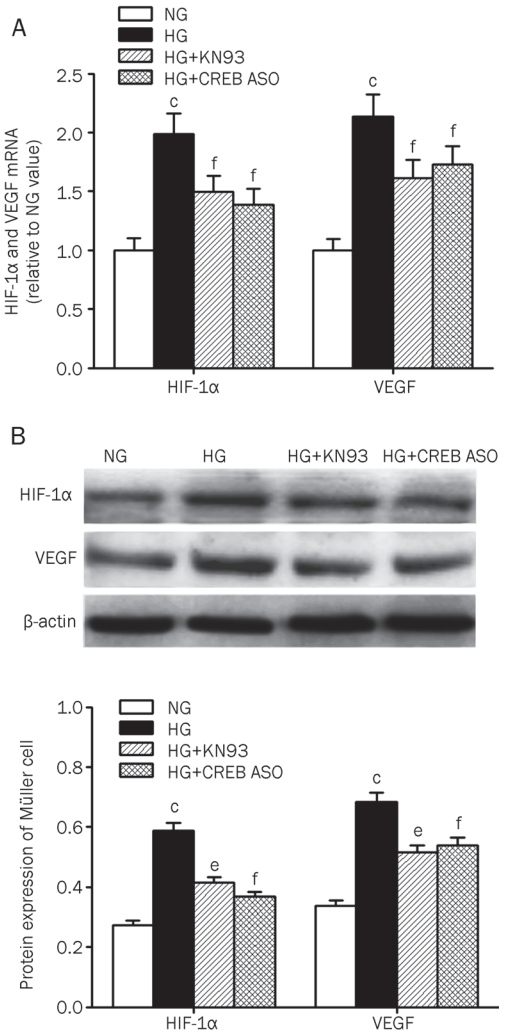

Figure 6. Hyperglycemia induced HIF-1α and VEGF expession through CaMKII/CREB pathway activation. (A) HIF-1α and VEGF mRNA in retinal Müller cells cultured in serum-free DMEM containing NG, HG, HG+KN93 (10 μmol/L) or HG in the presence of CREB antisense oligonucleotides (300 nmol/L) for 24 h was quantified by using real time RT-PCR. Results are expressed (relative to the NG values). (B) Western blot analysis of HIF-1α and VEGF protein expression in retinal Müller cells incubated in the four groups for 24 h. Equal protein loading was confirmed with the β-actin antibody. Mean±SD from nine cells per group. $^{c}P<0.01$ *vs* NG. $^{e}P<0.05$, $^{f}P<0.01$ *vs* HG.

demonstrated that the increased $[Ca^{2+}]_i$ is associated with aberrant HG-induced expression of HIF-1α and VEGF because increased $[Ca^{2+}]_i$ is an ubiquitous signal controlling gene expression[9, 10, 29, 30]. We evaluated HG-induced HIF-1α and VEGF expression in the presence of pharmacologic inhibitors of Ca^{2+} signaling. The calcium chelators BAPTA-AM significantly reduced the production of HIF-1α and VEGF in response to HG, while the Ca^{2+} ionophore A23187 significantly increased HIF-1α and VEGF expression in the presence of normal glucose. These results suggest that elevated $[Ca^{2+}]_i$ in retinal Müller cells can enhance HIF-1α expression, possibly triggering VEGF production.

Many of the cellular responses to Ca^{2+} are modulated by the CaMKs, among which CaMKII acts as a decoder of oscillating Ca^{2+} signals[31]. Previous reports demonstrated that the autophosphorylation of CaMKII is highly expressed in neurons, regulating the cell cycle and transcription[32], and the effects of CaMKII were mediated by CREB phosphorylation and CREB-dependent transcription. In the present work, we show that HG-induced phosphorylation of CREB is inhibited in retinal Müller cells treated with the CaMKII inhibitor KN93 but not with its inactive analog KN92. A recent report is consistent with our findings that the CREB protein is an intracellular serine kinase that can be directly activated by CaMKII in the retina through serine-133 phosphorylation[33]. However, there are very few studies investigating the downstream effects of the CaMKII-CREB pathway in retinal Müller cells. Therefore, we designed these experiments to examine the role of this pathway in the transduction of Ca^{2+} signals in Müller cells. Both HG and A23187 activated the CaMKII-CREB pathway and upregulated the expression of HIF-1a and VEGF in retinal Müller cells, while the chelation of calcium by BAPTA-AM partially blocked the upregulated expression of p-CaMKII/p-CREB. In addition, real time RT-PCR and Western blot experiments indicated that both the CaMKII inhibitor KN93 and a CREB antisense oligonucleotide blocked the HG-induced expression of HIF-1α and VEGF, suggesting that activation of the CaMKII-CREB pathway might be necessary for the HG-induced upregulation of HIF-1α and VEGF. Collectively, these results strongly suggest that CaMKII-CREB may act as a key signaling pathway in the transduction of upstream Ca^{2+} signals into downstream gene expression after HG stimulation. Our results also support the hypothesis that CaMKII plays a role in the Ca^{2+}-mediated transcriptional regulation of genes through the phosphorylation of CREB to mediate a survival response in retinal ganglion cells[34] because HIF-1α and VEGF could directly protect neurons from neuroexcitotoxicity.

In summary, our results demonstrate that calcium contributes to HG-induced expression of the major angiogenic factors HIF-1α and VEGF in retinal Müller cells and that this response is mediated by activation of the CaMKII-CREB pathway. Calcium increase may be responsible for the hyperglycemia-induced increase in the activation of retinal Müller cells and enhanced angiogenesis in patients with diabetic retinopathy. Conversely, suppressing this pathway may be a useful strategy for novel treatments to prevent visual impairment and blindness in patients with DR.

Acknowledgements

The authors thank Nian-ting TONG, Yan XU, and Qing GU for excellent technical assistance throughout the project. This work was supported by the National Natural Science Foundation of China (No 30872828) and the Opening Project of Shanghai Key Laboratory of Fundus Diseases (No 07Z22911).

Author contribution

Jun LI and Shu-zhi ZHAO performed the experiments and wrote the paper; Pei-pei WANG and Song-ping YU performed the experiments and analyzed the data; and Zhi ZHENG and Xun XU designed the study.

References

1 Bishara NB, Ding H. Glucose enhances expression of TRPC1 and calcium entry in endothelial cells. Am J Physiol Heart Circ Physiol 2010; 298: H171–8.
2 Pereira Tde O, da Costa GN, Santiago AR, Ambrosio AF, dos Santos PF. High glucose enhances intracellular Ca^{2+} responses triggered by purinergic stimulation in retinal neurons and microglia. Brain Res 2010; 1316: 129–38.
3 Symonian M, Smogorzewski M, Marcinkowski W, Krol E, Massry SG. Mechanisms through which high glucose concentration raises $[Ca^{2+}]_i$ in renal proximal tubular cells. Kidney Int 1998; 54: 1206–13.
4 Santiago AR, Rosa SC, Santos PF, Cristovao AJ, Barber AJ, Ambrosio AF. Elevated glucose changes the expression of ionotropic glutamate receptor subunits and impairs calcium homeostasis in retinal neural cells. Invest Ophthalmol Vis Sci 2006; 47: 4130–7.
5 Kohn EC, Alessandro R, Spoonster J, Wersto RP, Liotta LA. Angiogenesis: role of calcium-mediated signal transduction. Proc Natl Acad Sci U S A 1995; 92: 1307–11.
6 Kim JH, Yu YS, Kim DH, Lee TG, Moon DW, Kim KW. *In situ* calcium mapping in the mouse retina via time-of-flight secondary ion mass spectrometry: modulation of retinal angiogenesis by calcium ion in development and oxygen-induced retinopathy. Biochem Cell Biol 2008; 86: 459–67.
7 Gariano RF, Gardner TW. Retinal angiogenesis in development and disease. Nature 2005; 438: 960–6.
8 Koyama Y, Matsuzaki S, Gomi F, Yamada K, Katayama T, Sato K, *et al*. Induction of amyloid beta accumulation by ER calcium disruption and resultant upregulation of angiogenic factors in ARPE19 cells. Invest Ophthalmol Vis Sci 2008; 49: 2376–83.
9 Cordeiro S, Seyler S, Stindl J, Milenkovic VM, Strauss O. Heat-sensitive TRPV channels in retinal pigment epithelial cells: regulation of VEGF-A secretion. Invest Ophthalmol Vis Sci 2010; 51: 6001–8.
10 Swiatek-De Lange M, Stampfl A, Hauck SM, Zischka H, Gloeckner CJ, *et al*. Membrane-initiated effects of progesterone on calcium dependent signaling and activation of VEGF gene expression in retinal glial cells. Glia 2007; 55: 1061–73.
11 Rosenthal R, Heimann H, Agostini H, Martin G, Hansen LL, Strauss O. Ca^{2+} channels in retinal pigment epithelial cells regulate vascular endothelial growth factor secretion rates in health and disease. Mol Vis 2007; 13: 443–56.
12 Zhang B, Ma JX. SERPINA3K prevents oxidative stress induced necrotic cell death by inhibiting calcium overload. PLoS One 2008; 3: e4077.
13 De Koninck P, Schulman H. Sensitivity of CaM kinase II to the frequency of Ca^{2+} oscillations. Science 1998; 279: 227–30.
14 Mayr B, Montminy M. Transcriptional regulation by the phosphorylation-dependent factor CREB. Nat Rev Mol Cell Biol 2001; 2: 599–609.]
15 Lonze BE, Ginty DD. Function and regulation of CREB family transcription factors in the nervous system. Neuron 2002; 35: 605–23.
16 Wu D, Zhau HE, Huang WC, Iqbal S, Habib FK, Sartor O, *et al*. cAMP-responsive element-binding protein regulates vascular endothelial growth factor expression: implication in human prostate cancer bone metastasis. Oncogene 2007; 26: 5070–7.
17 Pierce EA, Avery RL, Foley ED, Aiello LP, Smith LE. Vascular endothelial growth factor/vascular permeability factor expression in a mouse model of retinal neovascularization. Proc Natl Acad Sci U S A

1995; 92: 905–9.
18 Hicks D, Courtois Y. The growth and behaviour of rat retinal Muller cells *in vitro*. 1. An improved method for isolation and culture. Exp Eye Res 1990; 51: 119–29.
19 Hu H, Zhang R, Zhang Y, Xia Z, Hu Y. Role of CREB in the regulatory action of sarsasapogenin on muscarinic M1 receptor density during cell aging. FEBS Lett 2010; 584: 1549–52.
20 West AE, Chen WG, Dalva MB, Dolmetsch RE, Kornhauser JM, Shaywitz AJ, *et al*. Calcium regulation of neuronal gene expression. Proc Natl Acad Sci U S A 2001; 98: 11024–31.
21 Torii S, Okamura N, Suzuki Y, Ishizawa T, Yasumoto K, Sogawa K. Cyclic AMP represses the hypoxic induction of hypoxia-inducible factors in PC12 cells. J Biochem 2009; 146: 839–44.
22 Dobroff AS, Wang H, Melnikova VO, Villares GJ, Zigler M, Huang L, *et al*. Silencing cAMP-response element-binding protein (CREB) identifies CYR61 as a tumor suppressor gene in melanoma. J Biol Chem 2009; 284: 26194–206.
23 Ferris FL, 3rd, Davis MD, Aiello LM. Treatment of diabetic retinopathy. N Engl J Med 1999; 341: 667–78.
24 Kowluru RA, Tang J, Kern TS. Abnormalities of retinal metabolism in diabetes and experimental galactosemia. VII. Effect of long-term administration of antioxidants on the development of retinopathy. Diabetes 2001; 50: 1938–42.
25 Ke Q, Costa M. Hypoxia-inducible factor-1 (HIF-1). Mol Pharmacol 2006; 70: 1469–80.
26 Semenza GL. Hypoxia-inducible factor 1 (HIF-1) pathway. Sci STKE 2007; 2007: cm8.
27 Wang J, Xu X, Elliott MH, Zhu M, Le YZ. Muller cell-derived VEGF is essential for diabetes-induced retinal inflammation and vascular leakage. Diabetes 2010; 59: 2297–305.
28 Lin M, Chen Y, Jin J, Hu Y, Zhou KK, Zhu M, *et al*. Ischaemia-induced retinal neovascularisation and diabetic retinopathy in mice with conditional knockout of hypoxia-inducible factor-1 in retinal Muller cells. Diabetologia 2011; 54: 1554–66.
29 Hui AS, Bauer AL, Striet JB, Schnell PO, Czyzyk-Krzeska MF. Calcium signaling stimulates translation of HIF-alpha during hypoxia. FASEB J 2006; 20: 466–75.
30 Yuan G, Nanduri J, Bhasker CR, Semenza GL, Prabhakar NR. Ca^{2+}/calmodulin kinase-dependent activation of hypoxia inducible factor 1 transcriptional activity in cells subjected to intermittent hypoxia. J Biol Chem 2005; 280: 4321–8.
31 Soderling TR, Chang B, Brickey D. Cellular signaling through multifunctional Ca^{2+}/calmodulin-dependent protein kinase II. J Biol Chem 2001; 276: 3719–22.
32 Tombes RM, Grant S, Westin EH, Krystal G. G1 cell cycle arrest and apoptosis are induced in NIH 3T3 cells by KN-93, an inhibitor of CaMK-II (the multifunctional Ca2+/CaM kinase). Cell Growth Differ 1995; 6: 1063–70.
33 Takeda H, Kitaoka Y, Hayashi Y, Kumai T, Munemasa Y, Fujino H, *et al*. Calcium/calmodulin-dependent protein kinase II regulates the phosphorylation of CREB in NMDA-induced retinal neurotoxicity. Brain Res 2007; 1184: 306–15.
34 Fan W, Li X, Cooper NG. CaMKIIalphaB mediates a survival response in retinal ganglion cells subjected to a glutamate stimulus. Invest Ophthalmol Vis Sci 2007; 48: 3854–63.

Acta Pharmacologica Sinica (2012) 33: 1037–1046
 1671-4083/12 $32.00
www.nature.com/aps

Original Article

8-(Tosylamino)quinoline inhibits macrophage-mediated inflammation by suppressing NF-κB signaling

Yongwoo JUNG[1, #], Se Eun BYEON[1, #], Dae Sung YOO[2], Yong Gyu LEE[2], Tao YU[1], Yanyan YANG[1], Ji Hye KIM[1], Eunji KIM[1], Deok JEONG[1], Man Hee RHEE[3], Eui Su CHOUNG[4], Sungyoul HONG[1], Jae Youl CHO[1, *]

[1]Department of Genetic Engineering, Sungkyunkwan University, Suwon 440–746, Republic of Korea; [2]College of Biomedical Science, Kangwon National University, Chuncheon 200–701, Republic of Korea; [3]College of Veterinary Medicine, Kyungpook National University, Daegu 702–701, Republic of Korea; [4]DanjoungBio, Wonju 220–842, Republic of Korea

Aim: The macrophage-mediated inflammatory response may contribute to the development of cancer, diabetes, atherosclerosis and septic shock. This study was to characterize several new compounds to suppress macrophage-mediated inflammation.
Methods: Peritoneal macrophages from C57BL/6 male mice and RAW264.7 cells were examined. Anti-inflammatory activity was evaluated in the cells exposed to lipopolysaccharide (LPS). The mechanisms of the anti-inflammatory activity were investigated via measuring transcription factor activation in response to specific signals and via assaying the activities of the target kinases.
Results: Of 7 candidate compounds tested, 8-(tosylamino)quinoline (8-TQ, compound 7) exhibited the strongest activities in suppressing the production of NO, TNF-α, and PGE_2 in LPS-activated RAW264.7 cells and peritoneal macrophages (the IC_{50} values=1–5 μmol/L). This compound (1.25–20 μmol/L) dose-dependently suppressed the expression of the pro-inflammatory genes for iNOS, COX-2, TNF-α, and the cytokines IL-1β and IL-6 at the level of transcription in LPS-activated RAW264.7 cells. 8-TQ (20 μmol/L) significantly suppressed the activation of NF-κB and its upstream signaling elements, including inhibitor of κB (IκBα), IκBα kinase (IKK) and Akt in LPS-activated RAW264.7 cells. In *in vivo* experiments, oral administration of 20 and 40 mg/kg 8-TQ for 3 d significantly alleviated the signs of LPS-induced hepatitis and HCl/EtOH-induced gastritis, respectively, in ICR mice.
Conclusion: 8-TQ (compound 7) exerts significant anti-inflammatory activity through the inhibition of the Akt/NF-κB pathway, thus may be developed as a novel anti-inflammatory drug.

Keywords: 8-(tosylamino)quinoline; anti-inflammatory effect; lipopolysaccharide; macrophage; RAW264.7 cell; hepatitis; gastritis; NF-κB; Akt

Acta Pharmacologica Sinica (2012) 33: 1037–1046; doi: 10.1038/aps.2012.52; published online 16 Jul 2012

Introduction

Macrophages, the terminally differentiated progeny of monocytes, are characterized by cell-surface markers of the inflammatory response, including toll-like receptors (TLRs), the Fc receptor, and the complement receptor. Although macrophages function primarily as phagocytes and antigen-presenting cells, they may also activate other immuno-regulatory cells, including neutrophils and T- and B-lymphocytes[1, 2], through the production of pro-inflammatory cytokines, such as interleukins (ILs) and tumor necrosis factor (TNF)-α; chemokines; and inflammatory mediators such as nitric oxide (NO) and prostaglandin E_2 (PGE_2). The activation and chemotactic migration of inflammatory and immune cells into tissues play essential roles in the defense against viral, bacterial, and fungal infections. Uncoupled from normal controls, however, components of the immune response may contribute to a variety of acute and chronic disorders, including cancer, diabetes, septic shock, autoimmune diseases, and atherosclerosis[3–5]. In these disorders, tissue-associated macrophages predominate among the cells that directly injure tissues. These considerations led us to seek to develop a drug that might suppress macrophage-mediated inflammation. A variety of *in vitro* and *in vivo* models of inflammatory disease have been used in drug-screening studies. Macrophages in these systems may be activated by treatment with ligands such as lipopolysaccha-

# These authors contributed equally to this work.
* To whom correspondence should be addressed.
E-mail jaecho@skku.edu
Received 2012-01-05 Accepted 2012-04-22

ride (LPS), peptidoglycan, and poly(I:C)[6].

Recent approaches to anti-inflammatory drug development have focused on key signaling proteins as targets and have tested compounds for activity against them. Previously targeted proteins include the transcription factors nuclear factor (NF)-κB and activator protein (AP)-1 and their upstream activating enzymes, including inhibitor of κB (IκBα), IκBα kinase (IKK), Akt, phosphoinositide-dependent kinase-1 (PDK1), phosphoinositide 3-kinase (PI3K), the tyrosine kinases Syk and Src, and enzymes in the mitogen-activated protein kinase (MAPK) cascade [extracellular signal-regulated kinase (ERK), c-Jun N-terminal kinase (JNK), and p38]. These proteins play critical roles in regulating pro-inflammatory gene expression.

BAY11-7082 is a representative IKK inhibitor that actively suppresses various inflammatory cytokines[7], the induction of heme oxygenase-1[8] and ICAM-1 expression[9] and may potentiate neutrophil apoptosis[10]. This compound may prove beneficial in the treatment of inflammatory conditions such as arthritis[11]. Because we did not initially identify this compound, however, we face restrictions in developing it further. We believe we can overcome such restrictions by using derivatives of the original compound. For this study, we selected seven commercially available compounds (1 through 7) based on structural similarity to BAY 11-7082. We evaluated the anti-inflammatory activities of these seven analogs and investigated their molecular mechanisms.

Materials and methods

Materials

Test compounds 1 through 7 were purchased from Sigma-Aldrich Co (St Louis, MO, USA) at greater than 95% purity. Sodium carboxymethylcellulose (NaCMC), polyethylene glycol 400, (3-4,5-dimethylthiazol-2-yl)-2,5-diphenyltetrazolium bromide (MTT), GM-CSF, and LPS (*E coli* 0111:B4) were also obtained from Sigma. LY294002 (LY), BAY11-7082 (BAY), U0126, and wortmannin were from Calbiochem (La Jolla, CA, USA). Luciferase constructs containing binding promoters for NF-κB and AP-1 were used as reported previously[12, 13]. Enzyme immunoassay (EIA) kits and enzyme-linked immunosorbent assay (ELISA) kits for PGE_2 and TNF-α were purchased from Amersham (Little Chalfont, Buckinghamshire, UK). Fetal bovine serum and RPMI-1640 medium were obtained from GIBCO (Grand Island, NY, USA). RAW264.7 cells were purchased from ATCC (Rockville, MD, USA). All other chemicals were of Sigma reagent grade. Phospho-specific or total antibodies to transcription factors (p65, p50, c-Jun, STAT-1, and c-Fos), ERK (extracellular signal-related kinase), p38, JNK (c-Jun N-terminal kinase), IκBα, IKKβ, Akt, p85/PI3K, γ-tubulin, β-actin, and non-receptor tyrosine kinases (Src and Syk) were obtained from Cell Signaling Technology Inc (Beverly, MA, USA).

Animals

C57BL/6 male mice (6–8 weeks old, 17–21 g) were obtained from Dae Han Bio Link Co Ltd, Chungbuk, Korea, and maintained in plastic cages under conventional conditions. Water and pellet diets (Samyang Corp, Daejeon, Korea) were available *ad libitum*. Studies were performed in accordance with the guidelines established by the Kangwon University Institutional Animal Care and Use Committee.

Preparation of peritoneal and bone marrow-derived macrophages

Peritoneal exudates were obtained from C57BL/6 male mice (7–8 weeks old, 17–21 g) by lavage 4 d after the intraperitoneal injection of 1 mL of sterile 4% thioglycolate broth (Difco Laboratories, Detroit, MI, USA) as reported previously[14, 15]. After washing with RPMI-1640 medium containing 2% FBS, peritoneal macrophages (1×10^6 cells/mL) were plated in 100-mm tissue culture dishes for 4 h at 37 °C in a 5% CO_2 humidified atmosphere. To prepare bone marrow-derived macrophages, femurs and tibias were isolated from mice, and the muscle was removed. Bones were cut with scissors at both ends and flushed with 5 mL of RPMI-1640 with a 25-gauge needle. Cells were seeded at a density of 2×10^5 nucleated bone marrow cells/cm^2 in RPMI-1640 containing 10% FBS, 100 U/mL penicillin, 0.1 mg/mL streptomycin, 2 mmol/L L-glutamine, and 50 ng/mL GM-CSF in 6-well CellBIND plates (Corning Life Sciences, Lowell, MA, USA) containing 3 mL per well. After a 24-h incubation, the cells were rinsed three times with 3 mL of RPMI-1640 to remove non-adherent cells and cultured further with 3 mL of RPMI-1640 containing 10% FBS, 100 U/mL penicillin, 0.1 mg/mL streptomycin, 2 mmol/L *L*-glutamine, and 50 ng/mL GM-CSF, hereafter referred to as "complete medium." The cell culture medium was replaced every 3 d with fresh complete medium. After 3 weeks in culture, experiments were performed in serum-free RPMI-1640 containing 50 ng/mL GM-CSF and additions as indicated.

Cell culture

Peritoneal macrophages and cell lines (RAW264.7 and HEK293 cells) were cultured with RPMI-1640 medium supplemented with 10% heat-inactivated fetal bovine serum (Gibco, Grand Island, NY, USA), glutamine, and antibiotics (penicillin and streptomycin) at 37 °C under 5% CO_2. For each experiment, cells were detached with a cell scraper. At our experimental cell density (2×10^6 cells/mL), the proportion of dead cells was less than 1% according to trypan blue dye exclusion tests.

NO, PGE_2, and TNF-α production

After the preincubation of RAW264.7 cells or peritoneal macrophages (1×10^6 cells/mL) for 18 h, the cells were pre-treated with test compounds 1 through 7 for 30 min and were then incubated with LPS (1 μg/mL) for 24 h. The inhibitory effects of the test compounds on NO, PGE_2, and TNF-α production were determined by analyzing the NO, PGE_2, and TNF-α levels with the Griess reagent and enzyme-linked immunosorbent assay (ELISA) kits, as described previously[16–18].

Cell viability test

RAW264.7 cells (1×10^6 cells/mL) were preincubated for 18 h and were then incubated for 24 h following the addition of

test compounds 1 through 7 to the cells. The cytotoxic effects were evaluated by the MTT assay[19]. At 3 h prior to culture termination, 10 μL of an MTT solution (10 mg/mL in phosphate buffered-saline, pH 7.4) was added, and the cells were returned to culture until the end of the experiment. Incubation was halted by the addition of 15% sodium dodecyl sulfate to each well to solubilize the formazan[20]. The absorbance at 570 nm ($OD_{570-630\ nm}$) was measured using a SpectraMax 250 microplate reader.

mRNA analysis by semiquantitative reverse-transcription polymerase chain reaction (RT-PCR)

To determine the cytokine mRNA expression levels, total RNA was isolated from LPS-treated RAW264.7 cells with TRIzol reagent (Gibco BRL), according to the manufacturer's instructions. Total RNA was stored at -70 °C until use. Analysis of mRNA was also performed using semiquantitative RT-PCR according to the manufacturer's instructions (Bioneer, Daejeon, Korea) as reported previously[21]. The results were expressed as the ratio of the optical density at 280 nm to the GAPDH mRNA concentration. The primers (Bioneer) used are listed in Table 1.

Luciferase reporter gene activity assay

HEK293 cells (1×10^6 cells/ml) were transfected with 1 μg of NF-κB-Luc, CREB-Luc, or AP-1-Luc plasmid, in addition to β-galactosidase plasmid, in the presence or absence of an Akt construct using the polyethyleneimine method in a 12-well plate according to the manufacturer's protocol[22]. The cells were used for experiments 48 h after transfection. Luciferase assays were performed using the Luciferase Assay System (Promega) as previously described[23, 24].

Preparation of total lysates and nuclear fractions, immunoblotting, and immunoprecipitation

RAW264.7 cells (5×10^6 cells/mL) or livers were washed 3 times in cold PBS with 1 mmol/L sodium orthovanadate and lysed in lysis buffer (20 mmol/L Tris-HCl, pH 7.4, 2 mmol/L EDTA, 2 mmol/L ethyleneglycotetraacetic acid, 50 mmol/L β-glycerophosphate, 1 mmol/L sodium orthovanadate, 1 mmol/L dithiothreitol, 1% Triton X-100, 10% glycerol, 10 μg/mL aprotinin, 10 μg/mL pepstatin, 1 mmol/L benzimide, and 2 mmol/L PMSF) for 30 min with rotation at 4 °C. The lysates were clarified by centrifugation at 16000×*g* for 10 min at 4 °C and stored at -20 °C until needed.

Nuclear lysates were prepared in a three-step procedure[25]. After treatment, cells were collected with a rubber policeman, washed with 1×PBS, and lysed in 500 μL of lysis buffer on ice for 4 min. The cell lysates were then centrifuged at 19326×*g* for 1 min in a microcentrifuge. In the second step, the pellet (the nuclear fraction) was washed once in wash buffer, which was the same as the lysis buffer without Nonidet P-40. In the final step, nuclei were treated with an extraction buffer containing 500 mmol/L KCl, 10% glycerol, and several other reagents as in the lysis buffer. The nuclei/extraction buffer mixture was frozen at -80 °C, thawed on ice and centrifuged at 19326×*g* for 5 min. The supernatant was collected as the nuclear extract.

For immunoprecipitation, cell lysates containing equal amounts of protein (500 μg) from RAW264.7 cells cultured at 1×10^7 cells/mL and treated or not treated with LPS (1 μg/mL) for 2.5 min were pre-cleared with 10 μL of protein A-coupled Sepharose beads (50% *v/v*) (Amersham, UK) for 1 h at 4 °C. Pre-cleared samples were incubated with 5 μL of anti-Akt antibody overnight at 4 °C. Immune complexes were mixed with 10 μL of protein A-coupled Sepharose beads (50% *vv*) and stirred by rotation for 3 h at 4 °C.

Soluble cell lysates or boiled immunoprecipitated beads were analyzed on Western blots, and the phosphorylated or total transcription factors (p65, c-Jun, and c-Fos), MAPK proteins (ERK, p38, and JNK), IκBα, IKKα/β, Akt, p85/PI3K, PDK1, γ-tubulin, β-actin, and non-receptor tyrosine kinases (Src and Syk) were visualized as previously reported[26].

Table 1. Primers for genes investigated using RT-PCR analysis.

Gene		Primer sequences
TNF-α	F	5′-TTGACCTCAGCGCTGAGTTG-3′
	R	5′-CCTGTAGCCCACGTCGTAGC-3′
IL-1β	F	5′-CAGGATGAGGACATGAGCACC-3′
	R	5′-CTCTGCAGACTCAAACTCCAC-3'
IL-6	F	5′-GTACTCCAGAAGACCAGAGG-3′
	R	5′-TGCTGGTGACAACCACGGCC-3′
IL-12 p40	F	5′-CAGAAGCTAACCATCTCCTGGTTTG-3′
	R	5′-TCCGGAGTAATTTGGTGCTTCACAC-3′
iNOS	F	5′-CCCTTCCGAAGTTTCTGGCAGCAGC-3′
	R	5′-GGCTGTCAGAGCCTCGTGGCTTTGG-3′
COX-2	F	5′-CACTACATCCTGACCCACTT-3′
	R	5′-ATGCTCCTGCTTGAGTATGT-3′
GAPDH	F	5′-CACTCACGGCAAATTCAACGGCAC-3′
	R	5′-GACTCCACGACATACTCAGCAC-3′

F, forward; R, reverse.

Akt and PI3K kinase assays

To evaluate the Akt- and PI3K kinase-inhibitory activity in the extracts using purified enzymes, a kinase profiler service from Millipore (http://www.millipore.com/life_sciences/flx4/ld_kinases) was used. In a final reaction volume of 25 μL, Akt (1, 2, and 3) or PI3K (α, β, and γ; human; 1–5 mU) protein was incubated with the reaction buffer. The reaction was initiated by the addition of MgATP. After incubation for 40 min at room temperature, the reaction was stopped by adding 5 mL of a 3% phosphoric acid solution. Ten microliters of the reaction product was then spotted onto a GF/P30 filtermat (PerkinElmer, Inc), which was then washed three times for 5 min in 75 mmol/L phosphoric acid and once in methanol prior to drying and scintillation counting.

EtOH/HCl-induced gastritis, LPS-induced hepatitis, and acute toxicity tests

Inflammation of the stomach was induced with EtOH/HCl

according to a published method[27]. Fasted ICR mice were orally treated with compound 7 (10 to 40 mg/kg) or ranitidine (40 mg/kg) suspended in 5% NaCMC. Thirty minutes later, 400 μL of 60% ethanol in 150 mmol/L HCl was administered orally. Each animal was euthanized with an overdose of urethane 1 h after the administration of the necrotizing agents. The stomach was excised and gently rinsed under running tap water. After opening the stomach along the greater curvature and spreading it out on a board, the area (mm^2) of the mucosal erosive lesions was measured using a pixel-counter. Inflammation of the liver was induced by the injection of LPS according to a published method[28]. Fasted C57BL/6 mice were orally treated with compound 7 (20 mg/kg) once per day for 6 d. One hour after the final administration, LPS (10 mg/kg) was intraperitoneally administered. Each animal was anesthetized with an overdose of urethane 1 h after the administration of hepatitis inducers, and blood was drawn from the portal vein. The livers were then excised and gently rinsed under running tap water. Serum was obtained by centrifugation of the blood at 3000 r/min for 15 min. The levels of serum alanine aminotransferase (ALT) and aspartate aminotransferase (AST) were measured with a Roche Modular spectrophotometric autoanalyser. In the acute toxicity test, compound 7 was dissolved in 20% PEG 400 diluted in 5% BSA in H_2O or suspended in 5% NaCMC and administered orally or by intraperitoneal injection. Lethality and body weight changes were determined after 7 d.

Statistical analysis

Data represent the mean±standard deviations (SD) from at least three independent experiments, each performed in triplicate, or are representative of three different experiments with similar results. For statistical comparisons, the results were analyzed using analysis of variance with Scheffe's *post-hoc* test and the Kruskal-Wallis/Mann-Whitney U-test. A P value <0.05 was considered to represent a significant difference. All statistical tests were carried out using SPSS (Statistical Package for the Social Sciences, SPSS Inc, Chicago, IL, USA).

Results and Discussion

In a search for novel anti-inflammatory drugs, we selected compounds (Figure 1A) similar in structure to BAY 11-7082, an IKK inhibitor, and tested them for inhibitory effects on the inflammatory mediators NO, TNF-α, and PGE_2. Compound 7 [8-(tosylamino)quinoline] suppressed NO production in a dose-dependent manner without affecting cell viability (Figure 2), whereas the other compounds tested showed no inhibitory effect (Figure 1B). Compound 7 suppressed the release of NO, PGE_2, and TNF-α by RAW264.7 cells (Figure 2A), peritoneal macrophages (Figure 2B), and bone-marrow derived macrophages (Figure 2C) during LPS exposure, with IC_{50} values of 1 to 5 μmol/L (Table 2). The inhibitory activity of compound 7 was comparable to that of BAY11-7082 (Figure 1C) when BAY11-7082 was tested as a treatment for arthritis[11]. These findings support the further development of compound 7 as an anti-inflammatory drug.

Table 2. The half-maximal inhibitory concentration (IC_{50}) of compound 7 for the inhibition of the production of NO, TNF-α, and PGE2 in RAW264.7 cells and peritoneal macrophages.

Cells	IC_{50} value (μmol/L)		
	NO	PGE_2	TNF-α
RAW264.7 cells	4.3	3.2	6.1
Peritoneal macrophages	7.9	3.9	4.1

To explore the inhibitory mechanism of compound 7, we analyzed the effects of this compound on the transcription of genes encoding inflammatory mediators. Compound 7 dose-dependently reduced the levels of TNF-α, IL-1β, IL-6, IL-12, COX-2, and iNOS mRNAs, implying that this drug inhibits inflammatory mediator production at the level of transcription (Figure 3). To identify the transcription factors targeted by compound 7, we measured transcription factor levels in nuclear fractions in cells exposed to LPS as an inflammatory stimulus. In this setting, compound 7 suppressed p65 upregulation after 15 min and 2 h without exerting inhibitory effects on c-Jun and c-Fos (Figure 4A left panel). We found a similar pattern of inhibition in LPS-treated peritoneal macrophages (Figure 4A, right panel). In the reporter gene assay performed with constructs containing NF-κB, CREB or AP-1 binding promoters, similar inhibitory patterns for the activation of transcription factors were observed. Thus, compound 7 suppressed NF-κB-mediated luciferase activities that were stimulated by PMA or cotransfection with other adaptor molecules such as TRIF and MyD88 (Figure 4B), but this compound did not suppress AP-1 or CREB activities (Figure 4C). These results indicate that compound 7 modulates NF-κB signaling at an early stage.

Because NF-κB activation is linked to a cascade of kinase activation, we sought to identify the exact target of compound 7 by determining the levels of phosphorylated IκBα, IKK, Akt, PDK1, PI3K, and Src or Syk after LPS stimulation. At 5 and 60 min, compound 7 strongly suppressed IκBα phosphorylation (Figure 5A). Because of the effect at 5 min, we turned our attention to early signaling events to investigate the target of compound 7. Interestingly, IκBα and its upstream kinase IKKα/β were phosphorylated at 1 min, and Akt phosphorylation had not diminished at this time. In agreement with this result, compound 7 did not suppress the phosphorylation of Syk or Src, tyrosine kinases that contribute to IκBα phosphorylation at 5 min[29]. These data imply that compound 7 targets molecules upstream of IKK, such as Akt kinase, either directly or indirectly. To confirm these possibilities, a direct kinase assay was performed with purified PI3K and Akt. Contrary to expectations, there was no inhibition of any type of PI3K and Akt (Figure 5C). Nonetheless, the molecular association between Akt and IKK observed after LPS treatment was clearly reduced by treatment with compound 7 (Figure 5D), suggesting that this compound seems to target to the binding event between Akt and its substrate protein IKK. Meanwhile,

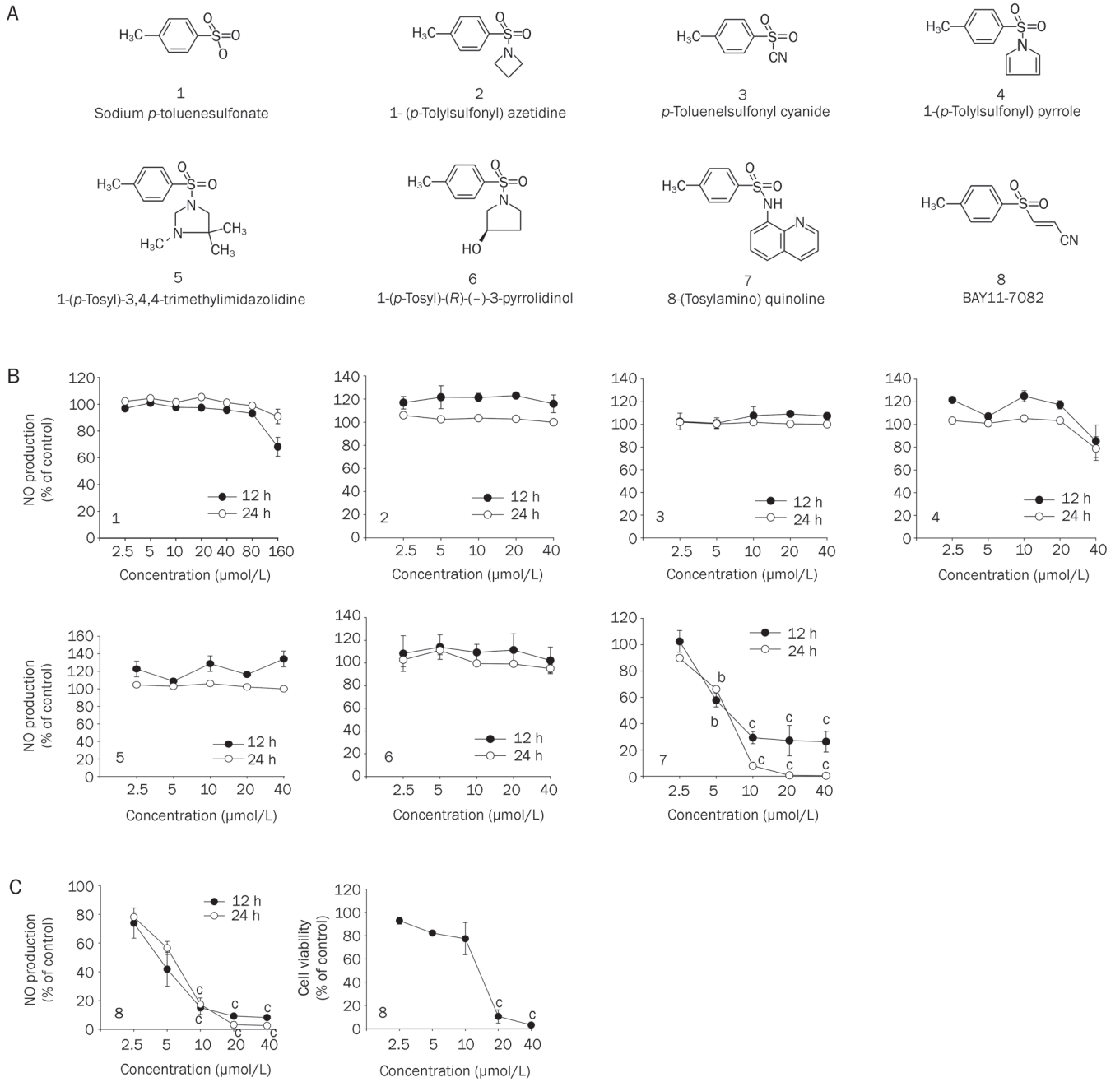

Figure 1. Effects of compounds 1 through 7 and BAY11-7082 on NO production. (A) Chemical structures of compounds 1 through 7. (B and C left panel) The Griess assay was used to determine the NO levels in culture supernatants of RAW264.7 cells or peritoneal macrophages treated with the test compounds and LPS (1 μg/mL) for 12 or 24 h. (C right panel) The viability of RAW264.7 cells was determined by the MTT assay. Mean±SD. n=4. ^{b}P<0.05, ^{c}P<0.01 *vs* the control.

to confirm that compound 7 does not inhibit AP-1, we evaluated the levels of phosphorylated MAPK-related kinases (ERK, JNK, and p38). As expected, compound 7 did not suppress the phosphorylation of these enzymes (Figure 5E).

The Akt pathway, considered to be one of the major targets of compound 7, was initially recognized as a significant cell survival signal and subsequently as a potential target for cancer therapy. Based on recent evidence, however, attention has shifted to the role of Akt signaling in LPS-induced inflammatory responses[30]. It is noteworthy that anti-inflammatory herbal extracts from *Eleutherococcus senticosus*, *Dichroa feb rifuga*, and *Cymbopogon citratus*[31–33] and ethnopharmacological agents such as curcumin, resveratrol, and quercetin[34–36] may suppress the Akt pathway. The Akt inhibitors LY294002 and wortmannin displayed anti-inflammatory activity, reflected by the suppression of NO and PGE_2 (Figure 6A). Furthermore,

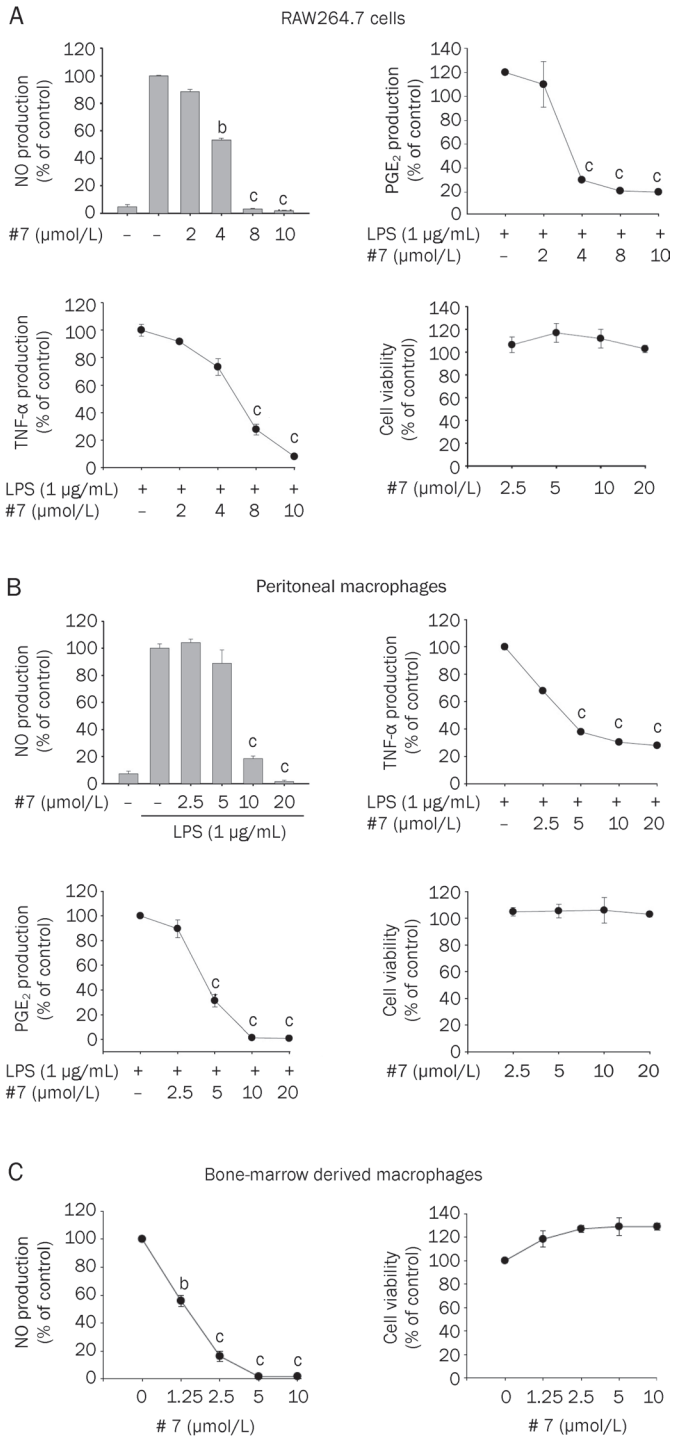

Figure 2. Effect of compound 7 on the production of inflammatory mediators. (A, B and C) The levels of NO, PGE_2, and TNF-α were determined by the Griess assay, EIA, and ELISA in culture supernatants of RAW264.7 cells, peritoneal macrophages or bone marrow-derived macrophages treated with compound 7 and LPS (1 μg/mL) for 6 or 24 h. The viability of RAW264.7 cells and peritoneal macrophages was determined using the MTT assay. $^bP<0.05$, $^cP<0.01$ *vs* the control.

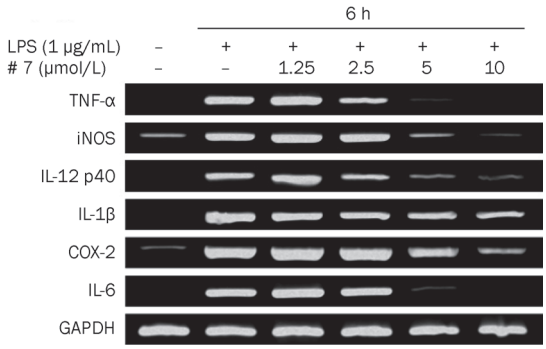

Figure 3. Effect of compound 7 on the expression of pro-inflammatory genes. The levels of iNOS, COX-2, TNF-α, IL-1β, IL-6, and IL-12 p40 mRNAs were determined by semiquantitative RT-PCR.

the overexpression of Akt induced NF-κB activation up to 2.5 fold as assessed by measuring NF-κB-mediated luciferase activity (Figure 6B). These findings suggest that Akt pathway inhibition may be a determining event in compound 7-mediated anti-inflammatory action. We will investigate how this compound mediates Akt-IKK binding inhibition without affecting Akt kinase activity in future experiments in our lab. In these experiments, the mode of binding between Akt and IKK and the inhibition of this binding by compound 7 will be analyzed using mutant constructs of these proteins and immunoprecipitation.

To determine whether compound 7 is active by the oral route, we tested its effect against EtOH/HCl-stimulated gastritis, an *in vivo* model of inflammatory disease that is widely used in drug development. At a single dose of 40 mg/kg, compound 7 significantly reduced gastric tissue injury following EtOH/HCl administration, as did ranitidine (40 mg/kg), the positive control (Figure 7A). In addition, this compound also suppressed LPS-induced hepatitis symptoms as assessed by measuring the serum levels of enzymes (ALT and AST) indicative of liver damage, implying that *in vivo* TLR4-mediated inflammatory symptoms are also ameliorated by this compound. The acute administration of compound 7 to mice at 500 mg/kg for 1 week by the oral or intraperitoneal route induced no perturbation in body weight or change in mortality (Figure 7C). These results support the further testing of compound 7 as an orally available, well-tolerated anti-inflammatory drug[37].

In summary, we have shown that compound 7 may suppress the production of NO, TNF-α, and PGE_2 in LPS-treated macrophages and may attenuate HCl/EtOH-induced gastritis. In exploring the anti-inflammatory mechanism of compound 7, we found that this compound can block NF-κB activation by suppressing upstream signaling by IκBα, IKK, and Akt (Figure 8). We propose that compound 7 might be used as a novel anti-inflammatory drug. To investigate this application, we will test compound 7 for efficacy *in vivo* using models of acute disorders (septic shock and carrageenan-induced arthritis) and chronic disorders (collagen- or adjuvant-induced arthritis) in a pre-clinical study.

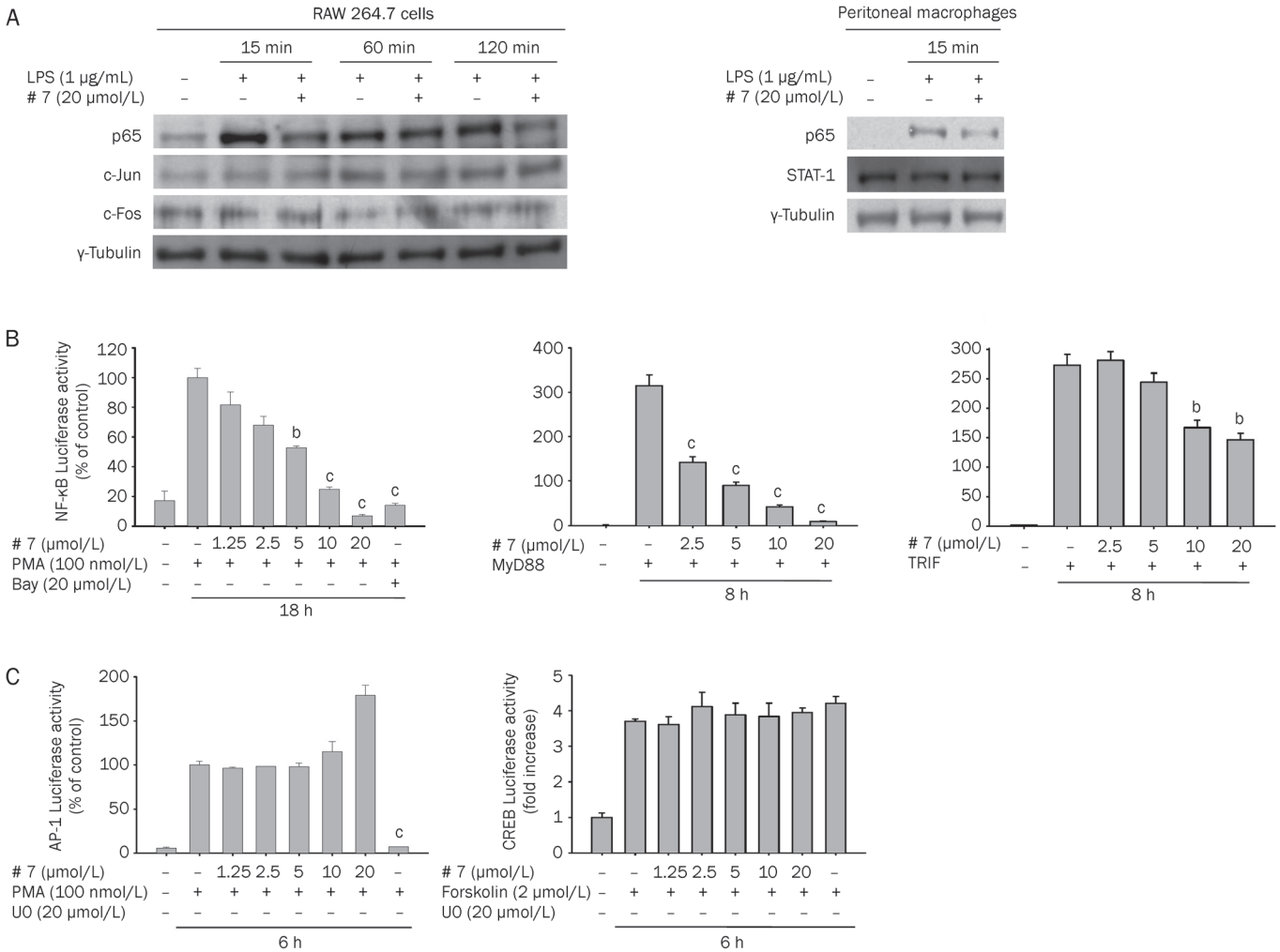

Figure 4. Effect of compound 7 on the activation of transcription factors (NF-κB and AP-1). (A) The levels of NF-κB (p65), STAT-1, and AP-1 (c-Jun/c-Fos) in nuclear fractions from LPS-treated RAW264.7 cells and peritoneal macrophages were determined by immunoblotting analysis with antibodies against the total proteins. (B and C) HEK293 cells cotransfected with plasmid constructs for NF-κB-Luc, CREB-Luc or AP-1-Luc; adaptor molecules (MyD88 and TRIF) (each at 1 μg/mL); and β-gal (as a transfection control) were treated with compound 7, BAY (BAY11-7082) or U0 (U0126) in the presence or absence of PMA (100 nmol/L). The luciferase activity was measured using a luminometer. $^{b}P<0.05$, $^{c}P<0.01$ *vs* the control.

Acknowledgements

This work was supported by a National Research Foundation of Korea (NRF) grant funded by the Korean government (MEST) (to Jae Youl CHO) (No 2011-0016397).

Author contribution

Yongwoo JUNG, Sungyoul HONG, and Jae Youl CHO designed the research; Yongwoo JUNG, Se Eun BYEON, Dae Sung YOO, Tao YU, Yanyan YANG, Ji Hye KIM, Eunji Kim, Yong Gyu LEE, and Deok JEONG performed the research; Yongwoo JUNG, Man Hee RHEE, Eui Su CHOUNG, Sungyoul HONG, and Jae Youl CHO analyzed the data; and Jae Youl CHO wrote the paper.

Abbreviations

ERK, extracellular signal-related kinase; TLR, Toll-like receptors; MAPK, mitogen-activated protein kinase; NF-κB, nuclear factor-κB; AP-1, activator protein-1; JNK, c-Jun N-terminal kinase; Akt, protein kinase B; ATF2, activating transcription factor 2; CREB, cAMP response element-binding; IKK, IκBα kinase; IRAK1, interleukin-1 receptor-associated kinase 1; MKK, MAP kinase kinase; MyD88, myeloid differentiation primary-response protein-88; TRAF6, tumor necrosis factor-receptor-associated factor-6; TAK1, TGF-β-activated kinase-1; PDK1, phosphoinositide-dependent protein kinase-1; Syk, spleen tyrosine kinase; TRIF, TIR-domain-containing adapter-inducing interferon-β; EIA, enzyme immunoassay; ELISA, enzyme-linked immunosorbent assay; MTT, 3-4,5-dimethylthiazol-2-yl)-2,5-diphenyltetrazolium bromide; PI3K, phosphoinositide 3-kinase; LPS, lipopolysaccharide; RT-PCR, reverse transcriptase polymerase chain reaction; ALT, serum alanine aminotransferase; AST, aspartate aminotransferase

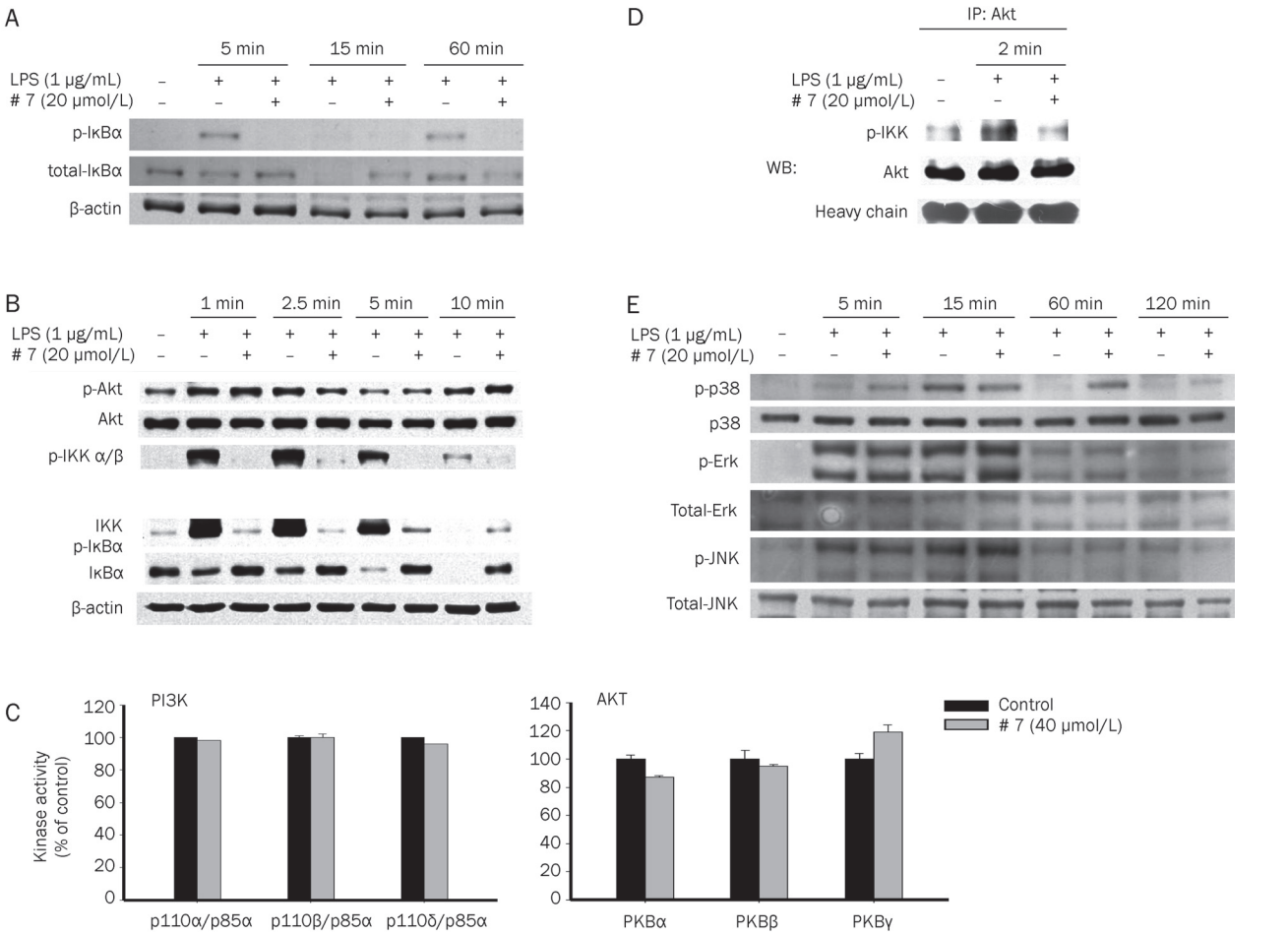

Figure 5. Effects of compound 7 on the activation of signaling enzymes upstream of NF-κB translocation. (A, B, and E) The levels of phospho- and total proteins of IκBα, IKKα/β, Akt, ERK, p38, JNK, and β-actin in cell lysates were determined using phospho-specific and total-protein antibodies, respectively. (C) The kinase activities of Akt and PI3K were determined by a direct kinase assay using purified enzymes. The control activity of each enzyme (Akt or PI3K) was set to 100%. (D) The effects of compound 7 on the formation of the signaling complex composed of Akt and phospho-IKK in the total lysates from LPS-treated RAW264.7 cells (5×10^6 cells/mL) were determined by immunoprecipitation with an anti-Akt antibody and immunoblotting with antibodies to p-IKK.

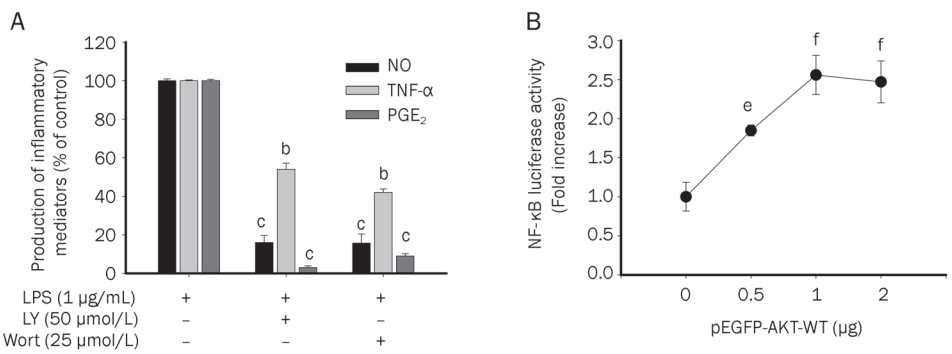

Figure 6. Functional role of Akt in the induction of inflammatory responses. (A) Culture supernatants prepared from LPS-treated RAW264.7 cells pre-treated with standard PI3K/Akt inhibitors [LY294002 (LY) and wortmannin (Wort)] were assayed for NO, TNF-α, and PGE_2. (B) HEK293 cells were cotransfected with plasmid constructs for either NF-κB-Luc or Akt (1 μg/mL each) and β-gal (as a transfection control). The luciferase activity was measured with a luminometer. $^bP<0.05$, $^cP<0.01$ *vs* the control. $^eP<0.05$, $^fP<0.01$ *vs* the normal.

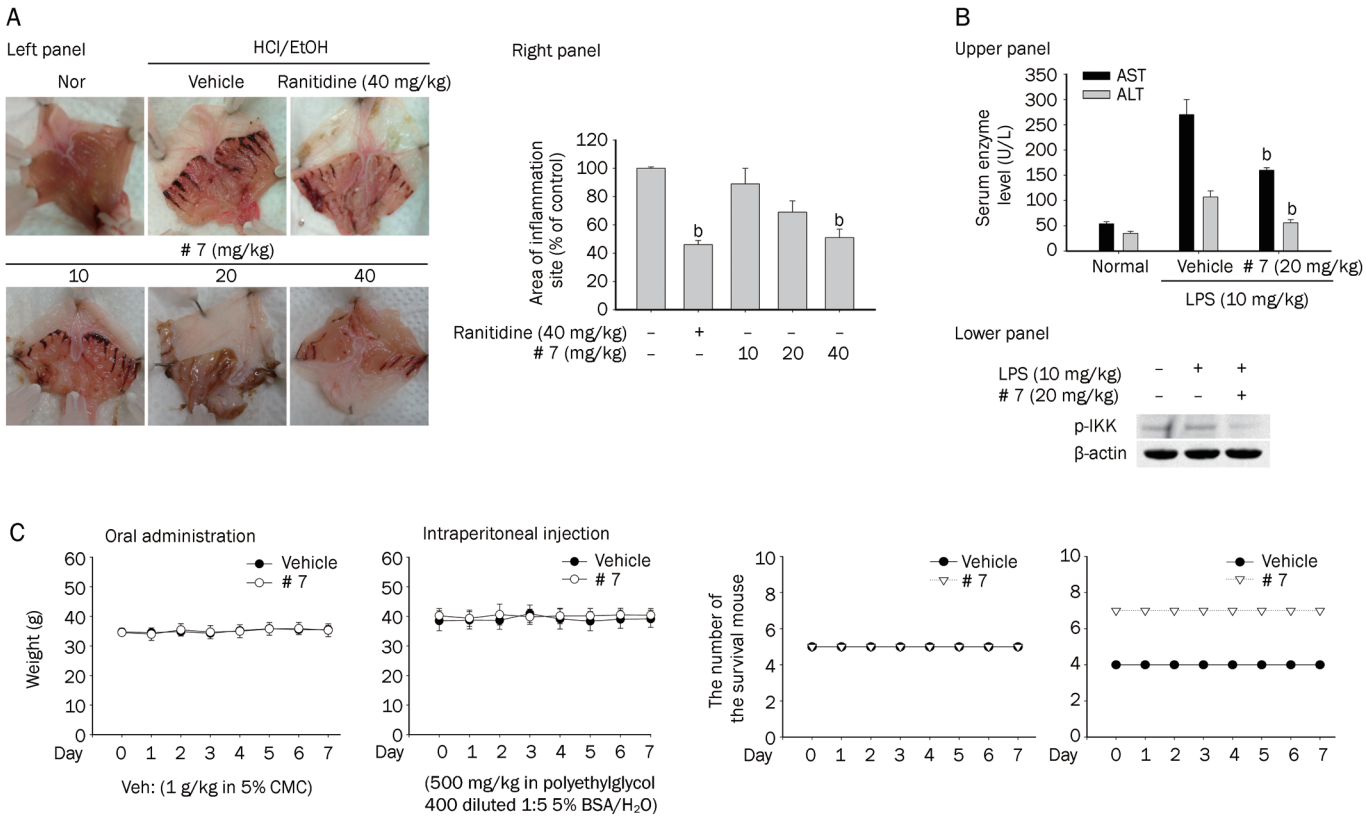

Figure 7. Effects of compound 7 on gastric inflammation in mice induced by HCl/EtOH treatment and on acute toxicity. (A) Mice were treated orally with compound 7 or ranitidine for 3 d and then treated orally with HCl/EtOH. After 24 h, the gastric lesions in the stomach were measured by pixel counting right panel) and photographed (left panel). The area of gastric lesions present after treatment with the inducer alone is represented by 100%. (B) Mice orally treated with compound 7 for 6 d were intraperitoneally treated with LPS. After 1 h, serum was prepared to measure the biochemical parameters (AST and ALT) (upper panel), and the levels of p-IKK and β-actin were analyzed by Western blotting of the liver lysate (lower panel). (C) Lethality and body weight changes were followed for 7 d after the oral administration (1 g/kg) or intraperitoneal injection of compound 7 (500 mg/kg). $^{b}P<0.05$ *vs* the control.

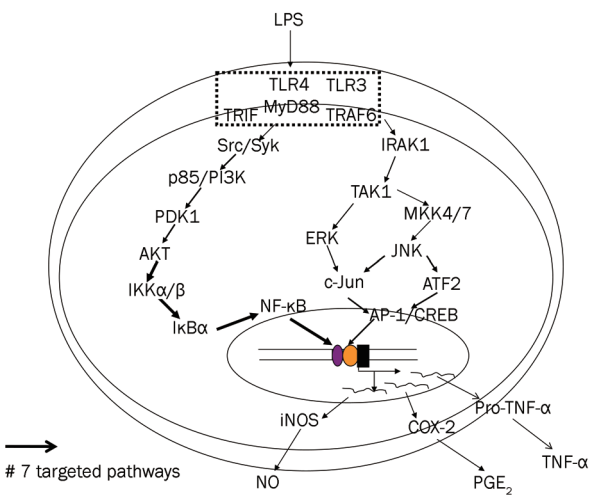

Figure 8. Putative pathway of the inhibition of LPS-activated inflammatory signaling by compound 7.

References

1 Kinne RW, Brauer R, Stuhlmuller B, Palombo-Kinne E, Burmester GR. Macrophages in rheumatoid arthritis. Arthritis Res 2000; 2: 189–202.

2 Owens T, Babcock AA, Millward JM, Toft-Hansen H. Cytokine and chemokine inter-regulation in the inflamed or injured CNS. Brain Res Brain Res Rev 2005; 48: 178–84.

3 Eizirik DL, Colli ML, Ortis F. The role of inflammation in insulitis and beta-cell loss in type 1 diabetes. Nat Rev Endocrinol 2009; 5: 219–26.

4 Brown KD, Claudio E, Siebenlist U. The roles of the classical and alternative nuclear factor-kappa B pathways: potential implications for autoimmunity and rheumatoid arthritis. Arthritis Res Ther 2008; 10: 212.

5 Grieco FA, Vendrame F, Spagnuolo I, Dotta F. Innate immunity and the pathogenesis of type 1 diabetes. Semin Immunopathol 2011; 33: 57–66.

6 Tsan MF, Gao B. Endogenous ligands of Toll-like receptors. J Leukoc Biol 2004; 76: 514–9.

7 Mendes Sdos S, Candi A, Vansteenbrugge M, Pignon MR, Bult H, Boudjeltia KZ, *et al*. Microarray analyses of the effects of NF-kappaB or PI3K pathway inhibitors on the LPS-induced gene expression profile in RAW264.7 cells: synergistic effects of rapamycin on LPS-induced MMP9-overexpression. Cell Signal 2009; 21: 1109–22.

8 Min KJ, Lee JT, Joe EH, Kwon TK. An IkappaBalpha phosphorylation

inhibitor induces heme oxygenase-1 (HO-1) expression through the activation of reactive oxygen species (ROS)-Nrf2-ARE signaling and ROS-PI3K/Akt signaling in an NF-kappaB-independent mechanism. Cell Signal 2011; 23: 1505–13.

9 Lee H, Lin CI, Liao JJ, Lee YW, Yang HY, Lee CY, *et al*. Lysophospholipids increase ICAM-1 expression in HUVEC through a Gi- and NF-kappaB-dependent mechanism. Am J Physiol Cell Physiol 2004; 287: C1657–66.

10 Dai Y, Rahmani M, Grant S. Proteasome inhibitors potentiate leukemic cell apoptosis induced by the cyclin-dependent kinase inhibitor flavopiridol through a SAPK/JNK- and NF-kappaB-dependent process. Oncogene 2003; 22: 7108–22.

11 Pierce JW, Schoenleber R, Jesmok G, Best J, Moore SA, Collins T, *et al*. Novel inhibitors of cytokine-induced IkappaBalpha phosphorylation and endothelial cell adhesion molecule expression show anti-inflammatory effects *in vivo*. J Biol Chem 1997; 272: 21096–103.

12 Yu T, Ahn HM, Shen T, Yoon K, Jang HJ, Lee YJ, *et al*. Anti-inflammatory activity of ethanol extract derived from *Phaseolus angularis beans*. J Ethnopharmacol 2011; 137: 1197–206.

13 Yu T, Lee YJ, Jang HJ, Kim AR, Hong S, Kim TW, *et al*. Anti-inflammatory activity of *Sorbus commixta* water extract and its molecular inhibitory mechanism. J Ethnopharmacol 2011; 134: 493–500.

14 Pyo S. The mechanism of poly I:C-induced antiviral activity in peritoneal macrophage. Arch Pharm Res 1994; 17: 93–9.

15 Jang SA, Kang SC, Sohn EH. Phagocytic effects of beta-glucans from the mushroom coriolus versicolor are related to Dectin-1, NOS, TNF-alpha signaling in macrophages. Biomol Ther 2011; 19: 438–44.

16 Cho JY, Baik KU, Jung JH, Park MH. *In vitro* anti-inflammatory effects of cynaropicrin, a sesquiterpene lactone, from *Saussurea lappa*. Eur J Pharmacol 2000; 398: 399–407.

17 Kang TJ, Moon JS, Lee S, Yirn D. Polyacetylene compound from *Cirsium japonicum* var ussuriense inhibits the LPS-Induced inflammatory reaction via suppression of NF-kappa B activity in RAW 264.7 cells. Biomol Ther 2011;19: 97-101.

18 Jung YH, Park KY, Jeon JH, Kwak YS, Song YB, Wee JJ, *et al*. Red ginseng saponin fraction A isolated from Korean red ginseng by ultrafiltration on the porcine coronary artery. J Ginseng Res 2011; 35: 325–30.

19 Pauwels R, Balzarini J, Baba M, Snoeck R, Schols D, Herdewijn P, *et al*. Rapid and automated tetrazolium-based colorimetric assay for the detection of anti-HIV compounds. J Virol Methods 1988; 20: 309–21.

20 Kim JR, Oh DR, Cha MH, Pyo BS, Rhee JH, Choy HE, *et al*. Protective effect of polygoni cuspidati radix and emodin on *Vibrio vulnificus* cytotoxicity and infection. J Microbiol 2008; 46: 737–43.

21 Kim YJ, Lee JH, Lee OR, Shim JS, Jung SK, Son NR, *et al*. Isolation and characterization of a type II peroxiredoxin gene from *Panax ginseng C*. A. Meyer. J Ginseng Res 2010; 34: 296–303.

22 Jin M, Park S, Pyo MY. Suppressive effects of T-412, a flavone on interleukin-4 production in T cells. Biol Pharm Bull 2009; 32: 1875–9.

23 Jung KK, Lee HS, Cho JY, Shin WC, Rhee MH, Kim TG, *et al*. Inhibitory effect of curcumin on nitric oxide production from lipopolysaccharide-activated primary microglia. Life Sci 2006; 79: 2022–31.

24 Shen T, Lee J, Park MH, Lee YG, Rho HS, Kwak YS, *et al*. Ginsenoside Rp(1), a ginsenoside derivative, blocks promoter activation of iNOS and COX-2 genes by suppression of an IKK beta-mediated NF-kappa B pathway in HEK293 cells. J Ginseng Res 2011; 35: 200–8.

25 Byeon SE, Lee YG, Kim BH, Shen T, Lee SY, Park HJ, *et al*. Surfactin blocks NO production in lipopolysaccharide-activated macrophages by inhibiting NF-kappaB activation. J Microbiol Biotechnol 2008; 18: 1984–9.

26 Sohn EH, Jang SA, Lee CH, Jang KH, Kang SC, Park HJ, *et al*. Effects of Korean red ginseng extract for the treatment of atopic dermatitis-like skin lesions in mice. J Ginseng Res 2011; 35: 479–86.

27 Okabe S, Miyake H, Awane Y. Cytoprotective effects of NC-1300 and omeprazole on HCl. ethanol-induced gastric lesions in rats. Jpn J Pharmacol 1986; 42: 123–33.

28 Cho JY, Yeon JD, Kim JY, Yoo ES, Yu YH, Park MH. Hepatoprotection by human epidermal growth factor (hEGF) against experimental hepatitis induced by D-galactosamine (D-galN) or D-GalN/lipopolysaccharide. Biol Pharm Bull 2000; 23: 1243–6.

29 Lee YG, Chain BM, Cho JY. Distinct role of spleen tyrosine kinase in the early phosphorylation of inhibitor of kappaB alpha via activation of the phosphoinositide-3-kinase and Akt pathways. Int J Biochem Cell Biol 2009; 41: 811–21.

30 Lee YG, Lee J, Byeon SE, Yoo DS, Kim MH, Lee SY, *et al*. Functional role of Akt in macrophage-mediated innate immunity. Front Biosci 2011; 16: 517–30.

31 Jung CH, Jung H, Shin YC, Park JH, Jun CY, Kim HM, *et al*. Eleutherococcus senticosus extract attenuates LPS-induced iNOS expression through the inhibition of Akt and JNK pathways in murine macrophage. J Ethnopharmacol 2007; 113: 183–7.

32 Park SY, Park GY, Ko WS, Kim Y. Dichroa febrifuga Lour inhibits the production of IL-1beta and IL-6 through blocking NF-kappaB, MAPK and Akt activation in macrophages. J Ethnopharmacol 2009; 125: 246–51.

33 Francisco V, Figueirinha A, Neves BM, Garcia-Rodriguez C, Lopes MC, Cruz MT, *et al*. Cymbopogon citratus as source of new and safe anti-inflammatory drugs: bio-guided assay using lipopolysaccharide-stimulated macrophages. J Ethnopharmacol 2011; 133: 818–27.

34 Poolman TM, Ng LL, Farmer PB, Manson MM. Inhibition of the respiratory burst by resveratrol in human monocytes: correlation with inhibition of PI3K signaling. Free Radic Biol Med 2005; 39: 118–32.

35 Larmonier CB, Midura-Kiela MT, Ramalingam R, Laubitz D, Janikashvili N, Larmonier N, *et al*. Modulation of neutrophil motility by curcumin: implications for inflammatory bowel disease. Inflamm Bowel Dis 2011; 17: 503–15.

36 Ruiz PA, Braune A, Holzlwimmer G, Quintanilla-Fend L, Haller D. Quercetin inhibits TNF-induced NF-kappaB transcription factor recruitment to proinflammatory gene promoters in murine intestinal epithelial cells. J Nutr 2007; 137: 1208–15.

37 Byeon SE, Chung JY, Lee YG, Kim BH, Kim KH, Cho JY. *In vitro* and *in vivo* anti-inflammatory effects of taheebo, a water extract from the inner bark of *Tabebuia avellanedae*. J Ethnopharmacol 2008; 119: 145–52.

Acta Pharmacologica Sinica (2012) 33: 1047–1054
 1671-4083/12 $32.00
www.nature.com/aps

Original Article

Immunostimulatory and anti-neoplasm effects of a novel palindrome CpG oligodeoxynucleotide in mice

Hai-yan DU[1, 2, #], Li-hou DONG[1, #], Bi-jun ZHAO[3, #], Jie FU[1], Qing-qing WANG[1], Fang CHEN[1], Lun OU[1], Na LI[1], Xiao SUN[1], Zhong-ming TANG[1], Hai-feng SONG[1, *]

[1]*Department of Pharmacology and Toxicology, Beijing Institute of Radiation Medicine, Beijing 100850, China;* [2]*Drug Clinical Trial Institution, Beijing Anzhen Hospital of Capital Medical University, Beijing 100029, China;* [3]*Department of Cardiovascular Surgery, Xijing Hospital, Fourth Military Medical University, Xi'an 710032, China*

Aim: DNAs containing unmethylated CpG motifs can stimulate innate and adaptive immunity. The aim of this study was to investigate the immunostimulatory and anti-neoplasm effects of a novel CpG oligodeoxynucleotide, ODN10, in tumor-bearing mice.
Methods: B16 melanoma-bearing C57BL/6 mice were administered ip or sc with ODN10 or conventional CpG ODN1826 on the indicated days post inoculation. The animal survival rate and the inhibitory effect on tumor growth were observed *in vivo*. B and T lymphocyte proliferation, natural killing cell cytotoxicity and the phagocytic ability of peritoneal macrophages from the animals were determined using [^{3}H]-thymidine incorporation assay, 4-h ^{51}Cr release assay and neutral red chromometry method, respectively. The serum levels of IL-12, IL-4, and IgE were quantified using ELISA assays. Histological examination of tumor tissues was performed after HE staining, and the expression of PCNA, CD63, and CD80 in tumor tissues was analyzed with immunohistochemistry.
Results: ODN10 (1, 5, and 25 mg/kg) significantly inhibited the growth and metastasis of the tumor, and significantly prolonged the survival of tumor-bearing mice, as compared with ODN1826. The immune status was suppressed in tumor-bearing mice. Both ODN10 and ODN1826 significantly reversed the suppressed immunoactivities in tumor-bearing mice, which included promoting B and T lymphocyte proliferation, enhancing NK cell and peritoneal macrophage activities, inducing IL-12 secretion and inhibiting IL-4 and IgE secretion. Further, CpG ODNs decreased PCNA and CD63 expression while induced expression of CD80. ODN10 presented more potent activity, and displayed the most prominent immunostimulatory potential.
Conclusion: ODN10 produces prominent immunomodulatory effects on cellular immunity in tumor-bearing mice, which might help reverse the established Th2-type responses to the Th1-type responses, thus may be used as a potent anti-tumor immunotherapy agent or adjuvant.

Keywords: CpG oligodeoxynucleotide; ODN10; ODN1826; melanoma; cancer; immunotherapy; cellular immunity

Acta Pharmacologica Sinica (2012) 33: 1047–1054; doi: 10.1038/aps.2012.54; published online 25 Jun 2012

Introduction

The immune system of vertebrates is comprised of two complementary systems, the innate and the adaptive. In the innate system, dendritic cells (DCs) are the major antigen presenting cells to T_{h0} T cells in lymph nodes that polarise into T_{h1} and T_{h2} cells, which subsequently produce different cytokines. Polarised T_{h1} cells produce interleukin (IL)-2, IL-12, and interferon (IFN)-γ, while polarised T_{h2} cells produce IL-4, IL-5, IL-6, IL-10, and IL-13. In healthy individuals, there is a T_{h1}/T_{h2} cytokine balance, whereas in the tumor-bearing individual, T_{h2} cytokine synthesis is increased. As such, researchers have tried to up-regulate the T_{h1} population and maintain the balance of T_{h1}/T_{h2} to reverse the abnormal immune status in tumor patients[1].

Bacterial and synthetic DNAs containing unmethylated CpG motifs were known to stimulate innate and adaptive immunity due to their interesting immunostimulatory properties in a number of vertebrates. The recognition of CpG DNAs by immune cells was mediated by Toll-like receptor 9 (TLR9), a receptor mainly expressed by B cells and plasmacytoid DC cells in humans and macrophages in mice[2]. TLR9-stimulated immune cells showed increased expression of co-stimulatory molecules, resistance to apoptosis, and up-regulation of T_{h1}-promoting chemokines and cytokines such as IL-2, IL-12, and IFN-γ[3]. *In vivo*, CpG DNAs were strong T_{h1}-inducing adjuvants[4–8].

# The first three authors contributed equally to this work.
* To whom correspondence should be addressed.
E-mail songhf@vip.163.com
Received 2011-11-03 Accepted 2012-04-23

Recently, CpG oligodeoxynucleotide (ODN)s have been explored for use as an anti-cancer therapy due to their immunostimulatory properties, such as inducing the release of large amounts of type I IFN, inhibition of the synthesis of T_{h2} cytokines, induction of T_{h1} cytokine synthesis, and the activation of NK cell cytotoxicity or cytotoxic T lymphocyte (CTL) precursors into anti-tumor CTL cells[9–13]. Further, CpG ODNs enhanced the anti-tumor efficacy of monoclonal antibodies or cancer vaccines when used as an adjuvant in animal tumor models[11, 14]. CpG ODNs alone were also capable of triggering potent anti-tumor immune responses against various experimental tumors, for example, lymphoma, melanoma, colon tumor, glioma, and neuroblastoma[15–21].

We previously investigated the relationship between primary and secondary structures of CpG ODNs and their immunostimulatory effects on murine spleen cells and found that specific structures of CpG ODNs could vary greatly in their ability to induce host immunity in mice[22]. We screened several novel CpG ODN sequences to identify those with superior immunostimulatory activities relative to the conventional linear control CpG ODN1826, which is a strong immune activator that induces protective and curative T_{h1} responses against infections and tumors *in vivo* in mice[9, 20, 21, 23–25]. Among them, ODN10, which possessed a holistic, self-complementary palindrome structure and promised the strongest immunostimulatory potential, was chosen for use in the present study. The immunostimulatory potential of ODN10 was evaluated by its activation of NK cells, T cells, B cells, macrophages, and the helper T cell related cytokine secretion profile in malignant melanoma-bearing mice. To characterise the most important outcome of immunomodulatory therapy, the *in vivo* anti-tumor efficacy of ODN10 was investigated as well. The results suggested that ODN10, a novel CpG ODN with self-palindrome structure, displayed outstanding anti-tumor activity superior to that of other conventional CpG-containing immunostimulatory ODN sequences. In addition, the anti-tumor activity of ODN10 may be attributed to its powerful immunoregulatory potential to reverse established T_{h2}-type responses to a T_{h1}-type response.

Materials and methods

CpG ODNs

Purified, single-stranded, phosphorothioated ODNs containing CpG motifs were synthesised by Sangon Biotech Company (Shanghai, China). The CpG ODNs used in this study were as follows: ODN10, 5′-TCCATGACGTTTT*AAAACGTCATGGA*-3′, ODN1826, 5′-TCCATGACGTTCCTGACGTT-3′, non-CpG ODN control, 5′-TGCTGCTTTTGTGCTTTTGTGCTT-3′. Schematic diagrams of the secondary structure of ODN1826 and ODN10 are shown in Figure 1. All ODNs were diluted in phosphate-buffered saline (PBS) (0.1 mol/mL, pH 7.3) and stored at 4 °C before use.

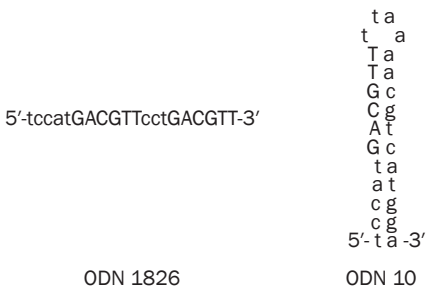

Figure 1. Schematic diagram of ODN1826 and ODN10. ODN1826 (left) is a typical linear type ODN. ODN10 (right) possesses a holistic, self-complementary palindrome structure.

Cells and cell lines

Spleen cells from 6- to 8-week-old C57BL/6 mice were cultured in RPMI-1640 medium supplemented with 10% (*v/v*) fetal bovine serum (FBS; GIBCO, Detroit, MI, USA) and antibiotics (100 IU/mL of penicillin and 100 IU/mL of streptomycin). The B16.F1 melanoma cells, which are syngeneic to C57BL/6 mice, were maintained *in vitro* as previously described[26, 27]. Yeast artificial chromosome-1 (YAC-1) cells were kindly provided by Prof Wen-xia ZHOU (Institute of Pharmacology and Toxicology, Beijing, China).

Experimental animals

Female C57BL/6 mice (6–8 weeks of age, 20.0±2.0 g), were purchased from the Experimental Animal Raising Center of the Academy of Military Medical Sciences (Beijing, China). All animal experiments and protocols were performed strictly in accordance with the Guide for the Care and Use of Laboratory Animals of the National Institutes of Health.

Tumor models

Exponentially growing B16.F1 melanoma cells were harvested when their viability exceeded 95%, which was determined by trypan blue staining. The cells were resuspended in 0.2 mL PBS and were injected subcutaneously (sc) at the dosage of 2×10^6 cells/animal into the right axilla of C57BL/6 mouse. The cells resuspended in 0.2 mL PBS were injected intraperitoneally (ip) into another group of individuals at a dose of 2×10^5 cells/animal.

Dose determination

Tumor-bearing mice (sc inoculated) were randomly divided into various treatment groups (10 animals in each group) and then treated ip with PBS or ODN10 on 9, 12, and 15 d post inoculation at the indicated doses (1, 5, or 25 mg/kg). Mice were checked daily for tumor growth. Tumor volume was calculated using the formula $1/2a\times b^2$, where a and b are the long and short diameters (in mm), respectively.

Survival assay

Tumor-bearing mice (ip inoculated) were divided randomly into various treatment groups (10 animals in each group). On 0, 3, and 7 d post inoculation and weekly thereafter, the mice received ip treatment of ODN10, ODN1826, or non-CpG ODN and PBS control, with all ODNs administered at the same dos-

age of 5 mg/kg. The survival of mice was checked daily until all animals died.

In vivo inhibitory effect on tumor growth

Subcutaneously inoculated tumor-bearing mice were divided randomly into four treatment groups (10 animals in each group) and then treated ip with various ODNs (ODN10, ODN1826, or non-CpG ODN, all at the dose of 5 mg/kg) or PBS on d 9 (when the tumor size reached approximately 5 mm in diameter), 12, 16, and 19 post tumor inoculation. Mice were checked daily for tumor growth, and the mice were sacrificed on d 20 post inoculation, when the tumor size from mice in the PBS control group reached approximately 25 mm on the long diameter. The tumors and spleens were collected from individual animals and weighed. The oxter lymph nodes and the ascites were collected for further study. The serum was collected into 2 mL microtubes and stored at -70 °C until measurement. The inhibitory effect of the ODNs on tumor growth *in vivo* was evaluated by the tumor growth inhibitory rate (TGI%), which was calculated by the formula $(W_0–W)/W_0×100\%$, where W represented the tumor weight of the ODN-treated groups, and W_0 was that of the PBS control group.

B and T lymphocyte proliferation assay

Proliferation of mouse B cells and T cells from tumor-bearing mice treated with different ODNs or the control, as well non-tumor-bearing mice was determined by a [^{3}H]-thymidine incorporation assay as described[28]. Briefly, splenocytes ($2×10^5$ cells) harvested from tumor-bearing mice or the normal mice were loaded in a 96-well culture plate with or without 5 μg/mL ConA or LPS (Sigma, St Louis, MO, US) and cultured at 37 °C in a 5% CO_2 atmosphere in RPMI-1640 for 72 h, with 1 μCi of [^{3}H]-thymidine ([^{3}H]-TdR, Institute of Atomic Energy, Beijing, China) added for the last 18 h. The cells were harvested, and the radioactivity was measured using a microBeta liquid scintillation counter (PerkinElmer, Waltham, MA, USA).

NK-mediated cytotoxicity assay

The NK cytotoxicity of splenocytes was detected with a 4 h ^{51}Cr release assay as previously described[27]. Briefly, splenocytes were harvested from tumor-bearing mice or non-tumor-bearing mice to serve as effector cells. One million YAC-1 cells/well (serving as target cells) were labelled with 50 μCi of ^{51}Cr for 1 h at 37 °C in a 96-well microplate and were then washed 3 times and incubated for 4 h with effector cells (with an E:T ratio of 50:1). Thereafter, supernatants were harvested, and the radioactivity was measured using a microBeta liquid scintillation counter (PerkinElmer, Waltham, MA, USA). The results are expressed as the mean percentage of specific lysis (triplicate wells)±SD, where percent specific lysis (%)=(experimental counts–target cell spontaneous release counts)/(maximal release counts–target cell spontaneous release counts)×100%. Spontaneous lysis was measured in wells containing only target cells, whereas maximum lysis was measured from the wells containing target cells incubated with 10% SDS.

Macrophage phagocytosis assay

The phagocytic ability of peritoneal macrophages was examined with a neutral red chromometry method strictly as described[29]. The data shown are representative of two replicate experiments.

Cytokines and chemokines ELISAs

Serum IL-12, IL-4, and IgE levels were measured twice by ELISA according to the manufacturer's instructions (IL-12 P40 and IL-4 kits were purchased from R&D Systems (Minneapolis, MN, USA), and the IgE kit was purchased from BETHYL (Montgomery, TX, USA). The plate reader was calibrated to the manufacturer's specifications, and the absorbance (450 nm) of the contents of each well was determined.

Histopathology and immunohistochemistry

After dissection, specimens of tumor, spleen, and oxter lymph nodes were fixed for 1 week in 4% buffered paraformaldehyde, embedded in paraffin, and stained with hematoxylin and eosin (H&E staining). PCNA, CD63, and CD80 expression levels in the tumor tissues were analysed by immunohistochemistry. Briefly, the paraffin-embedded sections were dewaxed and rehydrated. Antigen retrieval was performed in citrate buffer (pH 6.0) using the microwave technique. Endogenous peroxidase activity was quenched by 30% hydrogen peroxide in distilled water for 5–10 min and then washed in PBS. Primary antibodies (mouse anti-mouse monoclonal antibodies against PCNA, rabbit anti-mouse monoclonal antibodies against CD63 and CD80), the Mouse/Rabbit IgG SABC kit, and 3,3′-diaminobenzidine (DAB) solution were purchased from Wuhan Boster Biotechnology (Wuhan, China). Sections were sequentially incubated with primary antibody, the biotinylated anti-mouse/rabbit antibody, and the streptavidin peroxidase reagent. Peroxidase activity was detected with DAB solution. The same process performed without the primary antibody was used as a control. Sections were weakly counterstained with hematoxylin.

Statistical analysis

The data are shown as the mean±SD, and statistical significance was determined with the SPSS (v 10.0) software with Student's t test or analysis of variance (one-way ANOVA). Survival data were analysed by the Mantel-Cox logrank test. $P<0.05$ was considered to be statistically significant.

Results

Inhibitory effect on tumor growth *in vivo*

Inoculated B16 melanoma cells ($2×10^6$ cells/mouse) led to invasive tumors in 100% of the C57BL/6 mice. At d 8, when all mice presented a single mass (tumor size of ca 4 mm in diameter) in the right oxter, CpG ODNs were administered ip at the indicated doses (1, 5, and 25 mg/kg) on d 9, 12, and 14 after tumor inoculation. Mice were checked daily for tumor growth. The results showed that ODN10 inhibited the growth of the tumor *in vivo* in a dose-dependent manner (Figure 2A). Compared with the PBS control group, TGI rates of various

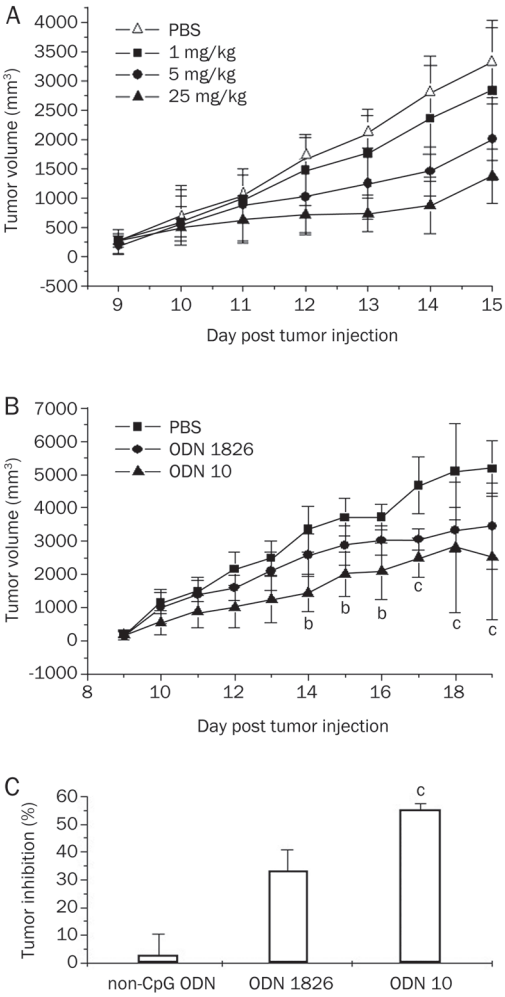

Figure 2. Effect of CpG ODNs on the growth of B16 melanoma in mice. C57BL/6 mice were inoculated *sc* with 2×10^6 B16 melanoma cells on d 0. Mice were treated with ODN1826 (positive control) and ODN10 at the indicated times and doses. (A) Dose-dependent effect of ODN10 (on d 9, 12, 14; at doses of 1, 5, and 25 mg/kg). (B) Tumor growth curve on d 20 post tumor inoculation at doses of 5 mg/kg at the indicated times (on d 9, 12, 16, and 19). $^bP<0.05$, $^cP<0.01$ *vs* PBS-treated mice; (C) Tumor growth inhibitory rate (TGI%) on d 20. $^cP<0.01$ *vs* ODN1826-treated mice. There were 10 mice in each group. The data shown represent two replicate experiments.

dosage groups (1, 5, and 25 mg/kg) were 13.4% ($P<0.05$), 35.5% ($P<0.01$), and 48.3% ($P<0.01$) on d 15, respectively. Figure 2B showed that the CpG ODN, at the same dosage level of 5 mg/kg, could inhibit the tumor proliferation significantly ($P<0.05$) from d 14, and more significantly ($P<0.01$) from d 17. On d 20, the TGI rate of the ODN10 treatment group was 51.1%, which is remarkably superior to that of ODN1826 (33.2%, $P<0.01$). The non-CpG ODN hardly showed any anti-tumor activity (Figure 2C). Compared with the positive ODN1826, ODN10 showed higher antitumor activity.

Prolonged survival assay

C57BL/6 mice received 2×10^5 cells/mouse B16 melanoma cells ip on d 0. The CpG or non-CpG ODN was administered ip on d 0, 3, 7, and weekly thereafter. As shown in Figure 3, on d 22, the survival rates of non-CpG ODN, ODN1826, and ODN10 groups were 0%, 20%, and 70%, respectively, compared with the PBS control group. CpG ODN can significantly prolong the survival of mice with B16 melanoma. ODN10 showed more effectiveness than ODN1826 and its potent antitumor activity *in vivo* was illustrated again.

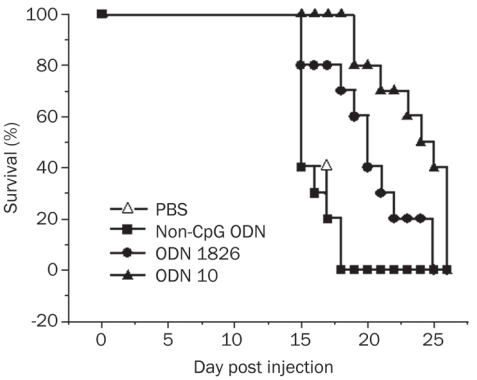

Figure 3. ODN10 prolonged the survival of mice implanted with B16 melanoma (2×10^5 cells/mouse). On d 0, 3, 7, and weekly thereafter, the mice received 5 mg/kg ip of the indicated ODN and were observed for survival. There were 10 mice in each group. The data shown represent two replicate experiments.

In vivo immunostimulatory activities of ODN10

We investigated the difference between the immune states of the tumor-bearing mice and normal mice, with the measurement indicators included in the study being the proliferation potential of B and T lymphocytes, NK cytotoxicity of splenocytes, and the phagocytic ability of peritoneal macrophages. The results showed that all of the above-mentioned immune activities were suppressed in tumor-bearing mice compared to their normal counterparts ($P<0.05$). However, the CpG immunostimulatory sequences significantly reversed the immunosuppression status in tumor-bearing mice. Among them, the ODN10 displayed the most prominent immunostimulatory potential (Figure 4).

As to the influences on chemokine or cytokine secretion, CpG ODN treatment is known to reverse established T_{h2} responses to T_{h1}-type responses[30, 31]. In the present study, IL-12 and the IL-4 were selected as the indicator cytokines, where the former is a T_{h1}-type cytokine, while the latter is a T_{h2}-type cytokine. As a result of induction of IL-4, B cells switch to IgE synthesis and inhibit IgG antibody synthesis; therefore, IgE levels in mice were also monitored as a marker of T_{h1}-T_{h2} response type conversion. The results showed that in the absence of CpG ODN treatment, serum from tumor-bearing mice contained markedly higher IL-4 and IgE levels and lower IL-12 levels than normal mice, suggesting a predominantly T_{h2} polarisation, while the CpG ODN treatment

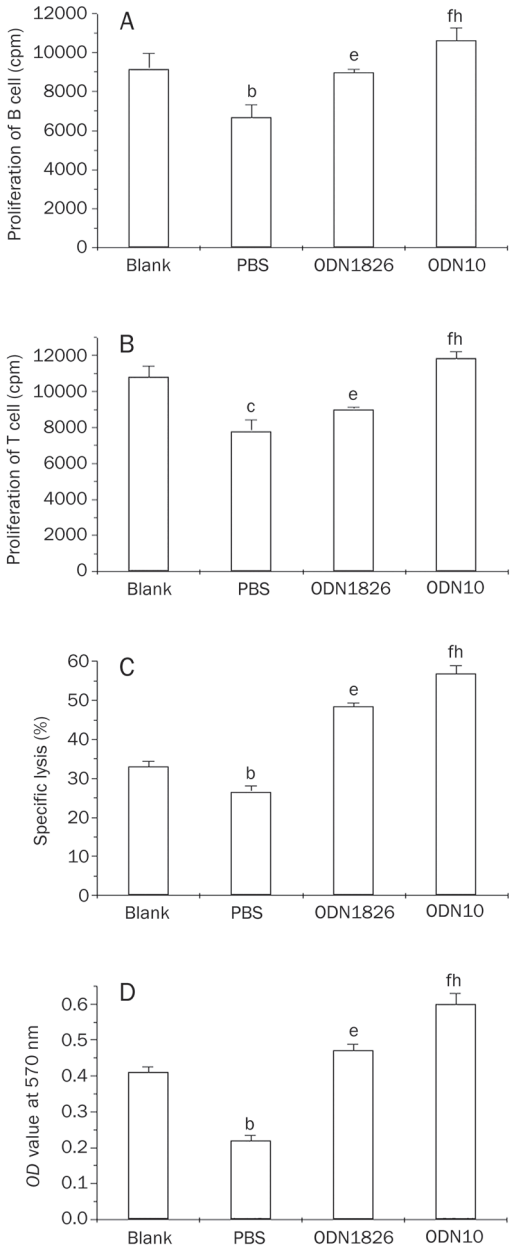

Figure 4. Immunostimulatory activity of CpG ODNs in tumor-bearing mice. Splenocytes were from the ODN-treated tumor-bearing mice (ODN1826 or ODN10), age-matched PBS-treated tumor-bearing mice (PBS), or age-matched normal mice (Blank). The peritoneal macrophages were also from the above groups. (A) Proliferation of the LPS-activated B cells. (B) Proliferation of the ConA-activated T cells. (C) NK cytotoxicity of splenocytes. (D) Phagocytic ability of peritoneal macrophage. $^{b}P<0.05$, $^{c}P<0.01$, PBS-treated tumor-bearing mice *vs* normal mice; $^{e}P<0.05$, $^{f}P<0.01$, ODN-treated tumor-bearing mice *vs* PBS-treated tumor-bearing mice; $^{h}P<0.05$, ODN10-treated tumor-bearing mice *vs* ODN1826-treated tumor-bearing mice. There were 10 mice in each group. The data shown represent two replicate experiments.

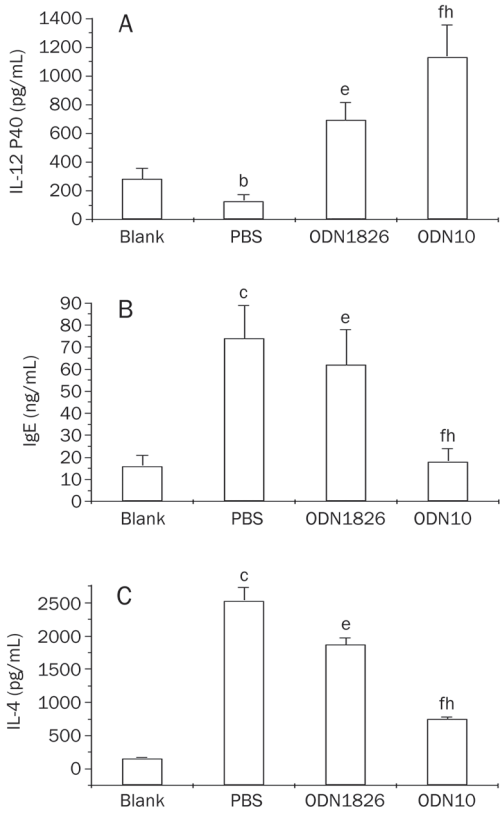

Figure 5. Induction of IL-12 P40 (A), IgE (B), or IL-4 (C) production by CpG ODN in mice. Sera were from the ODN-treated tumor-bearing mice (ODN1826 or ODN10), age-matched PBS-treated tumor-bearing mice (PBS), or age-matched normal mice (Blank). $^{b}P<0.05$, $^{c}P<0.01$, PBS-treated tumor-bearing mice *vs* normal mice; $^{e}P<0.05$, $^{f}P<0.01$, ODN-treated tumor-bearing mice *vs* PBS-treated tumor-bearing mice; $^{h}P<0.05$, ODN10-treated tumor-bearing mice *vs* ODN1826-treated tumor-bearing mice. There were 10 mice in each group. The data shown represent two replicate experiments.

markedly reversed the established T_{h2} responses to T_{h1}-type responses in tumor-bearing mice, characterised by the significant up-regulation of IL-12 and down-regulation of IL-4 and IgE. Again, ODN10 had more significantly robust immunostimulatory effects compared with ODN1826 (Figure 5).

Pathobiology and immunohistochemistry analysis

Figure 6 shows the H&E staining of tissue sections from formalin-fixed tumors obtained 20 d after tumor injection. PBS-treated tumors exhibited a solid growth pattern without necrosis. ODN10 treatment could make the tumor cell exhibit extensive cellular polymorphisms, including cavitate nuclei, swollen nuclei, and apoptosis. Figure 7 shows the H&E staining of tissue sections from spleen or oxter lymph nodes. The PBS group presented with large-scale necrosis and vasal infarct by metastatic melanoma masses in the spleen and metastatic melanoma in the vessels of oxter lymph nodes. Both the spleen and oxter lymph nodes were normal in the CpG ODN10 treatment group.

PCNA was expressed exclusively in tumor tissues of the melanoma mice, and ODN10 treatment decreased PCNA expression (Figure 8A–C). Expression of CD63 (Figure 8D–F), a melanoma metastasis-associated antigen, was similar to PCNA. On the contrary, ODN10 could induce expression of

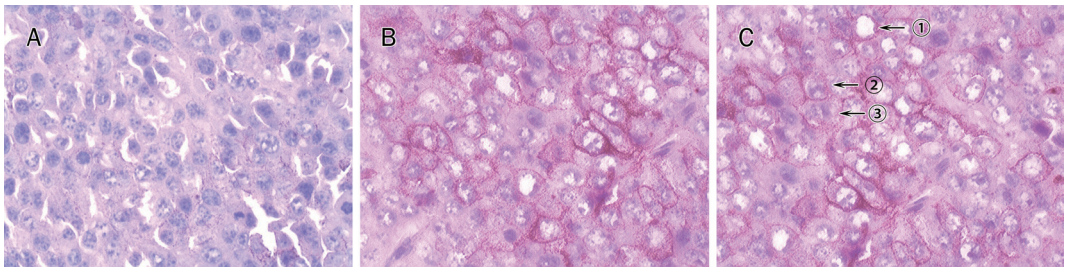

Figure 6. Tumor tissues were fixed in 4% buffered paraformaldehyde, embedded in paraffin and analysed histologically by H&E staining (×132). PBS-treated tumors showed a solid growth pattern without necrosis (A). Tumors treated with ODN1826 (B) or ODN10 (C) exhibited extensive cellular polymorphism, including cavitate nuclei (arrow①), swollen nuclei (arrow②), and apoptosis (arrow③).

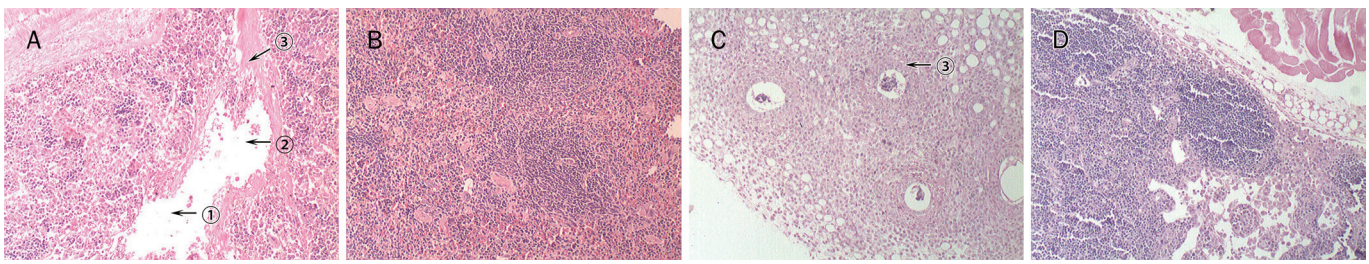

Figure 7. Histological analysis of spleen and oxter lymph nodes (HE staining, ×40). The PBS-treated group presented with large-scale necrosis (arrow①) and vasal infarct (arrow②) by a metastatic melanoma mass (arrow③) in the spleen (A), whereas the ODN10 treatment group was normal (B). The PBS-treated group showed a metastatic melanoma mass in the vessel of oxter lymph nodes (arrow③) (C), whereas the ODN10 treatment group was normal (D).

CD80, a cell-surface co-stimulatory molecule, in tumor tissues of melanoma-bearing mice (Figure 8G–I). The results from pathobiology and immunohistochemistry analysis indicated that CpG ODNs could activate the host anti-tumor immune response to inhibit the growth and metastasis of melanoma tumors in mice, and the novel ODN10 presented more potent activity.

Discussion

Bacterial and synthetic CpG DNAs promote B cell proliferation, immunoglobulin production and the secretion of a number of cytokines, including IL-6, IL-12, IFN-α, and IFN-γ, from B cells, monocytes/macrophages, DC cells and NK cells. ODN1826 is known as a strong immune activator that induces protective and curative T_{h1} responses against infections and tumorigenesis *in vivo* for mice[10, 23–25].

Our previous studies showed that ODN10, a novel CpG ODN containing a holistic self-complementary palindrome structure (5′-TCCATGACGTTT*AAAACGTCATGGA*-3′), possesses more potent immunostimulatory effects than a conventional CpG ODN (ODN1826), characterised by inducing a high level of IL-12 and IFN-α secretion and potentiating NK cell lytic activity[22]. We presume that their immunostimulatory properties may play roles in the CpG ODN-induced inhibition of B16 melanoma growth.

In our study, we found that the proliferation of B cells and T cells, NK cytotoxicity of splenocytes, and the phagocytic ability of peritoneal macrophages in tumor-bearing mice were lower than those in normal mice. Additionally, we also found that serum from tumor-bearing mice contained markedly higher IL-4 and IgE levels and lower IL-12 levels than normal mice, suggesting a predominantly T_{h2} polarisation. These phenomena indicated that the burden of the tumor might impair the function of an individual's innate and adaptive immune system. In tumor-bearing individuals, when IL-4, a type of T_{h2} cytokine, is produced at a higher level than normal, it can induce the IL-4 response genes in T cells and also shut off IgG synthesis by B cells and induce IgE synthesis. Under these conditions, the high T_{h2} cytokine level is dominant in the individual, an allergy-like inflammatory condition develops, the adaptive immune response is inhibited, and tumor development and progression continue. The increased IgE levels in cancer patients reflect impaired cellular immunity[1].

Our results also showed that the activities of the above-mentioned immune cells increased remarkably from the CpG ODN treatment, especially from ODN10 treatment. Meanwhile, we found that the antitumor activity of CpG ODNs was increased along with their immunomodulatory activity, for example, prolonged survival of mice with B16 melanoma, and inhibition of the tumor growth. Pathobiology and immunohistochemistry analysis also indicated that ODN10 could activate the host anti-tumor immune response to inhibit the *in vivo* growth and metastasis of melanoma tumors in mice.

Our study showed that ODN10 had potent antitumor activity, which was positively correlated with its superior immunomodulatory effects, including promoting B and T lymphocyte proliferation, enhancing NK cell and peritoneal macrophage activity, inducing IL-12 secretion, and inhibiting IL-4 and

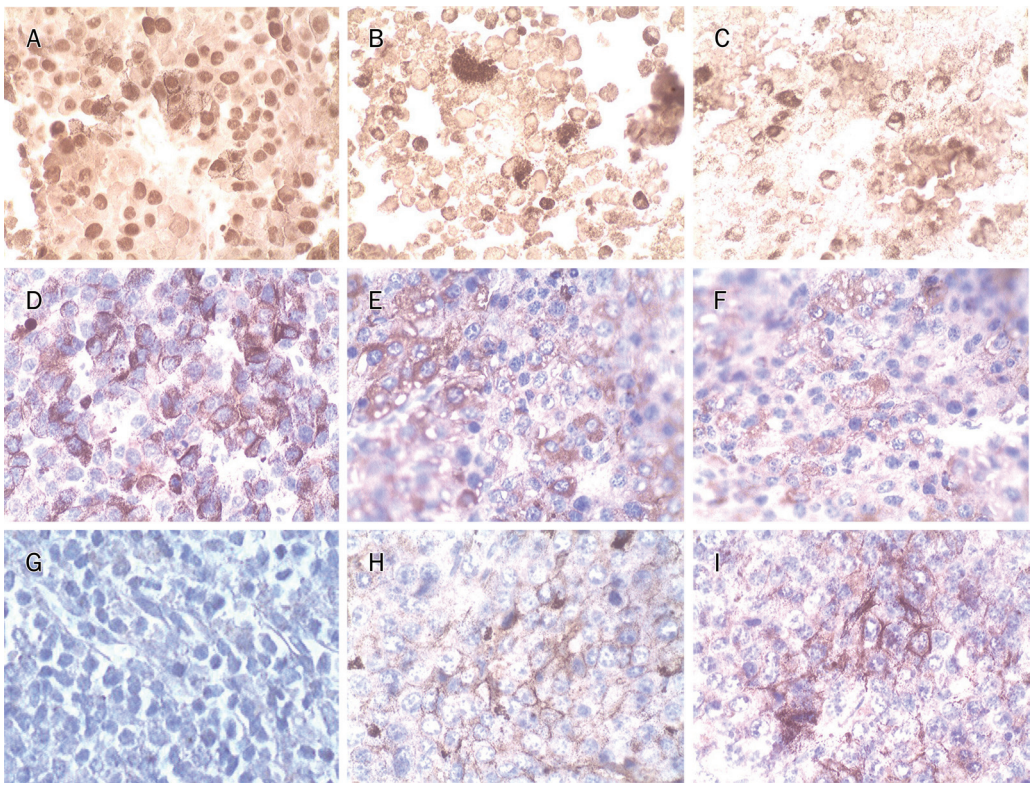

Figure 8. Immunohistochemistry analysis of tumor tissues (×132). Paraffin-embedded sections were dewaxed and rehydrated. Endogenous peroxidase activity was quenched by 30% hydrogen peroxide. Antigen retrieval was achieved by microwave treatment. Sections were sequentially incubated with primary antibody, the biotinylated anti-mouse/rabbit antibody, and the streptavidin peroxidase reagent. Peroxidase activity was detected with DAB solution, and sections were weakly counterstained with hematoxylin. PCNA was strongly expressed in PBS-treated mice (A), whereas it was remarkably decreased in ODN1826 (B) or ODN10-treated mice (C). CD63 was strongly expressed in PBS-treated mice (D), whereas it was remarkably decreased in ODN1826 (E) or ODN10-treated mice (F). The tumor stained negatively for co-stimulatory molecules CD80 in PBS-treated mice (G), whereas CD80 was expressed in ODN1826 (H) or ODN10-treated mice (I).

IgE secretions. We presume that ODN10 can induce pDC-mediated cellular adaptive immunity to release large amounts of type I IFN; the latter stimulates T_{h1} cells to secret IL-2 and IL-12, which induce the CTL precursors to differentiate into antitumor CTL cells and also induce B cells to synthesise antitumor IgG antibodies. Meanwhile, ODN10 can stimulate NK cells responsible for spontaneous cytotoxicity of a variety of tumor cells and can activate macrophages, scavengers of dead cell debris. In addition, our study also demonstrated that the novel ODN10 can reverse established T_{h2} responses to T_{h1}-type responses and change an individual's tumor microenvironment, which contributes to identifying and killing tumor cells.

In summary, our experimental results demonstrated that the novel ODN10 has more potent immunomodulatory and antitumor activity towards melanoma than other ODNs, and as such, displays a promising application in cancer immunotherapy in mice. Our study suggests that the palindrome may be essential to the immunostimulatory potency of a CpG ODN and contributes to its antitumor activity.

Acknowledgements

This work was supported by the National Natural Science Foundation of China (grant number 30572197) and the National High Biotechnology Development Program of China (grant number 2003AA2Z347B).

We gratefully acknowledge Prof Wen TAN (Cancer Institute & Hospital, Chinese Academy of Medical Sciences) for her excellent technical assistance.

Author contribution

Hai-yan DU, Li-hou DONG, Bi-jun ZHAO, Zhong-ming TANG, and Hai-feng SONG designed the research study; Jie FU, Lun OU, Xiao SUN, and Na LI performed the research; Qing-qing WANG and Fang CHEN analysed the data; Hai-yan DU, Li-hou DONG, and Bi-jun ZHAO wrote the manuscript.

References

1 Yechiel B. Molecular immunological approaches to biotherapy of human cancers — A review, hypothesis and implications. Anticancer Res 2006; 26: 1113–34.
2 Hemmi H, Takeuchi O, Kawai T, Kaisho T, Sato S, Sanjo H, *et al.* A Toll-like receptor recognizes bacterial DNA. Nature 2000; 408: 740–5.
3 Krieg AM. CpG motifs in bacterial DNA and their immune effects. Annu Rev Immunol 2002; 20: 709–60.
4 Klinman DM. Immunotherapeutic uses of CpG oligodeoxynucleotides.

Nat Rev Immunol 2004; 4: 249–58.
5 Latz E, Schoenemeyer A, Visintin A, Fitzgerald KA, Monks BG, Knetter CF, *et al*. TLR9 signals after translocating from the ER to CpG DNA in the lysosome. Nat Immunol 2004; 5: 190–8.
6 Verthelyi D, Klinman DM. Immunoregulatory activity of CpG oligonucleotides in humans and nonhuman primates. Clin Immunol 2003; 109: 64–71.
7 Marshall JD, Fearon K, Abbate C, Subramanian S, Yee P, Gregorio J, *et al*. Identification of a novel CpG DNA class and motif that optimally stimulate B cell and plasmacytoid dendritic cell functions. J Leukocyte Biol 2003; 73: 781–92.
8 Vollmer J, Weeratna R, Payette P, Jurk M, Schetter C, Laucht M, *et al*. Characterization of three CpG oligo-deoxynucleotide classes with distinct immunostimulatory activities. Eur J Immunol 2004; 34: 251–62.
9 Brunner C, Seiderer J, Schlamp A, Bidlingmaier M, Eigler A, Haimerl W, *et al*. Enhanced dendritic cell maturation of TNF-alpha or cytidine-phosphate-guanosine DNA drives T cell activation *in vivo* and therapeutic anti-tumor immune responses *in vitro*. J Immunol 2000; 165: 6278–86.
10 Ballas ZK, Krieg AM, Warren T, Rasmussen W, Davis HL, Waldschmidt M, *et al*. Divergent therapeutic and immunologic effects of oligodeoxynucleotides with distinct CpG ODN motifs. J Immunol 2001; 167: 4878–86.
11 Wooldridge JE, Ballas ZK, Krieg AM, Weiner GJ. Immunostimulatory oligodeoxynucleotides containing CpG motifs enhance the efficacy of monoclonal antibody therapy of lymphoma. Blood 1997; 89: 2994–8.
12 van Ojik HH, Bevaart L, Dahle CE, Bakker A, Jansen MJH, van Vugt MJ, *et al*. CpG-A and B oligodeoxynucleotides enhance the efficacy of antibody therapy by activating different effector cell populations. Cancer Res 2003; 63: 5595–600.
13 Heckelsmiller K, Beck S, Rall K, Sipos B, Schlamp A, Tuma E, *et al*. Combined dendritic cell and CpG oligonucleotide-based immune therapy cures large murine tumors that resist chemotherapy. Eur J Immunol 2002; 32: 3235–45.
14 Davila E, Celis E. Repeated administration of cytosine-phosphorothiolated guanine-containing oligonucleotides together with peptide/protein immunization results in enhanced CTL responses with anti-tumor activity. J Immunol 2000; 165: 539–47.
15 Blazar BR, Krieg AM, Taylor PA. Synthetic unmethylated cytosine-phosphateguanosine oligodeoxynucleotides are potent stimulators of antileukemia responses in naive and bone marrow transplant recipients. Blood 2001; 98: 1217–25.
16 Sharma S, Karakousis CP, Takita H, Shin K, Brooks SP. Intra-tumoral injection of CpG results in the inhibition of tumor growth in murine Colon-26 and B-16 tumors. Biotechnol Lett 2003; 25: 149–53.
17 Carpentier AF, Chen L, Maltonti F, Delattre JY. Oligodeoxynucleotides containing CpG motifs can induce rejection of a neuroblastoma in mice. Cancer Res 1999; 59: 5429–32.
18 Carpentier AF, Xie J, Mokhtari K, Delattre JY. Successful treatment of intracranial gliomas in rat by oligodeoxynucleotides containing CpG motifs. Clin Cancer Res 2000; 6: 2469–73.
19 Baines J, Celis E. Immune-mediated tumor regression induced by CpG-containing oligodeoxynucleotides. Clin Cancer Res 2003; 9: 2693–700.
20 Buhtoiarov IV, Sonde PM, Eickhoff JC, Rakhmilevich AL. Macrophages are essential for antitumour effects against weakly immunogenic murine tumours induced by class B CpG-oligodeoxynucleotides. Immunology 2007; 120: 412–23.
21 Mason KA, Neal R, Hunter N, Ariga H, Ang K, Milas L. CpG oligodeoxynucleotides are potent enhancers of radio- and chemoresponses of murine tumors. Radiother Oncol 2006; 80: 192–8.
22 Du HY, Xia SY, Song HF, Li N, Shang MM, Zou J, *et al*. Structure-efficacy relationships of immunostimulatory activity of CpG-containing oligodeoxynucleotides on mouse spleen cells. Acta Pharmacol Sin 2007; 28: 1637–44.
23 Walker PS, Scharton-Kersten T, Krieg AM, Love-Homan L, Rowton ED, Udey MC, *et al*. Immunostimulatory oligodeoxynucleotides promote protective immunity and provide systemic therapy for leishmaniasis via IL-12- and IFN-γ-dependent mechanisms. Proc Natl Acad Sci U S A 1999; 96: 6970–5.
24 Harandi AM, Eriksson K, Holmgren J. A protective role of locally administered immunostimulatory CpG oligodeoxynucleotide in a mouse model of genital herpes infection. J Virol 2003; 77: 953–62.
25 Gramzinski RA, Doolan DL, Sedegah M, Davis HL, Krieg AM, Hoffman SL. Interleukin-12- and gamma interferon-dependent protection against malaria conferred by CpG oligodeoxynucleotide in mice. Infect Immunol 2001; 69: 1643–9.
26 Blackwell SE, Krieg AM. CpG-A-induced monocyte IFN-gamma-inducible protein-10 production is regulated by plasmacytoid dendritic cell-derived IFN-alpha. J Immunol 2003; 170: 4061–8.
27 Ballas ZK, Rasmussen WL, Krieg AM. Induction of NK activity in murine and human cells by CpG motifs in oligodeoxynucleotides and bacterial DNA. J Immunol 1996; 157: 1840–5.
28 Shan BE, Hao JS, Li QX, Taqawa M. Antitumor activity and immune enhancement of murine interleukin-23 expressed in murine colon carcinoma cells. Cell Mol Immunol 2006; 3: 47–52.
29 Nie H, Meng LZ, Zhang H. Effects of accidental exposure to external cause of gingerol on endotoxemia mouse model induced by heat-stroke. Zhongguo Zhong Xi Yi Jie He Za Zhi 2006; 26: 529–32.
30 Serebrisky D, Teper AA, Huang CK, Lee SY, Zhang TF, Schofield BH, *et al*. CpG oligodeoxynucleotides can reserae T_{h2}-associated allergic airway responses and alter the B7.1/B7.2 expression in a murine model of asthma. J Immunol 2000; 165: 5906–12.
31 Kitagaki K, Jain VV, Businga TR, Hussain I, Kline JN. Immunomodulatory effects of CpG oligodeoxynucleotides on established T_{h2} responses. Clin Diagn Lab Immunol 2002; 9: 1260–9.

Acta Pharmacologica Sinica (2012) 33: 1055–1061
 1671-4083/12 $32.00
www.nature.com/aps

Original Article

Oridonin induces apoptosis and autophagy in murine fibrosarcoma L929 cells partly via NO-ERK-p53 positive-feedback loop signaling pathway

Yuan-chao YE[1], Hong-ju WANG[1], Lei XU[1], Wei-wei LIU[1], Bin-bin LIU[1], Shin-Ichi TASHIRO[2], Satoshi ONODERA[2], Takashi IKEJIMA[1, *]

[1]*China-Japan Research Institute of Medical and Pharmaceutical Sciences, Shenyang Pharmaceutical University, Shenyang 110016, China;* [2]*Department of Clinical and Biomedical Sciences, Showa Pharmaceutical University, Tokyo 194-8543, Japan*

Aim: To investigate the role of nitric oxide (NO) in oridonin-induced apoptosis and autophagy in murine fibrosarcoma L929 cells and the underlying molecular mechanisms.
Methods: Cell viability was measured using MTT assay. Intracellular NO level, $SubG_1$ cell ratio and autophagy cell ratios were analyzed with flow cytometry after diaminofluorescein-2 diacetate (DAF-2DA), propidium iodide (PI) and monodansylcadaverine (MDC) staining, respectively. Protein expression was examined using Western blot analysis.
Results: Exposure of L929 cells to oridonin (50 μmol/L) for 24 h led to intracellular NO production. Pretreatment with NOS inhibitor 1400w or *L*-NAME inhibited oridonin-induced apoptosis and autophagy in L929 cells. The pretreatment decreased the apoptosis-related protein Bax translocation and cytochrome *c* release, increased Bcl-2 level, reversed the autophagy-associated protein Beclin 1 increase and conversion of LC3 I to LC3 II. Furthermore, pretreatment with NO scavenger DTT completely inhibited oridonin-induced apoptosis and autophagy in L929 cells. In addition, oridonin (50 μmol/L) activated ERK and p53 in L929 cells, and the interruption of ERK and p53 activation by PD 98059, pifithrin-α, or ERK siRNA decreased oridonin-induced apoptosis and autophagy. The inhibition of NO production reduced oridonin-induced ERK and p53 activation, and NO production was down-regulated by blocking ERK and p53 activation.
Conclusion: NO played a pivotal role in oridonin-induced apoptosis and autophagy in L929 cells. Taken together with our previous finding that ERK contributes to p53 activation, it appears that NO, ERK, and p53 form a positive feedback loop. Consequently, we suggest that oridonin-induced apoptosis and autophagy are modulated by the NO-ERK-p53 molecular signaling mechanism in L929 cells.

Keywords: oridonin; murine fibrosarcoma L929 cells; apoptosis; autophagy; NO; ERK; p53

Acta Pharmacologica Sinica (2012) 33: 1055–1061; doi: 10.1038/aps.2012.53; published online 30 Jul 2012

Introduction

NO, which was identified as an endothelial-derived relaxing factor (EDRF) in 1987[1], is a ubiquitous cellular messenger molecule in the cardiovascular, nervous and immune systems, where it has been shown to participate in activities involving cardiovascular function, neurodegenerative diseases and cancer[2–4].

Oridonin (Figure 1A), an active diterpenoid that was isolated from *Rabdosia rubescens*, has various pharmacological and physiological functions, particularly for the treatment of cancers[5].

Apoptosis, also known as type I programmed cell death, is characterized by an ensemble of morphological features, including cellular shrinkage, plasma membrane blebbing, chromatin condensation, nuclear fragmentation and apoptotic body formation[6]. Apoptosis can be triggered by intrinsic and extrinsic pathways that involve either mitochondria or death receptors[7]. Macroautophagy (hereafter referred to as autophagy) is the most active form of autophagy and affects various physiological and pathological processes, including immunity, cancer and neurodegenerative diseases[8, 9]. Autophagy is the process by which organelles and cytosolic macromolecules are sequestered into double-membrane structures known as autophagosomes that are subsequently delivered to the lysosome for degradation[10]. Autophagy is regulated by several autophagy-related ATG genes, many of which have mammalian orthologs. Two well-known ATG genes in mammals are Beclin 1 and microtubule-associated

* To whom correspondence should be addressed.
E-mail ikejimat@vip.sina.com
Received 2012-02-23 Accepted 2012-04-20

protein light chain 3 (LC3). Beclin 1, which is the mammalian homolog of Atg6 and functions in either the autophagic pathway or the early formation of autophagosomes, plays a central role in the regulation of autophagy[11]. LC3, which is the mammalian homolog of Atg8, is associated with the autophagosomal membranes after autophagocytic processing. LC3 I normally exists in the cytosol; when autophagy is induced, LC3 I conjugates with phosphatidylethanolamine to form the autophagosome-associated LC3 II. The accumulation of LC3 II is correlated with the number of autophagosomes present[12].

The L929 murine fibrosarcoma cell line was derived in March 1948. Strain L was one of the first cell strains to be established in continuous culture, and clone 929 was the first cloned strain developed. The parent L strain was derived from normal subcutaneous areolar and adipose tissues of a 100-d-old male C3H/An mouse. Clone 929 was established (by the capillary technique for signal cell isolation) from the 95th subculture generation of the parent strain. It is widely believed that L929 is sensitive to tumor necrosis factor alpha (TNFα) and that TNFα-induced cell death is caspase-independent[13]. Our previous study demonstrated that oridonin could induce L929 cell caspase-independent apoptosis by the activation of the ERK-p53 signaling pathway[14, 15]. Interestingly, NO is known to activate both ERK and p53 via phosphorylation[16], and it appears to be involved in the regulation of apoptosis[17]. In this study, oridonin induced NO production, which mediated L929 cell apoptosis and autophagy and led to the activation of ERK and p53.

Materials and methods

Reagents

Oridonin was obtained from the Kunming Institute of Botany, Chinese Academy of Sciences (Kunming, China), and its purity was determined to be 99.4% by HPLC measurements. Fetal bovine serum was purchased from TBD Biotechnology Development (Tianjin, China); 3-(4,5-dimethylthiazol-2-yl)-2,5-diphenyl-tetrazolium bromide (MTT), propidium iodide (PI), monodansylcadaverine (MDC), RNase A, diaminofluorescein-2 diacetate (DAF-2DA), 1400w, *L*-NAME, sodium nitroprusside (SNP), DTT, PD98059 (PD), and pifithrin-α (PFT-α) were purchased from Sigma Chemical (St Louis, MO, USA). ERK small interfering RNA (siRNA), control siRNA and Lipofectamine 2000 were from Invitrogen (Invitrogen, Carlsbad, CA, USA). Rabbit polyclonal antibodies against Bax, Beclin 1, LC3, ERK, p-ERK, p53, and p-p53, mouse polyclonal antibodies against Bcl-2, cytochrome *c*, and β-actin and horseradish peroxidase-conjugated secondary antibodies were purchased from Santa Cruz Biotechnology (Santa Cruz, CA, USA).

Cell culture

L929 cells were cultured in RPMI-1640 medium (Gibco, NY, USA) supplemented with 10% fetal bovine serum (FBS) (Beijing Yuanheng Shenyang Research Institution of Biotechnology, Beijing, China), 100 μg/mL streptomycin, 100 U/mL penicillin, and 0.03% *L*-glutamine and maintained at 37 °C with 5% CO_2 in a humidified atmosphere. All of the experiments were performed on logarithmically growing cells.

Cell viability assay

Cells were seeded in 96-well plates at a concentration of 5×10^4 cells/mL. After 48 h of incubation, they were treated with oridonin in the presence or absence of the indicated inhibitors for 24 h. Cell viabilities were measured by MTT staining.

$$\text{Cell viability (\%)}=100-\frac{A_{492,\ \text{control}}-A_{492,\ \text{experimental}}}{A_{492,\ \text{control}}-A_{492,\ \text{blank}}}\times100$$

Flow cytometric analysis of NO levels

The intracellular NO was detected using the NO fluorescent probe diaminofluorescein-2 diacetate (DAF-2DA). Once diacetate groups of the DAF-2DA reagent are hydrolyzed by cytosolic esterases, DAF-2 is released and sequesters the reagent inside of the cell. NO production converts the non-fluorescent dye, DAF-2, to its fluorescent triazole derivative, DAF-2 triazole (DAF-2T)[18]. The L929 cells were treated with oridonin for the indicated periods or co-incubated with the given inhibitors for 24 h. They were then incubated with 10 μmol/L DAF-2DA at 37 °C for 30 min to measure NO production. Next, the cells were harvested, and the pellets were suspended in 0.5 mL PBS. Finally, the samples were analyzed by flow cytometry (Becton Dickinson, Franklin Lakes, NJ, USA).

Measurement of $SubG_1$ cells

The L929 cells were treated with oridonin for the indicated periods or co-incubated with the given inhibitors for 24 h. The collected cells were fixed in 70% ethanol, stained for DNA content with PI at 4 °C in the dark for 30 min, and measured by flow cytometry (Becton Dickinson, Franklin Lakes, NJ, USA).

Measurement of autophagy

After incubation with oridonin for the indicated periods, the cells were cultured with 0.05 mmol/L MDC at 37 °C for 1 h and then analyzed by flow cytometry.

siRNA transfection

The cells were transfected with siRNA by using Lipofectamine 2000 according to the manufacturer's instructions. The transfected cells were used for subsequent experiments 24 h later.

Western blot analysis

The L929 cells were treated with oridonin for the indicated periods or co-incubated with the given inhibitors for 24 h. Equivalent amounts (30 μg) of total protein were separated by SDS–PAGE and transferred to a nitrocellulose membrane. Immunoblot analysis was performed as described previously[19].

Preparation of mitochondrial and cytosolic extracts

Cells were collected by centrifugation at 200×*g* at 4 °C for 5 min and washed twice with ice-cold PBS. The cell pellets were resuspended in ice-cold homogenizing buffer (250 mmol/L sucrose, 20 mmol/L HEPES, 10 mmol/L KCl, 1 mmol/L

EDTA, 1.5 mmol/L $MgCl_2$, 1 mmol/L DTT, 1 mmol/L PMSF, 1 μg/mL aprotinin, and 1 μg/mL leupeptin). The cells were homogenized with 20 strokes of a Dounce homogenizer at 4 °C. Nuclei and intact cells were removed by centrifugation at 500×*g* at 4 °C for 12 min. The supernatants were subjected to centrifugation for 30 min (12 000×*g*, 4 °C) to precipitate the mitochondria. The resultant supernatants were used as the cytosolic fraction, and the pellets were lysed in lysis buffer (50 mmol/L HEPES, pH 7.4, 1% Triton X-100, 2 mmol/L sodium orthovanadate, 100 mmol/L sodium fluoride, 1 mmol/L EDTA, 1 mmol/L EGTA, and 1 mmol/L PMSF) on ice for 1 h. The lysates were subjected to centrifugation at 12 000×*g*, 4 °C for 30 min, and the supernatants were used as the mitochondrial fractions.

Statistical analysis

All of the presented data and results were confirmed in at least three independent experiments. The data are expressed as the mean±standard error (SEM). The data were analyzed with a one-way ANOVA using the Statistics Package for Social Science (SPSS) software (version 13.0; SPSS, Chicago, IL, USA), and the statistical comparisons were performed using least significant difference (LSD) *post-hoc* tests. $P<0.05$ was considered to be statistically significant.

Results

Oridonin induces NO production

The production of NO was evaluated by a flow cytometric analysis with the NO fluorescent probe DAF-2DA. In oridonin-treated L929 cells, the DAF-2T-positive cell ratio increased over time (Figure 1B). These data suggest that oridonin induces NO production.

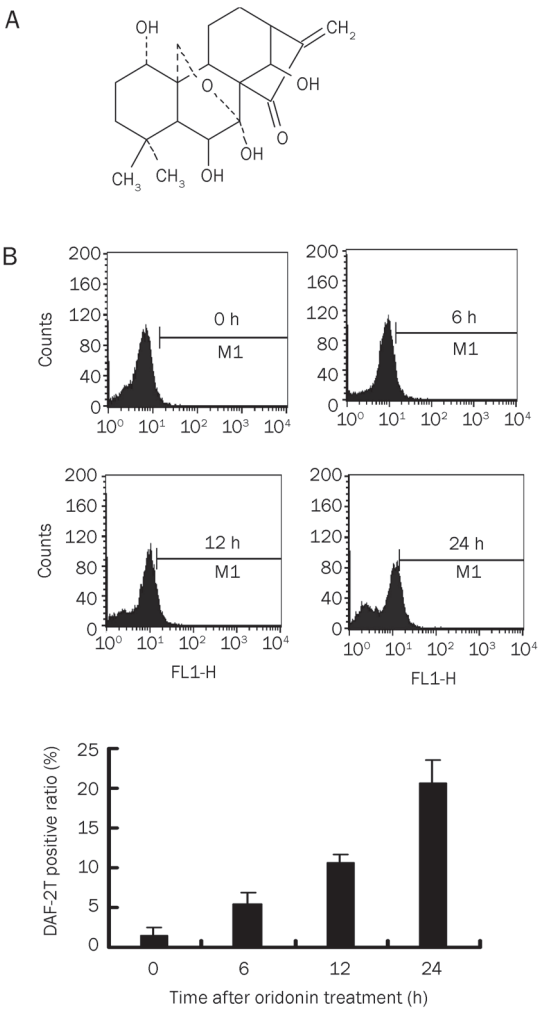

Figure 1. Oridonin induced the generation of nitric oxide. (A) Chemical structure of oridonin. (B) Cells were incubated with 50 μmol/L oridonin for 0, 6, 12, and 24 h followed by flow cytometric analyses of NO level changes after DAF-2DA staining. Mean±SEM. *n*=3.

NO mediates apoptosis and promotes cytoprotective autophagy in oridonin-treated L929 cells

Cellular NO is primarily synthesized from L-arginine by a family of NOSs[20]. Thus, we introduced the NOS inhibitors 1400w[21] and *L*-NAME[22] to investigate the role of NO in oridonin-induced cell growth inhibition. As shown in Figure 2A, the increase in NO was suppressed by 1400w or *L*-NAME. Additionally, the 1400w or *L*-NAME pretreatment reversed the oridonin-induced cell growth inhibition (Figure 2B). These results suggested that oridonin-induced NO production caused cell death in L929 cells.

Our previous study demonstrated that oridonin induced apoptotic cell death and protective autophagy[23]. To investigate the role of NO in oridonin-induced L929 cell apoptosis and autophagy, the cells were pretreated with 1400w and *L*-NAME. Pretreatment with 1400w or *L*-NAME decreased the number of $SubG_1$ cells compared to the oridonin alone treatment group (Figure 2C). These findings indicated that NO induced apoptosis in the oridonin-treated L929 cells. Our previous study also showed that oridonin induced apoptosis mainly through the mitochondrial pathway[15]. Hence, the expression of the mitochondria-related proteins Bax, cytochrome *c*, and Bcl-2 were examined using Western blot analyses (Figure 1S). Pretreatment with 1400w or L-NAME sequestered the mitochondrial Bax and cytosolic cytochrome c and increased Bcl-2 levels (Figure 2E). The inhibition of NO by 1400w or L-NAME also attenuated the induction of autophagy (Figure 2D). Furthermore, we obtained similar western blot results from the assessment of Beclin 1 levels and the conversion of LC3 I to LC3 II (Figure 2E). Collectively, these results indicated that NO was involved in oridonin-induced apoptosis and autophagy in L929 cells. To further confirm the role of NO in oridonin-induced apoptosis and autophagy, we introduced DTT to eliminate NO production[18] (Figure 2F). DTT pretreatment reversed oridonin-induced apoptosis (Figure 2G) and autophagy (Figure 2H). Further studies verified that pretreatment with DTT decreased Bax translocation and cytochrome *c* release and increased Bcl-2 levels, whereas this pretreatment reversed the Beclin 1 increase and conversion of LC3 I to LC3 II (Figure 2I). On the basis of the above results, we suggest that the oridonin-induced production of NO is

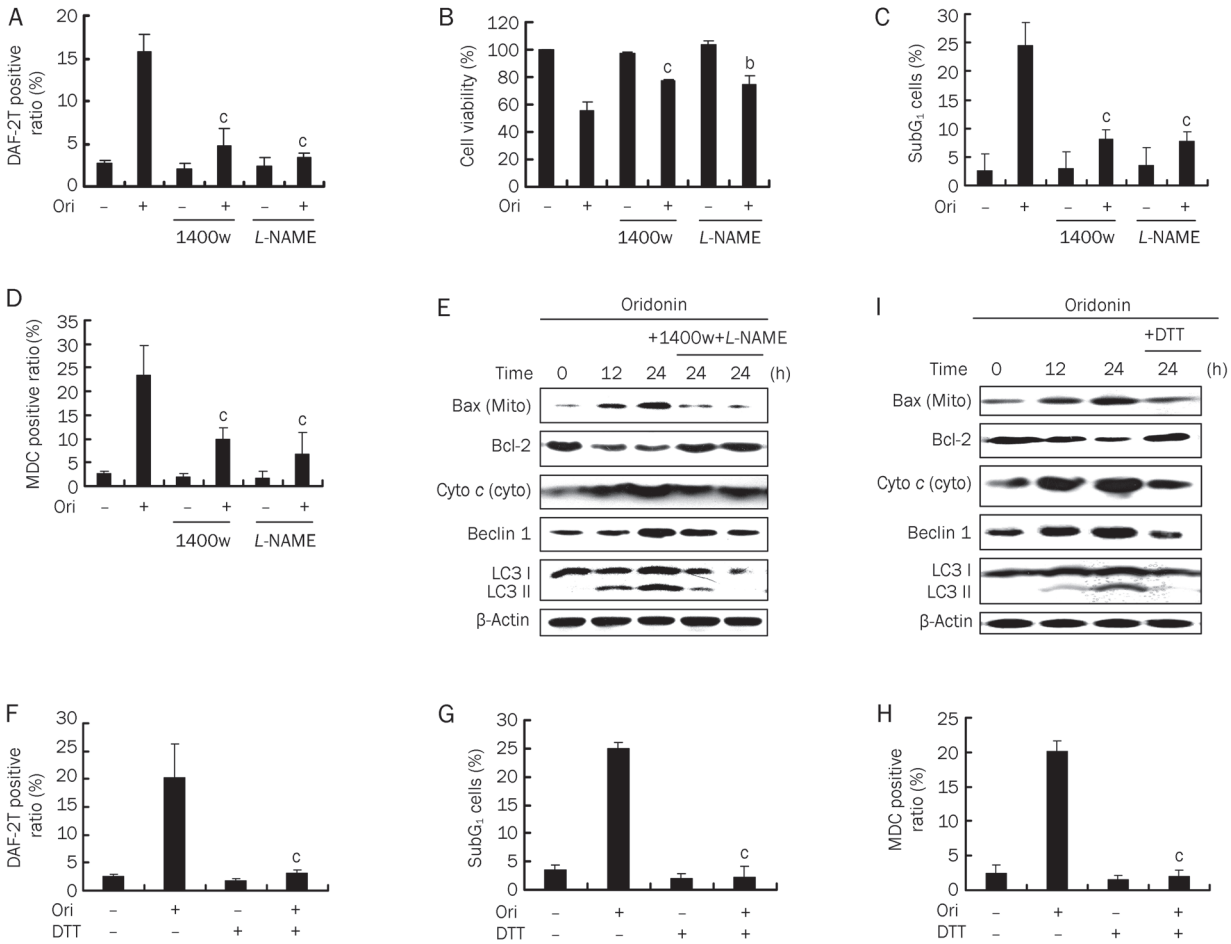

Figure 2. Effect of nitric oxide on oridonin-induced apoptosis and autophagy. (A) Cells were incubated with 50 μmoL/L oridonin for 24 h in the presence or absence of 1400w (10 μmoL/L) or *L*-NAME (20 μmoL/L) for 3 h and then analyzed by flow cytometry for NO level changes after DAF-2DA staining. (B) Cell viability was measured by MTT assay. (C–E) Cells were incubated with 50 μmoL/L oridonin for 24 h in the presence or absence of 1400w (10 μmoL/L) or L-NAME (20 μmoL/L) for 3 h. (C) Flow cytometric analyses of apoptotic cell ratios after PI staining ($SubG_1$ cells). (D) Flow cytometric analyses of autophagic cell ratios after MDC staining. (E) Western blot analyses for the detection of mitochondrial Bax, Bcl-2, cytosolic cytochrome c, Beclin 1, and LC3 levels. β-Actin was used as an equal loading control. (F–H) Cells were pretreated with 0.5 mmoL/L DTT and then cultured with 50 μmoL/L oridonin for 24 h. (F) Flow cytometric analyses of NO level changes after DAF-2DA staining. (G) Apoptotic cell ratios after PI staining ($SubG_1$ cells). (H) Autophagic cell ratios after MDC staining. (I) Cells were incubated with 50 μmoL/L oridonin for 24 h in the presence or absence of 0.5 mmoL/L DTT and then analyzed by Western blotting to detect mitochondrial Bax, Bcl-2, cytosolic cytochrome c, Beclin 1, and LC3 levels. β-Actin was used as a loading control. Mean±SEM. n=3. $^bP<0.05$, $^cP<0.01$ *vs* oridonin-only treatment group.

bifunctional in oridonin-induced cell death; it induces mitochondrial malfunction to promote the mitochondrial apoptotic pathway and simultaneously induces autophagy to protect the cells from dying.

ERK-p53 is involved in oridonin-induced apoptosis and autophagy

Extracellular signal-regulated kinase (ERK), which is a member of the mitogen-activated protein kinase family, and tumor suppressor protein p53 have been reported to be invovled in apoptosis and autophagy[24–26]. It is not known whether ERK and p53 participate in oridonin-induced cell apoptosis and autophagy. To address this question, the cells were pretreated with 5 μmol/L MEK inhibitor PD98059 (PD) and 5 μmol/L p53 inhibitor pifithrin-α (PFT-α) to inhibit ERK and p53 activation, respectively. As shown in Figure 3A, compared with the oridonin alone group, the PD pretreated group and the PFT-α pretreated group had significantly increased cell viabilities. The Western blot analyses demonstrated that p-ERK and p-p53 levels rose over time after oridonin administration, despite the lack of obvious changes in ERK and p53 levels (Figure 3B). Furthermore, the inhibition of ERK or p53 activation decreased apoptotic cell death (Figure 3C) and MDC positive ratios (Figure 3D). The Western blot analyses also showed that PD or PFT-α pretreatment reversed the oridonin-induced Bax translocation, cytochrome *c* release and declining Bcl-2 levels along with Beclin 1 activation and the conversion of LC3 I to LC3 II (Figure 3E). These results indicate that ERK and p53 are involved in oridonin-induced apoptosis and autophagy. In our previous work[15] oridonin-induced ERK contributed to p53 activation; thus, we introduced ERK-directed siRNA

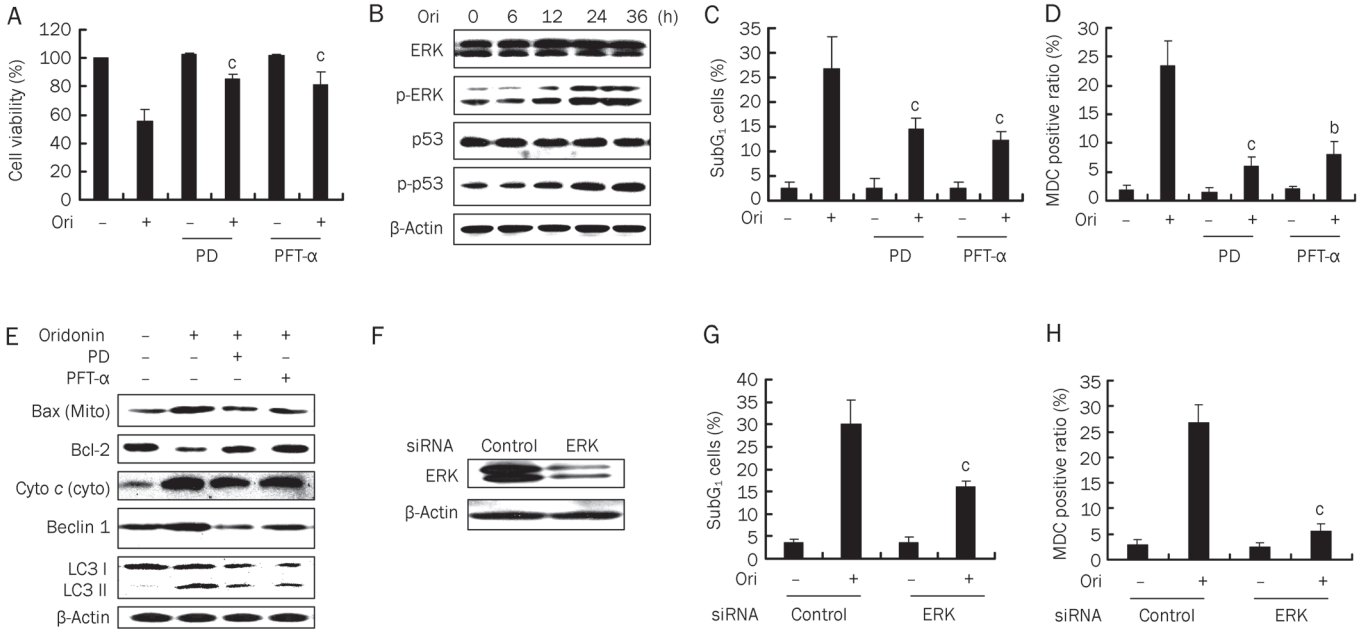

Figure 3. Effects of ERK and p53 on oridonin-induced apoptosis and autophagy. Cells were incubated with 50 μmol/L oridonin for 24 h in the presence or absence of PD 98059 (PD) (5 μmol/L) or pifithrin-α (PFT-α) (5 μmol/L) for 3 h. (A) Cell viabilities were measured by MTT assay. (B) Western blot analyses for the detection of ERK, p-ERK, p53, and p-p53 levels after oridonin treatment for the indicated time periods. β-Actin was used as a loading control. (C) Flow cytometric analyses of apoptotic cell ratios after PI staining ($SubG_1$ cells). (D) Autophagic cell ratios after MDC staining. (E) Western blot analyses for the detection of mitochondrial Bax, cytosolic cytochrome c, Beclin 1 and LC3 levels. β-actin was used as a loading control. (F) The cells were transfected with control or ERK-directed siRNA for 24 h, and then ERK levels were examined by Western blot analyses. β-Actin was used as a loading control. (G–H) After transfection, flow cytometric analyses of apoptotic (G) and autophagic (H) cell ratios were conducted after oridonin treatment. Mean±SEM. n=3. ^bP<0.05, ^cP<0.01 *vs* oridonin-only treatment group.

to confirm the above results (Figure 3F). As shown in Figure 3G and H, the oridonin-induced apoptotic and autophagic ratios decreased after transfection with ERK-directed siRNA. Collectively, these results provided strong evidence that the ERK-p53 pathway is involved in the apoptotic and autophagic pathways simultaneously.

NO contributes to ERK-p53 activation, which provokes NO production in oridonin-treated L929 cells

It should be noted that both NO, ERK and p53 participate in oridonin-induced apoptosis and autophagy. Hence, exploring the correlation between NO and ERK-p53 was the logical next step. Compared with the oridonin alone group, 1400w or *L*-NAME pretreated cells showed decreased ERK and p53 activities as shown by p-ERK and p-p53 protein levels, suggesting that NO contributes to ERK and p53 activation (Figure 4A). Next, to investigate whether ERK and p53 affected NO production, the cells were pretreated with PD, PFT-α or ERK-directed siRNA. As shown in Figure 4B and 4C, compared with the oridonin alone group, the PD, PFT-α, and ERK-

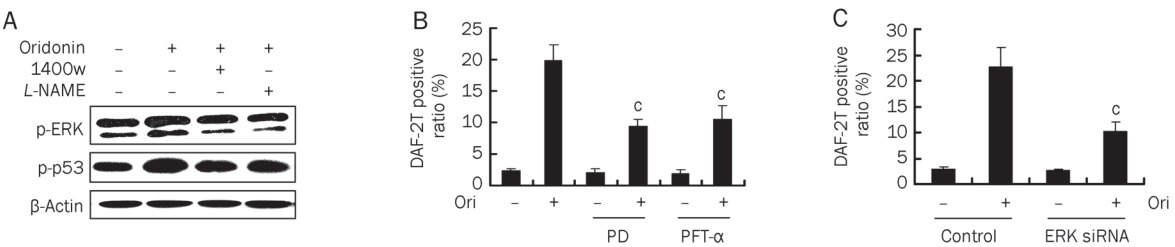

Figure 4. Relationship between nitric oxide and ERK-p53. (A) Cells were incubated with 50 μmol/L oridonin for 24 h in the presence or absence of 1400w (10 μmol/L) or *L*-NAME (20 μmol/L) for 3 h and then analyzed by Western blotting to assess the p-ERK and p-p53 levels. β-Actin was used as a loading control. (B) Cells were incubated with 50 μmol/L oridonin for 24 h in the presence or absence of PD98059 (PD) (5 μmol/L) and pifithrin-α (PFT-α) (5 μmol/L) for 3 h and then analyzed by flow cytometry to measure NO level changes after DAF-2DA staining. (C) Cells were transfected with control or ERK-directed siRNA for 24 h, and then flow cytometric analyses were carried out to evaluate NO levels after oridonin treatment. Mean±SEM. n=3. ^cP<0.01 *vs* oridonin-only treatment group.

directed siRNA pretreated groups showed markedly reduced DAF-2T ratios, indicating that ERK and p53 are positive regulators in oridonin-induced NO production.

Discussion

NO is a simple diatomic gas and free radical, and its biochemical features not only enable it to be an ideal signaling molecule but also exert a wide range of biological effects that can be summarized into three main categories: regulatory, deleterious and protective[27]. NO production during pre-apoptosis has been shown to be associated with mitochondrial dysfunction[28]. The mitochondrion works as a pivotal executioner in apoptotic signaling pathways. Here, we showed that the mitochondria-associated pro-apoptotic protein Bax translocated to the mitochondria, and cytochrome *c* was released from the mitochondria into the cytosol after oridonin treatment. In contrast, expression of the anti-apoptotic protein Bcl-2 was down-regulated. Moreover, the inhibition of NO production by 1400w or *L*-NAME reduced Bax translocation and cytochrome *c* release and increased Bcl-2 levels. These results indicate that oridonin-induced NO production results in mitochondrial dysfunction leading to apoptosis. As an inducer of apoptosis, little is known regarding the role of NO in the modulation of autophagy. In this study, we found that oridonin-induced NO production provoked autophagy as demonstrated by Beclin 1 activation and the conversion of LC3 I to LC3 II.

NO has been reported to induce the activation of ERK and p53 in various cell types, suggesting the involvement of ERK and p53 in oridonin-induced cell death[17, 29, 30]. Consistent with these observations, our results demonstrated that NO production regulated ERK and p53 activation, resulting in apoptotic cell death and protective autophagy in oridonin-treated L929 cells. Thomas *et al* have shown that low levels of NO induce ERK phosphorylation, whereas p53 phosphorylation occurs at considerably higher levels[16]. In our study, the activation of ERK and p53 via phosphorylation was accompanied by the sustained production of NO after oridonin administration. It should be noted that pretreatment with DTT but not 1400w or *L*-NAME was able to completely eliminate NO production and thoroughly inhibit apoptosis and autophagy. In addition to NO clearance, DTT is also a scavenger of reactive oxygen species (ROS) and peroxynitrite ($ONOO^-$)[31], and NO can react with superoxide radicals, leading to the formation of $ONOO^-$ [32]. Thus, we speculate that (in addition to NO) ROS and reactive nitrogen species (RNS), such as $ONOO^-$, may participate in ERK and p53 activation and mediate apoptosis and autophagy in oridonin-treated L929 cells.

Paradoxically, the NO-ERK-p53 pathway activated apoptotic cell death and autophagy, although autophagy has previously been demonstrated to antagonize apoptosis and thereby protect cells from dying[23]. This phenomenon might occur because of the crosstalk between apoptosis and autophagy, which was first recognized when Beclin 1 was initially identified as a Bcl-2-interacting protein[33]. The binding of the anti-apoptotic proteins Bcl-2 and Bcl-xL to Beclin 1 inhibits autophagosome formation to decrease Beclin 1-dependent autophagy[34]. Bcl-2, the first protein that has been found to interact with Beclin 1, has been shown to inhibit autophagy, in addition to its well-established role in apoptotic inhibition[9]. The oridonin treatment down-regulated Bcl-2 levels, whereas the 1400w or L-NAME pretreatment reversed this decline. The inhibition of ERK or p53 activation also reversed this decrease in Bcl-2 levels. These results support the idea that the inhibition of Bcl-2 levels by the NO-ERK-p53 pathway leads to Beclin 1 activation and thereby induces autophagy. By contrast, a series of studies have reported that cytoplasmic p53 suppresses autophagy and that nuclear p53 triggers it[7, 33, 34]. PFT-α has been shown to specifically block the transcriptional activity of p53[35]. In our study, the PFT-α pretreatment resulted in decreased apoptosis and autophagy, accompanied by reductions in Bax and cytochrome *c*, and increased Bcl-2 levels with the simultaneous suppression of expression of the autophagic protein Beclin 1 and the conversion of LC3 I to LC3 II. Although the total p53 levels did not significantly change over time, the p-p53 levels markedly increased, and p53 translocated from the cytoplasm to the nucleus (Figure 2S). It is conceivable that nuclear p53 both triggered autophagy and activated Bax-dependent apoptotic signaling pathways.

In conclusion, oridonin induced NO production, which mediated apoptosis and autophagy. NO production activated the ERK-p53 signaling pathway; in turn, ERK-p53 activation provided positive feedback for NO production, which stimulated apoptosis and autophagy. This dual action of NO as both an important player in apoptotic cell death and protective autophagy might aid in the development of an effective treatment to target NO toxicity.

Acknowledgements

This study was supported by the National Key Scientific Project for New Drug Discovery and Development, (2009ZX09301-012), 2009-2010, China.

Author contribution

Yuan-chao YE, Wei-wei LIU, Bin-bin LIU, and Takashi IKEJIMA designed the research; Yuan-chao YE, Hong-ju WANG and Lei XU performed the research; Shin-Ichi TASHIRO and Satoshi ONODERA contributed some reagents; Yuan-chao YE analyzed the data and wrote the paper; Takashi IKEJIMA revised the paper.

Supplementary information

Supplementary figures are available at the Acta Pharmacologica Sinica website.

References

1 Palmer RM, Ferrige AG, Moncada S. Nitric oxide release accounts for the biological activity of endothelium-derived relaxing factor. Nature 1987; 327: 524–26.

2 Strijdom H, Chamane N, Lochner A. Nitric oxide in the cardiovascular system: a simple molecule with complex actions. Cardiovasc J Afr 2009; 20: 303–10.

3 Gu Z, Nakamura T, Lipton SA. Redox reactions induced by nitrosative

stress mediate protein misfolding and mitochondrial dysfunction in eurodegenerative diseases. Mol Neurobiol 2010; 41: 55–72.
4 Ridnour LA, Thomas DD, Switzer C, Flores-Santana W, Isenberg JS, Ambs S, *et al*. Molecular mechanisms for discrete nitric oxide levels in cancer. Nitric Oxide 2008; 19: 73–6.
5 Kezoe T, Chen SS, Tong XJ, Heber D, Taguchi H, Koeffler HP. Oridonin induces growth inhibition and apoptosis of a variety of human cancer cells. Int J Oncol 2007; 23: 1187–9.
6 Taatjes DJ, Sobel BE, Budd RC. Morphological and cytochemical determination of cell death by apoptosis. Histochem Cell Biol 2008; 129: 33–43.
7 Elmore S. Apoptosis: a review of programmed cell death. Toxicol Pathol 2007; 35: 495–516.
8 Levine B, Mizushima N, Virgin HW. Autophagy in immunity and inflammation. Nature 2011; 469: 323–35.
9 Chen N, Debnath J. Autophagy and tumorigenesis. FEBS Lett 2010; 584: 1427–35.
10 Lleo A, Invernizzi P, Selmi C, Coppel RL, Alpini G, Podda M, *et al*. Autophagy: highlighting a novel player in the autoimmunity scenario. J Autoimmun 2007; 29: 61–8.
11 Morselli E, Galluzzi L, Kepp O, Vicencio JM, Criollo A, Maiuri MC, *et al*. Anti- and pro-tumor functions of autophagy. Biochim Biophys Acta 2009; 1793: 1524–32.
12 Kabeya Y, Mizushima N, Ueno T, Yamamoto A, Kirisako T, Noda T, *et al*. LC3, a mammalian homologue of yeast Apg8p, is localized in autophagosome membranes after processing. EMBO J 2000; 19: 5720–8.
13 Huang J, Wu L, Tashiro S, Onodera S, Ikejima T. A comparison of the signal pathways between the TNF alpha- and oridonin-induced murine L929 fibrosarcoma cell death. Acta Med Okayama 2005; 59: 261–70.
14 Cheng Y, Qiu F, Huang J, Tashiro S, Onodera S, Ikejima T. Apoptosis-suppressing and autophagy-promoting effects of calpain on oridonin-induced L929 cell death. Arch Biochem Biophys 2008; 475: 148–55.
15 Cheng Y, Qiu F, Ye YC, Tashiro S, Onodera S, Ikejima T. Oridonin induces G_2/M arrest and apoptosis via activating ERK-p53 apoptotic pathway and inhibiting PTK-Ras-Raf-JNK survival pathway in murine fibrosarcoma L929 cells. Arch Biochem Biophys 2009; 490: 70–5.
16 Thomas DD, Espey MG, Ridnour LA, Hofseth LJ, Mancardi D, Harris CC, *et al*. Hypoxic inducible factor 1alpha, extracellular signal-regulated kinase, and p53 are regulated by distinct threshold concentrations of nitric oxide. Proc Natl Acad Sci U S A 2004; 101: 8894–9.
17 Chan WH. Photodynamic treatment induces an apoptotic pathway involving calcium, nitric oxide, p53, p21-activated kinase 2, and c-Jun N-terminal kinase and inactivates survival signal in human umbilical vein endothelial cells. Int J Mol Sci 2011; 12: 1041–59.
18 Gumpricht E, Dahl R, Yerushalmi B, Devereaux MW, Sokol RJ. Nitric oxide ameliorates hydrophobic bile acid-induced apoptosis in isolated rat hepatocytes by non-mitochondrial pathways. J Biol Chem 2002; 227: 25823–30.
19 Ye YC, Yu L, Wang HJ, Tashiro S, Onodera S, Ikejima T. TNFα-induced necroptosis and autophagy via supression of p38-NF-κB survival pathway in L929 cells. J Pharmacol Sci 2011; 117: 160–9.
20 Knott AB, Bossy-Wetzel E. Nitric oxide in health and disease of the nervous system. Antioxid Redox Signal 2009; 11: 541–54.
21 Pacher P, Beckman JS, Liaudet L. Nitric oxide and peroxynitrite in health and disease. Physiol Rev 2007; 87: 315–424.
22 Yuan H, Perry CN, Huang C, Iwai-Kanai E, Carreira RS, Glembotski CC, *et al*. LPS-induced autophagy is mediated by oxidative signaling in cardiomyocytes and is associated with cytoprotection. Am J Physiol Heart Circ Physiol 2009; 296: H470–9.
23 Cheng Y, Qiu F, Ye YC, Guo ZM, Tashiro S, Onodera S, *et al*. Autophagy inhibits reactive oxygen species-mediated apoptosis via activating p38-nuclear factor-kappa B survival pathways in oridonin-treated murine fibrosarcoma L929 cells. FEBS J 2009; 276: 1291–306.
24 Lee YJ, Cho HN, Soh JW, Jhon GJ, Cho CK, Chung HY, *et al*. Oxidative stress-induced apoptosis is mediated by ERK1/2 phosphorylation. Exp Cell Res 2003; 291: 251–66.
25 Wang J, Whiteman MW, Lian H, Wang G, Singh A, Huang D, *et al*. A non-canonical MEK/ERK signaling pathway regulates autophagy via regulating Beclin 1. J Biol Chem 2009; 284: 21412–24.
26 Vousden KH, Lane DP. p53 in health and disease. Nat Rev Mol Cell Biol 2007; 8: 275–83.
27 Giustarini D, Milzani A, Colombo R, Dalle-Donne I, Rossi R. Nitric oxide and S-nitrosothiols in human blood. Clin Chim Acta 2003; 330: 85–98.
28 Snyder CM, Shroff EH, Liu J, Chandel NS. Nitric oxide induces cell death by regulating anti-apoptotic Bcl-2 family members. PLoS One 2009; 4: e7059.
29 Yamazaki M, Chiba K, Mohri T. Fundamental role of nitric oxide in neuritogenesis of PC12 cells. Br J Pharmacol 2005; 146: 662–9.
30 Brynczka C, Merrick BA. Nerve growth factor potentiates p53 DNA binding but inhibits nitric oxide-induced apoptosis in neuronal PC12 cells. Neurochem Res 2007; 32: 1573–85.
31 Jutooru I, Chadalapaka G, Sreevalsan S, Lei P, Barhoumi R, Burghardt R, *et al*. Arsenic trioxide downregulates specificity protein (Sp) transcription factors and inhibits bladder cancer cell and tumor growth. Exp Cell Res 2010; 316: 2174–88.
32 Ferdinandy P, Schulz R. Nitric oxide, superoxide, and peroxynitrite in myocardial ischaemia-reperfusion injury and preconditioning. Br J Pharmacol 2003; 138: 532–543.
33 Chen N, Karantza-Wadsworth V. Role and regulation of autophagy in cancer. Biochim Biophys Acta 2009; 1793: 1516–23.
34 Eskelinen EL, Saftig P. Autophagy: a lysosomal degradation pathway with a central role in health and disease. Biochim Biophys Acta 2009; 1793: 664–73.
35 Sohn D, Graupner V, Neise D, Essmann F, Schulze-Osthoff K, Janicke RU. Pifithrin-alpha protects against DNA damage-induced apoptosis downstream of mitochondria independent of p53. Cell Death Differ 2009; 16: 869–78.

Acta Pharmacologica Sinica (2012) 33: 1062–1068
 1671-4083/12 $32.00
www.nature.com/aps

Original Article

The essential role for aromatic cluster in the β3 adrenergic receptor

Hai-yan CAI, Zhi-jian XU, Jie TANG, Ying SUN, Kai-xian CHEN, He-yao WANG*, Wei-liang ZHU*

Drug Discovery & Design Center, Shanghai Institute of Materia Medica, Chinese Academy of Sciences, Shanghai 201203, China

Aim: To explore the function of the conserved aromatic cluster F213$^{5.47}$, F308$^{6.51}$, and F309$^{6.52}$ in human β3 adrenergic receptor (hβ3AR).
Methods: Point mutation technology was used to produce plasmid mutations of hβ3AR. HEK-293 cells were transiently co-transfected with the hβ3AR (wild-type or mutant) plasmids and luciferase reporter vector pCRE-luc. The expression levels of hβ3AR in the cells were determined by Western blot analysis. The constitutive signalling and the signalling induced by the β3AR selective agonist, **BRL** (**BRL**37344), were then evaluated. To further explore the interaction mechanism between **BRL** and β3AR, a three-dimensional complex model of β3AR and **BRL** was constructed by homology modelling and molecular docking.
Results: For F308$^{6.51}$, Ala and Leu substitution significantly decreased the constitutive activities of β3AR to approximately 10% of that for the wild-type receptor. However, both the potency and maximal efficacy were unchanged by Ala substitution. In the F308$^{6.51}$L construct, the EC_{50} value manifested as a "right shift" of approximately two orders of magnitude with an increased E_{max}. Impressively, the molecular pharmacological phenotype was similar to the wild-type receptor for the introduction of Tyr at position 308$^{6.51}$, though the EC_{50} value increased by approximately five-fold for the mutant. For F309$^{6.52}$, the constitutive signalling for both F309$^{6.52}$A and F309$^{6.52}$L constructs were strongly impaired. In the F309$^{6.52}$A construct, **BRL**-stimulated signalling showed a normal E_{max} but reduced potency. Leu substitution of F309$^{6.52}$ reduced both the E_{max} and potency. When F309$^{6.52}$ was mutated to Tyr, the constitutive activity was decreased approximately three-fold, and **BRL**-stimulated signalling was significantly impaired. Furthermore, the double mutant (F308$^{6.51}$A_F309$^{6.52}$A) caused the total loss of β3AR function. The predicted binding mode between β3AR and **BRL** revealed that both F308$^{6.51}$ and F309$^{6.52}$ were in the **BRL** binding pocket of β3AR, while F213$^{5.47}$ and W305$^{6.48}$ were distant from the binding site.
Conclusion: These results revealed that aromatic residues, especially F308$^{6.51}$ and F309$^{6.52}$, play essential roles in the function of β3AR. Aromatic residues maintained the receptor in a partially activated state and significantly contributed to ligand binding. The results supported the common hypothesis that the aromatic cluster F[Y]5.47/F[Y]6.52/F[Y]6.51 conserved in class A G protein-coupled receptor (GPCR) plays an important role in the structural stability and activation of GPCRs.

Keywords: β3 adrenergic receptor; constitutive activity; mutation; aromatic residue; G protein-coupled receptors

Acta Pharmacologica Sinica (2012) 33: 1062–1068; doi: 10.1038/aps.2012.55; published online 25 Jun 2012

Introduction

G protein-coupled receptors (GPCRs), which are characterised as seven transmembrane (TM) helices, comprise a large superfamily of membrane receptors involved in a wide range of signalling transduction pathways, which are mainly activated by agonists. Their activation mechanisms have been studied for decades, and the results show that they can transit through inactive-state and several active-state conformations with or without ligands[1, 2]. Although GPCRs are activated by ligands with different chemical natures, they are believed to share a common molecular activation mechanism[3, 4]. A number of biochemical and biophysical approaches, including site-directed spin labelling and various fluorescent technologies, have been applied to study the activation-associated conformational changes of GPCRs[5–8]. These studies indicated that the movement of the intracellular segments of TMs, especially the change of the orientations of TM-III and TM-VI, is likely a key element in the activation of GPCRs. Alternative experimental approaches including metal-ion site or disulphide engineering revealed that the extracellular segments of the TMs appear to move in the opposite direction of the intracellular segments. Thus, a global toggle switch mechanism for GPCR activation was proposed, whereby the extracellular segment of TM-VI was bent towards TM-III while the intracellular part moved away from TM-III[3, 9].

* To whom correspondence should be addressed.
E-mail wlzhu@mail.shcnc.ac.cn (Wei-liang ZHU)
hywang@mail.shcnc.ac.cn (He-yao WANG)
Received 2012-03-15 Accepted 2012-04-23

At the cytoplasmic surface, the E/DRY motif on TM-III is conserved among all classes of GPCRs. These amino acids form a network of polar interactions that bridge TM-III and TM-VI and that stabilise the inactive-state conformation, which is called the 'ionic lock'[10]. For β2 adrenergic receptor (β2AR), mutations of these residues, which weakened the strength of the ionic lock, increased constitutive activity[11]. This interaction network has been observed in crystal structures of the dark-state rhodopsin[12, 13], and it was broken in several other GPCR crystal structures bound with antagonists, such as β1 adrenergic receptor (PDB code: 2VT4[14]) and A2A adenosine receptor (PDB code: 3EML[15]). Microswitch during the process of GPCR activation has also been explored for decades. The W6.48 of the CWXP motif in GPCR, which is located at the bottom of the main ligand-binding pocket, is generally expected to function as a key microswitch in GPCR activation[16, 17]. The W6.48 changes position and interaction partners during receptor activation[17–19]. Moreover, the aromatic cluster around W6.48, F[Y]5.47/F[Y]6.52/F[Y]6.51, is proposed to play a role in initiating the receptor activation[20]. However, the detailed functional mechanisms of these residues need further investigation.

There are three members of βARs (β1AR, β2AR, and β3AR) that belong to class A GPCRs. β3AR was originally discovered in the 1980s. Early studies identified that human β3AR was mainly expressed on the surface of both white and brown adipocytes, mediating metabolic effects such as lipolysis and thermogenesis[21]. More recent reports showed that β3AR is also an attractive target for drugs against overactive bladder[22, 23], anxiety and depressive disorders[24, 25]. Understanding the mechanism of β3AR activation should facilitate rational drug discovery and the design of new types of β3AR agonists. In this study, we employed site-directed mutagenesis and molecular docking to explore the detailed function of the conserved aromatic cluster $F213^{5.47}/F309^{6.52}/F308^{6.51}$ in β3AR.

Materials and methods

Reagents

Ham's F12 nutrient medium, G418 and pCDNA3.1 were purchased from Invitrogen (Carlsbad, CA, USA). The human pCDNA3.1-β3AR (pCDNA3.1-hβ3AR) plasmid was obtained from Missouri S&T cDNA Resource Center (Rolla, MO, USA). The pCRE-Luc plasmid containing four copies of a consensus CRE was obtained from Stratagene (La Jolla, CA, USA). CHO-K1 and HEK-293 cells were purchased from ATCC (Rockville, MD, USA). Recombinant cell line CHO-mock was constructed in-house (CHO-K1 cells were stably co-transfected with pCDNA3.1-mock plasmid and pCRE-luc plasmid). Fetal bovine serum was supplied by Hyclone (Logan, UT, USA). FuGENE6 Transfection Reagent was supplied by Roche (Indianapolis, IN, USA). The Steady-Glo Luciferase Assay System was obtained from Promega (Madison, WI, USA). β3AR selective agonist **BRL**37344 (**BRL**) was obtained from Tocris Bioscience (Bristol, UK). Phosphatase and protease inhibitor cocktail was obtained from Sigma (St Louis, MO, USA). PVDF membranes were obtained from Bio-Rad Laboratories (Richmond, CA, USA). Anti-β3AR antibody (c-20) was obtained from Santa Cruz (Santa Cruz, CA, USA). Anti-β-Actin antibody was obtained from Sigma (St Louis, MO, USA). HRP-conjugated secondary antibodies were obtained from Jackson ImmunoResearch Laboratories (West Grove, PA, USA). ECL substrate was obtained from Pierce (Rockford, IL, USA).

Mutant construction, cell culture and transfections

Human β3AR mutants were constructed by a PCR-based site-directed mutagenesis approach. The PCR products were digested with *Dpn*I restriction enzyme and were then transformed into competent cells. All of the mutants were verified by DNA sequencing analysis. HEK-293 cells were plated at a density of approximately 20000 cells/well in 96-well plates with 100 μL of high glucose Dulbecco's modified Eagle's medium (DMEM) supplemented with 10% fetal bovine serum in a humidified 5% CO_2/95% air atmosphere at 37 °C. After 24 h, the cells were co-transfected with pcDNA3.1-hβ3AR (wild-type or mutant) and the luciferase reporter plasmid pCRE-Luc using FuGENE6 Transfection Reagent according to the manufacturer's instructions.

CRE-luciferase activity test

After 24 h of transfection, an additional 100 μL of DMEM containing different concentrations of **BRL**37344 (**BRL**) was added. Then, the plate was incubated at 37 °C (5% CO_2) for 3 h. The media were removed, and luciferase activities were detected using Steady-Glo Luciferase Assay System on the Flexstation III instrument (Molecular Devices, CA, USA).

Western blotting

Cells were harvested and homogenised in RIPA lysis buffer (50 mmol/L Tris, pH 7.4, 150 mmol/L NaCl, 1 mmol/L EDTA, 0.1% SDS, 1% Triton X-100, 1% sodium deoxycholate, 1 mmol/L PMSF) with a phosphatase and protease inhibitor cocktail. Proteins were separated by SDS-PAGE and transferred to PVDF membranes. Membranes were incubated with primary anti-β3AR antibody (1:200) and anti-β-Actin antibody (1:1000), followed by HRP-conjugated secondary antibodies (1:5000). The resulting immunoblots were visualised using ECL substrate.

Homology modelling and molecular docking

The construction of the homology model of β3AR (32-237, 282-361) was based on the structure of β2AR with InsightII[26]. GPCR has at least two functional states: inactive (R) and active (R*), which have different conformations. To obtain an active conformation of β3AR, the structure of β2AR binding with an agonist (PDB ID: 3P0G[27]) was used for our homology modelling, which was retrieved from the Protein Data Bank. On the basis of the sequence alignment result, the coordinates in conserved regions were assigned. The N and C terminal residues and loops were added using Loop_Search module and refined using Discover module. Disulfide bonds were defined between Cys110 and Cys196 and between Cys189 and Cys195. Finally, the whole structure model was minimised by SYB-

YL6.8 (Tripos Inc, St Louis, MO, USA). The stereochemical quality was assessed by Procheck[28].

Molecular docking was performed using AutoDock4.2[29]. To prepare both the receptor and **BRL**, all hydrogens were initially added, Gasteiger charges were computed, and the non-polar hydrogens were then merged with the corresponding non-polar atoms. The receptor was considered completely rigid for the docking study. The active site was defined by a grid box as large as 60×60×60 points with a grid spacing of 0.375Å using AutoGrid4. The box was centred on the centre of the Asp117 residue in the receptor. The docking parameters were prepared as follows: ga_pop_size, 150; ga_num_evals, 2500000; ga_num_generations, 27000; ga_run, 100 and rmstol, 2.0. The Lamarckian genetic algorithm was applied to account for protein-ligand interactions. Finally, the ligand conformation was selected considering both the predicted binding free energy and binding modes in the β3AR pocket.

Statistical analysis

EC_{50} values were determined by nonlinear regression using GraphPad Prism software (San Diego, CA, USA).

Results

The relationship between the expression level and the pharmacological properties of β3AR

To explore the influence of the protein expression level/transfection efficiency of plasmid DNAs on the detected pharmacological properties of β3AR, we adjusted the percentage of β3AR in DNA mixture (pCDNA3.1-hβ3AR and pCDNA3.1) to mimic the different expression level/transfection efficiency of the receptor. The constitutive activity (basal activity) and response stimulated by **BRL** were determined. The basal activity and maximal efficacy stimulated by **BRL** were both reduced less than 50%, and the EC_{50} value was reduced less than three-fold as the percentage of β3AR in the DNA mixture changed from 100% to 20% (Table 1). Therefore, in our experimental system, the expression level/transfection efficiency of β3AR or mutants did not significantly influence the pharmacological properties of β3AR.

Table 1. Changes in the potency (EC_{50}) and response (R_{max} and R_{min}) in relation to the levels of the receptor expression/transfection efficiency.

β3AR (%)	Basal activity (R_{min}) (%)	R_{max} (%)	lg EC_{50}
100%	100±12.7 (4)	265.6±19.9 (2)	-6.9±0.3
80%	78.8±10.3 (4)	194.5±9.1 (2)	-6.9±0.2
20%	67.9±9.1 (4)	220.3±8.1 (2)	-6.7±0.1

Expression levels of β3AR were mimicked by transfecting different ratios of pCDNA3.1-hβ3AR plasmid to pCDNA3.1. The pharmacological properties were determined by luciferase activity following stimulation by **BRL**. R_{min} represents the basal activity (constitutive activity). The maximal response (R_{max}) and R_{min} are given as percentages of R_{min} value of the one with 100% β3AR plasmid. Values are shown as mean±SEM, values for *n* are shown in parentheses.

Functional analysis of F308$^{6.51}$ in β3AR

To validate the function of F308$^{6.51}$, this aromatic residue was experimentally substituted with non-aromatic amino acid (Ala or Leu) and aromatic amino acid (Tyr), respectively. The results showed that all the mutants were well expressed in transfected HEK-293 cells as determined by Western blot analysis (the data for mutant F308$^{6.51}$Y were not obtained) (Figure S1A). The activities of mutants were examined in transfected HEK-293 cells by measuring receptor-mediated luciferase activities. As was observed with substitution of F308$^{6.51}$, both Ala and Leu substitution significantly decreased the constitutive activities of β3AR to approximately 10% of that for the wild-type receptor. However, both the potency and maximal efficacy were unchanged by Ala substitution. In the F308$^{6.51}$L construct, the EC_{50} value manifested as a "right shift" of approximately two orders of magnitude with an increased E_{max} (Table 2, Figures 1A and 1B). Impressively, the molecular pharmacological phenotype was similar to the wild-type receptor for the introduction of Tyr at position 308$^{6.51}$, though the EC_{50} value increased by approximately five-fold for the mutant (Table 2, Figure 1C). Thus, F308$^{6.51}$ is essential for the constitutive signalling for the β3AR, and it could be involved in the activation process to some extent.

Table 2. Pharmacological properties of the wild-type and mutated β3ARs.

β3AR (%)	Basal activity (E_{min}) (%)	E_{max} (%)	lg EC_{50}
Wide-type β3AR	100.0±1.9 (22)	260.6±5.2 (15)	-8.0±0.1
F308A	10.7±0.7 (5)	252.4±14.2 (3)	-7.8±0.2
F308L	9.5±0.9 (6)	314.3±6.0 (4)	-6.2±0.1
F308Y	96.2±7.0 (6)	260.0±14.1 (4)	-7.3±0.3
F309A	7.7±0.5 (6)	235.5±5.6 (4)	-6.6±0.1
F309L	5.3±0.4 (6)	119.5±3.4 (4)	-5.1±0.1
F309Y	29.4±1.2 (6)	–	–
F308A_F309A	5.9±0.2 (6)	9.8±0.4 (4)	–
F213A	6.7±0.5 (6)	92.5±4.3 (4)	-5.3±0.1
W305A	4.8±0.5 (6)	38.9±1.0 (4)	-6.3±0.1

The constructs were expressed in transiently transfected HEK-293 cells. The efficacy data on basal activity (E_{min}) and maximal response (E_{max}) are expressed as a percentage of the basal activity on the wild-type β3AR. Values are shown as mean±SEM, values for *n* are shown in parentheses.

Functional analysis of F309$^{6.52}$ in β3AR

F309$^{6.52}$ was also substituted with non-aromatic amino acid (Ala or Leu) and aromatic amino acid (Tyr), respectively. According to the Western blot analysis results, Ala substitution reduced the expression of the receptor in transfected HEK-293 cells by approximately 25%, while the expression level of the Leu substituted mutant was increased by approximately 25% compared with the wild-type receptor (Figure S1). However, constitutive signalling for both F309$^{6.52}$A and F309$^{6.52}$L constructs were strongly impaired (Table 2, Figures 1D and 1E). In the F309$^{6.52}$A construct, **BRL**-stimulated signalling showed a normal E_{max} but reduced potency (lgEC_{50}

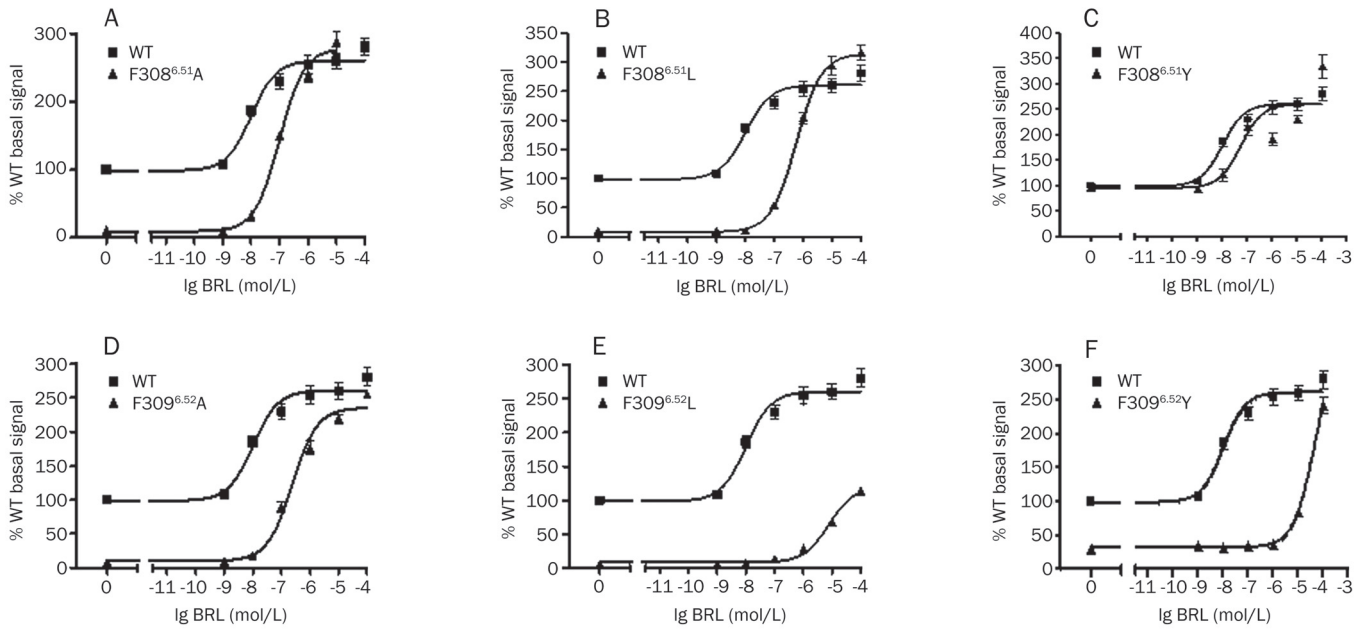

Figure 1. The pharmacological properties of HEK-293 cells transiently transfected with wild-type and mutated β3ARs (F308$^{6.51}$A, F308$^{6.51}$L, F308$^{6.51}$Y, F309$^{6.52}$A, F309$^{6.52}$L, and F309$^{6.52}$Y). The efficacy is detected as luciferase activity.

value is -6.6). Leu substitution of F309$^{6.52}$ reduced both the E_{max} and potency (Table 2, Figures 1D and 1E). When F309$^{6.52}$ was mutated to Tyr, the constitutive activity was decreased approximately three-fold, and **BRL**-stimulated signalling was significantly impaired (Table 2, Figure 1F). Thus, F309$^{6.52}$ is essential for the constitutive signalling of β3AR and is important for the agonist-induced signalling.

To further explore the importance of F308$^{6.51}$ and F309$^{6.52}$, the double mutant F308$^{6.51}$A_F309$^{6.52}$A was constructed. The result showed that the protein expression level was reduced to approximately 30%, and both the constitutive and **BRL**-stimulated signalling were almost totally diminished (Table 2, Figures 2A and S1B).

When F213$^{5.47}$ and W305$^{6.48}$ were mutated to Ala, we observed that the constitutive activities and maximum responses (stimulated by **BRL**) were also dramatically impaired for both mutants (Table 2 and Figures 2B and 2C). The result was similar to that for the molecular pharmacological phenotype for the ghrelin receptor, a member of class A GPCR[30].

The predicted binding model of β3AR and BRL

With the aim to explore the roles of the aromatic residues F213$^{5.47}$/F309$^{6.52}$/F308$^{6.51}$ on the structural level, the interaction mechanism of β3AR and **BRL** was predicted by molecular docking**.** The 3D structure of β3AR was constructed by homology as described in the Materials and methods, and the stereochemical quality of the β3AR model was finally examined by PROCHECK. The result of PROCHECK showed that 94.4% of the residues were in the most favoured regions and that no residue was in the disallowed regions (Figure S2). **BRL** was then docked (via software AutoDock4.2[29]) into the binding pocket of β3AR. As shown in Figure 3, **BRL** formed a hydrogen bond with residues Asp117, Ser208, and Asn312 (Figure 3A), which is consistent with the results reported for βAR family members[31–35]. F308$^{6.51}$ and F309$^{6.52}$ were in the

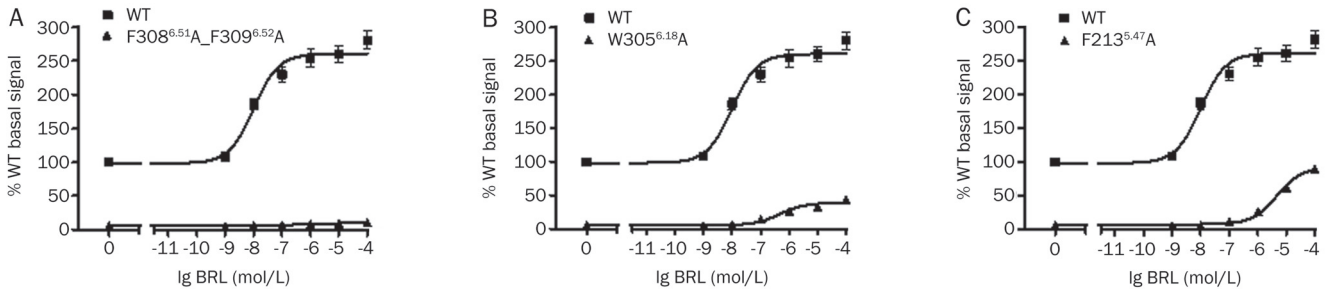

Figure 2. The pharmacological properties of HEK-293 cells transiently transfected with wild-type and mutated β3ARs (F308$^{6.51}$A_ F309$^{6.52}$A, W305$^{6.48}$A, F213$^{5.47}$A). The efficacy is detected as luciferase activity.

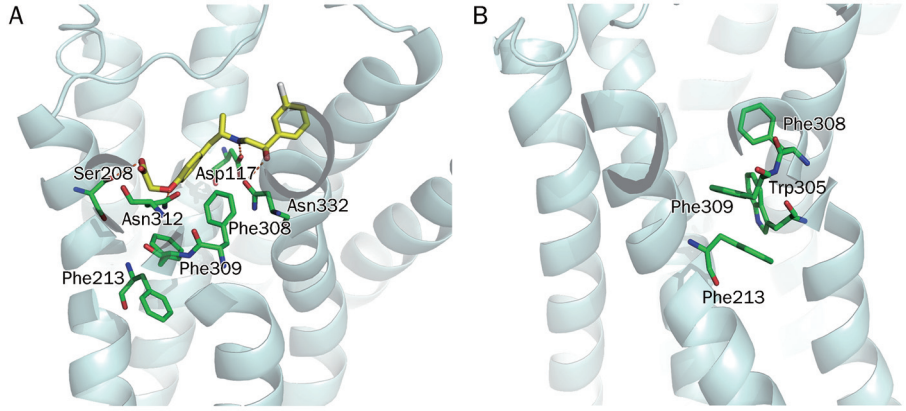

Figure 3. (A) The predicted binding mode of β3AR and **BRL**. (B) A π-π stacking is formed between F213$^{5.47}$ and F309$^{6.52}$ in the aromatic cluster F213$^{5.47}$/F309$^{6.52}$/F308$^{6.51}$ in β3AR. Residues of β3AR are indicated in green sticks. **BRL** is shown in yellow sticks. The dashed lines in red represent hydrogen bonds.

binding pocket, and they had hydrophobic interactions with **BRL,** while F213$^{5.47}$ was below the binding pocket (Figure 3A). A π-π stacking is formed between F2135.47 and F3096.52 in the aromatic cluster F2135.47/F3096.52/F3086.51 in β3AR (Figure 3B).

Discussion

The aromatic cluster F[Y]5.47/F[Y]6.52/F[Y]6.51 of GPCR is proposed to play a role in receptor activation[20]. F5.47 was found to serve as an aromatic lock for the proposed active conformation of the W6.48 "toggle switch" in seven-transmembrane receptor activation[30]. F6.52 was reported to be highly correlated with W6.48 and may mediate the TM6 Pro-kink[19]. In β3AR, the conserved aromatic cluster is F213$^{5.47}$/F309$^{6.52}$/F308$^{6.51}$, and we studied the cluster's function on a cellular and structural level.

For GPCR assays, the most common cells used for generating cell lines are CHO-K1 and HEK-293 cells. With the aim to obtain a sensitive luminescent signal for our luciferase reporter gene system, three cell lines were chosen and compared: CHO-K1, HEK-293 and the in-house cell line CHO-mock. The results indicated that HEK-293 was the most suitable cell line for the transient expression of β3AR (Figure S3A and S3B). Hence, HEK-293 cells were transfected with wild-type or mutated β3AR in our study.

To explore the influence of transfection efficiency on the luciferase signal, different ratios of pCDNA3.1-hβ3AR plasmid to pCDNA3.1 plasmid were designed to mimic the different protein expression levels of β3AR. The results demonstrated that the expression level of β3AR did not greatly influence the luciferase signal in our experimental system (Table 1). In fact, this result was confirmed in our later Western bolt analysis results. For example, on residue F309$^{6.52}$, Ala substitution reduced the expression of the receptor in transfected HEK-293 cells by approximately 25% and Leu substitution increased the expression approximately 25% compared to the wild-type receptor. In both cases, the constitutive signalling was strongly impaired (Table 2, Figures 1D and 1E).

From the results of the mutation of F308$^{6.51}$ and F309$^{6.52}$, and the double mutants, we discovered that both residues are essential for the constitutive activation of β3AR. Moreover, we showed that F309$^{6.52}$ was not only essential for the constitutive signalling but also very important for the agonist-induced signalling. However, the results for F308$^{6.51}$ demonstrated that this residue might not be critical for **BRL**-induced signalling efficacy, as both the potency and maximal efficacy were unaltered by Ala substitution (Table 2, Figures 1A). However, F308$^{6.51}$ could be involved in the activation process to some extent.

Homology and molecular docking were carried out to further explore the role of the aromatic cluster on structural level. The predicted binding mode demonstrated that both F308$^{6.51}$ and F309$^{6.52}$ were located in the binding pocket and that they had hydrophobic interactions with **BRL** (Figure 3A), which are consistent with our results and the newly reported observations[36]. However, through the homology and molecular docking studies, we could not conclude that F309$^{6.52}$ played a more important role than F308$^{6.51}$, which did not correspond exactly to our experimental results. One possible reason for these results is that during the docking process, the conformation of β3AR was completely rigid; however, it has been reported that the conserved residue W305$^{6.48}$ (W6.48) changes position during the receptor activation, which might drive the adjacent residues, F308$^{6.51}$ and F309$^{6.52}$ (Figure 3B), to undergo conformational changes[19]. Thus, rigid protein docking might not be accurate enough to predict the interaction mechanisms between ligands and GPCRs. Interestingly, as observed in Figure 3B, F213$^{5.47}$ could form a π-π stacking with F309$^{6.52}$. This interaction might have an essential role for both F213$^{5.47}$ and F309$^{6.52}$ in the signal transduction of β3AR.

As the aromatic cluster is highly conserved in GPCR, we carried out a statistic analysis throughout the class A GPCR. We surveyed all the members in the subfamily with the criterion of F[Y]5.47/F[Y]6.52/F[Y]6.51, as phenylalanine and tyrosine are highly homologous. The search results (Table S1) showed that the aromatic cluster resided in 18.5% of GPCR

Class A members, and to be more precise, 72.1% of the amine subfamily, 75.7% of the rhodopsin subfamily, 91.3% of the gonadotropin-releasing hormone subfamily, and 18.4% of the peptide subfamily (the alignment and classification were taken from GPCRDB, http://www.gpcr.org/). Hence, the aromatic cluster is highly conserved in amine, rhodopsin, and gonadotropin-releasing hormone subfamilies and is important in a portion of the peptide subfamily members. In the class A GPCR, Phe or Tyr are conserved in the position of 5.47 (41.9%), 6.51 (75.6%), and 6.52 (75.1%, including β-ionone for rhodopsin).

In summary, we explored the importance of the aromatic residues near the binding pocket of β3AR by applying cell biology technologies and the molecular docking method. We discovered that the aromatic properties of $F308^{6.51}$ and $F309^{6.52}$ were essential in maintaining the receptor in a partially activated state as shown by the constitutive activity. Moreover, both of the residues contributed to hydrophobic interactions with **BRL** in binding with β3AR. In addition, the π-π stacking between $F213^{5.47}$ and $F309^{6.52}$ might explain their major roles in the signal transduction of β3AR. From a survey of the class A GPCR, we found that the aromatic cluster F[Y]5.47/F[Y]6.52/F[Y]6.51 was highly conserved, therefore, the aromatic cluster might have a common mechanism in GPCR activation.

Acknowledgements

This work was supported by grants from the National Natural Science Foundation of China (20721003, 81072681), the International S&T Cooperation(2010DFB73280), and the Shanghai Committee of Science and Technology International Cooperation Project (09540703900).

Author contribution

Prof He-yao WANG and Prof Wei-liang ZHU designed and supervised the research and revised the manuscript; Hai-yan CAI performed the research, analysed data and wrote the manuscript; Prof Kai-xian CHEN helped with part of the research idea and helped revised the manuscript; Zhi-jian XU, Jie TANG, and Ying SUN helped with part of the research.

Supplementary information

Supplementary figures are available at website of Acta Pharmacologica Sinica on NPG.

References

1 Kenakin T. Agonist-receptor efficacy I: mechanisms of efficacy and receptor promiscuity. Trends Pharmacol Sci 1995; 16: 188–92.
2 Lefkowitz RJ, Cotecchia S, Samama P, Costa T. Constitutive activity of receptors coupled to guanine nucleotide regulatory proteins. Trends Pharmacol Sci 1993; 14: 303–7.
3 Schwartz TW, Frimurer TM, Holst B, Rosenkilde MM, Elling CE. Molecular mechanism of 7TM receptor activation — a global toggle switch model. Annu Rev Pharmacol Toxicol 2006; 46: 481–519.
4 Schwartz TW, Rosenkilde MM. Is there a 'lock' for all agonist 'keys' in 7TM receptors? Trends Pharmacol Sci 1996; 17: 213–6.
5 Gether U, Lin S, Ghanouni P, Ballesteros JA, Weinstein H, Kobilka BK. Agonists induce conformational changes in transmembrane domains III and VI of the beta2 adrenoceptor. EMBO J 1997; 16: 6737–47.
6 Gether U, Lin S, Kobilka BK. Fluorescent labeling of purified beta 2 adrenergic receptor. Evidence for ligand-specific conformational changes. J Biol Chem 1995; 270: 28268–75.
7 Sheikh SP, Zvyaga TA, Lichtarge O, Sakmar TP, Bourne HR. Rhodopsin activation blocked by metal-ion-binding sites linking transmembrane helices C and F. Nature 1996; 383: 347–50.
8 Ghanouni P, Steenhuis JJ, Farrens DL, Kobilka BK. Agonist-induced conformational changes in the G-protein-coupling domain of the beta 2 adrenergic receptor. Proc Natl Acad Sci U S A 2001; 98: 5997–6002.
9 Elling CE, Frimurer TM, Gerlach LO, Jorgensen R, Holst B, Schwartz TW. Metal ion site engineering indicates a global toggle switch model for seven-transmembrane receptor activation. J Biol Chem 2006; 281: 17337–46.
10 Vogel R, Mahalingam M, Ludeke S, Huber T, Siebert F, Sakmar TP. Functional role of the "ionic lock" — an interhelical hydrogen-bond network in family A heptahelical receptors. J Mol Biol 2008; 380: 648–55.
11 Rasmussen SG, Jensen AD, Liapakis G, Ghanouni P, Javitch JA, Gether U. Mutation of a highly conserved aspartic acid in the beta2 adrenergic receptor: constitutive activation, structural instability, and conformational rearrangement of transmembrane segment 6. Mol Pharmacol 1999; 56: 175–84.
12 Li J, Edwards PC, Burghammer M, Villa C, Schertler GF. Structure of bovine rhodopsin in a trigonal crystal form. J Mol Biol 2004; 343: 1409–38.
13 Okada T, Sugihara M, Bondar A-N, Elstner M, Entel P, Buss V. The retinal conformation and its environment in rhodopsin in light of a new 2.2Å crystal structure. J Mol Biol 2004; 342: 571–83.
14 Warne T, Serrano-Vega MJ, Baker JG, Moukhametzianov R, Edwards PC, Henderson R, *et al*. Structure of a beta1-adrenergic G-protein-coupled receptor. Nature 2008; 454: 486–91.
15 Jaakola VP, Griffith MT, Hanson MA, Cherezov V, Chien EY, Lane JR, *et al*. The 2.6 angstrom crystal structure of a human A2A adenosine receptor bound to an antagonist. Science 2008; 322: 1211–7.
16 Visiers I, Ballesteros JA, Weinstein H. Three-dimensional representations of G protein-coupled receptor structures and mechanisms. Methods Enzymol 2002; 343: 329–71.
17 Klein-Seetharaman J, Yanamala NV, Javeed F, Reeves PJ, Getmanova EV, Loewen MC, *et al*. Differential dynamics in the G protein-coupled receptor rhodopsin revealed by solution NMR. Proc Natl Acad Sci U S A 2004; 101: 3409–13.
18 Crocker E, Eilers M, Ahuja S, Hornak V, Hirshfeld A, Sheves M, *et al*. Location of Trp265 in metarhodopsin II: implications for the activation mechanism of the visual receptor rhodopsin. J Mol Biol 2006; 357: 163–72.
19 Shi L, Liapakis G, Xu R, Guarnieri F, Ballesteros JA, Javitch JA. Beta2 adrenergic receptor activation. Modulation of the proline kink in transmembrane 6 by a rotamer toggle switch. J Biol Chem 2002; 277: 40989–96.
20 Cherezov V, Rosenbaum DM, Hanson MA, Rasmussen SG, Thian FS, Kobilka TS, *et al*. High-resolution crystal structure of an engineered human beta2-adrenergic G protein-coupled receptor. Science 2007; 318: 1258–65.
21 Emorine LJ, Marullo S, Briend-Sutren MM, Patey G, Tate K, Delavier-Klutchko C, *et al*. Molecular characterization of the human beta 3-adrenergic receptor. Science 1989; 245: 1118–21.
22 Yamazaki Y, Takeda H, Akahane M, Igawa Y, Nishizawa O, Ajisawa Y. Species differences in the distribution of beta-adrenoceptor subtypes in bladder smooth muscle. Br J Pharmacol 1998; 124: 593–9.

23 Fujimura T, Tamura K, Tsutsumi T, Yamamoto T, Nakamura K, Koibuchi Y, *et al*. Expression and possible functional role of the beta3-adrenoceptor in human and rat detrusor muscle. J Urol 1999; 161: 680–5.
24 Lenard NR, Gettys TW, Dunn AJ. Activation of beta2- and beta3-adrenergic receptors increases brain tryptophan. J Pharmacol Exp Ther 2003; 305: 653–9.
25 Claustre Y, Leonetti M, Santucci V, Bougault I, Desvignes C, Rouquier L, *et al*. Effects of the beta3-adrenoceptor (Adrb3) agonist SR58611A (amibegron) on serotonergic and noradrenergic transmission in the rodent: relevance to its antidepressant/anxiolytic-like profile. Neuroscience 2008; 156: 353–64.
26 Accelrys. InsightII, Version 2005, Molecular modeling package. San Diego, CA: Molecular Simulation, Accelrys; 2005.
27 Rasmussen SG, Choi HJ, Fung JJ, Pardon E, Casarosa P, Chae PS, *et al*. Structure of a nanobody-stabilized active state of the beta(2) adrenoceptor. Nature 2011; 469: 175–80.
28 Laskowski RA, Macarthur MW, Moss DS, Thornton JM. Procheck — a program to check the stereochemical quality of protein structures. J Appl Crystallogr 1993; 26: 283–91.
29 Morris GM, Goodsell DS, Halliday RS, Huey R, Hart WE, Belew RK, *et al*. Automated docking using a Lamarckian genetic algorithm and an empirical binding free energy function. J Comput Chem 1998; 19: 1639–62.
30 Holst B, Nygaard R, Valentin-Hansen L, Bach A, Engelstoft MS, Petersen PS, *et al*. A conserved aromatic lock for the tryptophan rotameric switch in TM-VI of seven-transmembrane receptors. J Biol Chem 2010; 285: 3973–85.
31 Strader CD, Candelore MR, Hill WS, Dixon RA, Sigal IS. A single amino acid substitution in the beta-adrenergic receptor promotes partial agonist activity from antagonists. J Biol Chem 1989; 264: 16470–7.
32 Wong SK, Slaughter C, Ruoho AE, Ross EM. The catecholamine binding site of the beta-adrenergic receptor is formed by juxtaposed membrane-spanning domains. J Biol Chem 1988; 263: 7925–8.
33 Strader CD, Candelore MR, Hill WS, Sigal IS, Dixon RA. Identification of two serine residues involved in agonist activation of the beta-adrenergic receptor. J Biol Chem 1989; 264: 13572–8.
34 Takayuki S, Hiroyuki K, Taku N, Hitoshi K. Ser^{203} as well as Ser^{204} and Ser^{207} in fifth transmembrane domain of the human β2-adrenoceptor contributes to agonist binding and receptor activation. Br J Pharmacol 1999; 128: 272–4.
35 Wieland K, Zuurmond HM, Krasel C, Ijzerman AP, Lohse MJ. Involvement of Asn-293 in stereospecific agonist recognition and in activation of the β2-adrenergic receptor. Proc Natl Acad Sci U S A 1996; 93: 9276–81.
36 Jin F, Lu C, Sun X, Li W, Liu G, Tang Y. Insights into the binding modes of human beta-adrenergic receptor agonists with ligand-based and receptor-based methods. Mol Divers 2011; 15: 817–31.

Acta Pharmacologica Sinica (2012) 33: 1069–1079
 1671-4083/12 $32.00
www.nature.com/aps

Original Article

Intestinal absorption of forsythoside A in *in situ* single-pass intestinal perfusion and *in vitro* Caco-2 cell models

Wei ZHOU[1], Liu-qing DI[1, *], Juan WANG[1], Jin-jun SHAN[1], Shi-jia LIU[2], Wen-zheng JU[2], Bao-chang CAI[1]

[1]*College of Pharmacy, Nanjing University of Chinese Medicine, Nanjing 210046, China;* [2]*Department of Clinical Pharmacology, Affiliated Hospital of Nanjing University of Chinese Medicine, Nanjing 210093, China*

Aim: To investigate the mechanisms underlying the intestinal absorption of the major bioactive component forsythoside A (FTA) extracted from *Forsythiae fructus*.
Methods: An *in vitro* Caco-2 cell model and a single-pass intestinal perfusion *in situ* model in SD rats were used.
Results: In the *in vitro* Caco-2 cell model, the mean apparent permeability value (P_{app}-value) was 4.15×10^{-7} cm/s in the apical-to-basolateral (AP-BL) direction. At the concentrations of 2.6–10.4 μg/mL, the efflux ratio of FTA in the bi-directional transport experiments was approximately 1.00. After the transport, >96% of the apically loaded FTA was retained on the apical side, while >97% of the basolaterally loaded FTA was retained on the basolateral side. The P_{app}-values of FTA were inversely correlated with the transepithelial electrical resistance. The paracellular permeability enhancers sodium caprate and EDTA, the P-gp inhibitor verapamil and the multidrug resistance related protein (MRP) inhibitors cyclosporine and MK571 could concentration-dependently increase the Papp-values, while the uptake (OATP) transporter inhibitors diclofenac sodium and indomethacin could concentration-dependently decrease the P_{app}-values. The intake transporter SGLT1 inhibitor mannitol did not cause significant change in the P_{app}-values. In the *in situ* intestinal perfusion model, both the absorption rate constant (K_a) and the effective permeability (P_{eff}-values) following perfusion of FTA 2.6, 5.2, and 10.4 μg/mL via the duodenum, jejunum and ileum had no significant difference, although the values were slightly higher for the duodenum as compared to those in the jejunum and ileum. The low, medium and high concentrations of verapamil caused the largest increase in the P_{eff}-values for duodenum, jejunum and ileum, respectively. Sodium caprate, EDTA and cyclosporine resulted in concentration-dependent increase in the P_{eff}-values. Diclofenac sodium and indomethacin caused concentration-dependent decrease in the Peff-values. Mannitol did not cause significant change in the P_{app}-values for the duodenum, jejunum or ileum.
Conclusion: The results suggest that the intestinal absorption of FTA may occur through passive diffusion, and the predominant absorption site may be in the upper part of small intestine. Paracellular transport route is also involved. P-gp, MRPs and OATP may participate in the absorption of FTA in the intestine. The low permeability of FTA contributes to its low oral bioavailability.

Keywords: forsythoside A; *in situ* intestinal perfusion; Caco-2 cells; intestinal absorption; pharmacokinetics; P-gp; multidrug resistance related protein; uptake (OATP) transporter

Acta Pharmacologica Sinica (2012) 33: 1069–1079; doi: 10.1038/aps.2012.58; published online 9 Jul 2012

Introduction

Intestinal absorption evaluated using an *in vitro* Caco-2 model and a single-pass intestinal perfusion *in situ* model has become increasingly important in pharmaceutical designation[1, 2]. The human colon adenocarcinoma cell line (Caco-2) is now routinely cultivated as monolayers on permeable filters for the transepithelial transport of drugs[3], and this model has been used extensively to screen the absorptive capability and capacity of a variety of nutrients and pharmaceuticals[4–6]. However, one of the functional differences between normal cells and Caco-2 cells is the lack of expression of the cytochrome P450 isoenzymes, particularly CYP3A4, as well as some uridine diphosphate-glucuronosyltransferases (UGTs), such as UGT1A1[7]. In summary, Caco-2 cells do not always express the appropriate amounts of transporters or enzymes, which may introduce bias in the determination of some drug candidates that are transported via a carrier-mediated process or are metabolised via a particular pathway. Compared to the Caco-2 monolayer model, *in situ* intestinal perfusion in rats is a more reliable technique for investigating drug absorp-

* To whom correspondence should be addressed.
E-mail diliuqing@yahoo.com.cn
Received 2011-11-16 Accepted 2012-04-28

tion potential in combination with intestinal metabolism[8]. However, it is time consuming, and therefore is not normally recommended for screening purposes. Due to the advantages and disadvantages of each of these models, most of the published reports investigate the intestinal absorption of drugs using both models simultaneously. For example, Zuo *et al*, 2006[9] studied the intestinal absorption of hawthorn flavonoids using Caco-2 cells and *in situ* intestinal perfusion and found that hyperoside (HP), isoquercitrin (IQ) and epicatechin (EC) had quite limited permeability. EC and IQ demonstrated more extensive metabolism in the rat *in situ* intestinal perfusion model than in the Caco-2 monolayer model.

Forsythoside A (FTA), the major active component of the extracts from *Forsythiae fructus*[10], is present in traditional Chinese medicinal preparations such as Shuang-Huang-Lian or the *Forsythiae fructus-Lonicerae japonicae flos* herb couple, which possesses strong antibacterial, antioxidant and antiviral activities[11]. However, its oral bioavailability (BA) in rats was low (0.5%)[12]. Surprisingly, until recently, the absorption mechanism of FTA was completely unknown. In a previous study, Lu *et al*, 2010[13] found that the oral BA of the FTA oily formulation was fivefold higher than that of the non-oily formulation, but the reason for this difference was not studied. Zhang *et al*, 2002[11] conducted a physicochemical study of FTA, showing it to be a highly hydrophilic compound that was almost completely dissociated in biological fluids. This physicochemical property of the drug led us to postulate that the low permeability of the drug in the intestinal mucosa was one important reason for its reported low bioavailability. The Food and Drug Administration (FDA) also recognises that the poor permeation of drugs across the intestinal mucosa (usually due to their high hydrophilicity) was one of the common factors leading to failed absorption and thus to low drug BA[14]. Whether the improvement of the lipid solubility of FTA can increase its oral BA and whether other influencing factors such as efflux transporters, P-glycoprotein (P-gp), multidrug resistance related proteins (MRPs) also decrease the bioavailability of FTA are yet to be investigated.

Therefore, verapamil (VER), a P-gp inhibitor[15]; cyclosporine (CSA) and MK571, MRP inhibitors[16]; mannitol (MAN), a SGLT1 inhibitor[17, 18]; diclofenac sodium (DFS) and indomethacin (INDO), OATP inhibitors[19, 20] and sodium caprate and EDTA, paracellular permeability enhancers (PPEs)[21, 22] were selected to study the absorption mechanism and the factors that influence the intestinal absorption of FTA using an *in vitro* Caco-2 model and an *in situ* intestinal perfusion model to elucidate why the oral BA of FTA was low and to identify suitable pharmaceutical methods to improve the BA of FTA.

Materials and methods

Materials

FTA (98% purity, structure shown in Figure 1) was purchased from Shanghai NatureStandard Biotech Co, Ltd. Chlorogenic acid (CHA) (used as an internal standard, IS), VER, CSA, mannitol, DFS and INDO were purchased from the National Institute for the Control of Pharmaceutical and Biological Products. MK571, EDTA, sodium caprate, Lucifer yellow (LY) and DMSO were purchased from Sigma Chemical Co (St Louis, MO, USA). Methanol and acetonitrile (HPLC grade) were purchased from Merck (Merck, Germany), and water was purified using a Milli-Q water purification system (Millipore, Bedford, MA, USA). All other chemicals and reagents were of analytical grade.

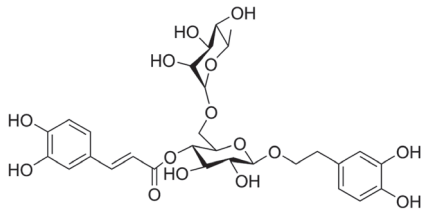

Figure 1. Chemical structure of forsythoside A (FTA).

In vitro Caco-2 cell model

Preparation of the calibration standard and quality control (QC) samples

Stock solutions of IS and FTA with concentrations of 10.28 and 26 μg/mL were prepared in Hanks' Balanced Salt Solution (HBSS) with a pH 6.0[23] and stored at -20 °C away from light. The working solutions used for HBSS were all freshly prepared by diluting the stock solution with HBSS to the appropriate concentrations.

The calibration standard samples were prepared in HBSS at concentrations of 5.28–264 ng/mL for FTA and processed as described in the sample preparation. The QC samples used for the intra-day and inter-day accuracy and precision, extraction recovery and stability study were prepared in the same way as the calibration standard samples.

Cell culture

Caco-2 cells obtained from the Chinese Academy of Medical Sciences were cultured in high glucose Dulbecco's modified Eagle's medium (DMEM, Gibco, Bethesda, MD, USA) with 10% fetal bovine serum (Gibco) and 1% nonessential amino acids (Gibco). Cells were cultured in a humidified atmosphere of 5% CO_2 at 37 °C. After reaching 80% confluence, the Caco-2 cells were harvested with a 0.25% trypsin-EDTA solution and seeded in Transwell inserts (Corning Coster Corp, Action, MA, USA) in 12-well plates at a density of 1.0×10^5 cells/cm^2. The protocols for cell culture in the Transwell inserts were similar to those described previously.

FTA transport experiments

Caco-2 cells at passages of 50–55 were used for transport experiments after 21 days post seeding. The integrity of the monolayer was verified by measuring the transepithelial electrical resistance (TEER) value across the monolayer using a Millicell-ERS Volt-Ohm meter (Millipore, Billerica, MA, USA) and monitoring the permeability of the paracellular leakage marker LY across the monolayer. The cell monolayer was con-

sidered tight enough for transport experiments when the P_{app} for LY <0.3×10^{-6} cm/s and the TEER value >350 Ω/cm^2. All transport studies were conducted in an orbital shaker incubator at 37 °C and a constant stirring rate (50–60 r/min). Prior to the experiment, the cells were washed twice and equilibrated for 30 min with the transport medium, HBSS containing 25 mmol/L of HEPES. The stock solutions of compounds were prepared in DMSO and diluted to the desired final concentration using HBSS. The concentration of DMSO in the final solutions was less than 0.10% (*v/v*). The transport studies were conducted in both the absorptive and efflux directions, separately. The transport solutions were added on either the apical (A, 0.4 mL) or the basolateral (B, 0.6 mL) side of the inserts, while the receiving compartment contained the corresponding volume of blank transport medium. After 30, 60, 90, and 120 min of incubation, aliquots of 200 μL or 150 μL were withdrawn from the basolateral or the apical receiver chambers, respectively, and replenished with an equal volume of HBSS. The concentrations of the test compound were analysed immediately using the HPLC-MS method described below. The effects of different concentrations, paracellular permeability enhancers (PPEs; EDTA and sodium caprate) and various transporter inhibitors, such as CSA, MK571, VER, mannitol, DFS and INDO, on the absorption of FTA were investigated.

Sample preparation

Samples were removed from -80 °C storage and thawed under ambient conditions. Samples of 100 μL were extracted using a liquid-liquid extraction technique after the addition of 10 μL of IS solutions, 20 μL of HCl (1 mol/L) and 1000 μL of ethyl acetate. After vortexing for 120 s and centrifugation at 12 000 r/min for 5 min, the organic phase was transferred into a clean centrifuge tube and evaporated to dryness under a nitrogen stream at 25 °C away from light. The residue was reconstituted in 100 μL of methanol aqueous solution containing 20% water. After centrifugation at 10 464×*g* for 10 min, the supernatant was injected to the LC–MS system.

Determination of FTA in HBSS

The chromatographic separation was achieved on an Agilent Zorbax SB-C18 column (2.1 mm id×150 mm, 5 μm, Agilent Technologies, Wilmington, DE, USA) with a security guard column (2.1 mm id×12.5 mm, 5 μm, Agilent Zorbax SB-C18, DE, USA) and was eluted with an isocratic mobile phase of MeOH and water (20:80). The mobile phase was delivered at a flow-rate of 0.2 mL/min, and the column temperature was maintained at 30 °C. An Alliance 2695 LC system (Waters, Milford, MA, USA) coupled with a Waters Quattro Micro tandem triple quadrupole mass spectrometer was used. The Mass Lynx 4.1 software was used for instrumental control and for the acquisition and processing of the data. A MS detector with an electrospray ionisation (ESI) interface in negative ion model (ESI$^-$) was used for quantitative analysis, and an MRM model was used for acquisition. The *m/z* ratios, [M-H]$^-$, *m/z* 623.8→161.3 for FTA and [M-H]$^-$, *m/z* 353.3→191.2 for IS, were recorded simultaneously. The optimised electrospray conditions were: capillary voltage - 3.0 kV; cone voltage - 30 V; source temperature - 110 °C; desolation temperature - 350 °C; desolation gas flow - 500 L/h. The method was fully validated for its specificity, linearity, lower limits of quantification (LLOQ), accuracy and precision. To evaluate assay specificity, six independent lots of blank Caco-2 receiver solutions were analysed to exclude any endogenous co-eluting interferences by comparing them with the assay of the receiver solutions spiked with analytes. The precision was calculated as the relative standard deviation (RSD), and the accuracy was evaluated as analytical recovery. The intra-day precision and accuracy were evaluated at three different concentrations (5.28, 26.4, and 132 ng/mL) of the receiver solutions spiked with analytes by replicate analysis of five samples on the same day. The inter-day precision and accuracy determinations were carried out on three different days. The recovery experiments were performed by comparing the analytical results of the extracted samples at three concentrations with pure standards without extraction. The LLOQ was defined as the concentration that produced a signal-to-noise (S/N) ratio greater than 10. The sample solution stability was assessed at three concentration levels (5.28, 26.4, and 132 ng/mL). For the freeze/thaw stability study, samples at three concentrations were stored at -20 °C and subjected to two freeze-thaw cycles. The short-term stability test of FTA during storage in the autosampler at 4 °C was performed by repeated injections every 2 h for a period of 24 h. The long-term stability of FTA in HBSS was assessed at three concentration levels after storage at -20 °C for 4 weeks.

Data analysis

The apparent permeability coefficient (P_{app}) and efflux ratio were calculated using the following equations:

$$P_{app} = \frac{dQ}{dt} \times \frac{1}{A*C_0} \quad (1)$$

$$Efflux\ ratio = \frac{P_{app}\ (BL \rightarrow AP)}{P_{app}\ (AP \rightarrow BL)} \quad (2)$$

Notes: dQ/dt (μg/s) was the flux rate, A was the effective surface area of the cell monolayer (0.67 cm^2), and C_0 (μg/mL) was the initial drug concentration in the donor chamber. The net efflux was expressed as the quotient of P_{app} (B→A) to P_{app} (A→B). The data are expressed as the mean±SD of six determinations (performed on two different days).

The parameters obtained above were compared via an analysis of variance (following logarithmic transformation of the P_{app}, efflux ratio and two-tailed *t*-tests). The differences were considered to be significant when P<0.05.

The single-pass intestinal perfusion *in situ* model

Preparation of the perfusion buffer (Krebs-Ringer buffer containing 20 mg/L of phenol red)

The perfusion buffer contained 133.3 mmol/L NaCl, 4.7 mmol/L KCl, 0.2 mmol/L $MgCl_2$, 3.3 mmol/L $CaCl_2$, 2.7 mmol/L NaH_2PO_4, 7.8 mmol/L glucose, 16.3 mmol/L $NaHCO_3$, and 56.4 μmol/L phenol red in 1000 mL water and was adjusted to pH 6.0 using concentrated phosphoric acid[23].

Preparation of calibration standard and quality control (QC) samples

Stock solutions of IS and FTA with concentrations of 508 and 123 μg/mL were prepared in Krebs-Ringer buffer with pH 6.0 and stored at -20 °C away from light. The working solutions used for the Krebs-Ringer buffer were all freshly prepared by diluting the stock solution with Krebs-Ringer buffer to the appropriate concentrations.

The calibration standard samples were prepared in Krebs-Ringer buffer at concentrations of 0.615–12.3 μg/mL for FTA and processed as described for the sample preparation. The QC samples used for the intra-day and inter-day accuracy, precision, extraction recovery and stability study were prepared in the same way as the calibration standard samples.

The in situ uptake experiment

Male Sprague Dawley (SD) rats weighing 250 g to 300 g were supplied by the Experimental Animal Center of Nanjing University of Chinese Medicine (Certificate No SCXK2008-0033). The rats were fasted for 12 h prior to the experiment but were allowed free access to water. The SD rats were anesthetised with a 20% urethane solution (6 mg/kg). A midline abdominal incision was made, and the small intestine was exposed. The bile duct was ligated to avoid bile secretion into the perfusate. For the regional absorption of FTA, three intestinal sections were isolated and cannulated (all were 10 cm long): the duodenum, the jejunum and the ileum. Each segment was rinsed with normal saline at 37 °C for 20 min until the wash appeared clear. After that, the FTA perfusion solution was connected to each segment and perfused through each part of the three intestine sections. After 30 min, the circulation rate was 0.2 mL/min, controlled by a peristaltic pump to pre-balance. The perfusate samples were collected at 30–60, 60–90, 90–120, and 120–150 min. A 0.5 mL sample was taken to determine the concentration of phenol red, and the remaining samples were stored at -80 °C until analysis following centrifugation at 10 464×*g* for 5 min. The effects of different concentrations, intestinal sections, PPEs (EDTA and sodium caprate) and various transporter inhibitors, including CSA, VER, mannitol, DFS and INDO, on the absorption of FTA were investigated.

Sample preparation

Samples were removed from -80 °C storage and thawed under ambient conditions. Samples (100 μL) were extracted using a protein precipitation technique after the addition of 5 μL of IS solution, 10 μL HCl (10^{-3} mol/L) and 90 μL of methanol. After vortexing for 120 s and centrifugation at 10 464×*g* for 5 min, the supernatant was injected into the HPLC system.

Determination of phenol red

The phenol red in the phosphate buffer (pH 6.0) had a characteristic red colour, which was measured spectrophotometrically at 558 nm.

Determination of FTA in the intestinal perfusion fluid

The analyses were performed using an Agilent 1100 liquid chromatography system equipped with a quaternary solvent delivery system, an autosampler and a DAD detector. The separation was carried out on a Hedera ODS-2 column (250 mm×4.6 mm, 5 μm). The mobile phase consisted of solvent A (0.2% Phosphate) and solvent B (methanol). The gradient elution was as follows: initial 0–7 min, linear change from A–B (67:33, *v/v*) to A–B (63.5:36.5, *v/v*); 7–9 min, linear change from A–B (63.5:36.5, *v/v*) to A–B (60.5:39.5, *v/v*); 9–15 min, linear change from A–B (60.5:39.5, *v/v*) to A–B (57.5:42.5, *v/v*); 15–17 min, linear change from A–B (57.5:42.5, *v/v*) to A–B (67:33, *v/v*) and hold for 3 min. The mobile phase flow rate was 1 mL/min. The chromatogram was recorded at 332 nm. The column temperature was controlled at 30°C, and the sample injection volume was 40 μL. Calibration curves were generated by plotting the IS to analyte peak area ratios against analyte concentrations. The intra-day and inter-day precision and accuracy were carried out by quantifying three QC samples (n=5) on the same day and on three consecutive validation days, respectively. The results of the intra-day and inter-day precision were determined by the RSD, and the detected concentration/nominal concentration was calculated to evaluate the accuracy. The recovery was determined as the ratio of the peak area of the precipitated QC samples to that of the samples without precipitation at equivalent concentrations. The storage stability was evaluated by determining QC samples at five replicates stored at -80 °C for 30 d.

Data analysis

The concentration of the perfusion fluid, the effective permeability coefficient (P_{eff}) and the absorption rate constant (K_a) were calculated using the following equations:

$$C_{out\ (corrected)} = \frac{C_{out} PR_{in}}{PR_{out}} \quad (3)$$

$$P_{eff} = \frac{Q \ln[C_{in}/C_{out\ (corrected)}]}{2\pi rL} \quad (4)$$

$$K_a = [1 - \frac{C_{out\ (corrected)}}{C_{in}}]\ Q/\pi r^2 L \quad (5)$$

Notes: $C_{out\ (corrected)}$ is the effluent drug concentration with correction; C_{out} is the effluent drug concentration without correction; C_{in} is the influent drug concentration; PR_{in} is the influent phenol red concentration; PR_{out} is the effluent phenol red concentration; Q is the perfusate flow rate; r is the radius of intestinal segment and l is the length of intestinal segment.

The reported values are presented as the mean±SD. The data were analysed using the Student's t-test or a one-way ANOVA. For all tests, P<0.05 was considered significant.

Results

In vitro Caco-2 cell model

Determination of FTA in HBSS

Under the current chromatography conditions, all analyses were completed within 3.0 min. The negative mass spectra of

FTA and IS are shown in Figure 2. The mass spectra of FTA and IS exhibited a protonated molecular ion at *m/z* 623.8 and 353.3, respectively. The high collision energy gave the most abundant production at *m/z* 161.3 and 191.2, respectively. Therefore, the precursor to product transition was assigned in the multi-reaction-monitoring (MRM) model as follows: *m/z* 623.1→161.3 for FTA and *m/z* 353.3→191.2 for IS. The MRM chromatograms of FTA and IS are shown in Figure 3. No significant interference from endogenous substances with the analytes or IS was detected. The calibration curve was linear in the range of 5.28 to 132 ng/mL, with a correlation coefficient of 0.992 (n=6). The regression equation was as follows: Y= 0.0002X–0.0002 (Y: the ratio of peak area, X: the concentration of FTA) when a 10 μL sample was used for assay. The precision and accuracy data for the within-run and between-run assays are shown in Table 1. The results indicate that the present method had good reproducibility with precision less than 10.64% and excellent accuracy ranging from 93.15% to 104.25% at low (5.28 ng/mL) to high (264 ng/mL) concentrations. The extraction recoveries of FTA had average values ranging from 56.06% to 63.26% at the three QC concentrations (Table 2). The matrix effect of the blank Caco-2 cell receiver solutions spiked after the sample preparation with 5.28, 26.4, and 132 ng/mL of FTA were found to be within the acceptable range (Table 2). The same evaluation was performed on the IS, and no significant peak area differences were observed (Table 2). The results of the short-term stability, freeze/thaw stability, autosampler stability and long-term stability are shown in Table 3. The mean percentages of the deviation of calculated versus theoretical concentrations were less than or equal to 14.97% for short-term stability, less than or equal to 14.06% for freeze/thaw stability, less than or equal to 11.93% for autosampler stability, and less than or equal to 8.32% for long-term stability, indicating that the analytes were stable during the analytical procedures.

Characteristics of the transepithelial transport of FTA

The bi-directional permeation of FTA across Caco-2 cell monolayers was examined (Table 4). The permeation of FTA in the apical-to-basolateral direction was similar to that in the basolateral-to-apical direction at a medium concentration, and all of the efflux ratios were less than 1.5, indicating that the

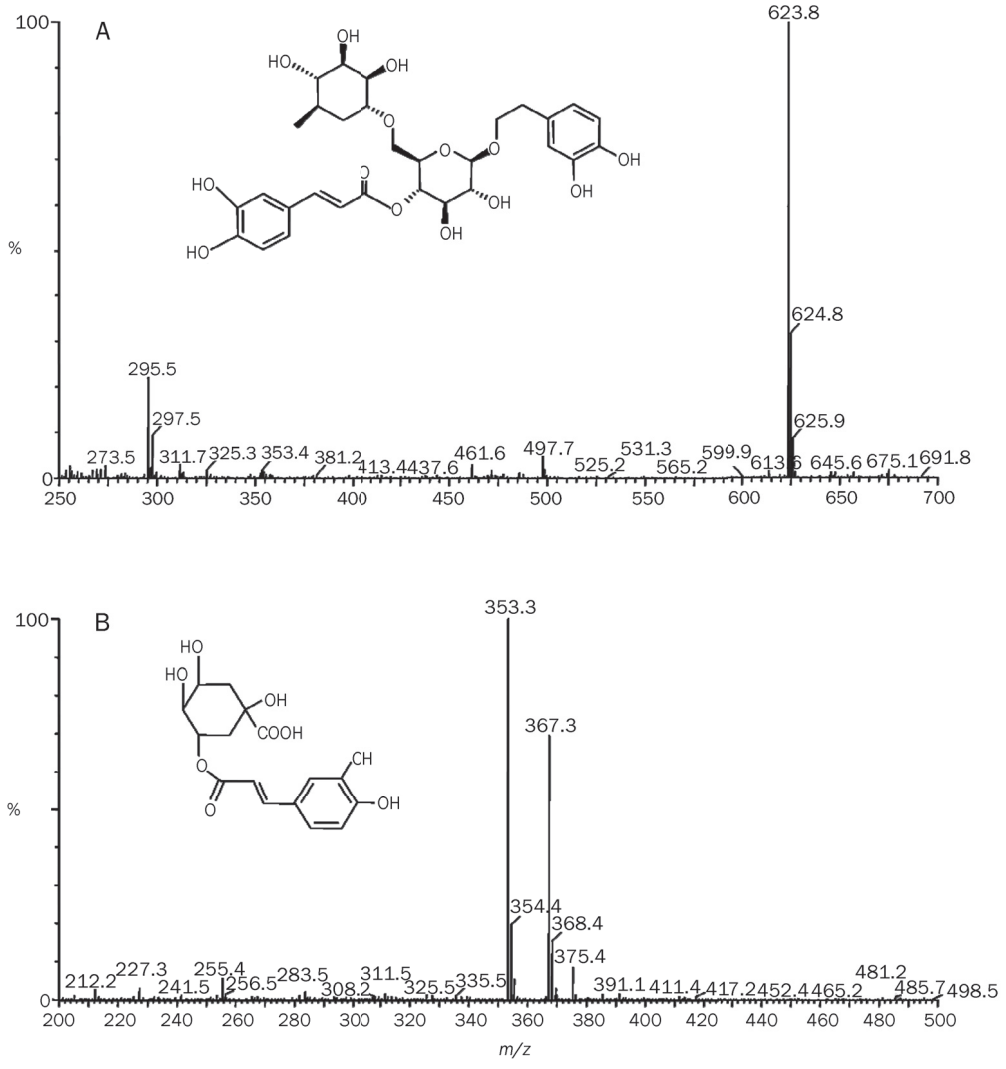

Figure 2. Full-scan product ion spectra of $[M-H]^-$ of FTA (A) and CHA (IS) (B) in negative ion mode.

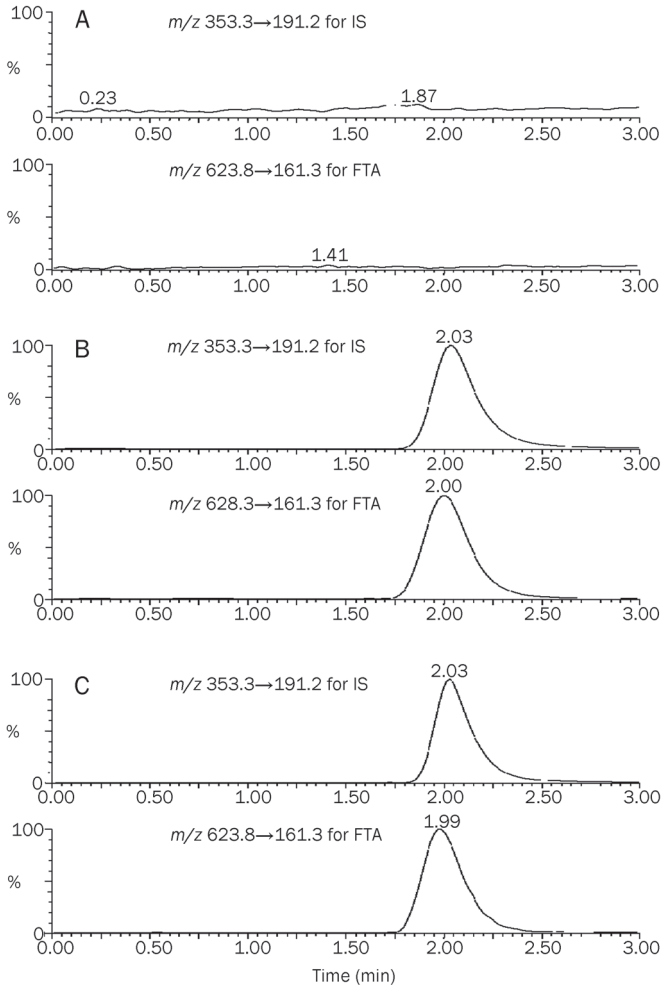

Figure 3. Typical MRM chromatograms of FTA and IS. (A) Blank Caco-2 receiver solution. (B) Blank HBSS spiked with IS and FTA. (C) Samples collected in Caco-2 cell model spiked with IS.

absorption of FTA was not affected by the transport direction.

The distribution of FTA

After the transport experiments, >96% of the apically loaded FTA was retained on the apical side and >97% of the basolaterally loaded FTA was retained on the basolateral side when the TEER value was 424±35 Ω/cm^2, suggesting that the permeability of FTA may be restricted by tight junctions (Table 5).

Table 2. Recovery of FTA and CHA (internal standard) in Caco-2 cells. mean±standard deviation (SD). *n*=3

Sample	Concentration (ng/mL)	Recovery (%)	Matrix effect (%)
FTA	5.28	56.06±5.84	97.0±2.3
FTA	26.4	63.26±9.36	92.3±1.3
FTA	132	59.70±1.41	91.4±4.7
IS	2056	88.02±1.39	92.4±2.6

The paracellular transport of FTA across the Caco-2 cell monolayers

Caco-2 cell monolayers exhibiting different TEER values were prepared by treatment with cytochalasin D. The apical-to-basolateral transport of FTA was then characterised using the monolayers. As illustrated in Figure 4, the P_{app}-values of FTA were inversely correlated with the TER, suggesting that they permeated across Caco-2 cell monolayers via the paracellular pathways. This finding also suggests that the intestinal absorption of FTA is restricted when the epithelial tight junction was tight enough. As shown in Figure 5, the P_{app} values also increased significantly (P<0.01) to 779% (31.87±5.92)×10^{-7} cm/s, 1126% (46.07±2.92)×10^{-7} cm/s and 1540% (62.98±6.76)×10^{-7} cm/s following a prior 40-min exposure of the Caco-2 cells to 10, 20 and 30 μmol/L of the paracellular permeability enhancer sodium caprate, suggesting that FTA permeates via the paracellular pathways. the P_{app}-values increased significantly (P<0.01) to 528% (21.60±3.88)×10^{-7} cm/s, 934% (38.22±7.10)×10^{-7} cm/s and 1538% (62.91±4.82)×10^{-7} cm/s following a prior 40-min exposure of the Caco-2 cells to 10, 20, and 30 μmol/L of the paracellular permeability enhancer EDTA.

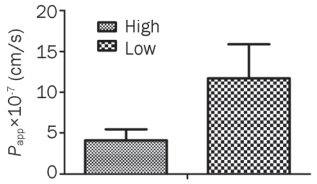

Figure 4. Correlation between TEER and the P_{app}-values. TEER values are indicated as follows: high, 800, and low, 383 Ω/cm^2. Each point is the mean±SD of three experiments.

Table 1. Intra- and inter-day accuracy and precision of FTA assay in Caco-2 cells.

	Intra-day (overall mean, *n*=5)			Inter-day (overall mean, *n*=15)		
Concentration (ng/mL)	Concentration found (ng/mL)	Accuracy (%)	CV (%)	Concentration found (ng/mL)	Accuracy (%)	CV (%)
5.28	5.50	104.25	9.83	5.15	97.59	11.40
26.4	25.05	94.89	10.99	25.73	97.45	6.40
132	126.52	95.85	10.64	122.95	93.15	6.08

Table 3. Stability of FTA in Caco-2 cells. *n*=3. Mean±SD.

	FTA nominal concentration (ng/mL)		
	5.28	26.4	132
Room temperature (4 h) Measured concentration (ng/mL)	5.78±0.79	24.62±2.32	125.10±10.81
Accuracy (%)	109.52±14.97	93.27±8.79	94.77±8.19
Three freeze/thaw cycles Measured concentration (ng/mL)	5.46±0.80	26.30±3.10	124.99±10.93
Accuracy (%)	103.40±14.06	98.59±11.73	94.69±8.28
Autosampler rack for 24 h Measured concentration (ng/mL)	5.43±0.63	24.50±1.31	123.32±11.64
Accuracy (%)	102.92±11.93	92.81±4.97	93.43±8.81
Stored at -20 ℃ for 4 weeks Measured concentration (ng/mL)	5.09±0.19	24.96±2.20	122.78±8.01
Accuracy (%)	96.34±3.57	94.54±8.32	93.01±6.07

Table 4. Transport parameters of different concentrations of FTA in Caco-2 cells. *n*=3. Mean±SD.

Concentration (μg/mL)	P_{app}×10^{-7} (cm/s)		P_{BA}/P_{AB}
	AP-BL	BL-AP	
2.6	3.99±0.23	3.99±0.69	1.00
5.2	4.15±1.20	3.52±0.73	0.85
10.4	4.09±1.37	3.89±0.87	0.95

Table 5. Distribution of FTA after transepithelial transport experiments.

Transport direction	% Compound recovered from		
	Apical side	Basolateral side	Cells
AP-BL	96.84±0.55	3.10±0.56	0.02±0.01
BL-AP	2.51±0.12	97.44±0.12	0.04±0.02

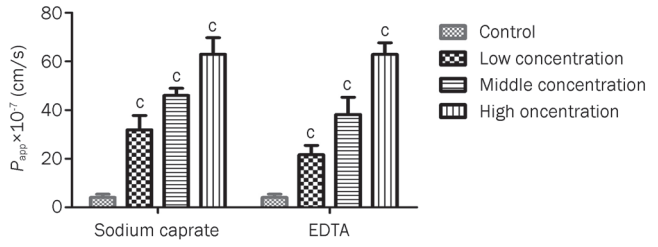

Figure 5. Effects of paracellular permeability enhancers at different concentrations on absorption parameters of FTA in Caco-2 cell model. Results are expressed as the mean±SD of at least four experiments. ^{c}P<0.01 compared with the control group. Low, Middle, High: 10, 20, 30 μmol/L for both sodium caprate and EDTA.

The concentration dependence of FTA

As shown in Table 4, there were no significant differences in permeability calculated by different concentrations ranging from 2.6 μg/mL to 10.4 μg/mL, suggesting that passive diffusion might be involved. This result is in good agreement with the distribution study and the results shown in Figure 4 and 5, showing that FTA was mainly permeated via paracellular diffusion. LY, a marker compound for paracellular transport, also showed this trend[24].

The influence of different inhibitor concentrations on the transport parameters of FTA in the Caco-2 cell model

Figure 6 summarises the permeability coefficients of FTA in the absence and presence of inhibitors. Our statistical analysis revealed that exposure to VER (50 and 100 μmol/L), CSA (5 μmol/L) and MK571 (50 μmol/L) did not increase the P_{app}-values significantly. However, the P_{app}-values increased significantly (P<0.05) to 184% (7.52±0.35)×10^{-7} cm/s in the presence of 150 μmol/L of VER. The P_{app}-values increased significantly (P<0.05) to 152% (6.23±1.47)×10^{-7} cm/s and 298% (12.20±3.46)×10^{-7} cm/s in the presence of 10 and 15 μmol/L of CSA, and the P_{app}-values increased significantly (P<0.05) to 220% (9.00±7.60)×10^{-7} cm/s and 249% (10.20±4.40)×10^{-7} cm/s in the presence of 100 and 150 μmol/L of MK571. These results indicate that the permeability of FTA is enhanced as the concentrations of VER, CSA, MK571 are increased, exhibiting a clear concentration-dependent effect. However, the P_{app}-values decreased gradually in the presence of 40 μmol/L of DFS and INDO. In addition, the P_{app}-values in the presence of

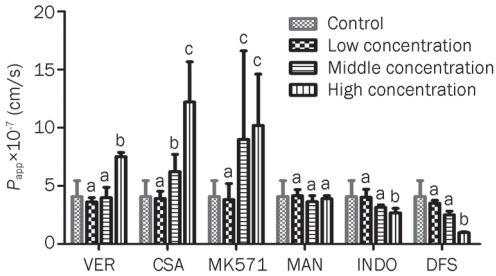

Figure 6. Effects of inhibitors of different concentrations on absorption parameters of FTA in Caco-2 cell model. Results are expressed as the mean±SD of at least four experiments. ^{a}P>0.05, ^{b}P<0.05, ^{c}P<0.01 compared with the control group. VER: 50, 100, 150 μmol/L; CSA: 5, 10, 15 μmol/L; MK571: 50, 100, 150 μmol/L; MAN: 10, 20, 30 μmol/L; INDO and DFS: 10, 20, 40 μmol/L.

10, 20, and 30 μmol/L of mannitol did not change significantly compared to the control group. Together, these results indicate that FTA absorption might be influenced by efflux transporters (P-gp, MRPs) and uptake transporters (OATP).

The single-pass intestinal perfusion *in situ* model

The determination of phenol red

A linear relationship between the phenol red concentration in the range of 10 to 50 mg/L and the absorbance was found. The calibration was A=0.0098C–0.0038, (A: absorbance, C: the concentration of phenol red), r=0.9999 (n=6). The average recovery was 100.03%, and the precision (RSD) was less than 1.18%. These results indicate that this method is suitable for the determination of phenol red in the intestinal perfusion fluid.

The determination of FTA in the intestinal perfusion fluid

No interfering peak was observed in the blank intestinal perfusion fluid under the assay conditions. The retention time was approximately 14.7 min for FTA and 5.8 min for IS. The calibration curve was linear in the range of 0.615–12.3 μg/mL with a correlation coefficient of 0.9985 (n=7). The regression equation was as follows: Y=0.023X+0.0006 (Y: the concentration of FTA, X: the ratio of peak area) when 100 μL of perfusion fluid was used for assay. The precision and accuracy data for the within-run and between-run assays are shown in Table 6. The results indicate that the developed HPLC method had good reproducibility with precision less than 4.61% and excellent accuracy ranging from 88.65% to 110.83% at low (1.23 μg/mL) to high (11.07 μg/mL) concentrations. The extraction recoveries of FTA had average values ranging from 96.86% to 102.98% at the three QC concentrations (Table 6). The stability results (data not shown) showed that the concentrations of FTA were between 96.8% and 108.5% of the initial values, indicating that the analytes were stable in the intestinal perfusion fluid for at least 30 d storage at -80 °C.

The absorption parameters of different concentrations in different segments of rat intestine

As shown in Table 7, the K_a and P_{eff}-values changed little (P>0.05, ANOVA) in the presence of 2.6, 5.2, and 10.4 μg/mL of FTA after perfusion via the duodenum, jejunum and ileum, indicating that the absorption of FTA might be primarily through passive diffusion. In addition, it was shown that the K_a and P_{eff}-values in the duodenum were slightly higher compared to the jejunum and ileum, but this difference was not significant (Table 7). This indicates that the predominant absorption site might be in the upper part of small intestine.

The influence of different concentrations of inhibitors and paracellular permeability enhancers on the absorption parameters of FTA

As shown in Figure 7, the addition of VER induced the greatest increase in the P_{eff}-values at a relatively low concentration (50 μmol/L) in the duodenum, a medium concentration (100 μmol/L) in the jejunum and a high concentration (150 μmol/L) in the ileum. CSA at low (2 μg/mL), medium (4 μg/mL) and high (8 μg/mL) concentrations produced a significant, dose-dependent increase in the P_{eff}-value, and the duodenum, jejunum and ileum showed the same trend in P_{eff}-values when CSA was added. The treatment with a high concentration of CSA led to a significant increase in the P_{eff}-value compared to the control (P<0.05), and the P_{eff}-value in the duodenum group when CSA was added was higher than that of the jejunum and ileum groups. Both sodium caprate and EDTA at the same low (5 μg/mL), medium (10 μg/mL) and high (15 μg/mL) concentrations caused a significant, concentration-dependent increase in the P_{eff}-value compared to the control group (P<0.05). Treatment with sodium caprate and EDTA at the same high concentrations had the highest P_{eff}-value. These

Table 6. Within-run and between-run precision and accuracy, and extraction recovery of the method for determination of FTA in rat intestinal perfusate.

Concentration	Within-run (n=5)		Between-run (n=5, three runs)		Recovery (%)	
(μg/mL)	Precision (RSD%)	Accuracy (%)	Precision (RSD%)	Accuracy (%)	Mean	RSD%
1.23	2.60	88.65	4.61	95.90	102.98	4.54
4.92	0.29	95.44	0.99	110.83	96.86	0.04
11.07	0.12	98.06	2.45	106.92	101.27	1.12

Table 7. Absorption parameters of three concentrations of FTA in different segments of rat intestine. n=5. Mean±SD.

Concentration	Parameter	Duodenum	Jejunum	Ileum
Low (2.6 μg/mL)	$P_{eff}\times10^{-6}$ (cm/s)	5.485±2.621	3.811±3.036	3.008±2.249
	$K_a\times10^{-5}$ (min^{-1})	5.707±2.410	3.907±2.419	3.115±2.325
Middle (5.2 μg/mL)	$P_{eff}\times10^{-6}$ (cm/s)	4.550±0.417	4.433±2.704	4.306±2.107
	$K_a\times10^{-5}$ (min^{-1})	5.671±0.516	5.554±1.534	5.370±0.149
High (10.4 μg/mL)	$P_{eff}\times10^{-6}$ (cm/s)	5.494±3.883	4.682±2.971	3.191±2.519
	$K_a\times10^{-5}$ (min^{-1})	5.501±4.309	4.385±3.714	4.720±1.298

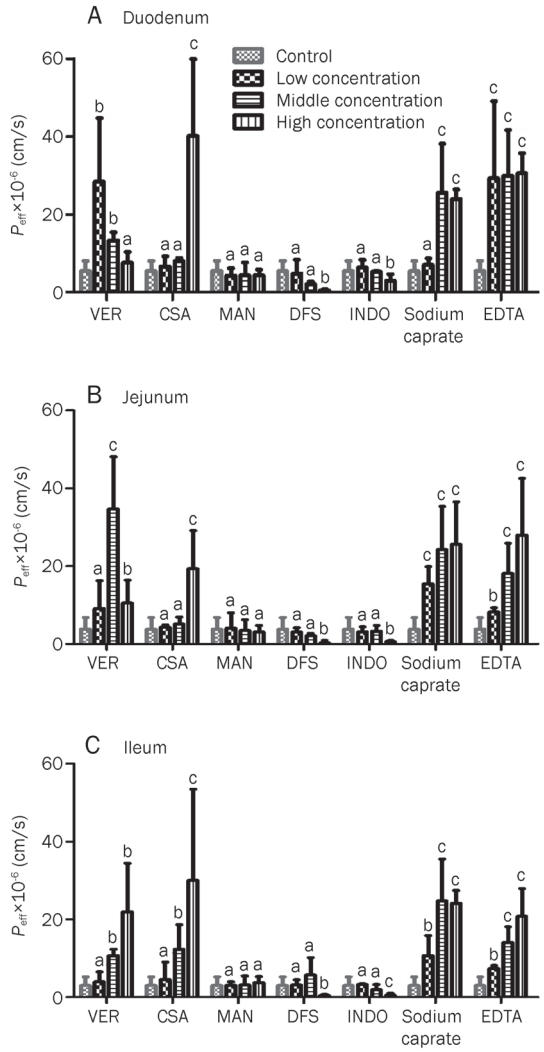

Figure 7. Effects of inhibitors at different concentrations and paracellular permeability enhancers on absorption parameters of FTA in rat single pass intestinal perfusion via duodenum, jejunum and ileum *in situ* model. Results are expressed as the mean±SD of at least four experiments. [a]*P*>0.05, [b]*P*<0.05, [c]*P*<0.01 compared with the control group. VER: 50, 100, 150 μmol/L; CSA: 5, 10, 15 μmol/L; MK571: 50, 100, 150 μmol/L; MAN: 10, 20, 30 μmol/L; INDO and DFS: 10, 20, 40 μmol/L.

results show that the permeability of FTA is enhanced as the concentrations of EDTA and sodium caprate increase, exhibiting a clear concentration-dependent effect. However, DFS and INDO at the same low (25 μg/mL), medium (50 μg/mL) and high (100 μg/mL) concentrations resulted in a significant, dose-dependent decrease in the P_{eff}-value. Treatment with DFS and INDO at the same high concentration led to a significant decrease in the P_{eff}-value compared to the control (P<0.05, P<0.01) in the duodenum, jejunum and ileum. The P_{eff}-value in the duodenum group when DFS and INDO were added showed less of a decrease than that of the jejunum and ileum groups. In addition, there was no significant difference between treatments with MAN at low (5 mg/mL), medium (10 mg/mL) and high (15 mg/mL) concentrations and the control in the duodenum, jejunum or ileum groups. Together, these results indicate that the absorption of FTA may be influenced by paracellular permeability enhancers, efflux transporters (P-gp, MRPs) and uptake transporters (OATP), which is in accordance with the results from the Caco-2 cell model.

Discussion

For drugs to be therapeutically effective, they have to possess favourable characteristics to cross the biological membranes into systemic circulation and reach the site of action. Drugs cross membranes via transcellular or paracellular routes. The transcellular pathway involves the passage of the drug across the cells, while the paracellular pathway refers to the passage of drugs between adjacent cells. The major pathway for the absorption or transport of a drug depends on its physicochemical characteristics as well as the membrane features. Salama *et al*, 2006[25] reported that lipophilic drugs cross biological membranes transcellularly, while hydrophilic drugs cross the membrane paracellularly. The results of the distribution study (Table 5) and the permeability study (Figure 5) support the conclusion that the absorption of FTA mainly involved paracellular diffusion owning to its high hydrophilicity.

Based on the single-pass intestinal perfusion *in situ* model, VER was reported as an inhibitor of P-gp and the CYP3A enzyme. The finding that the addition of VER induced the greatest increase in the P_{eff}-values at a relatively low concentration (50 μmol/L) in duodenum, a medium concentration (100 μmol/L) in the jejunum and a high concentration (150 μmol/L) in the ileum while exhibiting no concentration-dependent effect might be explained by the fact that P-gp expression was increased gradually, but CYP3A enzyme expression showed the opposite pattern. As shown in Table 7, the K_a-value of the duodenum was slightly higher than the jejunum and ileum, which is consistent with this expression pattern. Furthermore, it was also reported that CSA inhibits MRPs and OATP, while DFS and INDO inhibit OATP. Our finding that the P_{eff}-value in the duodenum group treated with CSA was higher than that of the jejunum and ileum groups while the P_{eff}-value in the duodenum group treated with DFS and INDO was decreased less than that of the jejunum and ileum groups are consistent with the report by Kusuhara *et al*, 2003[19] showing that the uptake transporter (OATP) is expressed mainly in the jejunum and ileum. Ma *et al*, 2007[18] reported that MAN was an inhibitor of SGLT1. As shown in Figure 7, there was no significant difference between the MAN and control treatments in the duodenum, jejunum or ileum groups, indicating that the absorption of FTA was not influenced by intake transport (SGLT1). The mechanism of the absorption enhancing effect of sodium caprate was proposed to be an effect on tight junctions (TJs) through PLC-dependent IP3/DAG pathways. The P_{eff}-value of FTA was enhanced as the concentration of sodium caprate was increased, exhibiting a clear concentration-dependent effect. Zornoza *et al*, 2004[26] reported that the absorption enhancing effect of sodium caprate for acamprosate showed a clear concentration-dependent effect. Therefore, our present results are consistent with the previous report. In

addition, calcium depletion by a chelating agent (EDTA) was also reported to increase paracellular permeability[21], and the P_{eff}-value of FTA was increased as the concentration of EDTA was increased, further illustrating that the absorption of FTA involved paracellular transport.

In the Caco-2 cell model *in vitro*, the P_{app}-value of FTA was enhanced as the concentrations of VER, CSA, and MK571 were increased, exhibiting a clear concentration-dependent effect. However, the P_{app}-values decreased significantly as DFS and INDO were added. In addition, the P_{app}-values increased significantly in the presence of paracellular permeability enhancers (EDTA and sodium caprate). These results indicate that the absorption of FTA primarily involves the paracellular transport route, and P-gp, MRPs and OATP might participate

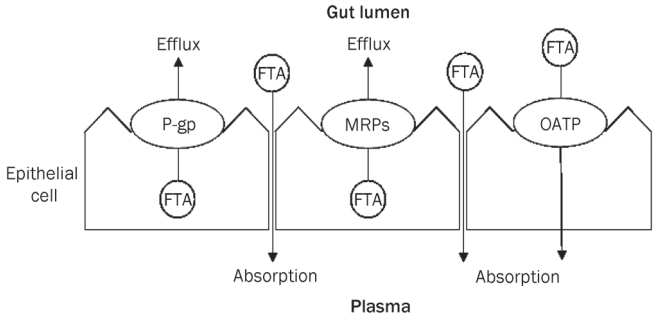

Figure 8. Possible routes for absorption of FTA.

in the absorption of FTA in the intestine as shown in Figure 8.

As shown in Table 4, the efflux ratio was <1.5 over the range of 2.6–10.4 μg/mL of FTA in the bi-directional transport studies, suggesting that the absorption of FTA is not influenced by efflux/uptake transporters[27]. However, our present study showed that the absorption of FTA was affected by the inhibitor of P-gp (VER) and the inhibitor of MRPs (CSA, MK571), as illustrated in Figure 6 and 7, which suggests that efflux transporters might influence the absorption of FTA little or that uptake transporters might participate in the absorption of FTA to counteract the effect of efflux transporters[28]. Evidence supporting this hypothesis is shown in Figure 6 and 7. The P_{app}-value and P_{eff}-value of FTA were decreased significantly by the addition of OATP inhibitors (DFS, INDO) in both the *in vitro* Caco-2 cell model and the *in situ* single-pass intestinal perfusion model. Therefore, the absorption of FTA may involve not only efflux (P-gp, MRPs) but also uptake (OATP) transporters.

As shown in Tables 4 and 7, FTA was transported at approximately a 10-fold slower rate in the Caco-2 monolayers than in the rat small intestine. Plausible explanations for the different values were that the permeability of the paracellular pathway and the absorptive surface areas of the two models were different[29, 30]. In addition, the differences in metabolism between *in situ* single-pass intestinal perfusion and *in vitro* Caco-2 cell models resulting from intestinal bacteria and enzymes[31] could also explain the differences in the absorption parameters.

According to Table 4, $P_{app\ (AP\rightarrow BL)}$ was less than 2×10^{-6} cm/s[32] due to the efflux (P-gp, MRPs) function and high hydrophilicity paired with low lipid solubility, indicating that FTA might belonged to the class III of the biopharmaceutical classification system (BCS)[33]. The permeation through biomembranes is a rate-limiting process that results in low oral BA. It was reported that chitosan and its derivatives[34], sodium caprate[35], *L*-arginine[36] and glycyrrhetinic acid, an active ingredient in *Radix Liquiritiae*[37], could modulate TJs to enhance paracellular transport. Pluronic block copolymers, like Pluronic F68, could inhibit P-gp/CYP3A4[38]. In addition, prodrug designations, like peptide prodrug modifications, could also shield FTA from the efflux pump[39]. Therefore, investigations into improving the permeability of FTA using pharmaceutical methods based on the above research and evaluating the toxicity of pharmaceutical excipients (functional excipients or additives) are required to improve the oral BA of FTA.

Acknowledgements

The present study was supported financially by the "Qing Lan" Project from Jiangsu Provincial Technology Innovation Team Support Scheme, the priority Academic Program Development of Jiangsu Higher Education Institution (No ysxk-2010) and 2012 program sponsored for scientific innovation research of college graduate in Jiangsu province (623).

Author contribution

Wei ZHOU designed experiments, performed research, analysed data, and wrote the paper. Liu-qing DI performed the research. Juan WANG, Jin-jun SHAN, Shi-jia LIU, Wen-zheng JU, and Bao-chang CAI helped write the paper.

References

1 Liu Y, Hu M. Absorption and metabolism of flavonoids in the Caco-2 cell culture model and a perfused rat intestinal model. Drug Metab Dispos 2002; 30: 370–7.
2 Helen Chan O, Sinz MW, Stewart BH. Multiple-model evaluation of absorption of a tachykinin receptor antagonist. Adv Drug Deliv Rev 1997; 23: 121–31.
3 Artursson P, Palm K, Luthman K. Caco-2 monolayers in experimental and the oretical predictions of drug transport. Adv Drug Deliv Rev 2001; 46: 27–43.
4 Hidalgo IJ, Li J. Carrier-mediated transport and efflux mechanisms in Caco-2 cells. Adv Drug Deliv Rev 1996; 22: 53–66.
5 Wang XD, Meng MX, Gao LB, Liu T, Xu Q, Zeng S. Permeation of astilbin and taxifolin in Caco-2 cell and their effects on the P-gp. Int J Pharm 2009; 378: 1–8.
6 Yu LS, Zeng S. Transport characteristics of zolmitriptan in a human intestinal epithelial cell line Caco-2. J Pharm Pharmacol 2007; 59: 655–60.
7 Painc MF, Fisher MB. Immunochemical identification of UGT isoforms in human small bowel and in Caco-2 cell monolayers. Biochem Biophys Res Commun 2000; 273: 1053–7.
8 Bohets H, Annaert P, Mannens G, Van Beijsterveldt L, Anciaux K, Verboven P, *et al*. Strategies for absorption screening in drug discovery and development. Curr Topic Med Chem 2001; 1: 367–83.
9 Zuo Z, Zhang L, Zhou LM, Chang Q, Chow M. Intestinal absorption of hawthorn flavonoids — *in vitro*, *in situ* and *in vivo* correlations. Life Sci 2006; 79: 2455–62.

10 State Pharmacopoeia Committee, 2010. Chinese Pharmacopoeia, vol.1, Beijing: Chemical Industry Press; 2010. p159.
11 Zhang LW. Extraction method, and biological activities of forsythiaside. Taiyuan: Shanxi University; 2002.
12 Wang GN, Pan RL, Liao YH, Chen Y, Tang JT, Chang Q. An LC-MS/MS method for determination of forsythiaside in rat plasma and application to a pharmacokinetic study. J Chromatogr B 2010; 878: 102–6.
13 Lu WG, Wang LL, Chen TT, Yu LF, Yang YJ, inventors; Shang ZX. Patent Agent LTD, assignee. One forsythiaside combination. China patent CN101919869A. 2010 Dec 22.
14 Zornoza T, Cano-Cebrian MJ, Nalda-Molina R, Guerri C, Granero L, Polache A. Assessment and modulation of acamprosate intestinal absorption: comparative studies using *in situ*, *in vitro* (CACO–2 cell monolayers) and *in vivo* models. Eur J Pharm Sci 2004; 22: 347–56.
15 Du Q, Di LQ, Shan JJ, Liu TS, Zhang XZ. Intestinal absorption of daphnetin by rats single pass perfusion *in situ*. Yao Xue Xue Bao 2009; 44: 922–6.
16 Walgren RA, Karnaky KJ Jr, Lindenmayer GE, Walle T. Efflux of dietary flavonoid quercetin 4′-beta-glucoside across human intestinal Caco-2 cell monolayers by apical multidrug resistance-associated protein–2. J Pharmacol Exp Ther 2000; 294: 830–6.
17 Wolffram S, Block M, Ader P. Quercetin-3-glucoside is transported by the glucose carrier SGLT1 across the brush border membrane of rat small intestine. J Nutr 2002; 132: 630–5.
18 Ma G. Study on absorptive mechanism and modulation of Hawthorn Leaves Flavonoids [D]. Chengdu: Sichuan University; 2007.
19 Kusuhara H, He Z, Nagata Y, Nozaki Y, Ito T, Masuda H, *et al*. Expression and functional involvement of organic anion transporting polypeptide subtype 3 (Slc21a7) in rat choroid plexus. Pharm Res 2003; 20: 720–7.
20 Wang L. Preparation of feisuoweima double-layer sustained release tablets and studies on fexofenadine hydrochloride intestinal absorption in rat *in vitro* [D]. Shengyang: Shengyang Pharmaceutical University; 2003.
21 Deli MA. Potential use of tight junction modulators to reversibly open membranous barriers and improve drug delivery. Biochim Biophys Acta 2009; 1788: 892–910.
22 Lindmark T, Kimura Y, Artursson P. Absorption enhancement through intracellular regulation of tight junction permeability by medium chain fatty acids in Caco-2 cells. J Pharmacol Exp Ther 1998; 284: 362–9.
23 Zhou W, Di LQ, Shan JJ, Bi XL, Chen LT, Wang LC. Intestinal absorption of forsythoside A in different compositions of Shuang-Huang-Lian. Fitoterapia 2011; 82: 375–82.
24 Konishi Y, Hagiwara K, Shimizu M. Transepithelial transport of fluorescein in Caco-2 cell monolayers and its use in *in vitro* evaluation of phenolic acids availability. Biosci Biotech Biochem 2002; 66: 2449–57.
25 Salama NN, Eddington ND, Fasano A. Tight junction modulation and its relationship to drug delivery. Adv Drug Delivery Rev 2006; 58: 15–28.
26 Zornoza T, Cano-Cebrián MJ, Nalda-Molina R, Guerri C, Granero L, Polache A. Assessment and modulation of acamprosate intestinal absorption: comparative studies using *in situ*, *in vitro* (Caco-2 cell monolayers) and *in vivo* models. Eur J Pharm Sci 2004; 24: 347–56.
27 Ping QN, editors. Gastrointestinal transport and pharmaceutical designation of ingredients in Chinese medicine. Beijing: Chemical Industry Press; 2010. p 257.
28 Rodrigues AC, Curi R, Genvigir FD, Hirata MH, Hirata RD. The expression of efflux and uptake transporters are regulated by statins in Caco-2 and HepG2 cells. Acta Pharmacol Sin 2009; 30: 956–64.
29 Pinto M, Robine-Leon S, Appay MD. Enterocyte-like differentiation and polarization of the human colon carcmoma cell line Caco-2 in culture. Biol Cell 1983; 47: 323–30.
30 Artursson P. Epithelial transport of drugs I. A model for studying the transport of drugs (β-blocking agents) over an intestinal epithelial cell line (Caco-2). J Pharm Sci 1990; 79: 476–82.
31 Zhou W, Di LQ, Bi XL, Chen LT, Du Q. Intestinal absorption of forsythoside A by rat circulation *in situ*. Yao Xua Xue Bao 2010; 45: 1373–8.
32 Rinaki E, Dokoumentzidis A, Valsami G, Macheras P. Identification of biowaivers among class II drugs: theoretical justification and practical examples. Pharm Res 2004; 21: 1567–72.
33 Sachan NK, Bhattacharya A, Pushkar S, Mishra A. Biopharmaceutical classification system: A strategic tool for oral drug delivery technology. Asian J Pharm 2009; 3: 76–81.
34 Gao Y, He L, Katsumi H, Sakane T, Fujita T, Yamamoto A. Improvement of intestinal absorption of insulin and water-soluble macromolecular compounds by chitosan oligomers in rats. Int J Pharm 2008; 359: 70–8.
35 Lindmark T, Kimura Y, Artursson R. Absorption enhancement through intracellular regulation of tight junction permeability by medium chain fatty acids in Caco-2 cells. J Pharmacol Exp Ther 1998; 284: 362–9.
36 Motlekar NA, Srivenugopal KS, Wachtel MS, Youan BC. Modulation of gastrointestinal permeability of low-molecular-weight heparin by *L*-arginine: *in-vivo* and *in-vitro* evaluation. J Pharm Pharmacol 2006; 58: 591–8.
37 Motlekar NA, Srivenugopal KS, Wachtel MS, Youan BB. Evaluation of the oral bioavailability of low molecular weight heparin formulated with glycyrrhetinic acid as permeation enhancer. Drug Develop Res 2006; 67: 166–74.
38 Huang JG, Si LQ, Jiang LL, Fan Z, Qiu J, Li G. Effect of pluronic F68 block copolymer on P-glycoprotein transport and CYP3A4 metabolism. Int J Pharm 2008; 356: 351–3.
39 Jain R, Duvvuri S, Kansara V, Mandava NK, Mitra AK. Intestinal absorption of novel-dipeptide prodrugs of saquinavir in rats. Int J Pharm 2007; 336: 233–40.

Acta Pharmacologica Sinica (2012) 33: 1080–1084
 1671-4083/12 $32.00
www.nature.com/aps

Original Article

A pharmacodynamic analysis of factors affecting recovery from anesthesia with propofol-remifentanil target controlled infusion

Bon-nyeo KOO[1, 2], Jeong-rim LEE[1, 2], Gyu-jeong NOH[3], Jae-hoon LEE[1, 2], Young-ran KANG[1], Dong-woo HAN[1, 2, *]

[1]Department of Anesthesiology and Pain Medicine and [2]Anesthesia and Pain Research Institute, Yonsei University College of Medicine, Seoul 120–752, Korea; [3]Department of Clinical Pharmacology and Therapeutics/Anesthesiology and Pain Medicine, Asan Medical Centre University of Ulsan College of Medicine, Seoul 138–736, Korea

Aim: To examine individual patient's demographic parameters and clinical variables related to return of consciousness (ROC) and the pharmacodynamic relationship between propofol effect-site concentration (C_e) and ROC from propofol-remifentanil anesthesia.
Methods: Ninety-four patients received propofol-remifentanil anesthesia using the effect-site target-controlled infusion (TCI) system. All clinical events were noted, and variables possibly related to propofol C_e at ROC were examined using linear correlation analyses. Pharmacodynamic modeling incorporating covariates was performed using NONMEM (Nonlinear Mixed Effects Modeling) VII software.
Results: The C_e values of propofol at loss of consciousness (LOC) and ROC were 4.4±1.1 μg/mL and 1.1±0.3 μg/mL, respectively. Age was negatively correlated with propofol C_e at ROC (r=-0.48, P<0.01). Including age as a covariate in C_{e50} (the effect-site concentration associated with 50% probability of return of consciousness) and λ (the steepness of the concentration-versus-response relationship) significantly improved the performance of the basic model based on the likelihood ratio test, with a significant decrease in the minimum value of the objective function. The C_{e50} in 25-, 50-, and 75-year-old patients was predicted to be 1.38, 1.06, and 0.74 μg/mL, respectively. The λ in 25-, 50-, and 75-year-old patients was predicted to be 12.23, 8.70, and 5.18, respectively.
Conclusion: Age significantly affects the relationship between propofol C_e and ROC, and pharmacodynamic modeling including age could lead to better predictions of ROC during emergence from propofol-remifentanil anesthesia.

Keywords: anesthesia; effect-site concentration; propofol; pharmacodynamic modeling; return of consciousness; target-controlled infusion

Acta Pharmacologica Sinica (2012) 33: 1080–1084; doi: 10.1038/aps.2012.85; published online 30 Jul 2012

Introduction

Anesthesiologists are concerned not only about inducing rapid and safe anesthesia, but also about achieving a comfortable and precise return of consciousness (ROC) after surgery[1]. To date, studies have focused mainly on individual effects of anesthesia induction. The ability to predict the individual propofol effect-site concentration (C_e) for ROC would allow the dose of propofol to be adjusted to achieve an adequate ROC. It would also reduce the anesthesiologists workload, save time and resources, and allow for safer patient recovery[2]. Some studies of ROC show large variations (0.8–2.7 μg/mL) in propofol C_e producing ROC from anesthesia[3,4], making it difficult to predict the minimum concentration for effective sedation and the concentration of propofol during emergence. In the absence of individual pharmacodynamic information, propofol is usually dosed on the basis of the average population requirement. Hence pharmacodynamic modeling incorporating a population approach with covariates could be clinically useful for describing the dose-response relationship.

The objectives of our study were: 1) to identify the clinical variables related to the propofol C_e at ROC and 2) to apply a population pharmacodynamic modeling approach to data from propofol-remifentanil anesthesia.

Materials and methods

This study was approved by the ethics committee of the Yonsei University Health System (4-2010-0580). Patients (aged ≥ 20 years, ASA I–II) scheduled for elective minor surgery at the Eye and ENT Severance Hospital were included from January 2011 to September 2011. Exclusion criteria were as follows: cardiac, pulmonary, hepatic or renal disease; hearing loss or other neurological deficit; past history of allergy or adverse

* To whom correspondence should be addressed.
E-mail hanesth@yuhs.ac
Received 2012-03-01 Accepted 2012-06-03

reaction to medication; any type of medication affecting the central nervous system; or body mass index more than 30. All of the patients provided written informed consent.

Anesthesia was induced according to the same standard protocol in all patients. Patients were premedicated iv with 0.1 mg of glycopyrrolate. Anesthesia was induced by effect-site target-controlled infusion (TCI) (Orchestra® Base Primea, Fresenius Vial, France) of propofol and remifentanil after the patients anthropometric data were entered. The pump was operated according to the model for propofol developed by Schnider *et al*[5, 6] and the model for remifentanil developed by Minto *et al*[7, 8]. The initial target C_e values of propofol and remifentanil were 4 μg/mL and 2 ng/mL, respectively, for induction. Loss of consciousness (LOC) was defined as a patient's inability to open their eyes in response to their name being called loudly, *ie*, a score of 3 on the Observer's Assessment of Alertness/Sedation Scale (OAA/S)[9]. If LOC was not obtained with this initial C_e, the C_e of propofol was increased in increments of 0.5 μg/mL until LOC occurred. The remifentanil C_e was maintained at 2 ng/mL. Consciousness was assessed every 10 s. At the moment of LOC, the BIS index (BIS VISTA™, Aspect Medical System, Inc, Norwood, MA, USA) and the C_e of propofol and remifentanil were recorded. Rocuronium was given (0.6 mg/kg iv) as a neuromuscular blockade. After endotracheal intubation, ventilation was mechanically controlled with 50% oxygen in an air mixture to maintain the end-tidal carbon dioxide tension at 35 to 40 mmHg. After anesthesia was induced, the C_e of propofol was titrated to maintain BIS values between 40 and 60 throughout the intraoperative period. In addition, the C_e of remifentanil was adapted to intraoperative hemodynamics throughout the surgical procedure.

At the end of surgery, propofol and remifentanil infusion was stopped. The neuromuscular block was antagonized with 0.2 mg of glycopyrrolate and 1.0 mg of neostigmine. Return of consciousness was defined as a score of 3 on the OAA/S. At the end of surgery and at ROC, the BIS value and the C_e of propofol and remifentanil were recorded by an investigator blinded to the conditions. The total amount of propofol and remifentanil, duration of infusion, and the duration of anesthesia and surgery were also recorded. The duration of anesthesia was defined as the time from the start of propofol infusion for induction to extubation of the trachea; the duration of surgery was defined as the time from surgical incision to the application of the last suture. All of the patients were administered ramosetron (Astellas Pharma Inc, Seoul, Korea) 0.3 mg and ketorolac (Hana Pharm Co, Seoul, Korea) 60 mg iv for the prevention of postoperative nausea, vomiting and pain in the operating room before the end of surgery.

Correlations between ROC and several clinical variables were determined by linear correlation analysis. Using the observed ROC, propofol C_e in the basic pharmacodynamic model was distributed between 0 (unconscious) or 1 (conscious). The relationship between the probability of ROC and the propofol C_e was analyzed using a sigmoidal E_{max} model:

$$P=1-\frac{C_e^{\lambda}}{C_{e50}^{\lambda}+C_e^{\lambda}}$$

where P is the probability of ROC from anesthesia, C_{e50} is the C_e associated with 50% probability of ROC, and λ is the steepness of the concentration-versus-response relationship.

The likelihood, L, of the observed response, R (unconscious=0, conscious=1) is described by the following equation:

$$\text{Likelihood} = R\times P+(1-R)\times(1-P),$$

where P is the probability of ROC.

Model parameters were estimated using the option "LIKELIHOOD LAPLACE METHOD=conditional" in the NONMEM (Nonlinear Mixed Effects Modeling) software (version VII; GloboMax, Hanover, MD, USA). The inter-individual random variability of C_{e50} and λ was modeled using a log-normal model. For each analysis, NONMEM computes the minimum value of the objective function, a statistic that is proportional to negative twice the log likelihood of the data. To determine the relevant covariates in the final model, a forward inclusion and backward elimination approach was used in consecutive NONMEM runs. A covariate was considered significant when its inclusion lowered the minimum value of the objective function by at least 3.85 points. The difference in the minimum value of the objective function between two nested models was approximately χ^2-distributed and could therefore be used for significance tests (P<0.05, with one degree of freedom).

Results

Ninety-four patients met the selection criteria. Fifty-five patients underwent eye surgery and 39 patients underwent ENT surgery. The duration of surgery and anesthesia were 66.9±53.0 and 97.5±54.0 min. The BIS values at baseline and LOC were 92.8±4.9 and 67.0±15.1. At LOC, the effect-site concentrations (C_es) of propofol and remifentanil were 4.4±1.1 μg/mL and 2.0±0.3 ng/mL, respectively. At the end of surgery, the BIS value, the C_es of propofol and remifentanil were 43.8±10.6, 3.2±1.0 μg/mL and 2.3±0.4 ng/mL, respectively. At ROC, the BIS value, the C_es of propofol and remifentanil were 75.7±6.0, 1.1±0.3 μg/mL and 0.8±1.0 ng/mL, respectively. Table 1 shows the data and correlation coefficients between the propofol C_e at ROC and the analyzed variables. The propofol C_e at LOC had a tendency to be positively correlated with the propofol C_e at ROC, but this correlation was not statistically significant (P=0.08). With the exception of age, no other clinical variable had a significant correlation with propofol C_e at ROC (Table 1). Age was significantly correlated with the propofol C_e at ROC, with a negative slope (P<0.01, Figure 1).

Because age was the only factor that was found to be correlated with propofol C_e at ROC, we included this as a covariate in C_{e50} and λ. This pharmacodynamic modeling including age significantly improved the performance of the basic model based on the likelihood ratio test, with a decrease the minimum value of the objective function (P<0.01). Table 2 lists the model parameter estimates for the final selected model. The

Table 1. Data values and correlation coefficients between several clinical variables and propofol effect-site concentration at return of consciousness. Data are presented as mean±SD or number.

Clinical variables	Data values	Correlation coefficient	*P* value
Sex (male/female)	53/41	0.03	0.76
Age (year)	42.8±16.5	0.48	<0.0001
Height (cm)	167±10.6	0.11	0.28
Weight (kg)	71.1±14.4	0.03	0.80
Body mass index (kg/m^2)	24.8±4.4	0.02	0.86
Propofol effect-site concentration at LOC (μg/mL)	4.4±1.1	0.23	0.08
Remifentanil effect-site concentration at ROC (ng/mL)	0.7±0.8	0.02	0.88
Duration of propofol infusion (min)	79.3±51.9	0.13	0.31
Mean propofol dose during surgery (μg·kg^{-1}·min^{-1})	176.3±97.0	0.12	0.24
Mean remifentanil dose during surgery (μg·kg^{-1}·min^{-1})	0.1±0.1	0.16	0.13

LOC, loss of consciousness; ROC, return of consciousness.

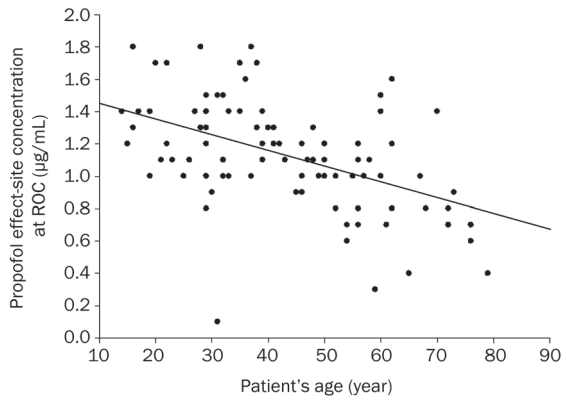

Figure 1. Linear regression between age and propofol effect-site concentration at return of consciousness (ROC). The formula of the regression is Y=-0.0097X+1.5472 (r=-0.48; P<0.01).

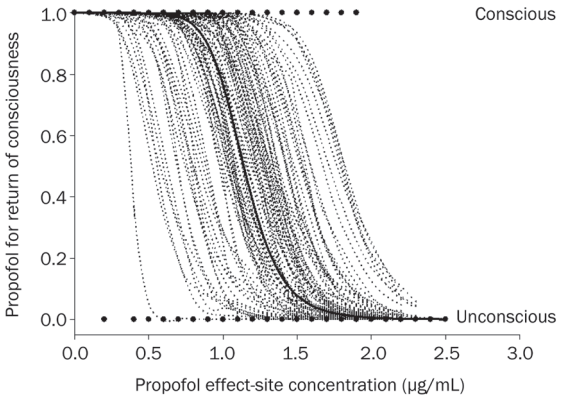

Figure 2. The relationship between the probability of return of consciousness and propofol effect-site concentration. The scattered dots are the raw data observed for all patients. The dotted lines represent individual patient fits, whereas the bold line represents the typical curve of the population data.

Table 2. Pharmacodynamic parameters.

Model	Parameter	Value	%CV	OBJF
Basic	C_{e50} (μg/mL)	1.14	32.1	643.4
	λ	9.03	–	
Final	C_{e50} (μg/mL)	1.15–0.0128×(AGE–43)	26.0	602.6
	λ	9.69–0.141×(AGE–43)	–	

AGE, age in years; CV, coefficient of variation; OBJF, minimum value of objective function; C_{e50}, effect-site concentration associated with 50% probability of return of consciousness; λ, steepness of the concentration-versus-response relationship.

relationship between the probability of ROC and propofol C_e is shown in Figure 2. The effect of age on the probability of ROC as evaluated by computed estimation is presented in Figure 3. The values of age used for the predictions correspond to the 25-, 50-, and 75-year-old patients as distributed within the studied population. The C_{e50} in 25-, 50-, and 75-year-old patients was predicted to be 1.38, 1.06, and 0.74 μg/mL, respectively. The λ in 25-, 50-, and 75-year-old patients was predicted to be 12.23, 8.70, and 5.18, respectively.

Discussion

In this study, we searched for clinical factors influencing ROC during emergence from propofol-remifentanil anesthesia and found that age was strongly correlated with ROC. In addition, upon pharmacodynamic modeling, age proved to be a significant covariate of C_{e50} and λ in the dynamic relationship between propofol C_e and ROC. This study is the first clinical investigation in which pharmacodynamic modeling of ROC has been carried out by incorporating covariates of ROC. It would be clinically advantageous if the individual propofol C_e for ROC could be predicted and applied rather than simply targeting a population-based average concentration. A nonlinear dynamic model was chosen to describe the relationship between propofol C_e and ROC, as quantal response data

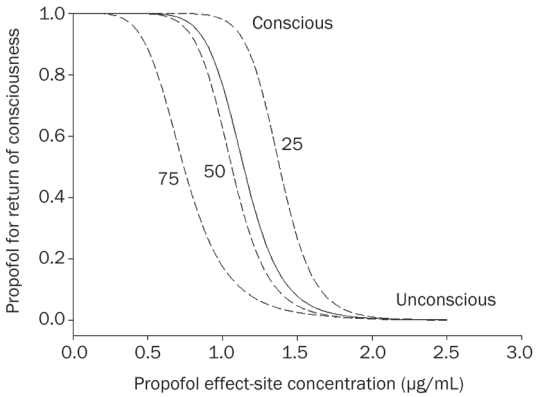

Figure 3. The fit of the logistic regression model is shown. The solid line represents the fit through the data with the age-independent model. The dotted lines are the fits predicted by the age-adjusted regression model for 25-, 50-, and 75-year-old participants.

exhibit a sigmoid relationship. A sigmoidal E_{max} model using the Hill equation provided a better model than a linear regression since this combination can estimate not only the C_{e50} value but the shape or, alternatively, the scale of the concentration-effect relationship (λ)[10]. Moreover, the C_{e50} values derived from a sigmoidal E_{max} model are not affected by extreme values to the same extent as in a linear regression model[3].

In the present study, inter-individual variability in propofol C_e at ROC could be explained by incorporating age as a covariate. Although the patients anthropometric factors except age had little influence on ROC, other potential covariates such as genetics or environmental factors might also play an important role in determining individual ROC and hence contribute to the variability of inter-individual data sets[11]. The Schnider pharmacokinetic model was developed based on data from Caucasians, so it may be necessary to examine whether the administration of propofol using a TCI technique based on the Schnider model will provide the same estimated concentration and result in the same dynamic end points in Korean patients.

According to our prediction of the probability of ROC, the propofol C_{e50} for a 25-year-old patient is around twice that for a 75-year-old patient. Younger patients may recover consciousness after receiving higher propofol concentrations than could be administered to elderly patients. The C_{e5} value, which indicates a 95% probability that a 25-year-old patient does not recover consciousness, is around 1.8 μg/mL based on our concentration-response curve. To prevent accidental awareness in young patients with propofol-remifentanil anesthesia, levels at least above this C_e should be maintained during surgery. The value of λ, representing the steepness of the dose-response curve, was greater in younger patients than in older patients. This finding suggests that younger patients may recover more abruptly than older patients, which means that young patients may be easily arousable, able to be extubated, and oriented. However, this may lead to the possibility of trauma as a result of sudden movement, and more attention should be paid to patients safety. The reverse situation could also occur. Elderly patients may experience long and more difficult recovery times. Close monitoring is necessary for elderly patients to prevent re-sedation or respiratory depression due to residual sedative effects during post-anesthetic care after initial ROC.

In older patients, a smaller propofol C_e is required at ROC for both pharmacokinetic and pharmacodynamic reasons. We used the Schnider propofol pharmacokinetic model[5, 6], which takes age into consideration, and hence the pharmacokinetic inter-patient variability caused by age would be excluded. In addition, the Schnider model, although still not perfect, has fewer limitations than the other pharmacokinetic models for propofol and therefore has the potential for being the recommended model of choice to be used for TCI[12]. The significant correlation between propofol C_e at ROC and age suggests that age has a considerable influence on the patient's sensitivity to propofol from a pharmacodynamic point of view.

When the effect of remifentanil C_e on ROC was analyzed, we did not find a significant correlation, which is consistent with previous reports[13, 14]. The C_e of remifentanil (0.7±0.8 ng/mL) at ROC was probably too low to affect ROC. However, when predicting the propofol C_e for ROC, it should be kept in mind that the C_e values of propofol might be different if another sedative, such as a benzodiazepine or a large dose of remifentanil, is also used. The type of surgery may also influence the propofol C_e at ROC. The C_e of propofol for ROC may be slightly increased in the presence of severe pain caused by major surgeries, *eg*, thoracic or abdominal surgery, compared to minor surgeries like those in our study[15]. The C_e of propofol at ROC was not correlated with the duration of propofol infusion or the mean dose of propofol during surgery, which is consistent with a previous study by Kazama *et al*[16]. These clinical contexts (duration or dose) would influence the time taken to reach an individual's propofol C_e for ROC. Current TCI devices display the time required for a calculated C_e to decline to a predetermined value of propofol C_e if the infusion is to be stopped. This allows anesthesiologists to predict the time to ROC, provided that the individual C_e at ROC is known[17].

Although not statistically significant (P=0.08), there was a tendency for the C_e of propofol for LOC to positively correlate with the propofol C_e at ROC, which suggests that patients requiring a higher propofol C_e at LOC tend to recover consciousness at a higher propofol C_e as well. We also found that the mean propofol C_e for LOC was higher than that reported in other studies (4.4±1.1 μg/mL *vs* 1.25–2.35 μg/mL)[6, 18]. One possible explanation for the higher C_e observed in our study is the use of a different pharmacokinetic model. The Schnider model predicts much faster effect-site equilibration with the blood than the Marsh model, as the equilibration constant (K_{eo}) is larger in the Schnider model than in the Marsh model (0.459 min^{-1} *vs* 0.26 min^{-1}). The predicted C_e in the Schnider model will be higher than that in the Marsh model during the induction period[19].

We note that our study has some limitations. We collected the data of dissipating propofol concentrations after stopping

infusion, which could lead to a high performance error of TCI-based predictions of propofol C_e rather than stable propofol C_e. To eliminate the confounding effects of pharmacokinetic and pharmacodynamic variability in the response of patients to a certain stimulus, constant C_e values and blood to effect-site equilibration are required[16]. However, our study design is more applicable to daily clinical practice during emergence from propofol-remifentanil anesthesia.

We conclude that age significantly affects the pharmacodynamic relationship between propofol C_e and ROC. The propofol C_e for ROC can be predicted for individual patients of different ages, and patients can be expected to require shorter recovery times and awaken quickly with early titration of propofol upon surgery completion.

Acknowledgements

This work was supported in part by the Yonsei University Research Fund of 2009.

The authors thank Dr Go Un ROH MD (Department of Anesthesiology and Pain Medicine and Anesthesia and Pain Research Institute, Yonsei University College of Medicine, Seoul, Korea) for her assistance with analysis of the data.

Author contribution

Dong-woo HAN and Bon-nyeo KOO designed research; Young-ran KANG and Jae-hoon LEE performed research; Dong-woo HAN, Jeong-rim LEE, Gyu-jeong NOH, and Jae-hoon LEE analyzed data; Dong-woo HAN wrote the paper.

References

1 Larsen B, Seitz A, Larsen R. Recovery of cognitive function after remifentanil–propofol anesthesia: a comparison with desflurane and sevoflurane anesthesia. Anesth Analg 2000; 90: 168–74.

2 Nunes CS, Ferreira DA, Antunes L, Amorim P. Clinical variables related to propofol effect-site concentrations at recovery of consciousness after neurosurgical procedures. J Neurosurg Anesthesiol 2005; 17: 110–4.

3 Wessén A, Persson PM, Nilsson A, Hartvig P. Concentration-effect relationships of propofol after total intravenous anesthesia. Anesth Analg 1993; 77: 1000–7.

4 Chortkoff BS, Eger EI 2nd, Crankshaw DP, Gonsowski CT, Dutton RC, Ionescu P. Concentrations of desflurane and propofol that suppress response to command in humans. Anesth Analg 1995; 81: 737–43.

5 Schnider TW, Minto CF, Gambus PL, Andresen C, Goodale DB, Shafer SL, *et al*. The influence of method of administration and covariates on the pharmacokinetics of propofol in adult volunteers. Anesthesiology 1998; 88: 1170–82.

6 Schnider TW, Minto CF, Shafer SL, Gambus PL, Andresen C, Goodale DB, *et al*. The influence of age on propofol pharmacodynamics. Anesthesiology 1999; 90: 1502–16.

7 Minto CF, Schnider TW, Egan TD, Youngs E, Lemmens HJ, Gambus PL, *et al*. Influence of age and gender on the pharmacokinetics and pharmacodynamics of remifentanil. I. Model development. Anesthesiology 1997; 86: 10–23.

8 Minto CF, Schnider TW, Shafer SL. Pharmacokinetics and pharmacodynamics of remifentanil. II. Model application. Anesthesiology 1997; 86: 24–33.

9 Chernik DA, Gillings D, Laine H, Hendler J, Silver JM, Davidson AB, *et al*. Validity and reliability of the Observer's Assessment of Alertness/Sedation Scale: study with intravenous midazolam. J Clin Psychopharmacol 1990; 10: 244–51.

10 Lu W, Ramsay JG, Bailey JM. Reliability of pharmacodynamic analysis by logistic regression: mixed-effects modeling. Anesthesiology 2003; 99: 1255–62.

11 Dahaba AA, Zhong T, Lu HS, Bornemann H, Liebmann M, Wilfinger G, *et al*. Geographic differences in the target-controlled infusion estimated concentration of propofol: bispectral index response curves. Can J Anaesth 2011; 58: 364–70.

12 Masui K, Upton RN, Doufas AG, Coetzee JF, Kazama T, Mortier EP, *et al*. The performance of compartmental and physiologically based recirculatory pharmacokinetic models for propofol: a comparison using bolus, continuous, and target-controlled infusion data. Anesth Analg 2010; 111: 368–79.

13 Nunes CS, Ferreira DA, Antunes L, Lobo F, Santos IA, Amorim P. Individual effect-site concentrations of propofol at return of consciousness are related to the concentrations at loss of consciousness and age in neurosurgical patients. J Clin Anesth 2009; 21: 3–8.

14 Nho JS, Lee SY, Kang JM, Kim MC, Choi YK, Shin OY, *et al*. Effects of maintaining a remifentanil infusion on the recovery profiles during emergence from anaesthesia and tracheal extubation. Br J Anaesth 2009; 103: 817–21.

15 Iwakiri H, Nagata O, Matsukawa T, Ozaki M, Sessler DI. Effect-site concentration of propofol for recovery of consciousness is virtually independent of fentanyl effect-site concentration. Anesth Analg 2003; 96: 1651–5.

16 Kazama T, Ikeda K, Morita K, Sanjo Y. Awakening propofol concentration with and without blood-effect site equilibration after short-term and long-term administration of propofol and fentanyl anesthesia. Anesthesiology 1998; 88: 928–34.

17 McCormack J, Mehta D, Peiris K, Dumont G, Fung P, Lim J, *et al*. The effect of a target controlled infusion of propofol on predictability of recovery from anesthesia in children. Paediatr Anaesth 2010; 20: 56–62.

18 Iwakiri H, Nishihara N, Nagata O, Matsukawa T, Ozaki M, Sessler DI. Individual effect-site concentrations of propofol are similar at loss of consciousness and at awakening. Anesth Analg 2005; 100: 107–10.

19 Barakat AR, Sutcliffe N, Schwab M. Effect site concentration during propofol TCI sedation: a comparison of sedation score with two pharmacokinetic models. Anaesthesia 2007; 62: 661–6.

Acta Pharmacologica Sinica (2012) 33: 1085–1094
 1671-4083/12 $32.00
www.nature.com/aps

Original Article

Tolerability, pharmacokinetics and pharmacodynamics of CMAB001, an anti-CD11a antibody, in Chinese healthy volunteers and psoriatic patients

Xian-ping LI[1, 2, 3, #], Jing LI[1, 2, 3, #], Heng YAN[4, #], Bo ZHOU[1, 2, 3], Bo-hua LI[1, 2, 3], Wei-zhu QIAN[1, 2, 3], Sheng HOU[1, 2, 3], Hao WANG[1, 2, 3, *], Fei HAO[4, *], Ya-jun GUO[1, 2, 3, *]

[1]International Cancer Research Institute, Second Military Medical University, Shanghai 200433, China; [2]National Engineering Research Center of Antibody Medicine, Shanghai 201203, China; [3]PLA General Hospital Cancer Center, PLA Postgraduate School of Medicine, Beijing 100853, China; [4]Xi-nan Hospital, Third Military Medical University, Chongqing 400038, China

Aim: To evaluate the pharmacokinetics (PK), pharmacodynamics (PD) and primary tolerability of an anti-CD11a monoclonal antibody (CMAB001) in Chinese healthy volunteers and psoriatic patients.
Methods: Two open-label studies were conducted. One was a parallel-group, single-center, dose-escalation test, including 24 healthy adult volunteers from 18 to 45 years in age. All subjects randomly received a single subcutaneous injection dose of 0.5, 1.0, or 2.0 mg/kg. The other was a multiple-dose study: 10 adult psoriatic patients were administered weekly subcutaneous injections of 1.0 mg/kg for 7 weeks.
Results: CMAB001 was well tolerated in the single- and multiple-dose studies. Slow absorption was observed in both studies. In the single-dose study, the concentration of CMAB001 reached its highest level 2 d later after the injection, and the C_{max} increased in an approximate dose-proportionate manner, while the area under curve (AUC) showed much greater than dose-proportionate increase. In the multiple-dose study, the steady-state serum concentration level was attained following the 4th injection.
Conclusion: CMAB001 exhibited a nonlinear pharmacokinetic profile over the dose range from 0.5 to 2.0 mg/kg, and was well tolerated in healthy volunteers and psoriatic patients.

Keywords: chronic plaque psoriasis; CD11a; humanized antibody; CMAB001; pharmacokinetics; pharmacodynamics; tolerability; open-label study

Acta Pharmacologica Sinica (2012) 33: 1085–1094; doi: 10.1038/aps.2012.65; published online 16 Jul 2012

Introduction

Psoriasis, a common skin disease, is an autoimmune disorder of the dermis and epidermis characterized by leukocyte infiltration into the skin and localized deregulated skin growth. Clinical manifestations in patients with this disease include white or silver scaly and raised plaques that are either red or salmon pink in color[1]. Although the precise cause of psoriasis remains an enigma, it has become increasingly clear that the activity of the lymphocytic infiltration, which consists primarily of T cells, is the driving force for the induction of the skin changes observed in psoriasis and is also required for maintenance of the plaques[1, 2].

Currently, a class of therapeutics, the "biologics", has shown promise by specifically interfering with the T-lymphocyte-mediated immune responses that are characteristic of psoriasis and other autoimmune diseases[2–9]. CD11a-specific mAb is a typical biotherapeutic product. T-lymphocyte activation and infiltration into tissues is mediated by events involving the specific interaction between a T-cell receptor and the major histocompatibility complex on antigen-presenting cells (APCs). Full activation of T lymphocytes, however, occurs only after other T-cell surface molecules engage with the APC. This costimulatory process involves the interaction between lymphocyte function–associated antigen-1 (LFA-1) and intercellular adhesion molecule-1 (ICAM-1). LFA-1 is an adhesion molecule expressed in leukocytes and is character-

# These authors contributed equally to this work.
* To whom correspondence should be addressed.
E-mail yjguo@smmu.edu.cn (Ya-jun GUO);
haofei@mail.tmmu.com.cn (Fei HAO);
hwang_smmu@163.com (Hao WANG).
Received 2012-01-18 Accepted 2012-05-09

ized by heterodimers with a common β chain (CD18) and a unique α chain (CD11a). The LFA-1: ICAM-1 interaction is a key element in stabilizing the immunologic synapse that forms between T cells and APCs and also mediates the binding of T cells to endothelial cells[2, 10, 11]. Blocking the costimulatory signaling process and inhibiting the interaction of these ligands pairs have been shown to be effective in the treatment of autoimmune diseases, such as psoriasis[4, 7, 12].

Efalizumab (Raptiva®) is a recombinant, humanized CD11a-specific mAb developed by Genentech Inc that can bind to CD11a, preventing LFA-1 binding to ICAM-1[6]. The restricted expression of CD11a limits the potential effects of efalizumab to cells that express LFA-1[13]. Since its approval in the United States in 2003, efalizumab has proven efficacious in the treatment of psoriasis. However, four cases of the rare neurological condition progressive multifocal leukoencephalopathy (PML) were reported in plaque psoriasis patients treated with efalizumab. Subsequently, in April 2009, efalizumab was withdrawn from the market by its manufacturer.

CMAB001 is a novel recombinant humanized CD11a-specific mAb that recognizes a different epitope than efalizumab. CMAB001 was developed by the National Engineering Research Center of Antibody Medicine (NERCAM) in China and is an IgG1 kappa immunoglobulin that contains human constant region sequences and murine light- and heavy-chain complementary determining region sequences. In this study, our aim is to explore the PK, PD and primary safety profiles of single/multiple doses of CMAB001 in healthy volunteers and psoriatic patients.

Materials and methods

Drug nomenclature

CMAB001 is a novel recombinant humanized CD11a-specific mAb developed by NERCAM in China. CMAB001 is directed against a different epitope than efalizumab and is an IgG1 kappa immunoglobulin that contains human constant region sequences and murine light- and heavy-chain complementary determining region sequences. The apparent molecular weight of this mAb is 150 kDa and is constructed based on DNA-recombination technology, produced as a secreted protein in a Chinese hamster ovary mammalian cell expression system, purified and formulated as a pharmaceutical-grade product. The reagent contains 80 mg active component, 16 mg sucrose, 4.53 mg *L*-histidine hydrochloride, 2.87 mg *L*-histamine, and 2.0 mg polysorbate per vial, supplied as a sterile, white-to-off-white, preservative-free, lyophilized powder for subcutaneous (sc) administration, following reconstitution with 1 mL of sterile water.

Study design and subjects

In animal studies, the highest dose tested was 50 mg/kg in experimental monkeys. According to FDA and EMEA guidelines on maximum safe starting doses in healthy volunteers, this value was divided by 6.2 to obtain the human-equivalent dose and then further divided by 15, the safety factor, to arrive at a dose of 0.5 mg/kg. Additional doses were calculated based on an escalation factor of approximately two. At the same time, we performed the efalizumab trials as a reference.

This study was conducted according to the ethical principles of the revised Declaration of Helsinki and Good Clinical Practice (GCP) requirements. The study protocol was approved by the identifiable ethics committee of the First Affiliated Hospital of the Third Military Medical University and the State Food and Drug Administration of China (SFDA). The approval number of SFDA was 2005L03600. The subjects consented to the study after a full explanation of what was involved, and signed informed consent forms prior to participation.

Part one was a single-dose, dose-escalation study. Twenty-four eligible, healthy, adult volunteers were randomly divided into three groups to receive a single subcutaneous injection with a dosage of 0.5, 1.0, or 2.0 mg/kg after consuming a standardized breakfast. The ages of these volunteers varied from 18 to 45 years; their weights were within normal limits; clinical laboratory values, ECG, and chest X-rays were within the normal ranges 7 d before medication. Each subject entered the study unit the day before administration, received CMAB001, was discharged temporarily after 24 h of observation and was then required to return to the ward for blood sample collection and a trial-related physical examination.

Part two was conducted in psoriatic patients: 10 patients were assigned to receive subcutaneous injection and were dosed with 1.0 mg/kg weekly for 7 weeks. Enrolled patients were aged 18 to 65 years, and each had a moderate-to-severe, chronic, stable condition lasting more than 6 months, body surface involvement ≥10%, PASI ≥12. After each injection, the patients were observed following a consistent amount of time. Concomitant medication was prohibited during the entire study period.

Major exclusion criteria included suspected or documented severe infection, such as erysipelas or nephritis; having received any other test drug within 3 months before medication; history of donating blood within 3 months; abnormal ECG and chest X-ray test; transaminase levels 1.5 times higher than the upper normal limit; severe concomitant disease or complications in the kidneys, heart, lung, and blood system or a malignant tumor or family history of cancer. Women had to receive a negative pregnancy test before medication. During the entire study duration, women and men had to agree to the use of contraception.

Sample collection for pharmacokinetics

In part one, blood samples for the determination of drug concentration were taken from the radial vein before administration of the drug and 0.5, 4, 12, 24, and 36 h after the injection. Blood samples were also drawn 2, 3, 5, 7, 9, 11, 14, 21, 28, 35, and 49 d after the injection. In part two, blood samples for drug concentration detection were obtained before each injection and within 48 h after the fourth, fifth, and sixth injections. Other blood samples were collected 1, 3, 5, 9, 14, 28, and 42 d after the last injection. For each sample, serum was harvested by centrifugation from 3 mL of whole blood and stored for analysis at -20 °C. Blood samples were also obtained from

subjects during their routine clinic visit for full blood count and biochemistry tests.

Sample collection for monitoring lymphocyte subsets

Blood samples were collected in tubes containing sodium citrate before administration as well as 2, 7, 28, and 49 d after the injection in part one of the study; and before the first injection and on d 14, 28, 42, 56, and 84 after the first dose (but before each injection) in part two of the study.

Anti-antibody and neutralizing anti-antibody antibody

Serum samples were drawn before injection, 14 and 49 d after injection in part one; before the first injection, d 7, 14, 21, 56, and 84 after the first dose (but before each injection) in part two, for detection of anti-CMAB001 antibodies using antibody-bridge methods.

CMAB001 serum concentration level assay

A cell-based competitive flow cytometric (C-FCM) assay was developed to determine the serum concentration of CMAB001. We chose KG-1a, a cell line expressing CD11a, as target cells. The target cells were coated with FITC-labeled-CMAB001, and these labeled CMAB001 could compete with unlabelled CMAB001 in the test samples. The FITC-labeled CMAB001 and a series of calibration standards were provided by NERCAM. The standard test protocol is summarized below: KG-1a cells were harvested from culture by centrifugation and resuspended in wash buffer (PBS buffer with 1% new bovine serum, PBSS) to give approximately 1×10^6 cells/mL. One hundred microliters of FITC-labeled-CMAB001 (2 μg/mL) and a series of calibration standards (or the test samples) were mixed with a 100-μL cell suspension in a sample tube, and then, the mixture was incubated on ice for 45 min. Wash buffer was added, and the cells were pelleted by centrifugation at 200×*g* for 5 min, and then, the supernatants were removed. This procedure was repeated three times, and then, the cells were resuspended in 300 μL of PBSS. Finally, the cells were analyzed on a FACScan (BD, NJ, USA). All serum samples were diluted and run in duplicate. Calibration standards and quality control (QC) samples were run three times. The standard curve was established using the four-parameter logistic equation: $Y=(A_1-A_2/[1+(X/X_0)^P]+A_2$. Y represents the fluorescence intensity of the sample; X represents the concentration of CMAB001; A_1 and A_2 represent the maximal and the minimal fluorescence intensity, respectively; X_0 represents half of the maximal effective concentration and P represents the slope of the logit-log plot. The calculated value of each sample was required to be within the range of the standard curve.

T lymphocyte subset monitoring assay

Psoriasis is a T cell mediated immune disorder in which $CD3^+$, $CD4^+$, and $CD8^+$ memory T cells stimulate the hyperproliferation of keratinocytes. Thus, we selected $CD3^+$, $CD4^+$, and $CD8^+$ T cells as pharmacodynamic markers to investigate the influence of CMAB001 on circulating lymphocytes. Circulating peripheral blood T cells were monitored by flow cytometric analysis. MAbs used for immunophenotyping included the following (all purchased from Becton Dickinson): mouse anti human CD3-FITC (IgG1); mouse anti human CD3-PC (IgG1); mouse anti human CD4-FITC (IgG1) and mouse anti human CD8-PE (IgG1). FITC/dimethyl formamide was added to purified mAb at 1:10 weight/weight and incubated at 25 °C for 4 h, followed by dialysis into phosphate-buffered saline containing an anion exchange resin (AG1-X8, 200-400 mesh, chloride form, Bio-Rad, New York, NY, USA). Aggregates were removed by centrifugation. Staining of peripheral blood lymphocytes (PBL) with fluorochrome-labeled mAb was performed in whole blood and analyzed on a FACScan flow cytometer (Becton Dickinson Immunocytometry Systems, San Jose, CA, USA).

Enzyme-linked immunoabsorbent assay for anti-CMAB001 antibody

Serum anti-CMAB001 antibody formation was monitored using a double-antigen enzyme-linked immunoabsorbent assay (ELISA). CMAB001 was used as the solid-phase capture reagent, and binding of anti-CMAB001 antibodies to the coated and blocked wells was detected using an HRP-conjugated CMAB001 antibody. Colorimetric measurement and data analysis were performed with an ELISA plate reader. Regression of sample optical densities from a calibration curve using rabbit anti-CMAB001 antibodies results in a quantitative range of approximately 160 to 20 000 ng/mL anti-CMAB001 idiotype equivalents. When the samples were positive, neutralizing anti-antibody antibody would subsequently be detected by the above cell-based competitive flow cytometric assay.

Validity of the method for determination

A specificity test of the assay demonstrated that 0.5 μg/mL human serum would not interfere with CMAB001 quantification. Proteins, such as human immunoglobulin, globulin and anti-CD25 monoclonal antibody, did not interfere with the determination of CMAB001 serum concentration. The recovery rates of blank serum fortified with 0.02, 0.5, and 12.5 μg/mL were 0.020%±0.002%, 0.498%±0.020%, and 11.529%±1.536%, respectively. The range of serum concentration quantification was 0.02–12.5 μg/mL. The limitation of quantification (LOQ) of the assay was demonstrated to be 0.02 μg/mL. The pass/fail criteria for the assay were determined by the performance of QC in each assay. The results were acceptable if the ratio of (detected concentration)/(QC sample concentration) was between 75% and 125% and the bias of (detected concentration–QC sample concentration)/(QC sample concentration) was between -20% and 20%. The validity of the method demonstrated that the C-FCM assay was reliable for the determination of serum levels. The specificity, sensitivity, accuracy, and precision met the requirements for the study of PK and PD.

Statistical analysis

Statistical analysis was performed with SPSS 13.0 software for Windows operating system (SPSS Inc, Chicago, IL, USA). All

grouped data were expressed as the mean±standard deviation (SD). For the comparison of the data among at least three groups, analysis of variance (ANOVA) was applied to test the differences in the data on a normal distribution, and the Kruskal-Wallis test (K–W H test) was used when data were not normally distributed. For a difference between the two groups, the *t*-test was employed when the data were of normal distribution and when the variance was homogenous; otherwise, the Wilcoxon test was used. A P value <0.05 was considered statistically significant.

Data analysis

The PK parameters in the single-dose study included the following: area under the concentration-time curve (AUC); AUC from 0 to last time point (AUC_{0-z}), AUC from 0 to infinity ($AUC_{0-\infty}$), maximum serum concentration (C_{max}), dose-normalized AUC (AUC/D), dose-normalized C_{max} (C_{max}/D), time to C_{max} (T_{max}), half-life ($t_{1/2}$), clearance rate (Cl) and distribution volume (V_d). The pharmacokinetic parameters in part two also included the AUC in steady state (AUC_{ss}), clearance rate in steady state (Cl_{ss}), distribution volume in steady state (V_{ss}), maximum steady-state concentration ($C_{max\ ss}$), minimum steady-state concentration ($C_{min\ ss}$) and the average steady-state concentration (C_{avg}). The individual PK parameters were calculated by WinNonLin® statistics software (Pharsight Corporation, USA) using non-compartment methods of analysis. AUC was calculated using the linear-up/log-down approach. C_{max} and T_{max} were defined as observed.

Results

Demographics

In part one, volunteers were college students, aged 22.8±1.4, 22.1±1.6, and 22.1±1.5 years, respectively. The three groups were well matched with respect to demographic characteristics. All of the groups remained at the hospital study unit for 24 h after each injection. In part two, the ten patients (five men, five women) were between 18 and 65 years in age (Table 1).

Single-dose pharmacokinetics of CMAB001 in healthy volunteers

No blood samples were missed in part one. The mean (±SD) serum concentration-time curves of CMAB001 following a dose of 0.5, 1.0, and 2.0 mg/kg are shown in Figure 1. Pharmacokinetic parameters were observed by non-compartmental analysis (Table 2). The data indicated that the drug concentration reached its peak level two days after injection. T_{max} ranged from 2.1 to 3.3 d among the three groups. The mean (±SD) C_{max} was 1.348±0.222 μg/mL, 3.006±0.402 μg/mL, and 5.128±0.467 μg/mL in the 0.5, 1.0, and 2.0 mg/kg dose groups, respectively. Concentrations slowly decreased with $t_{1/2}$ at 3.49±0.31 d, 5.81±0.41 d, and 7.55±0.81 d, respectively. MRT and $t_{1/2}$ showed the same tendency. Cl decreased from approximately 54.9 to 31.7 $mL^{-1}\cdot d^{-1}\cdot kg^{-1}$ among the three groups. Dose-normalized C_{max} (C_{max}/D) was 2.295±0.444 $d\cdot kg\cdot L^{-1}$, 3.006±0.402 $d\cdot kg\cdot L^{-1}$, and 2.564±0.233 $d\cdot kg\cdot L^{-1}$ in the 0.5, 1.0, and 2.0 mg/kg dose groups, respectively. Dose-normalized AUC_{0-z} showed more than a dose-proportional increase. Taken together, these results indicated that CMAB001 exhibited a nonlinear pharmacokinetic profile over the dose range of 0.5–2.0 mg/kg in healthy volunteers. A significant difference was observed in parameter dose-normalized AUC_{0-z}, Cl, C_{max}, MRT, and $t_{1/2}$ among the three groups (P<0.001, K–W H test). A dose-proportional increase of C_{max} was observed; AUC_{0-z}, $t_{1/2}$, and Cl showed non-linear pharmacokinetic profiles (Figure 2).

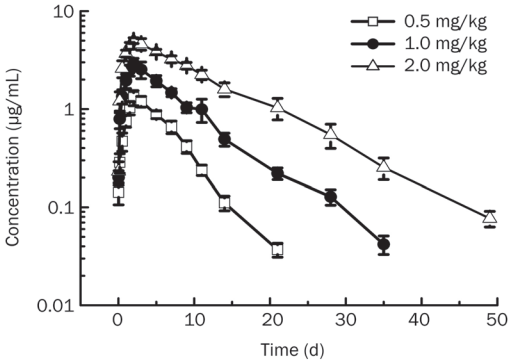

Figure 1. Logarithmic mean concentration-time curves of CMAB001 in healthy volunteers after a single subcutaneous infusion of 0.5 mg/kg. Data are expressed as the mean±SD. n=8.

Lymphocyte subset proportion in single-dose groups

We measured proportions of $CD3^+$, $CD4^+$, and $CD8^+$ T cell subsets using FCM before and after CMAB001 injection. The most rapid increases in $CD3^+$, $CD4^+$, and $CD8^+$ T cells levels were observed 7 d after the administration of CMAB001 in the three single-dose groups (Figure 3). The increase in $CD3^+$ T cells showed statistical significance compared with baseline level in all three groups, while there was not a statistically significant difference found in the 2.0 mg/kg group for $CD4^+$

Table 1. Demographic characteristics of subjects enrolled in single- and multiple-dose studies. Values were shown as mean±SD (range).

	Single-dose (part one)			Multiple-dose (part two)
	0.5 mg/kg (n=8)	1.0 mg/kg (n=8)	2.0 mg/kg (n=8)	1.0 mg/kg (n=10)
Age (years)	22.8±1.4 (20–24)	22.1±1.6 (20–24)	22.1±1.5 (20–24)	35.5±1.4 (19–48)
Sex	0 female, 8 male	0 female, 8 male	0 female, 8 male	5 female, 5 male
Height (cm)	168.3±5.5 (166–171)	166.9±5.4 (165–172)	167.6±5.9 (165–174)	166.4±2.9 (163–171)
Weight (kg)	61.8±6.6 (57–68)	59.6±5.0 (56–69)	58.2±3.5 (55–70)	61.2±3.9 (58–71)

Table 2. Pharmacokinetic parameters after a single-dose subcutaneous injection in healthy volunteers. AUC_{0-z}, area under the concentration-time curve from 0 to the last time point; $AUC_{0-\infty}$, area under the concentration-time curve from 0 to infinity; MRT, mean retention time. C_{max}/D, dose-normalized C_{max}; AUC_{0-z}/D, dose-normalized AUC_{0-z}. Data were expressed as mean±SD. n=8. ^cP≤0.001 *vs* 0.5 mg/kg. ^fP≤0.001 *vs* 2.0 mg/kg (Student's *t*-test).

Parameters	0.5 mg/kg	1.0 mg/kg	2.0 mg/kg	*P*
$AUC_{(0-z)}$ (d·μg·mL^{-1})	8.99±0.82	24.97±2.27^{cf}	62.78±6.25^{c}	<0.001 (K W H-test)
$AUC_{(0-z)}$/D	17.98±1.64	24.97±2.27^{cf}	31.39±3.13	<0.001(K W H-test)
$AUC_{(0-\infty)}$ (d·μg·mL^{-1})	9.18±0.83	25.33±2.29^{cf}	63.62±6.20^{c}	<0.001 (K W H-test)
Cl (mL^{-1}·d^{-1}·kg^{-1})	54.9±5.1	39.8±3.5^{cf}	31.7±3.0^{c}	<0.001 (K W H-test)
V_d (mL·kg^{-1})	277.0±41.0	333.0±39.0	347.0±64.0	0.026 (ANOVA)
C_{max} (μg·mL^{-1})	1.348±0.222	3.006±0.402^{cf}	5.128±0.467^{c}	<0.001 (K-W-test)
C_{max}/D	2.695±0.444	3.006±0.402	2.564±0.233	0.07 (K W H-test)
$t_{1/2}$ (d)	3.49±0.31	5.81±0.41^{cf}	7.55±0.81^{c}	<0.001 (K W H-test)
MRT (d)	6.09±0.32	8.03±0.66^{cf}	12.02±0.82^{c}	0.001 (ANOVA)
T_{max} (d)	2.13±0.35	3.25±3.15	2.13±0.35	1.000 (ANOVA)

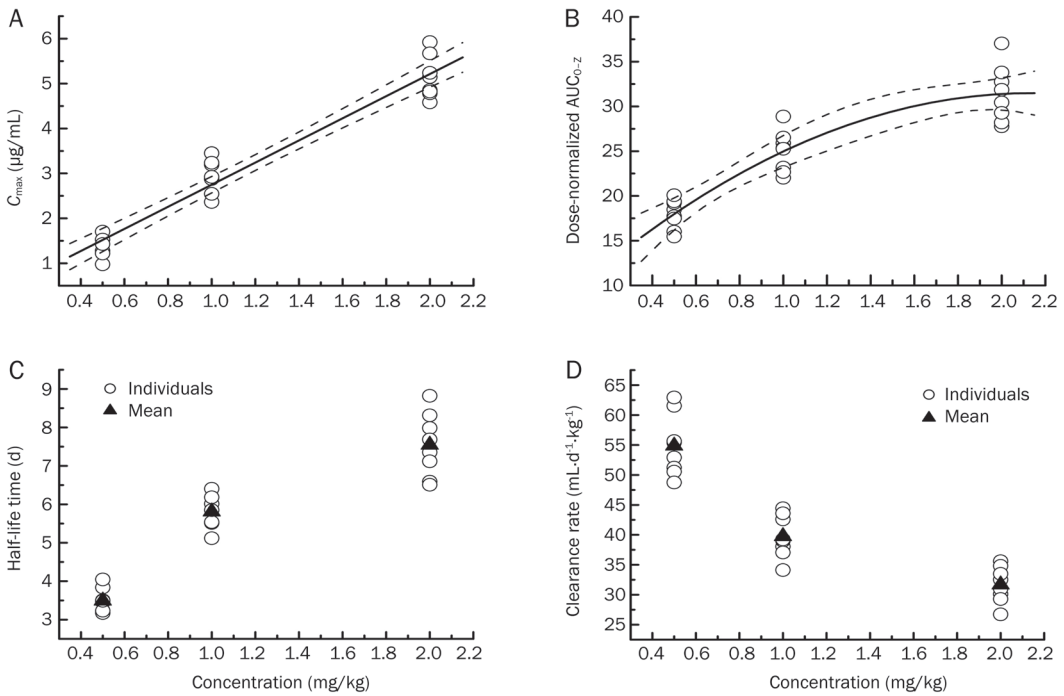

Figure 2. Linear regression analyses of C_{max} (A), polynomial regression analyses of dose-normalized AUC_{0-z} (B), graphical display scatter chart of $T_{1/2}$ (C) and Cl (D) as a function of CMAB001 over the range of 0.5–2.0 mg/kg in the single-dose groups. Dashed lines in 2A and 2B represent 95% CI.

T cells. For $CD8^+$ T cells, a statistically significant difference in increase was found only in the 0.5 mg/kg group. For $CD4^+$ T cells, the highest increase from the baseline level was observed in the 0.5 mg/kg group (Figure 3D). Increases in the absolute counts of circulating lymphocytes and white blood cells (WBC) were also observed following single-dose injections (Figure 4). Lymphocyte absolute counts increased more than 50% from baseline seven days after injection in all three groups (Figure 4B). We observed that the greatest increase in absolute lymphocyte count was 81.3% in the 1.0 mg/kg group, and the increases were 76.5% and 52.9% in the 0.5 and 2.0 mg/kg groups, respectively. The increase in absolute lymphocyte count among the three groups was significantly different (P<0.01 in the 0.5 and 1.0 mg/kg groups, P<0.05 in the 2.0 mg/kg group. Paired *t*-test). The largest increase in white blood cell count also occurred in the 1.0 mg/kg group (Figure 4D, P<0.01. Paired *t*-test).

Multiple-dose pharmacokinetics of CMAB001 in psoriatic patients

In this part of the study, 150 blood samples were collected for pharmacokinetic analysis. The mean (±SD) serum concentration-time curves of CMAB001 following multiple subcutaneous injection with a dose of 1.0 mg/kg are shown in Figure 5. The pharmacokinetics parameters are summarized in Table 3 and Table 4. The analysis showed that the steady-state serum

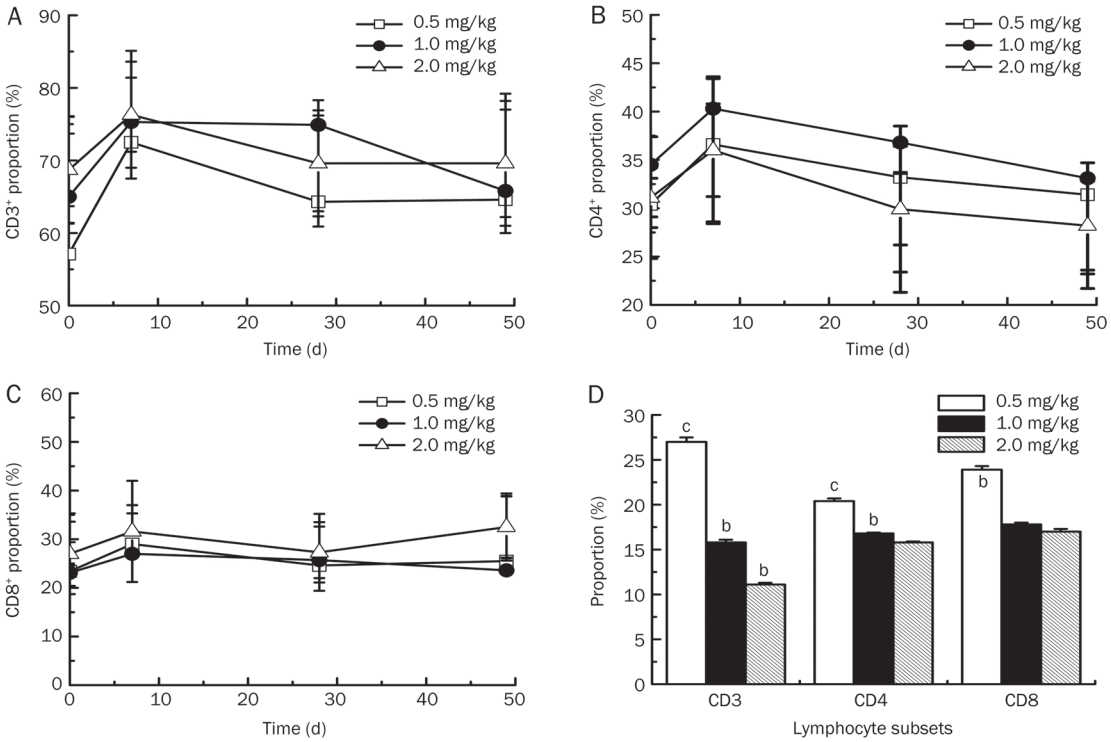

Figure 3. Mean proportion of T cell subsets [$CD3^+$ (A), $CD4^+$ (B), and $CD8^+$ (C)] before and after a single-dose subcutaneous injection of 0.5, 1.0, and 2.0 mg/kg of CMAB001 in healthy volunteers. The increased degrees of T cell subsets on d 7 after injection are compared with the baseline level (D). $^bP<0.05$, $^cP<0.01$ *vs* baseline level. Data are expressed as the mean±SD. $n=8$.

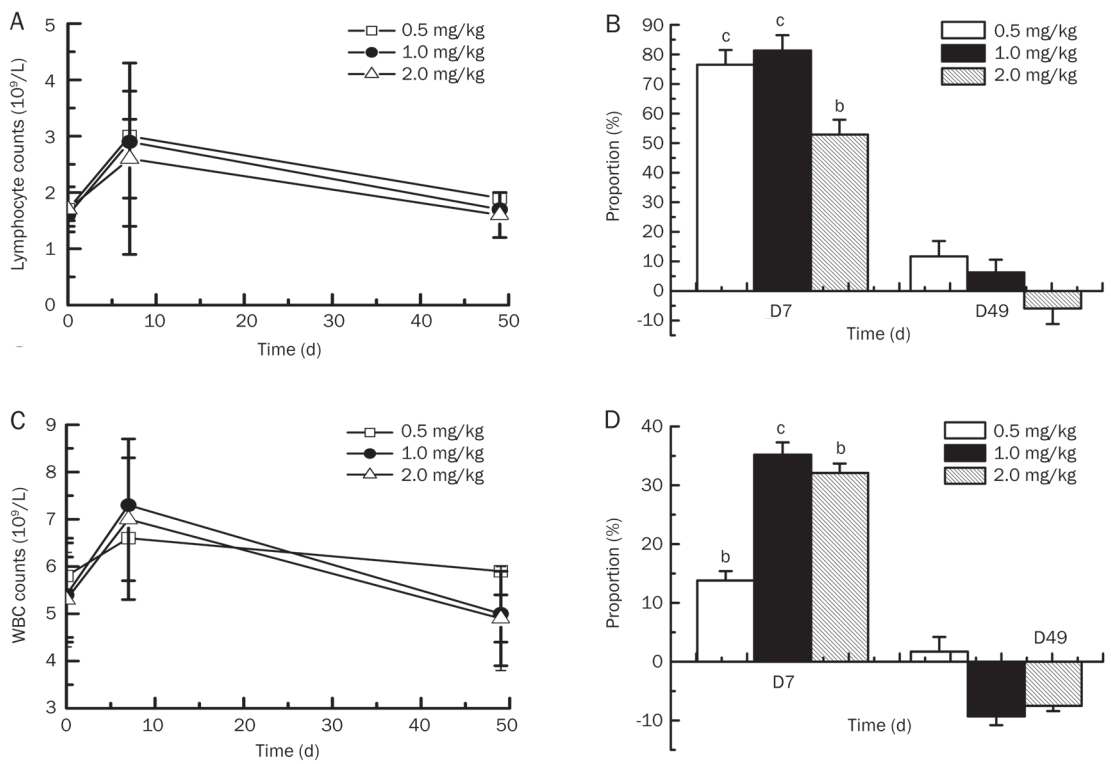

Figure 4. Mean absolute counts of lymphocytes (A) and white blood cells (WBC) (C) before and after a single-dose subcutaneous injection of 0.5, 1.0, and 2.0 mg/kg of CMAB001. The increased levels of lymphocytes (B) and white blood cells (D) on d 7 and d 49 after injections are compared with the baseline level. $^bP<0.05$, $^cP<0.01$ *vs* baseline level. Data are expressed as the mean±SD. $n=8$.

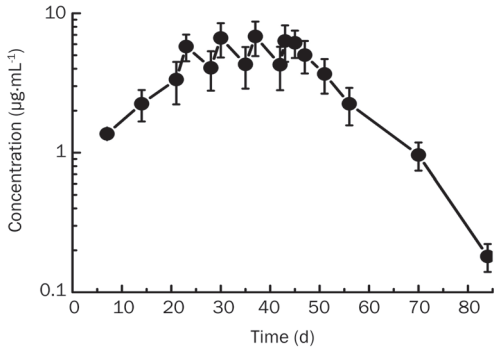

Figure 5. Logarithmic mean concentration-time curve of CMAB001 in psoriatic patients after weekly, consecutive subcutaneous injections for seven weeks at a dose of 1.0 mg/kg. Data are expressed as the mean±SD. *n*=10.

Table 3. Steady-state pharmacokinetic parameters of CMAB001 following multiple dose subcutaneous administration of 1.0 mg/kg in patients with chronic plaque psoriasis (*n*=10). AUC_{ss}, represents observed AUC_{0-z} after the last dose at steady-state.

Para-meters	$C_{min\ ss}$ (μg·mL^{-1})	$C_{max\ ss}$ (μg·mL^{-1})	C_{avg} (μg·mL^{-1})	AUC_{ss} (d·μg·mL^{-1})	Fluctua-tion (%)	Accumula-tion_index
1	7.488	10.984	8.685	60.797	40.25	2.09
2	5.025	6.911	5.976	41.835	31.55	2.14
3	5.245	7.361	6.381	44.667	33.16	2.26
4	2.902	5.106	4.350	30.447	50.67	2.29
5	3.019	4.973	4.258	29.804	45.90	2.18
6	3.957	5.961	5.098	35.683	39.31	2.34
7	3.114	5.362	4.649	32.540	48.36	2.03
8	2.835	4.667	3.908	27.357	46.86	2.25
9	4.091	5.814	5.043	35.300	34.16	2.29
10	5.086	6.722	5.854	40.977	27.93	2.19
mean	4.276	6.386	5.420	37.941	39.82	2.21
SD	1.472	1.845	1.403	9.819	7.91	0.10

concentration level was achieved following 7 weekly doses based on the similarity of peak concentrations on weeks 4, 5, 6, and 7. The mean (±SD) $C_{max\ ss}$ and $C_{min\ ss}$ were (6.386±1.845) and (4.276±1.472) μg/mL, respectively. The mean (±SD) fluctuation% and accumulation index at the steady state were 39.82%±7.91% and 2.21±0.1, respectively. The fluctuation% among patients was lower than anticipated. As the administration interval was 7 d, which is slightly shorter than the half-life (8 d) of the drug, the accumulation index was lower, suggesting that no systemic accumulation would appear upon repeated treatments with 1.0 mg/kg weekly in psoriatic patients. The mean (±SD) $t_{1/2}$ and MRT were 8.03±0.48 d and 12.84±0.78 d, respectively. After multiple injections of CMAB001, the mean (±SD) Cl was (27.7±6.0) mL·d^{-1}·kg^{-1}. The mean (±SD) V_{ss} was (322.2±76.6) mL/kg.

We also compared the pharmacokinetics of CMAB001 between healthy volunteers and psoriatic patients (Table 5). Compared with a single injection at a dose of 1.0 mg/kg in healthy volunteers, no significant difference was found in V_{ss} (P=0.719. Student's *t*-test) after multiple injections in psoriatic patients. However, significant differences were found in $t_{1/2}$, C_{max}, and Cl between the two groups (P<0.001. Student's *t*-test).

Lymphocyte subset proportion in multiple-dose group of psoriatic patients

The mean proportion of $CD3^+$, $CD4^+$, $CD8^+$ T cell subsets and the absolute value of white blood cells and lymphocyte cells were also measured in the multiple-dose study. The results showed that the absolute value of white blood cells increased by approximately 60% from the baseline level (data not shown) and then returned to baseline levels after discontinuation of CMAB001 treatment. $CD3^+$ and $CD8^+$ T-cell subsets increased sharply during the treatment period and decreased slowly after the treatment ended (Figure 6). The largest increase in $CD3^+$ and $CD8^+$ T-cell subsets was found on d 28 after the first injection, while the largest increase in $CD4^+$ T-cell

Table 4. Pharmcokinetic parameters of CMAB001 after multiple-dose infusions of 1.0 mg/kg in patients with chronic plaque psoriasis (*n*=10). MRT, mean retention time.

Parameters	AUC_{0-z} (d·μg·mL^{-1})	$AUC_{0-\infty}$ (d·μg·mL^{-1})	MRT (d)	Cl_{ss} (mL·d^{-1}·kg^{-1})	V_{ss} (mL·kg^{-1})	$t_{1/2}$ (d)	C_{max} (μg·mL^{-1})	T_{max} (d)
1	133.96	136.53	12.01	16.4	177.4	7.48	10.984	7.48
2	94.59	96.66	12.49	23.9	265.6	7.70	6.911	7.70
3	106.13	108.95	13.42	22.4	267.6	8.29	7.361	8.29
4	68.11	70.28	12.52	32.8	400.7	8.46	5.106	8.46
5	65.68	67.21	12.14	33.6	383.1	7.92	4.973	7.92
6	87.41	90.00	13.99	28.0	351.3	8.69	5.961	8.69
7	73.54	74.70	12.45	30.7	317.2	7.15	5.362	7.15
8	59.60	61.40	12.02	36.6	434.3	8.23	4.667	8.23
9	83.66	86.06	13.40	28.3	345.3	8.45	5.814	8.45
10	101.40	103.35	13.97	24.4	279.9	7.95	6.722	7.95
mean	87.41	89.51	12.84	27.7	322.2	8.03	6.386	8.03
SD	22.58	22.90	0.78	6.0	76.6	0.48	1.845	0.48

Table 5. Comparison of pharmacokinetic parameters of CMAB001 at a dose of 1.0 mg/kg in healthy adult volunteers and patients with chronic plaque psoriasis.

Parameters	Healthy volunteers (1.0 mg/kg×1) *n*=8	Psoriasis patients (1.0 mg/kg×4) *n*=10	*P* value
C_{max} ($\mu g \cdot mL^{-1}$)	3.006±0.402	6.386±1.845	<0.001 (Paired *t*-test)
$t_{1/2}$ (d)	5.81±0.41	8.03±0.48	<0.001 (Paired *t*-test)
Cl_{ss} ($mL \cdot d^{-1} \cdot kg^{-1}$)	39.8±3.5	27.7±6.0	<0.001 (Paired *t*-test)
V_{ss} ($mL \cdot kg^{-1}$)	333.0±39.0	322.2±76.6	0.719 (Paired *t*-test)
MRT (d)	8.03±0.66	12.84±0.78	<0.001 (Paired *t*-test)

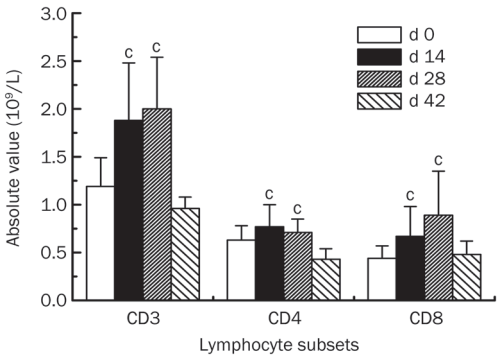

Figure 6. Absolute counts of T-cell subsets before and after consecutive subcutaneous injections of CMAB001 weekly for 7 weeks in psoriatic patients detected on d 0, 14, 28, and 42 after the first administration. $^cP<0.01$ *vs* baseline level. Data are expressed as the mean±SD. *n*=10.

subset was observed on d 14 after the first injection. These changes were clearly statistically significant. An outstanding change (202.3%) was found in the $CD8^+$ T-cell subset, which increased from baseline level (0.44×10^9/L) to the highest level (0.89×10^9/L) ($P<0.001$. Paired *t*-test).

Tolerability

Tolerability of CMAB001 was carefully monitored during the treatment and follow-up period by collection of all adverse events (AEs) and serious adverse events (SAEs). All events were summarized and any relationship to the test drug was reported. There appeared to be a dose-related increase in the occurrence of AEs in the single-dose study. In the 2.0 mg/kg group, all subjects experienced one or two AEs, but in the 0.5 and 1.0 mg/kg groups, incidence rates were only 25% and 62.5%, respectively. These AEs included common cold, fever, dizziness, and cough, all of which were considered to be related to the medication in this study but were classified as minor to moderate in severity and resolved without treatment. There were no significant clinical changes in laboratory parameters, vital signs or results of electrocardiogram examinations. In the multiple-dose study, nearly half of all AEs were first-dose effects; most of AEs occurred 2 or 4 h after the first dose administration. Other AEs were sleepiness, cough, injection-site reaction and sore throat. All of AEs were minor in severity, and disappeared without treatment. No SAEs were experienced during the entire study period. No patients withdrew from the study due to AEs.

Primary efficacy in the multiple-dose group

In a phase I trial, the main tasks are to evaluate PD, PK, and the primary safety profile of the test drug. Therefore, there was little information about the clinical response from the phase I study. In our multiple-dose study, we observed therapeutic efficacy in psoriatic patients. The Psoriasis Area and Severity Index (PASI) is the most commonly used method to evaluate disease severity. In part two, after 7 weeks of CMAB001 treatment, 20%, 20%, and 30% of patients achieved PASI90 (at least a 90% reduction in PASI score from baseline), PASI75, and PASI50, respectively. The total efficacy rate was 70%. However, 20% of patients experienced a rebound in psoriasis symptoms 2 weeks after CMAB001 discontinuation.

Anti-antibody and neutralizing anti-antibody antibody

No anti-antibody antibodies or neutralizing anti-antibody antibodies were detected.

Discussion

Antibodies to LFA-1 or its ligands that interfere with the LFA-1/ICAM-1 adhesion mechanism attenuate a broad range of T-cell-mediated reactions *in vitro* and in animal models[14-16]. In the phase I clinical study, we aimed to investigate the safety, PK, and PD parameters of CMAB001 and expected to select an appropriate dose and schedule for further phase II studies. Specifically, it was the first study in humans and was conducted in the Chinese.

In these two studies, CMAB001 exhibited a predictable PK profile and was well tolerated in both healthy volunteers and patients. No SAEs occurred after injection, and no subjects withdrew from the study because of AEs. Some drug-related, treatment-emergent AEs were observed in the single-dose studies but were minor in severity and did not require treatment. In the multiple-dose study, no serious clinical or laboratory events were observed during the course of the study. In summary, following multiple injections of a dose of 1.0 mg/kg weekly for 4 weeks, the patients were generally safe. How-

ever, in April 2009, efalizumab was withdrawn from the market after reports of an association between long-term therapy and the development of PML emerged[17]. This result raises cause for concern that CMAB001 will also increase the risk for PML. When compared with efalizumab, CMAB001 binds a different epitope on CD11a. CMAB001 has been studied in a phase II randomized, double-blind, placebo-controlled trial involving 240 Chinese patients with moderate to severe plaque psoriasis (data not shown). The patients were followed for 12 weeks. Consistent with the results of all pivotal studies prior to the approval of efalizumab, CMAB001 was generally well tolerated, no cases of PML or infections predominantly associated with immunosuppression were recognized, and there were no reports of death. The absence of PML in CMAB001 clinical trials may be attributable to a special population or the different epitopes recognized by CMAB001 and efalizumab. Nonetheless, we did not have enough evidence to rule out the possibility of PML risks of CMAB001. Additional efforts are required to investigate its potential for immunosuppression, JC-virus reactivation, and the development of PML with further treatment. Considering every newly diagnosed or suspected cases of PML, we should also take into account intensive risk-management initiatives. Recently, preliminary evidence for the treatment of other autoimmune diseases (Crohn's disease, for example) with efalizumab has attracted wide interest in these therapeutic areas[18]. This highlights the urgent need for greater awareness of and research into the screening, diagnosis and treatment of this potentially fatal disease in patients undergoing immunosuppressive therapy for chronic inflammatory disorders.

Data demonstrated that the subcutaneous injection of CMAB001 exhibited a nonlinear pharmacokinetic profile over the doses of 0.5–2.0 mg/kg in the single-dose study (Figure 2 and Table 3), which may be explained by the saturation of the specific binding to its cell surface receptor, CD11a[19, 20]. To understand the pharmacokinetic behavior of CMAB001 at different doses, we selected different approaches to assess our pharmacokinetic parameters. Linear regression was selected for C_{max} analysis; polynomial regression for dose-normalized AUC_{0-z} analysis; and graphical display scatter chart for $t_{1/2}$ and Cl was used to support our non-linear PK profile conclusion. Our data showed that there was a linear relationship between C_{max} and dosage over the range of 0.5-2.0 mg/kg (Figure 2A, R^2=0.937). There was a nonlinear behavior in dose-normalized AUC_{0-z} (Figure 2B, R^2=0.854), $t_{1/2}$ (Figure 2C), and Cl (Figure 2D). The same results were demonstrated in Table 2. The dose-normalized AUC_{0-z} were significantly different among the groups, whereas the dose-normalized C_{max} was not. $t_{1/2}$ and MRT presented gradually extended tendency, while the Cl demonstrated a decreasing trend over the dose range of 0.5–2.0 mg/kg. The data may be interpreted as the $t_{1/2}$ of the combination of two clearance mechanisms: first-order Fc-mediated clearance and zero-mediated CD11a receptor-mediated clearance of CMAB001. In our study, the V_d value was similar among the three single-dose groups and the multiple-dose group, indicating that CMAB001 was distributed primarily through the entire body fluid system. These results support the current body weight-adjusted dosing strategy. Negligible accumulation of CMAB001 was observed after multiple dosing. Because of nonlinear clearance, extended half-life, and extended mean retention time, more attention should be paid to the detection of potential accumulation toxicity in future trials.

In psoriasis, the $CD4^+$ T-cell subset seems to be important mainly during the early phase of plaque development[21, 22], but the $CD8^+$ T-cell subset represents the largest population in the epidermis and dermis in active psoriasis[23], and thus, the increase in the $CD4^+$ T-cell subset was not the key element in selecting the dosage for the multiple-dose study. In our study, the greatest increase in absolute lymphocyte and white blood cell counts occurred in the 1.0 mg/kg group. Simultaneously considering pharmacokinetics, pharmacodynamics, safety profile, and referring to the previous trial, we selected the 1.0 mg/kg dose for the multiple-dose study.

In clinical studies of efalizumab, the results showed that efalizumab can induce a marked but reversible increase in peripheral lymphocytes in psoriasis patients[23–25]. Both populations of $CD4^+$ and $CD8^+$ T cells in the peripheral blood increased, with the largest increase observed in memory $CD8^+$ T cells. A marked increase in lymphocyte count was present by d 14 of efalizumab treatment[23, 24]. In our study, similar results were obtained. In our phase I trial, the results showed that subcutaneous administration of CMAB001 induced a significant but reversible increase in peripheral white blood cell and lymphocyte cell counts. In the multiple-dose study, the increases in $CD3^+$ and $CD8^+$ T cells were more predominate. Increases in leukocyte counts and lymphocyte subsets are due to the reversal of leukocyte adhesion to the blood vessel walls[8, 16, 26, 27], which can be considered as predominantly accumulating in the peripheral blood under CMAB001 treatment of psoriasis. The blockade of percutaneous entry of the highly disease-relevant memory $CD4^+$ and $CD8^+$ T-cell populations is the therapeutic mechanism of anti-CD11a antibodies[23]; our results are consistent with this mechanism. These increases in the subset levels have clinical significance. The results show that the absolute count increases in circulating lymphocytes are unrelated to AE. However, further evaluation of the safety and efficacy of CMAB001 should be investigated in the future, pivotal phase III clinical trials.

Acknowledgements

This project was supported by the National Natural Science Foundation of China, Shanghai Commission of Science & Technology, Ministry of Science and Technology of China (973 & 863 Program Projects), National Key projects for New Drug Development and Manufacture, Shanghai Pudong Commission of Science & Technology and Shanghai Leading Academic Discipline Project (B905). Special thanks to the study subjects and referring physicians for their participation in this study.

Author contribution

Ya-jun GUO, Hao WANG, and Jing LI designed the research

study; Xian-ping LI, Jing LI, Bo ZHOU, Bo-hua LI, Heng YAN, Wei-zhu QIAN, Sheng HOU, and Fei HAO performed the research; Hao WANG contributed new analytical tools and reagents; Xian-ping LI and Jing LI analyzed the data; and Ya-jun GUO, Xian-ping LI, Jing LI, and Bo-hua LI wrote the manuscript.

References

1 Li S, Wang H, Peng B, Zhang M, Zhang D, Hou S, *et al*. Efalizumab binding to the LFA-1 αL I domain blocks ICAM-1 binding via steric hindrance. Proc Natl Acad Sci U S A 2009; 106: 4349–54.
2 Mehlis SL, Gordon KB. The immunology of psoriasis and biologic immunotherapy. J Am Acad Dermatol 2003; 49: S44–50.
3 Jullien D, Prinz JC, Langley RG, Caro I, Dummer W, Joshi A, *et al*. T-cell modulation for the treatment of chronic plaque psoriasis with efalizumab (Raptiva): mechanisms of action. Dermatology 2004; 208: 297–306.
4 Lee KH, Dinner AR, Tu C, Campi G, Raychaudhuri S, Varma R, *et al*. The immunological synapse balances T cell receptor signaling and degradation. Science 2003; 302: 1218–22.
5 Gottlieb A, Krueger JG, Bright R, Ling M, Lebwohl M, Kang S, *et al*. Effects of administration of a single dose of a humanized monoclonal antibody to CD11a on the immunobiology and clinical activity of psoriasis. J Am Acad Dermatol 2000; 42: 428–35.
6 Papp K, Bissonnette R, Krueger JG, Carey W, Gratton D, Gulliver WP, *et al*. The treatment of moderate to severe psoriasis with a new anti-CD11a monoclonal antibody. J Am Acad Dermatol 2001; 45: 665–74.
7 Dedrick RL, Bodary S, Garovoy MR. Adhesion molecules as therapeutic targets to autoimmune diseases and transplant refection. Expert Opin Biol Ther 2003; 3: 85–95.
8 Mortensen DL, Walicke PA, Wang X, Kwon P, Kuebler P, Gottlieb AB, *et al*. Pharmacokinetics and pharmacodynamics of multiple weekly subcutaneous efalizumab doses in patients with plaque psoriasis. J Clin Pharmacol 2005; 45: 286–98.
9 Gottlieb AB, Krueger JG, Wittkowski K, Dedrick R, Walicke PA, Garovoy M. Psoriasis as a model for T cell-mediated disease: immunobiologic and clinical effects with multiple doses of efalizumab, an anti-CD11a antibody. Arch Dermatol 2002; 138: 591–600.
10 Dedrick RL, Walicke P, Garovoy M. Anti-adhesion antibodies efalizumab, a humanized anti-CD11a monoclonal antibody. Transpl Immunol 2002; 9: 181–6.
11 Singri P, West DP, Gordon KB. Biologic therapy for psoriasis: the new therapeutic frontier. Arch Dermatol 2002; 138: 657–63.
12 Gottlieb AB, Miller B, Lowe N, Shapiro W, Hudson C, Bright R, *et al*. Subcutaneously administered efalizumab (anti-CD11a) improves signs and symptoms of moderate to severe plaque psoriasis. J Cutan Med Surg 2003; 7: 198–207.
13 Springer TA. Adhesion receptors of the immune system. Nature 1990; 346: 425–34.
14 Kuypers TW, Roos D. Leukocyte membrane adhesion proteins LFA-1, CR3 and p150, 95: a review of functional and regulatory aspects. Res Immunol 1989; 140: 461–86.
15 Gordon EJ, Myers KJ, Dougherty JP, Rosen H, Ron Y. Both efalizumab (LFA-1) and anti-CD11b (MAC-1) therapy delay the onset and diminish the severity of experimental autoimmune encephalomyelitis. J Neuroimmunol 1995; 62: 153–60.
16 Coffey GP, Stefanich E, Palmieri S, Eckert R, Padilla-Eagar J, Fielder PJ, *et al*. *In vitro* internalization, intercellular transport, and clearance of an anti-CD11a antibody (Raptiva) by human T-cells. J Pharmacol Exp Ther 2004; 310: 896–904.
17 Berger JR, Houff SA, Major EO. Monoclonal antibodies and progressive multifocal leukoencephalopathy. MAbs 2009; 1: 583–9.
18 James DG, Seo DH, Chen J, Vemulapalli C, Stone CD. Efalizumab, a human monoclonal anti-CD11a antibody, in the treatment of moderate to severe Crohn's disease: An open-label pilot study. Dig Dis Sci 2011; 56: 1806–10.
19 Homepage of the Food and Drug Administration. Available from: http://www.fda.gov/ohrms/ac/03/briefing/3983B1_01_Genentech-Raptiva.pdf.
20 Coffey GP, Fox JA, Pippig S, Palmieri S, Reitz B, Gonzales M, *et al*. Tissue distribution and receptor-mediated clearance of anti-CD11a antibody in mice. Drug Metab Dispos 2005; 33: 623–9.
21 Langewouters AM, van Erp PE, de Jong EM, van de Kerkhof PC. Lymphocyte subsets in peripheral blood of patients with moderate-to-severe versus mild plaque psoriasis. Arch Dermatol Res 2008; 300: 107–13.
22 Joshi A, Bauer R, Kuebler P, White M, Leddy C, Comptom P, *et al*. An overview of the pharmacokinetics and pharmacodynamics of efalizumab: a monoclonal antibody appoved for use in psoriasis. J Clin Pharmacol 2006; 46: 10–20.
23 Vugmeyster Y, Kikuchi T, Lowes MA, Chamian F, Kagen M, Gilleaudeau P, *et al*. Efalizumab (anti-CD11a)-induced increase in peripheral blood leukocytes in psoriasis patients is preferentially mediated by altered trafficking of memory CD8+ T cells into lesional skin. Clin Immunol 2004; 113: 38–46.
24 Shear NH, Langley RG, Ho V. Efalizumab, a reversible T-cell modulator for psoriasis. J Cutan Med Surg 2006; 9: 4–9.
25 Harper EG, Simpson EL, Takiquchi RH, Boyd MD, Kurtz SE, Bakke AC, *et al*. Efalizumab therapy for Atopic Dermatitis causes marked increases in circulating effector memory CD4+ T cells that express cutaneous lymphocyte antigen. J Invest Dermatol 2008; 128: 1173–81.
26 Krueger JG. The immunologic basis for the treatment of psoriasis with new biologic agents. J Am Acad Dermatol 2002; 46: 1–23.
27 Bonnekoh B, Malykh Y, Bockelmann R, Bartsch S, Pommer AJ, Gollnick H. Profiling lymphocyte subpopulations in peripheral blood under efalizumab treatment of psoriasis by multi epitope ligand cartography (MELC) robot microscopy. Eur J Dermatol 2006; 16: 623–35.

Acta Pharmacologica Sinica (2012) 33: 1095–1100
 1671-4083/12 $32.00
www.nature.com/aps

Original Article

Pharmacokinetic interactions between ilaprazole and clarithromycin following ilaprazole, clarithromycin and amoxicillin triple therapy

Shan CAO[1], Gan ZHOU[1], Dong-sheng OU-YANG[1], Hui-zi WU[1], Kui XIAO[2], Yao CHEN[1], Dong GUO[1], Lan FAN[1], Zhi-rong TAN[1], Hai-tang HU[1], Xiang-hong QIN[1], Hong-hao ZHOU[1], Wei ZHANG[1, *]

[1]*Institute of Clinical Pharmacology, Hunan Key Laboratory of Pharmacogenetics, Central South University, Changsha 410078, China;*
[2]*Department of Respiratory Medicine, The Second Xiangya Hospital, Central South University, Changsha 410011, China*

Aim: To investigate the drug interactions between ilaprazole, a new proton pump inhibitor, and clarithromycin following ilaprazole, clarithromycin and amoxicillin combination therapy.
Methods: Twelve healthy Chinese volunteers were recruited in a randomized, open-label, 3-period crossover study. All subjects were administered ilaprazole (5 mg), clarithromycin (500 mg) or a triple therapy, including ilaprazole (5 mg), clarithromycin (500 mg) and amoxicillin (1 g), twice daily for 6 consecutive days. On the 7th day, the drugs were given once, and blood samples were collected and analyzed using a well-validated HPLC/MS/MS method.
Results: Following the triple therapy, the peak concentration (C_{max}) and the area under the concentration-time curve from 0 h to 12 h ($AUC_{0\to12}$) of ilaprazole were significantly decreased, as compared with the single medication group (C_{max}: 1025.0±319.6 *vs* 1452.3±324.6 ng/mL; $AUC_{0\to12}$: 9777.7±3789.8 *vs* 11363.1±3442.0 ng·h/mL). Similar changes were found for ilaprazole sulfone (C_{max}: 5.9±0.5 *vs* 9.3±1.7 ng/mL; $AUC_{0\to12}$: 201.4±32.1 *vs* 277.1±66.2 ng·h/mL). The triple therapy significantly elevated the C_{max} of clarithromycin (3161.5±702.2 *vs* 2541.9±476.2 ng/mL).
Conclusion: The *H pylori* eradication therapy with clarithromycin, amoxicillin and ilaprazole may cause pharmacokinetic interactions that decrease the amount of ilaprazole and its metabolites and elevate that of clarithromycin.

Keywords: peptic ulcer; *Helicobacter pylori* infection; eradication therapy; clarithromycin; amoxicillin; ilaprazole; pharmacokinetics; drug interaction

Acta Pharmacologica Sinica (2012) 33: 1095–1100; doi: 10.1038/aps.2012.64; published online 23 Jul 2012

Introduction

Seventy to 90% of all peptic ulcer disease cases, one of the most common diseases influencing health around the world, are caused by *Helicobacter pylori* (*H pylori*) infection[1]. The choice of a treatment regimen for *H pylori*-positive cases is based on the principle of infection eradication[2]. With single antibiotic treatment, the eradication rate achieved is between 15% and 54% when the macrolide antibiotic, clarithromycin (CLR), is given[3] and is between 20% to 30% when the penicillin antibiotic, amoxicillin (AMX), is administrated[4]. A triple therapy comprised of a proton pump inhibitor (PPI), such as omeprazole, lansoprazole or rabeprazole, with AMX and CLR has been strongly recommended as a first-line therapy for *H pylori* eradication[5].

Previous reports indicate that following triple therapy, the rate of *H pylori* eradication achieved was 84%–95%[4, 6]. The synergistic effect of these therapies is related to pharmacokinetic interactions. It has been confirmed that triple therapy increases both the AUC and C_{max} of clarithromycin and its active metabolite 14-OH-clarithromycin[7–9]. However, the AUC of omeprazole increased almost 2-fold after concomitant administration of CLR[7], and the AUC of lansoprazole significantly increased from 3.65 to 4.59 mg·h/L after co-administration of CLR and AMX[8]. The pharmacokinetic drug interactions are likely a result of alterations in the hepatic metabolism of PPIs following combination therapy with clarithromycin, which is considered a potent inhibitor of CYP3A[10–12]. Ushiama *et al* previously published data using partial cortisol clearance as a CYP3A activity probe *in vivo* to assess the inhibition of CYP3A activity. In their study, two experimental

* To whom correspondence should be addressed.
E-mail yjsd2003@163.com
Received 2012-02-02 Accepted 2012-05-07

groups were given clarithromycin (400 mg or 800 mg), and they observed a dose-dependent inhibition of *in vivo* CYP3A activity and resultant elevation in plasma lansoprazole concentrations, which were not present in the control group that did not receive clarithromycin[13].

A new proton pump inhibitor, ilaprazole (Ila), was recently introduced. In a double-blind, parallel, randomized study, ilaprazole was shown to be as effective and well-tolerated as omeprazole for the treatment of gastric and duodenal ulcers (healed in 67.1% *vs* 62.3% and 83.7% *vs* 78.9% of patients, respectively), at a much lower dose (5 *vs* 20 mg, respectively)[14]. In another multicenter trial, 10 mg ilaprazole was found to be more effective than 20 mg omeprazole and other doses of ilaprazole over a 4-week treatment period[15].

A study on rat livers using on-line HPLC/ESI mass spectrometry found two metabolites of ilaprazole — a major product, ilaprazole sulfone, and a minor product, hydroxyl-ilaprazole[16] — implying that ilaprazole might be predominantly metabolized in the liver by CYP3A and partially by CYP2C19 in a manner similar to that of omeprazole and lansoprazole, which are metabolized into sulfoxidation and hydroxylation metabolites. However, data published by Li and Cho *et al* indicate that CYP3A5 and CYP2C19 genotypes have no impact on ilaprazole metabolism[17, 18]. Therefore, further investigation is required to determine whether pharmacokinetic interactions play a role in triple therapy using ilaprazole as a PPI.

Although its pharmacological interaction mechanisms are not fully understood, triple therapy has been used for many years in the treatment of *H pylori*-related peptic ulcer disease. Our study use ilaprazole as a novel PPI within a triple therapy regimen. The present study was designed to determine the effect of (1) clarithromycin and amoxicillin on the pharmacokinetics of ilaprazole and its metabolites and (2) ilaprazole and amoxicillin on the pharmacokinetics of clarithromycin.

Materials and methods

Materials and reagents

Ilaprazole, ilaprazole sulfone and ilaprazole thiol ether standards were obtained from the Livzon Pharmaceutical Group, Inc (purity: 99.1%, Zhuhai, China). Omeprazole standards were obtained from Sigma Chemical Company (purity: 99.5%, USA). Ilaprazole tablets were obtained from the Livzon Pharmaceutical Group, Inc (Zhuhai, China). HPLC-grade acetonitrile, methanol and methyl tert-butyl ether (MTBE) were purchased from Dikma Comp (Guangzhou, China). HPLC-grade water was obtained using a Milli-Q system (Millipore, USA). All other reagents were of analytical grade.

Subjects

This study was conducted under the approval of the Xiangya institutional review boards and with the informed consent of all the subjects. Twelve healthy, Chinese Han male volunteers with normal hepatic, renal, and hematologic function were selected for this study. All results were within the normal limits (see Table 1S). The age of the participants ranged from 21 to 27 years (mean±SD, 23.9±1.9 years), their weight ranged from 55 to 77 kg (63.7±7.8 kg), and their height ranged from 162 to 178 cm (172.2±4.2 cm). The exclusion criteria included any use of medication within 2 weeks prior to the commencement of the study, the use of tobacco or alcohol during the study, and any clinically significant illness within 3 months prior to the study. A physical examination was performed, and common laboratory parameters for hematological, hepatic and renal functions were determined, before, during and after the study to monitor the safety of drug treatment.

Study protocol

This was a randomized, open-labeled, self-controlled, 3-way crossover study. Twelve subjects were randomized into 3 groups: ilaprazole (5 mg); clarithromycin (500 mg); or ilaprazole (5 mg), clarithromycin (500 mg) and amoxicillin (1 g) combination therapy. All drugs were administered twice daily for 6 consecutive days and only once on the 7th d. After 12 h of fasting, the volunteers were given the drugs with 200 mL tap water on the morning of the 7th d. Then, 5 mL or 8 mL blood samples were collected before and 0.5, 1, 1.5, 2, 3, 4, 6, 8, 12, 24, 48, and 72 h after drug administration. The whole blood sample was centrifuged immediately, and the upper layer serums were transferred to polyethylene tubes and stored at -80 °C until analysis. After a 7-d drug elimination period between each dose, the subjects proceeded to the next phase.

Measurement of serum drug concentration

The quantitative determination of ilaprazole and its two metabolites was based on an improved LC/MS/MS method published by Zhou *et al*[16, 19]. Briefly, the chromatographic condition included a Thermo HyPURITY C18 column (150 mm×2.1 mm, 5 μm) with a mobile phase consisting of 10 mmol/L ammonium formate water-acetonitrile solution (50:50, *v/v*) at a flow rate of 0.25 mL/min. The API4000 triple quadruple mass spectrometer (Applied Biosystems, USA) was operated in multiple reactions monitoring mode via positive electrospray ionization interface.

This method displayed linearity over the concentration range of 0.23–2400.00 ng/mL for ilaprazole, 0.05–105.00 ng/mL for ilaprazole thiol ether and 0.06–45.00 ng/mL for ilaprazole sulfone. The lower limits of quantification were 0.23, 0.05, and 0.06 ng/mL for ilaprazole, ilaprazole sulfone and ilaprazole thiol ether, respectively. The intra- and inter-day precisions were all less than 15% in terms of relative standard deviation (RSD), and the accuracy was within 15% in terms of relative error (RE) for ilaprazole, ilaprazole sulfone and ilaprazole thiol ether.

The concentration of clarithromycin in plasma was determined using HPLC-MS/MS. Separation of the analytes and the internal standard (IS), roxithromycin, was performed on a Waters Xterra MS C18 column (2.11 mm×50 mm, 5 μm), with a mobile phase consisting of 20 mmol/L ammonium acetate water-acetonitrile solution (40:60, *v/v*), at a flow rate of 0.25 mL/min. The API4000 triple quadruple mass spectrometer was operated in multiple reactions monitoring mode via a positive electrospray ionization interface. The standard

curves displayed excellent linearity with no systematic bias. The lower limit of quantification of clarithromycin was 6.035 ng/mL, the intra- and inter-day precisions were all less than 15% for medium and high concentrations and less than 20% for low concentration in terms of the relative standard deviation (RSD), and the accuracy was within 15% in terms of the relative error (RE) for clarithromycin at all concentrations.

Pharmacokinetic analysis

Pharmacokinetic parameters were calculated according to a non-compartmental model using Winnonlin (Pharsight Corporation, ver 3.0, Mountain View, CA, USA). The peak concentration (C_{max}) and the time of peak concentration (T_{max}) were directly analyzed by visual inspection of the plasma concentration-time profile. The elimination rate constant (λ) was obtained by the least square fitted terminal log-linear portion of the slope of the plasma concentration-time profile, and the elimination half-life ($t_{1/2}$) was evaluated according to 0.693/λ. The area under the plasma concentration-time curve (AUC_{∞}) was evaluated by the linear trapezoidal rule and further extrapolated to infinity by dividing the last measurable concentration by λ, according to the following equation: $AUC_{\infty}=AUC_{0-t}+C_{last}/\lambda$.

Statistical analysis

All data are expressed as the mean±SD. Statistical comparisons of the mean values between different groups were performed using a paired *t*-test or an AVONA. The data were analyzed using the statistical program SPSS (Statistical Package for the Social Sciences) 11.0 for Windows (SPSS, Chicago, IL, USA). Differences were considered statistically significant at $P<0.05$. The 90% confidence intervals of the log-values of the AUC and C_{max} were determined for the bio-equivalence test. The resulting data beyond 70%–143% for C_{max} and 80%–125% for AUC in single treatment groups were considered significantly different.

Results

All 12 of the volunteers completed the 3 phases of the study under the well-performed protocol. No severe adverse events or clinically relevant deviations of laboratory parameters occurred during the study.

The pharmacokinetic interaction effect of triple therapy on clarithromycin or ilaprazole and its metabolites (ilaprazole sulfone and ilaprazole thiol-ether) were investigated by comparing the concentration and kinetic parameters of the single administration cycle with combination therapy. The pharmacokinetic parameters for the indicated drugs and ilaprazole metabolites after single and triple drug therapy are summarized in Table 1, and serum concentration-time profiles are presented in Figure 1.

The maximum concentration (C_{max}) of ilaprazole was significantly decreased after combination therapy compared with single treatment (1025.0±319.6 *vs* 1452.3±324.6 ng/mL, $P=0.002$). The $AUC_{0\to12}$ and $AUC_{0\to\infty}$ of ilaprazole were 9777.7±3789.8 and 9870.5±3910.7 ng·h/mL in the triple therapy group, which were much lower than the corresponding values in the single treatment group (11363.1±3442.0 and 11438.8±3473.5 ng·h/mL, respectively), but the differences did not reach statistical significance.

Following triple therapy, the mean residence time (MRT) and the total clearance/systemic bioavailability (CL_{tot}/f) of ilaprazole increased compared to the single treatment period, whereas the elimination half-life ($t_{1/2}$) decreased slightly.

In the triple therapy group, the 90% confidence intervals (CIs) of C_{max}, $AUC_{0\to12}$, and $AUC_{0\to\infty}$ were 58.3% to 80.5%, 70.7% to 99.9%, and 70.7% to 100.1% (Table 2), respectively, which represents a decrease of 24.9%, 8.3%, and 8.2% compared with the corresponding values in the single treatment group, respectively. All of these data fell completely beyond the equivalence range of 80%–125% for AUC and 70%–143% for C_{max}.

The changes tendency of pharmacokinetic parameters of

Table 1. Pharmacokinetic parameters of ilaprazole (IIa) and its metabolites (Sulfone and Thiol ether), clarithromycin (CLR), following single and ilaprazole clarithromycin and amoxicillin (AMX) triple therapy. Mean±SD. $n=12$. [b] $P<0.05$.

Treatment	$T_{1/2}$ (h)	C_{max} (ng/mL)	T_{max}* (h)	$AUC_{(0\to t)}$ (ng·h/mL)	$AUC_{(0\to\infty)}$ (ng·h/mL)	MRT (h)	CL/F (L/h)
IIa	10.1±3.2	1452.3±324.6	3 (2–4)	11363.1±3442.0	11438.8±3473.5	9.8±3.0	0.4±0.2
IIa+AMX+CLR	9.3±3.7	1025.0±319.6[b]	3 (1.5–6)	9777.7±3789.8[b]	9870.5±3910.7[b]	10.1±2.9	0.5±0.2
Sulfone (IIa)	19.1±9.1	9.3±1.7	4 (0.5–8)	277.1±66.2	308.0±95.6	21.6±3.1	
Sulfone (IIa+AMX+CLR)	20.8±6.0	5.9±0.5[b]	6 (0.5–12)	201.4±32.1[b]	224.7±47.7[b]	22.7±2.5	
Thiol ether (IIa)	11.9±7.2	15.7±7.1	4 (1.5–6)	246.0±178.3	272.8±214.5	13.6±5.3	
Thiol ether (IIa+AMX+CLR)	13.1±6.1[b]	16.0±7.7	3 (0.5-6)[b]	268.4±220.9	279.3±220.5	17.6±9.4[b]	
CLR	10.9±2.9	2541.9±476.2	1.5 (1.5–2)	29772.7±4781.9	30254.9±5240.4	12.8±2.6	16.5±3.0
CLR+AMX+IIa	8.5±1.4	3161.5±702.2[b]	1.5 (1.5–4)	29953.4±6474.4	30045.5±6490.6	10.4±1.2[b]	16.6±4.2

* T_{max} was described by median (range).

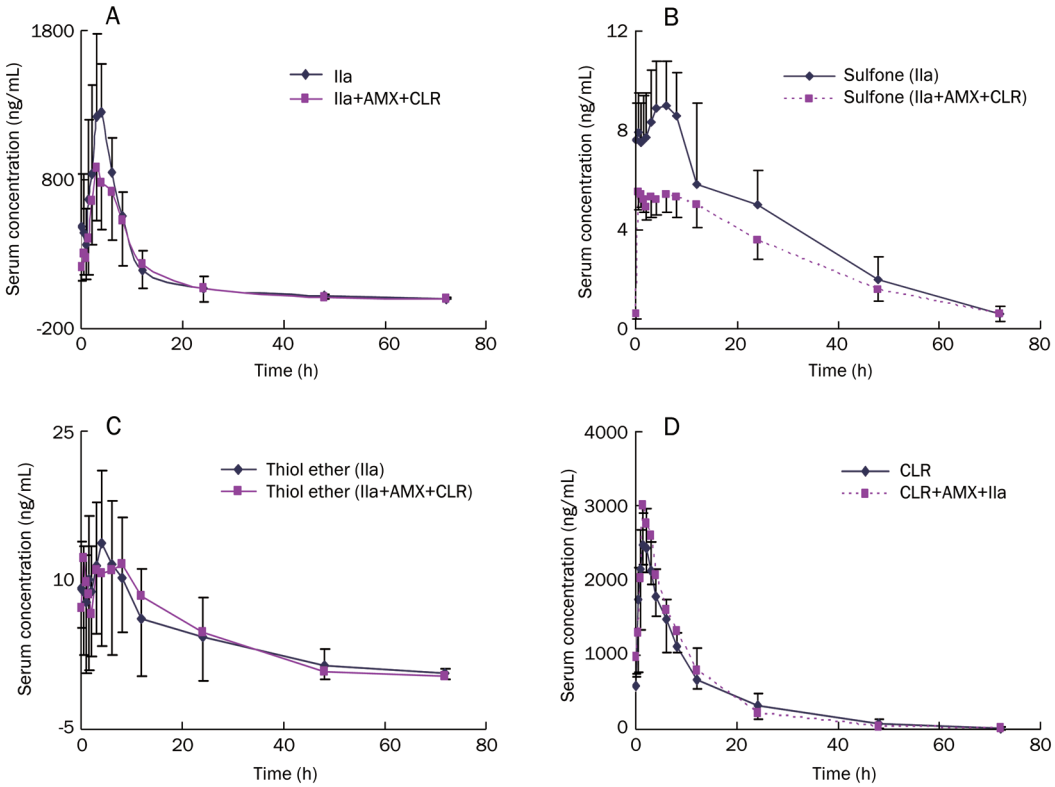

Figure 1. Serum concentrations of ilaprazole (A), ilaprazole sulfone (B), ilaprazole thiolether (C), clarithromycin (D), expressed as mean±SD and regression line after administration of ilaprazole alone and with amoxicillin and clarithromycin. IIa, ilaprazole; AMX, amoxicillin; CLR, clarithromycin.

Table 2. Test of bio-euivalence after administration of ilaprazole alone and with amoxicillin and clarithromycin.

Treatment	Point estimates (90% confidence interval)		
	$AUC_{0\to t}$	$AUC_{0\to\infty}$	C_{max}
IIa IIa+AMX+CLR	81.4 (70.7–99.9)[a]	84.1 (70.7–100.1)[a]	68.5 (58.3–80.5)[a]
Sulfone Sufone (IIa+AMX+CLR)	80.4 (69.4–96.4)[a]	83.5 (69.5–96.4)[a]	66.3 (58.4–77.2)[a]
Thiol ether Thiol ether (IIa+AMX+CLR)	109.1 (69.9–170.3)[a]	107.7 (72.9–159.1)[a]	102.8 (76.8–137.4)
CLR CLR+AMX+IIa	99.5 (81.5–121.5)	98.4 (80.1–120.9)	122.6 (100.7–149.2)[a]

[a] Point estimates (90% confidence interval) in triple therapy beyond the set value in single therapy.

ilaprazole sulfone, the major ilaprazole metabolite, was similar to that of its parent drug, ilaprazole. We observed a large difference in the C_{max} values between the triple therapy group (5.9±0.5 ng/mL) and the single therapy group (9.3±1.7 ng/mL; P=2.25×10^{-5}). A smaller difference was observed between the $AUC_{0\to12}$ and $AUC_{0\to\infty}$ of ilaprazole sulfone following triple therapy and single therapy (201.4±32.1 *vs* 277.1±66.2 ng·h/mL, P=1.46×10^{-9} and 224.7±47.7 ng·h/mL *vs* 308.0±95.6 ng·h/mL, P=2.36×10^{-8}, respectively). In the triple therapy group, the 90% CIs of C_{max}, $AUC_{0\to12}$ and $AUC_{0\to\infty}$ were significantly decreased by 30.4%, 22.1%, and 21.3% compared with the corresponding values in the single treatment group (Table 2).

For ilaprazole thiol ether, the T_{max} was reached at 3 h (median, range 0.5–6 h) after combination treatment, which was significantly faster than that of single treatment, which was reached at 4 h (median, range 1.5–6 h) (P=0.009). A small increase was observed in the C_{max} of the combination treatmeant group (16.0±7.7 ng/mL) compared with the single therapy group (15.7±7.1 ng/mL), but this difference was not significant. A slight increase was observed in $AUC_{0\to12}$ and $AUC_{0\to\infty}$ after combination therapy compared to single therapy (268.4±220.9 *vs* 246.0±178.3 ng·h/mL, P=0.728; 279.3±220.5 *vs*

272.8±214.5 ng·h/mL, P=0.736, respectively). The 90% CIs of $AUC_{0\to12}$ and $AUC_{0\to\infty}$ in the combination treatment group were beyond 80%–125%, and the C_{max} was within the 70%–143% CI range in the single treatment group.

For clarithromycin, a 29.8% increase in C_{max} was measured after combination treatment compared with single treatment (3161.5±702.2 *vs* 2541.9±476.2 ng/mL, P=0.0089. The 90% CIs of C_{max} following the three-drug regimen was beyond the range of 70%–143%, and the other parameters were altered slightly without any statistical significance.

Discussion

No significant positive synergistic effect was found between ilaprazole, clarithromycin and amoxicillin in this study. Unexpectedly, when combined with clarithromycin and amoxicillin, the plasma concentrations of ilaprazole were lower than those of single ilaprazole administration over a 6-day course of therapy. The mean C_{max}, $AUC_{0\to12}$, and $AUC_{0\to\infty}$ were decreased by 24.9%, 8.3%, and 8.2%, respectively, when ilaprazole was given in combination compared to its administration as a single agent. The significant decrease in C_{max}, the decreased AUC and the lack of alteration in the $T_{1/2}$ of ilaprazole in serum indicate that the reduced plasma concentrations observed in our study were likely due to diminished absorption as opposed to alterations in metabolism.

The significant decrease in the C_{max} and AUC of ilaprazole sulfone after triple therapy support this consideration. The same trend was considered to be due to decreased absorption of the parent drug; however, the AUC of ilaprazole thiol ether did not change after triple therapy, which supports Zhou's report demonstrating that it is a relatively minor metabolite[16].

Early studies investigated the effect of clarithromycin — an accepted, potent inhibitor of CYP3A — on the pharmacokinetics of PPIs because *in vivo* and *in vitro* studies suggested that PPIs, such as omeprazole and lansoprazole, are metabolized, at least in part, by CYP3A4. It was previously demonstrated that the plasma exposure of omeprazole and lansoprazole increased almost 2-fold[7, 13] and 1.3-fold[8], respectively, when given simultaneously with clarithromycin. Compared with omeprazole, esomeprazole metabolism is more dependent on CYP3A. One study indicated that clarithromycin decreased the rate of esomeprazole metabolism, which doubled the AUC values, regardless of the CYP2C19 genotype[9]. The pharmacokinetics of rebeprazole, which is metabolized by a non-enzymatic pathway with minor CYP2C19 and CYP3A4 involvement, were not altered by clarithromycin or verapamil (a potent CYP3A inhibitor), irrespective of the CYP2C19 genotype[20].

For ilaprazole, Li and Cho reported that the CYP3A5 and CYP2C19 genotypes had no impact on ilaprazole metabolism in healthy Chinese and Korea subjects[17, 18]. Additionally, our previous study evaluating the effect of the CYP3A phenotype (indicated by 1-OH midazolam/midazolam ratio) on ilaprazole metabolism showed no correlation between the CYP3A phenotype and ilaprazole metabolism. The reduced influence of CYP3A on ilaprazole metabolism may explain why ilaprazole and clarithromycin did not produce synergistic effects in our study. To date, no transporters involved in ilaprazole absorption and metabolism have been identified. The reason for the decreased absorption of ilaprazole after triple therapy warrants further investigation.

It is well established that amoxicillin is primarily excreted as a pro-drug and is not metabolized in the liver. Mainz reported that the pharmacokinetics of amoxicillin were not altered by combination therapy with lansoprazole and clarithromycin[8], which is consistent with other reports that demonstrated no effects of omeprazole on the pharmacokinetics of amoxicillin[21–23]. Therefore, in present study, we did not compare the plasma concentration of amoxicillin alone with combination therapy because of its non-metabolic characteristics.

In this study, the pharmacokinetic parameters of clarithromycin were comparable with those of other studies[23, 24]. Early studies found that the AUC of CLR increased when omeprazole was given simultaneously with clarithromycin[7], whereas only the T_{max} was increased with lansoprazole coadministration[8]. In our study, an increased C_{max} of CLR was the only alteration observed after combination therapy, and this effect was likely a result of increased absorption due to the effect of ilaprazole on gastric pH elevation[10, 11]. Because clarithromycin tends to be degraded into an inactive form in low pH environments, one possible reason for the observed synergy was due to the higher bioavailability of clarithromycin in low hypoacidic environments[10, 11]. Therefore, PPIs may enhance the absorption of clarithromycin due to a sustained elevation of pH[12].

Our study did not measure ilaprazole concentrations in urine, which may have given us direct evidence of the bioavailability of this compound. However, we observed a decline in the major metabolite of ilaprazole after simultaneous administration with clarithromycin and amoxicillin, which indicates that the decrease in ilaprazole absorption is due to another mechanism. Thus, the urine concentration of clarithromycin should be analyzed in further studies to provide more evidence for this hypothesis.

In summary, our study reveals a drug interaction between a new proton pump inhibitor, ilaprazole, and clarithromycin after triple drug combination therapy. We observed a decrease of ilaprazole and a slight increase of clarithromycin. However, these effects were not dose-dependent and did not affect the therapeutic effects of these drugs.

Acknowledgements

We would like to thank Mary W ROEDERER, PharmD, BCPS, at the UNC Eshelman School of Pharmacy, Chapel Hill, NC, USA, for her contribution to the preparation of this manuscript.

This work was supported by the National Natural Science Foundation of China (No 30801421, 30901834, and 30873089), the Huge Project to Boost Chinese Drug Development, (No 2009ZX09501-032), the 863 Project (No 2009AA022710, 2009AA022703, and 2009AA022704), the New Century Excellent Talents Project (NCET-10-0843) and Funda-

mental Research Funds for the Central Universities (No 2010QZZD010).

Author contribution

Shan CAO, Dong-sheng OU-YANG, Dong GUO, Lan FAN, Hong-hao ZHOU, and Wei ZHANG designed research; Shan CAO, Gan ZHOU, Hui-zi WU, Kui XIAO, Yao CHEN, and Zhi-rong TAN performed research; Hai-tang HU and Xiang-hong QIN contributed new reagents or analytic tools; Shan CAO, Dong-sheng OU-YANG, and Wei ZHANG analyzed data; Shan CAO, Lan FAN, and Wei ZHANG wrote the paper.

Supplementary information

Supplementary table (Table 1S) is available at the Acta Pharmacologica Sinica website.

References

1 Pounder RE, Ng D. The prevalence of Helicobacter pylori infection in different countries. Aliment Pharmacol Ther 1995; 9: 33–9.
2 Malfertheiner P, Megraud F, O'Morain C, Hungin AP, Jones R, Axon A, *et al*. Current concepts in the management of Helicobacter pylori infection — the Maastricht 2–2000 Consensus Report. Aliment Pharmacol Ther 2002; 16: 167–80.
3 Peterson WL, Graham DY, Marshall B, Blaser MJ, Genta RM, Klein PD, *et al*. Clarithromycin as monotherapy for eradication of Helicobacter pylori: a randomized, double-blind trial. Am J Gastroenterol 1993; 88: 1860–4.
4 Hirschl AM, Rotter ML. Amoxicillin for the treatment of Helicobacter pylori infection. J Gastroenterol 1996; 31: 44–7.
5 van der Hulst RW, Keller JJ, Rauws EA, Tytgat GN. Treatment of Helicobacter pylori infection: a review of the world literature. Helicobacter 1996; 1: 6–19.
6 Lamouliatte H, Cayla R, Zerbib F, Forestier S, de Mascarel A, Joubert-Collin M, *et al*. Dual therapy using a double dose of lansoprazole with amoxicillin versus triple therapy using a double dose of lansoprazole, amoxicillin, and clarithromycin to eradicate Helicobacter pylori infection: results of a prospective randomized open study. Am J Gastroenterol 1998; 93: 1531–4.
7 Calabresi L, Pazzucconi F, Ferrara S, Di Paolo A, Tacca MD, Sirtori C. Pharmacokinetic interactions between omeprazole/pantoprazole and clarithromycin in health volunteers. Pharmacol Res 2004; 49: 493–9.
8 Mainz D, Borner K, Koeppe P, Kotwas J, Lode H. Pharmacokinetics of lansoprazole, amoxicillin and clarithromycin after simultaneous and single administration. J Antimicrob Chemother 2002; 50: 699–706.
9 Hassan-Alin M, Andersson T, Niazi M, Liljeblad M, Persson BA, Rohss K. Studies on drug interactions between esomeprazole, amoxicillin and clarithromycin in healthy subjects. Int J Clin Pharmacol Ther 2006; 44: 119–27.
10 Gustavson LE, Kaiser JF, Edmonds AL, Locke CS, DeBartolo ML, Schneck DW. Effect of omeprazole on concentrations of clarithromycin in plasma and gastric tissue at steady state. Antimicrob Agents Chemother 1995; 39: 2078–83.
11 Unge P, Andersson T. Drug interactions with proton pump inhibitors. Drug Saf 1997; 16: 171–9.
12 Ateshkadi A, Lam NP, Johnson CA. Helicobacter pylori and peptic ulcer disease. Clin Pharm 1993; 12: 34–48.
13 Ushiama H, Echizen H, Nachi S, Ohnishi A. Dose-dependent inhibition of CYP3A activity by clarithromycin during Helicobacter pylori eradication therapy assessed by changes in plasma lansoprazole levels and partial cortisol clearance to 6beta-hydroxycortisol. Clin Pharmacol Ther 2002; 72: 33–43.
14 hHo KY, Kuan A, Zano F, Goh KL, Mahachai V, Kim DY, *et al*. Randomized, parallel, double-blind comparison of the ulcer-healing effects of ilaprazole and omeprazole in the treatment of gastric and duodenal ulcers. J Gastroenterol 2009; 44: 697–707.
15 Wang L, Zhou L, Lin S, Hu H, Xia J. A new PPI, ilaprazole compared with omeprazole in the treatment of duodenal ulcer: a randomized double-blind multicenter trial. J Clin Gastroenterol 2011; 45: 322–9.
16 Zhou G, Shi S, Zhang W, Tan Z, Chen Y, Guo D, *et al*. Identification of ilaprazole metabolites in human urine by HPLC-ESI-MS/MS and HPLC-NMR experiments. Biomed Chromatogr 2010; 24: 1130–5.
17 Cho H, Choi MK, Cho DY, Yeo CW, Jeong HE, Shon JH, *et al*. Effect of CYP2C19 genetic polymorphism on pharmacokinetics and pharmacodynamics of a new proton pump Inhibitor, Ilaprazole. J Clin Pharmacol 2012; 52:976–84.
18 Li Y, Zhang W, Guo D, Zhou G, Zhou H, Xiao Z. Pharmacokinetics of the new proton pump inhibitor ilaprazole in Chinese healthy subjects in relation to CYP3A5 and CYP2C19 genotypes. Clin Chim Acta 2008; 391: 60–7.
19 Zhou G, Tan ZR, Zhang W, Ou-Yang DS, Chen Y, Guo D, *et al*. An improved LC-MS/MS method for quantitative determination of ilaprazole and its metabolites in human plasma and its application to a pharmacokinetic study. Acta Pharmacol Sin 2009; 30: 1330–6.
20 Shimizu M, Uno T, Yasui-Furukori N, Sugawara K, Tateishi T. Effects of clarithromycin and verapamil on rabeprazole pharmacokinetics between CYP2C19 genotypes. Eur J Clin Pharmacol 2006; 62: 597–603.
21 Londong W, Gorgas R, Pommerien W, Marsch–Ziegler U, Semmler P, Rost KL, *et al*. Effect of different omeprazole doses combined with amoxicillin on intragastric pH, amoxicillin bioavailability and Helicobacter pylori eradication in duodenal ulcer patients. Gastroenterology 1995; 108: A153.
22 Pommerien W, Braun M, Idström JP, Wrangstadh M, Londong W. Pharmacokinetic and pharmacodynamic interactions between omeprazole and amoxicillin in Helicobacter pylori-positive healthy subjects. Aliment Pharmacol Ther 1996; 10: 295–301.
23 Goddard AF, Jessa MJ, Barrett DA, Shaw PN, Idstrom JP, Cederberg C, *et al*. Effect of omeprazole on the distribution of metronidazole, amoxicillin, and clarithromycin in human gastric juice. Gastroenterology 1996; 111: 358–67.
24 Ferrero JL, Bopp BA, Marsh KC, Quigley SC, Johnson MJ, Anderson DJ, *et al*. Metabolism and disposition of clarithromycin in man. Drug Metab Dispos 1990; 18: 441–6.